SYNTHESIS OF INTEGRATED NANOCATALYSTS WITH MESOPOROUS SILICA/SILICATE AND MICROPOROUS MOFS

ZHAN GUOWU

(B.Eng. & M.Eng., Xiamen University, China)

A THESIS SUBMITTED

FOR THE DEGREE OF DOCTOR OF PHILSOPHY

NUS GRADUATE SCHOOL FOR INTEGRATIVE SCIENCES AND ENGINEERING

NATIONAL UNIVERSITY OF SINGAPORE

2016

Declaration

I hereby declare that the thesis is my original work and it has been written by me in its entirety. I have duly acknowledged all the sources of information which have been used in the thesis.

This thesis has also not been submitted for any degree in any university previously.

_____

Zhan Guowu

10 July 2016

Acknowledgements

I would like to express my sincere gratitude to all who have given me help and support on my PhD study and research.

Firstly, I would like to thank my supervisor Prof. Zeng Hua Chun for his kind guidance and continuous support in the past four years. His vast knowledge and skills in nanomaterials synthesis, characterization and application always provide me the right research directions in all projects presented in this dissertation. He also gave me the freedom to explore my scope of knowledge in other research fields besides of nanomaterials research. His encouragement gave me the confidence to overcome the difficulties in all the time of research experiments and writing of this dissertation.

I would also like to thank my thesis advisor committee (TAC) members: Prof. Chung Tai-Shung and Prof. Li Xu, for their encouragement and insightful comments during my TAC meetings. Their valuable suggestions always help me solve the problems in my projects more easily.

I am grateful to our research group members in NUS. Their support made my research life fruitful and enjoyable.

I would like to thank NUS Graduate School for Integrative Sciences and Engineering (NGS) for providing my scholarship. My sincere thanks also goes

to the lab technologists and staff members in both NGS and department of chemical and biomolecular engineering, for all the help rendered.

Last but not least, I thank my parents and my wife (Dr. Hua Dan) for their support throughout my life and my PhD studies.

Table of Contents

Summary

Integrated nanocatalysts (INCs) with multicomponent and hierarchically complex structures have recently drawn extensive research attention in terms of their fundamental sciences and industrial applications. To date, many innovative strategies have been established for the synthesis of INCs by thoughtful design. This dissertation focuses on the development of INCs with different porous materials for catalyst technology and heterogeneous catalysis. In choosing host materials for INCs, the mesoporous siliceous materials (*viz.*, silica and metal silicates) and microporous metal-organic frameworks (MOFs) were employed, since they represent the two most attractive classes of porous materials known today. Therefore, the INCs presented in this dissertation comprise the mesoporous and microporous solids with special emphasis on their roles as supports, encapsulating shells, and metal sources.

Firstly, we proposed a general strategy for preparation of carbon nanotubes (CNTs) based INCs: core materials (*i.e.*, metal catalysts) will be wrapped by permeable shells along with a cavity space between them, wherein the catalyst nanoparticles can be precisely placed on CNTs and be protected by the porous shells. Besides their pristine properties, the CNTs also endow inherent tubular geometry, and it would be very interesting to see whether one dimensional (1D) INCs can be fabricated or not using CNTs as a support or template. The

synthetic investigation for the 1D INCs can be divided into three parts: (i) preparing catalytic core materials; (ii) generating cavity space and engineering shell structure and functionality; and (iii) forming targeted 1D INCs. Furthermore, the prepared catalysts were also used in benzyl alcohol oxidation to demonstrate their workability and performance advantage.

Secondly, pure or doped manganese silicate in bubble-like morphology was used as a versatile platform to prepare a new class of yolk-shell INCs. Mesoporosity of shell was generated from the inter-bubble space and the bubble structure of manganese silicate was used to hold and support nanoparticles (*e.g.*, Au, Ag, Pt, Co, Ni, Au-Pd alloy, MoO_2, Fe_3O_4, carbon nanotubes and their combinations). Therefore, the INCs have been made with pure or metal-doped manganese silicate nanobubbles as shells or carriers. We also demonstrate their enhanced catalysis for both liquid reaction (*e.g.*, 4-nitrophenol reduction) and gas reaction (*e.g.*, CO_2 hydrogenation). It was found that the manganese silicate material also allows doping of rare-earth ions into its silicate framework, therefore catalytic properties brought in by the dopants were further tuned.

Thirdly, we designed a new type of INCs which showed selective catalytic activities towards substrates carrying different charges. More significantly, such “smart” catalysts possess switchable surface charges under different pH environments, and thus the catalytic performance with controllable substrate

selectivity can be achieved. These INCs have sandwich-like structures, encompassing three basic components: (i) metal nanoparticles serving as catalytically active centres for chemical reactions (*i.e.*, 4 nm Pt), (ii) charge-switchable polymer shell (*i.e.*, polydopamine layer, PDA) working as dual-function membrane (*i.e.*, screening substrates and protecting metal catalysts underneath), and (iii) carrier material providing large reaction area/space (*i.e.*, hollow mesoporous support, such as Mn, Fe, Co, Ni silicates) for immobilization of metal catalysts. Importantly, in a typical advanced oxidation process, the exemplary nanocatalyst MnSi@Pt@PDA shows selective degradation of cationic dyes (*e.g.*, rhodamine 6G, methylene blue) at pH values higher than the isoelectric point (IEP = 3.1), whereas anionic dyes (*e.g.*, Congo red, methyl orange, thymol blue) were degraded preferably at pH values lower than the IEP.

Fourthly, we reported a facile route at room temperature and ambient pressure for the preparation of copper based MOFs with low dimensional shapes (*i.e.*, nanofibers, nanorods, nanosheets and nanocuboids), *via* thermodynamic and kinetic controls over the anisotropic growth. Importantly, the as-prepared two dimensional (2D) MOF nanosheets with monocrystalline nature (100% exposed {010} = facets) and ultrathin thickness (~6 nm) provides a materials platform to the fabrication of 2D supported metal nanocatalysts. Firstly, the MOF nanosheets can serve as a self-templating solid precursor to prepare different CuO and CuO-Cu_2O nanocomposites, or even

Cu metals *via* thermolysis or reduction under controlled atmospheres. Upon their formation, secondly, ultrafine noble metal nanoparticles (*e.g.*, Au, Ag, Pt, Pd, $Au_{0.4}Pt_{0.6}$, $Au_{0.4}Pd_{0.6}$ and $Au_{0.3}Pt_{0.3}Pd_{0.4}$) can be exclusively anchored on the external surfaces of MOF nanosheets. To show their open accessibility, catalytic activities of the derived catalysts have been evaluated using CO_2 hydrogenation and 4-nitrophenol reduction in gas phase and liquid phase, respectively. Our catalytic results suggest there is a strong synergistic effect of the supported $Au_{0.3}Pt_{0.3}Pd_{0.4}$ nanocatalyst, leading to much higher catalytic performance than previously reported ones. This work establishes a new application of MOFs in the field of heterogeneous catalysis when they are prepared into low-dimensional nanostructures by manipulating coordination environments for their metal ions and organic ligands.

List of Figures

Chapter 1 Introduction

1.1. Overview

Catalytic phenomena and processes are very common in nature, and the best-known example is photosynthesis in plants. Catalysis also plays a key role in modern society, as more than 90% of reaction processes in existing chemical industry rely on catalysts for accelerating reactions or enhancing yields of desired products.[1, 2] Therefore, the development of high-performance catalysts with aimed catalytic activity, selectivity, and prolonged lifetime would benefit the chemical industry enormously; such research endeavors have been persistently pursued by both academia and industry.[3-6] In a more traditional view, heterogeneous catalysts (*e.g.*, supported metal catalysts) commonly comprise single support plus active metal centers of one or more than one component. Such catalysts are generally prepared by methods such as impregnation, co-precipitation, deposition–precipitation, and so on. Usually, the catalyst structure and composition have to be optimized based on tedious empirical trial-and-error experiments in association with reaction testing.

In order to control the size, morphology, and spatial allocation of both catalytically active nanoparticles (NPs) and high surface area supports, a concept in catalyst design, known as *integrated nanocatalysts* (INCs), has been proposed, taking advantage of rapidly advanced nanoscience and

nanotechnology.[7, 8] It should be noted that the term "INCs" has been used only in recent years,[7] although the rational design of nanostructured catalysts with multicomponent had been pursued long time ago. The "INCs" generally stands for the boundary-defined catalysts that are compositionally and structurally more complex than conventional catalysts, as illustrated in Figure 1.1. Analogical to integrated circuit (IC) design in microelectronic industry, fabrication of INCs involves chemically controllable multi-step integration of various catalytic active centers (*e.g.*, NPs of noble metals, transition metals, rare-earth metals, as well as their alloys and oxides) into some active porous supports and/or protective/selective membrane-like shells to form a single robust catalyst device with more elaborate architectures, which not only gathers the properties of individual components, but would also create interfaces and unprecedented collective and synergetic features, compared to their conventional counterparts including unsupported free-standing nanocatalysts. In fact, INCs are capable of realizing the springing developments in both basic and applied research on model catalysts. In the perspective of chemical processes for synthesis and integration of functional materials, more and more academic attention has also been directed to INCs in recent years covering the design, fabrication, and characterization, in addition to their potential important applications.

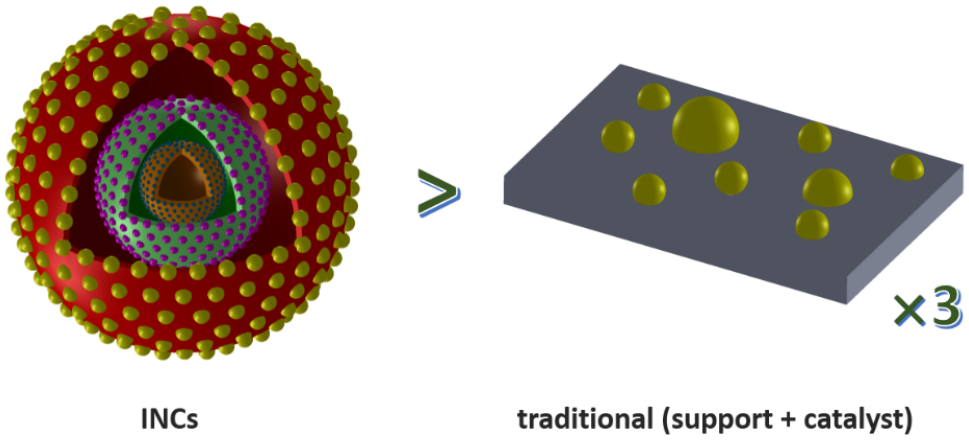

Figure 1.1 Schematic representation for the difference between the INCs and conventional supported catalysts: the three-shelled spherical INC is illustrated herein as an example because the sphere is the most common geometry adopted by any matter aggregates in order to minimize their surface energy; "×3" is just to "multiply" the grey surface area by 3 in order to account for the 3 shells in the depicted INC.

Among the numerous materials for building INCs, siliceous solids, mainly as forms of silica or silicates, have long been used as catalyst supports or as catalyst precursors. One important reason to choose these materials is their low-cost. Silicon is the second most abundant element in the Earth's crust following oxygen. In particular, mesoporous siliceous materials have aroused tremendous research interest and activities since the discovery of using organic surfactants as template for the pore formation in 1990s.[9-11] After that time, remarkable success in the synthesis, structural characterization, and application of mesoporous silica/silicate materials, has been made. In particular, soft "surfactant template" and rigid "hard template" (sometimes described as nanocasting) are two of the most commonly used methods to produce the mesopores within siliceous materials.[12] Generally, the template

acts as a space filler or a structure director during the formation of building units of 4-fold oxygen coordinated tetrahedral silicon, and after removal of the templates, materials with uniform or even hierarchical pore structures are obtained. As of now, mesoporous silica/silicate materials possess fascinating properties, including high surface area (up to 1000 m^2g^{-1}), tunable pore size (2–50 nm), large pore volume, controlled pore geometries (hexagonal, cubic, and lamellar, *etc*.), as well as a multitude of compositions (*e.g.*, inclusion of heteroatoms in silica to form silicates).[13, 14] As such, mesoporous siliceous materials are frequently used in the fabrication of INCs, mainly as the supports and encapsulating shells. The former category (supports) serves as substrates to support and disperse the catalytic NPs, while the latter category (encapsulating shells) protects the catalytic NPs and at the same time imposes constrained conditions for selected chemical reactions. Therefore, the *supports* and *encapsulating shells* herein are viewed together as *host materials*. Note that active catalytic components can also be loaded onto the inner and/or outer surfaces of encapsulating shells, or onto the walls of the shell pores. In these cases, encapsulating shells should also be considered as catalyst supports (Figure 1.1).

Microporous metal–organic frameworks (MOFs) are another class of very suitable materials for the construction of INCs, which are comparable to the commercial zeolites by virtue of ultrahigh internal surface areas (typically 1000–10000 m^2g^{-1}), low density, good crystallinity, as well as uniform

micropores and cavity sizes.[15, 16] The development of MOF materials is currently a field of extensive research, but the previous research efforts were mainly devoted to preparing new MOF structures by extending new organic ligands and exploring their applications majorly in gas storage and separation. Although the inorganic nodes in MOFs can be intrinsic active sites for catalysis, only Lewis-acid catalytic activity and Brønsted-acid catalytic activity were reported, and the reactive site (*i.e.*, the inorganic moiety) is the one that holds the MOFs structure together which might suffer a structural collapse during catalytic reactions.[17] Therefore some research efforts now have switched to the preparation of INCs with incorporation of metal or metal oxide NPs, by including them within the cavities, or embedding them within the matrixes, or anchoring them on the external surfaces of MOFs, which greatly enhances their catalytic functionality and performance. With addition of more active components or phases, applications of such functionalized MOFs for tandem reactions are also envisioned. A number of intriguing results regarding microporous MOFs based INCs have been reported.[18-24]

1.2. Objectives and Scope

It is undeniable that the development of mesoporous silica/silicate and microporous MOF based INCs will have significant impacts on both academia and industry. There is still much room for catalyst researchers to conceive new synthetic routes while improving the existing ones. Up till now, the

understanding of relationships between the structure of INCs and catalytic performance at a molecular-level is still lacking. At present, the research efforts are basically curiosity-driven, but a paradigmatic move to "make-on-demand" can be anticipated when more fundamental investigations in real reaction environments are in place. Therefore, the aim of this thesis is to design newer INCs based on mesoporous or microporous materials, *via* a "make-on-demand" manner, and their use in heterogeneous catalysis were also discussed. The INCs were prepared based on rational design on multiple scales. In choosing host materials for INCs, this thesis focuses on the mesoporous siliceous materials (*viz.*, silica and metal silicates) and MOFs (*e.g.*, ZIF-8, HKUST-1, *etc.*), since they represent the two most attractive classes of porous materials known today. In order to demonstrate the workability of the INCs, both liquid phase reactions (*e.g.*, selective oxidation of benzyl alcohol to benzaldehyde, reduction of 4-nitrophenol, advanced oxidation process towards organic dyes, *etc*.) and gas phase reactions (CO_2 hydrogenation to CO, CH_4 and methanol) were applied in this thesis.

1.3. Structure of the Thesis

This thesis contains 6 chapters besides this introductory chapter. In Chapter 2, the active catalytic components (such as nanostructured metals, metal oxides, and their hybrids), and the existing INCs in literatures were classified and reviewed. In Chapter 3, carbon-nanotubes (CNTs) based INCs with hollow

cavities and mesoporous shells were deigned and prepared, in which CNTs serve as a backbone to support catalytic components and mesoporous silica and/or MOFs (*e.g.*, ZIF-8) or transition metal oxides (*e.g.*, Nb_2O_5) act as membrane-like shells for molecular screening, catalyst protection, and surface functionality. Several types of catalytic nanoparticles (*e.g.*, noble metals Au, Pd, and Au-Pd alloy; and transition metal oxides Co_3O_4, ZnO, and TiO_2) have been anchored onto the CNTs and encapsulated or sheathed with the mesoporous silica shell. In Chapter 4, manganese silicate in bubble-like morphology was used as a versatile platform to prepare a new class of yolk–shell structured INCs. The mesoporosity of the shell was generated from the inter-bubble space and the bubble structure of manganese silica was used to hold and support nanoparticles (*e.g.*, Au, Ag, Pt, Co, Ni, Au-Pd alloy, MoO_2, Fe_3O_4, CNTs and their combinations). In Chapter 5, a new type of polydopamine (PDA) based INCs was designed and prepared, which show selective catalytic activities towards substrates carrying different charges. More significantly, such "smart" catalysts possess switchable surface charges under different pH environments, and thus the catalytic performance with controllable substrate selectivity can be achieved. These INCs have sandwichlike structures, encompassing three basic components: (i) metal nanoparticles serving as catalytically active centres for chemical reactions (*i.e.*, 4 nm Pt), (ii) charge-switchable polymer shell (*i.e.*, PDA layer) working as dual-function membrane (*i.e.*, screening substrates and protecting metal

catalysts underneath), and (iii) carrier material providing large reaction area/space (*i.e.*, hollow mesoporous support, such as Mn, Fe, Co, Ni silicates) for immobilization of metal catalysts. In Chapter 6, a facile synthetic route for the preparation of copper based MOFs with low dimensional shapes (*i.e.*, nanofibers, nanorods, nanosheets and nanocuboids) was reported. Importantly, the as-prepared 2D MOF nanosheets with monocrystalline nature (100% exposed {010} facets) and ultrathin thickness (~6 nm) provides a materials platform to the fabrication of 2D supported INCs. For instance, the MOF nanosheets can serve as a self-templating solid precursor to prepare different CuO and CuO-Cu_2O nanocomposites, or even Cu metals *via* thermolysis or reduction under controlled atmospheres. Upon the formation of 2D nanosheets, ultrafine noble metal nanoparticles (*e.g.*, Au, Ag, Pt, Pd, $Au_{0.4}Pt_{0.6}$, $Au_{0.4}Pd_{0.6}$ and $Au_{0.3}Pt_{0.3}Pd_{0.4}$) can also be exclusively anchored on the external surfaces of MOF nanosheets. And finally, Chapter 7 presents brief conclusions and some perspectives on the future research of this field.

1.4. References

1. C. J. Zhong and M. M. Maye, *Adv. Mater.*, 2001, **13**, 1507-1511.

2. H. Mao, H. Yu, J. Chen and X. Liao, *Sci. Rep.*, 2013, **3**, 2226.

3. V. Polshettiwar and R. S. Varma, *Green Chem.*, 2010, **12**, 743-754.

4. D. Wang and D. Astruc, *Chem. Rev.*, 2014, **114**, 6949-6985.

5. M. B. Gawande, P. S. Branco and R. S. Varma, *Chem. Soc. Rev.*, 2013, **42**, 3371-3393.

6. M. B. Gawande, Y. Monga, R. Zboril and R. K. Sharma, *Coordin. Chem. Rev.*, 2015, **288**, 118-143.

7. H. C. Zeng, *Acc. Chem. Res.*, 2013, **46**, 226-235.

8. M. B. Gawande, R. Zboril, V. Malgras and Y. Yamauchi, *J. Mater. Chem. A*, 2015, **3**, 8241-8245.

9. J. S. Beck, J. C. Vartuli, W. J. Roth, M. E. Leonowicz, C. T. Kresge, K. D. Schmitt, C. T. W. Chu, D. H. Olson, E. W. Sheppard, S. B. McCullen, J. B. Higgins and J. L. Schlenker, *J. Am. Chem. Soc.*, 1992, **114**, 10834-10843.

10. C. T. Kresge, M. E. Leonowicz, W. J. Roth, J. C. Vartuli and J. S. Beck, *Nature*, 1992, **359**, 710-712.

11. T. Yanagisawa, T. Shimizu, K. Kuroda and C. Kato, *B. Chem. Soc. Jpn.*, 1990, **63**, 988-992.

12. A. Stein, S. G. Rudisill and N. D. Petkovich, *Chem. Mater.*, 2013, **26**, 259-276.

13. F. Hoffmann, M. Cornelius, J. Morell and M. Fröba, *Angew. Chem. Int. Ed.*, 2006, **45**, 3216-3251.

14. J. M. Thomas and R. Raja, *J. Organomet. Chem.*, 2004, **689**, 4110-4124.

15. J. Lee, O. K. Farha, J. Roberts, K. A. Scheidt, S. T. Nguyen and J. T. Hupp, *Chem. Soc. Rev.*, 2009, **38**, 1450-1459.

16. H. Furukawa, K. E. Cordova, M. O'Keeffe and O. M. Yaghi, *Science*, 2013, **341**, 1230444.

17. M. Ranocchiari and J. A. v. Bokhoven, *Phys. Chem. Chem. Phys.*, 2011, **13**, 6388-6396.

18. X. Gu, Z.-H. Lu, H.-L. Jiang, T. Akita and Q. Xu, *J. Am. Chem. Soc.*, 2011, **133**, 11822-11825.

19. Z. Li and H. C. Zeng, *Chem. Mater.*, 2013, **25**, 1761-1768.

20. Z. Li and H. C. Zeng, *J. Am. Chem. Soc.*, 2014, **136**, 5631-5639.

21. H.-L. Jiang, T. Akita, T. Ishida, M. Haruta and Q. Xu, *J. Am. Chem. Soc.*, 2011, **133**, 1304-1306.

22. M. Müller, S. Hermes, K. Kähler, M. W. E. van den Berg, M. Muhler and R. A. Fischer, *Chem. Mater.*, 2008, **20**, 4576-4587.

23. C.-H. Kuo, Y. Tang, L.-Y. Chou, B. T. Sneed, C. N. Brodsky, Z. Zhao and C.-K. Tsung, *J. Am. Chem. Soc.*, 2012, **134**, 14345-14348.

24. G. Lu, S. Li, Z. Guo, O. K. Farha, B. G. Hauser, X. Qi, Y. Wang, X. Wang, S. Han, X. Liu, J. S. DuChene, H. Zhang, Q. Zhang, X. Chen, J. Ma, S.

C. J. Loo, W. D. Wei, Y. Yang, J. T. Hupp and F. Huo, *Nat. Chem.*, 2012, **4**, 310-316.

Chapter 2 Literature Review

2.1. Catalytic Nanoparticles for INCs

Presence of long lasting active sites is decisive for the catalytic performance of INCs. In general, small NPs or nanoclusters (NCs) offer the main active sites for catalysis. Rapid advances in the field of colloidal nanomaterials in the past decades endow us new ability to prepare catalytically active NPs with high product uniformity. Therefore, monodisperse metal and metal oxide NPs with desired size, predetermined shapes, crystal facets, and controlled composition, can serve as primary building blocks for constructing INCs. In principle, INCs are superior to the conventional heterogeneous catalysts in the following four aspects: (i) catalysts in nanoscale will increase the population of active surface sites (*viz.*, higher surface-to-volume ratios through downsizing) and thus better utilization of matter is evident; (ii) enhancement of catalyst-support interaction and thus better performance can be achieved through intimate interfacial contact and/or highly populated boundary regions between NPs and supports;[1] (iii) catalytic activities of NPs are closely dependent on their size, shape (and thus facets), and composition, which can be thoroughly manipulated through rationale design and synthesis.

To make effective INCs, the size of NPs is the most pivotal factor determining their catalytic properties. Following the pioneer findings on gold catalysis,[2] considerable progresses have been made in size-dependency of

different kinds of metal NPs in catalysis reactions over the past two decades. A number of colloidal approaches have been established for controlling the size of NPs, thus enabling researchers to tune the catalytic properties with many degrees of freedom. Particularly, formation of ultra-small NPs (< 2 nm) with well-defined numbers of metal atoms (*i.e.*, NCs) is drawing increasing research attention.[3]

Similarly, the shape of NPs not only determines their physicochemical properties, but also their actual performance.[4] For instance, gold NPs can be prepared into various platonic crystal forms (*e.g.*, tetrahedron, cube, octahedron, dodecahedron, and icosahedron; Structures 1 to 5 in Figure 2.1).[5, 6] Crystals with different shapes actually have different types of surface facets. With regard to the facet-dependent catalytic performances, numerous NPs, such as Au, Pd, Pd-Pb alloy, Cu_2O, *etc*, have been well-studied.[7-9] For example, the ORR (oxygen reduction reaction) activity of Pd nanocubes (with six {100} facets) was up to 10 times higher than that of Pd octahedrons (with eight {111} facets).[10] In the case of Au-Pd alloy, NPs with exposed {*hkl*} high-index facets were found to be more active in formic acid electro-oxidation than the conventional NPs.[11] Previous research efforts allow one to finely tune the shape of NPs based on chemical synthesis with the assistance of growth-regulating surfactants or added foreign ions. Shown in Figure 2.1 (Structures 6 to 10), poly-vinylpyrrolidone (PVP) and Pb ions have been adopted as shape-directing reagents for the geometrical transformation of

cuprite Cu_2O and Pd NPs, respectively, from cube to truncated cube, cuboctahedron, truncated octahedron, and finally to octahedron (where the exposed facets are gradually shifting from {100} to {111} with a progressive increasing surface ratio of {111} to {100}).[8, 12] The NPs with uniform facets can be further self-assembled into supracrystals and superstructures by magnetic-moment alignment (*e.g.*, with isotropic superparamagnetic surface)[13] or by van der Waals interaction (*e.g.*, choosing properly surface capping agents).[14] In addition, the synthesis and assembly of noble metal NPs (*e.g.*, Au, Pt, and Pd) into defined shapes can be simultaneously carried out by using their metal halides, together with surfactant (cetyltrimethylammonium bromide, CTAB) and reducing agent (thiourea) *via* variable micellar templates.[15]

Besides the size and shape for monodisperse NPs, in order to fabricate multifunctional INCs, preparation of hybrid NPs may become necessary, by which multiple functionalities can be integrated to meet new types of application such as for cascade reactions. Over the last decade, Zeng *et al* have prepared a lot of metal, metal oxide/sulfide NPs, and their hybrid nanostructures with control over their dimension, shape, facet, structure, and surface chemistry. Some representative metal-oxide/sulfide hybrids are also depicted in Figure 2.1 (Structures 11 to 20), including Ag_2S/Ag heterodimers (Ag triangular nanoprisms with Ag_2S nanospheres,[16] or Ag nanospheres with Ag_2S hollow spheres[17]), Au/ZnO heterodimers (Au nanospheres on the

vertexes of ZnO nanopyramids),[18] Cu_2O/Au heterodimers,[19] Au_xAg_{1-x} alloy,[20] core–shell structured CoO@ZnO composites,[21] core–satellite structured $Zn_{1-x}Co_xO$@$Co_{1-y}Zn_yO$ composites,[21] yolk–shell structured Au@TiO_2,[22] cable-like Cu@Ni nanowires,[23] belt-like ZnO/TiO_2/pentatitanate composites,[24] and a wide range of heterodimers comprised of catalytic metals and metal chalcogenides (*e.g.*, Au−$CuInS_2$, Au−Ag_3AuSe_2, Au−$CuInSe_2$, and Pt−$AgInS_2$, *etc*.).[25] Moreover, some other hybrid materials with novel and hollow structures were also studied.[26, 27] It can be envisioned that other matter combinations or hybrids with three, four or even more components could also be prepared whenever needed.

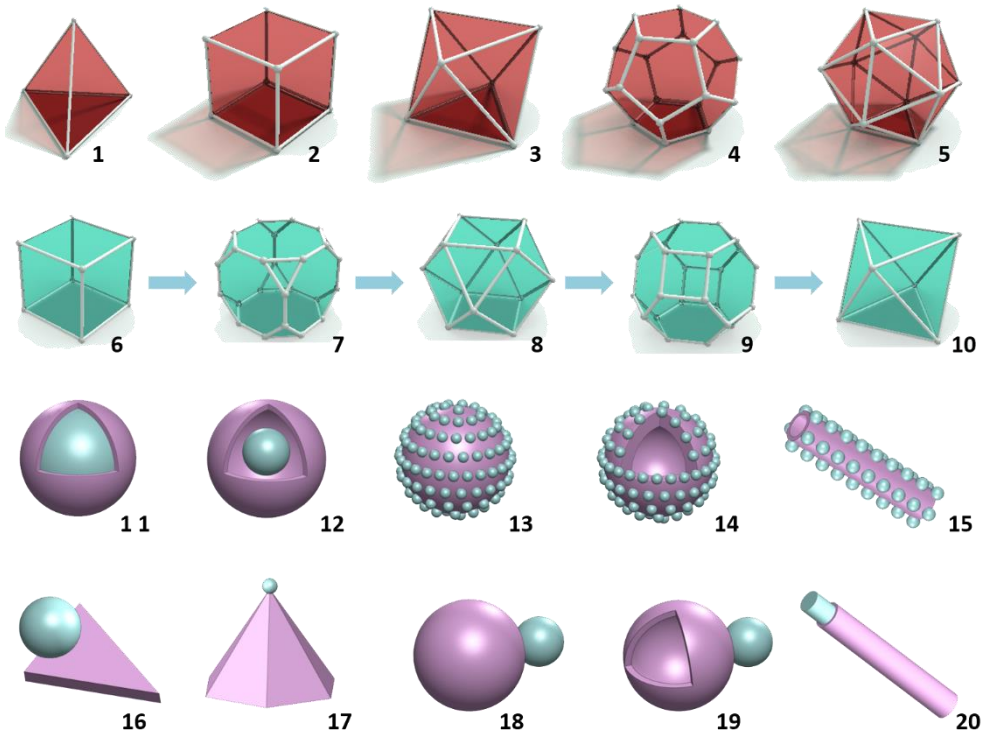

Figure 2.1 Structural models of active components acting as building blocks for INCs: (1-5) geometric models of Platonic solids (from left to right: tetrahedron, cube, octahedron, dodecahedron, and icosahedron); (6-10) shape-evolutions of cube to truncated cube, cuboctahedron, truncated octahedron,

and finally to octahedron with a progressive increasing surface ratio of {111} to {100}; and (11-20) some examples of the hybrid nanostructures that have been reported.

2.2. Mesoporous Siliceous Solids for INCs

2.2.1. Mesoporous silica as supports

Usually, pristine silica materials do not show appreciable catalytic activity, unless heteroatoms are incorporated into their frameworks (*i.e.*, doping or forming silicate materials, *vide infra*). However, mesoporous silica is an ideal and the most common support for loading catalytically active components (*e.g.*, all the NPs mentioned above), due to its high surface-area, excellent chemical affinity, and ease of functionalization because of the presence of abundant surface silanol groups, offering additional advantage of catalyst recyclability compared to the free-standing NPs. Meanwhile, addition of active catalytic components into mesoporous silica matrixes would introduce new functionalities. Prior to the proposal of the concept of INCs, a large number of studies have been published covering formation and immobilization of various highly dispersed NPs on mesoporous silica and their applications in a wide range of catalytic reactions. In particular, SBA family (*e.g.*, SBA-11, SBA-12, SBA-15, SBA-16) and M41S phase (*e.g.*, MCM-41, MCM-48, MCM-50) and KCC-1, *etc* [28-31] have been used for the preparation of silica-supported catalysts. Generally, there are two methods for loading NPs with mesoporous silica. The first one is *on-site* generation of NPs *via* reduction,

oxidation, or thermal decomposition process of preloaded precursors (usually inorganic metal salts). Sometimes, the metal precursors are also mixed with silica precursors (*e.g.*, silicon alkoxides, $Si(OR)_4$) for the one-pot synthesis. The other method is the immobilization of pre-synthesized NPs onto silica matrixes; in most cases, the catalytic NPs are capped by organic surfactants or else the silica surfaces are grafted with organic binding groups (*e.g.*, amine or thiol groups) that can improve the affinity between the catalysts and the support. Therefore, the former method is often known as sequential adsorption–reduction method and the latter one as sol–immobilization method.

Multicomponent system should be the first feature for usable INCs, because industrial catalysts are usually very complex, containing more than one type of active components besides supports.[32, 33] For example, the silica-supported molybdate catalysts used for ammoxidation of propylene include many active components such as $Fe_2(MoO_4)_3$, β-$CoMoO_4$, $NiMoO_4$, and $Bi_2O_3 \cdot MoO_3$.[33] This type of catalysts cannot be categorized as INCs due to uncontrolled mixing active components on silica support rather than a systematically targeted integration of various components. In contrary, INCs are featured with the global control over location of active metal species on support, that is, the three-dimensional (3D) spatial distributions of their supported NPs are rationalized. As shown in Figure 2.2a-c, in a recent report, Jongh *et al* presented an alternative strategy to create CuZn/SBA-15 catalysts, where metal NPs were specifically assembled within the one dimensional (1D) pore

channels of silica support, and hence the NPs appear as 1D configuration.[34] In addition, the growth (sintering) of the NPs could be effectively inhibited by tuning the spatial distribution of the NPs and maximizing their interparticle spacing (*e.g.*, the average distances of 13.9 and 33.2 nm to the nearest and second nearest neighbors respectively, were achieved for the 4-nm-sized Cu NPs). These fine-controlled catalysts showed high stability towards production of methanol from synthesis gas ($CO/CO_2/H_2$), retaining even >82% of the initial activity after a continuous experiment for 240 h. In another study, Co_3O_4 nanoclusters were exclusively loaded inside the mesoporous channel of SBA-15, and the resultant system had been used for efficient catalysts for oxygen-evolving from water.[35] Albeit the NPs are deposited on supports in a controlled manner in these studies, strictly speaking, such SBA-15 supported catalysts are not treated as INCs, because the SBA-15 phase do not have a uniform structural boundary; thereby it is difficult to further integrate them into superstructures (*vide infra*). Therefore, INCs also require additional control over the shape and size of host materials, besides the regulation of NPs.[36] Using mesoporous siliceous hosts, the commonly adopted shapes of INCs could be spheres, fibers, tubes, and platelets.

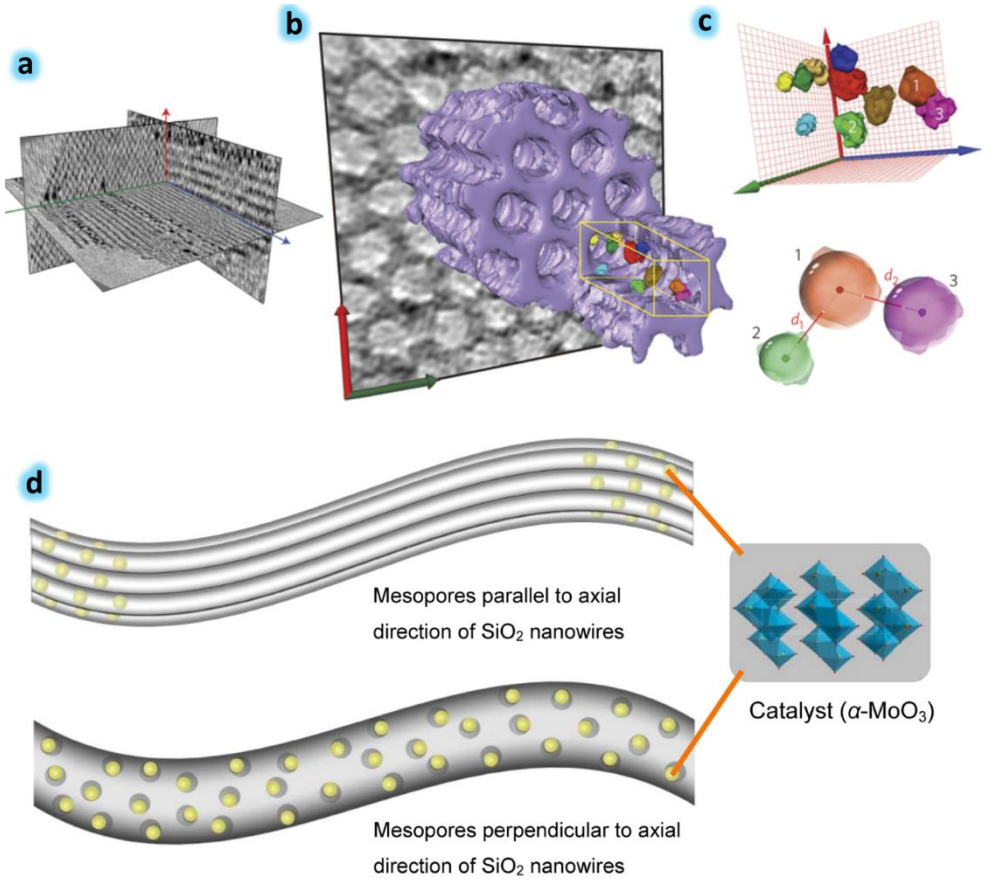

Figure 2.2 (a-c) The size and 3D spatial distribution of metal NPs in the mesopores of SBA-15, which reveals the near-maximum interparticle spacings of NPs as quantitatively derived from electron tomograms. Reprinted from Ref.[34] with permission from Nature Publishing Group. (d) Schematic illustrations for α-MoO_3 NPs loaded on two different types of silica nanowires (top: mesopores parallel to axial direction of silica nanowires; bottom: mesopores perpendicular to the axial direction). Reprinted from Ref.[37] with permission from the American Chemical Society.

While many existing porous silica materials can provide large specific surface areas, their surface cannot be fully utilized in most cases due to the limited accessibility (particularly MCM-41 and SBA-15 with ordered pores), that is, approach of reactants to inside NPs can only be realized through the two open ends of 1D channels (*viz.*, need to travel through a long pathway) because few porosity perpendicular to the 1D channels is present in such a

structure. How to improve the accessibility of active catalysts inside the 1D channels became an important research topic. To tackle this problem, Zeng *et al* have prepared an integrated α-MoO_3/*m*SiO_2 (*m*SiO_2 = mesoporous SiO_2) catalyst for oxidative desulfurization application.6 nm) and framework mesopores (~19.9 nm). In another study, He *et al* also reported the synthesis of hierarchically porous silica nanostructures with both small and large mesopores; the coexistence of different kinds of porosity could facilitate mass transport within the inorganic networks.[38]

In addition to the compositional aspect, the structural complexity is another distinct feature for INCs. Compared to the former, however, structural design of INCs requires the designer to think more thoroughly due to there are many ways of spatial integration even just for a single catalytic component. Device parameters such as overall geometry, location of NPs, array patterns of NPs, interior space for reactions, and internal and external surfaces for supports, *etc* must be clearly thought out.[36] As illustrated in Figure 2.3a, Yin *et al* reported the synthesis of hierarchical assemblies of silica@Au colloidal particles with a highly complex configuration (core–shell–satellite).[39] The obtained INCs have a Fe_3O_4@SiO_2 in the center, and many satellite silica@Au spheres are uniformly distributed in a polymer shell network (poly(N-isopropylacrylamide), which was coated on the outer surface of Fe_3O_4@SiO_2 core). Note that the magnetic core can help for an easy separation through external magnetic fields. Importantly, such catalysts exhibited significantly

enhanced stability of Au NPs for the reduction reaction of 4-nitrophenol with $NaBH_4$ through preventing their detachment and subsequent aggregation.

As utilization of mesoporous silica as supports, we would normally expect that inorganic/organic materials are deposited on the internal and/or external surfaces of the mesoporous silica. As a special case for INCs herein, furthermore, the active components can also be grafted only on the inner wall of the mesopores. Recently, Zeng *et al* have proposed an "inside-out" preinstallation-infusion-hydration method for targeted synthesis of Keggin heteropoly acids ($H_4SiMo_{12}O_{40}$) within the mesopores of silica.[40] As displayed in Figure 2.3b, discrete MoO_2 NPs are firstly synthesized as both a molybdenum source and a solid template in this process. Then, the as-synthesized MoO_2 NPs are used as cores to form uniform MoO_2@*m*SiO_2 core−shell spheres. Next, thermal treatment of MoO_2@*m*SiO_2 spheres at 550°C for 6 h leads to oxidation and infusion of the encapsulated MoO_2 cores, which results in highly dispersed heptamolybdate species ($Mo_7O_{24}^{6-}$ or Mo^{VI} species) within the mesoporous silica shells, giving rise to hollow cavities in the center of the spheres at the same time. Finally, hydration of the Mo^{VI}@*m*SiO_2 hollow spheres generates silicomolybdic acid ($H_4SiMo_{12}O_{40}$) that is highly dispersed on the inner walls of the mesopores. In this way, by fully using the surfaces of shell mesopores, the INCs exhibited excellent catalytic activity toward Friedel–Crafts alkylation, nearly 2.6 times as high as that of the commercial Amberlyst-15 catalyst.[40]

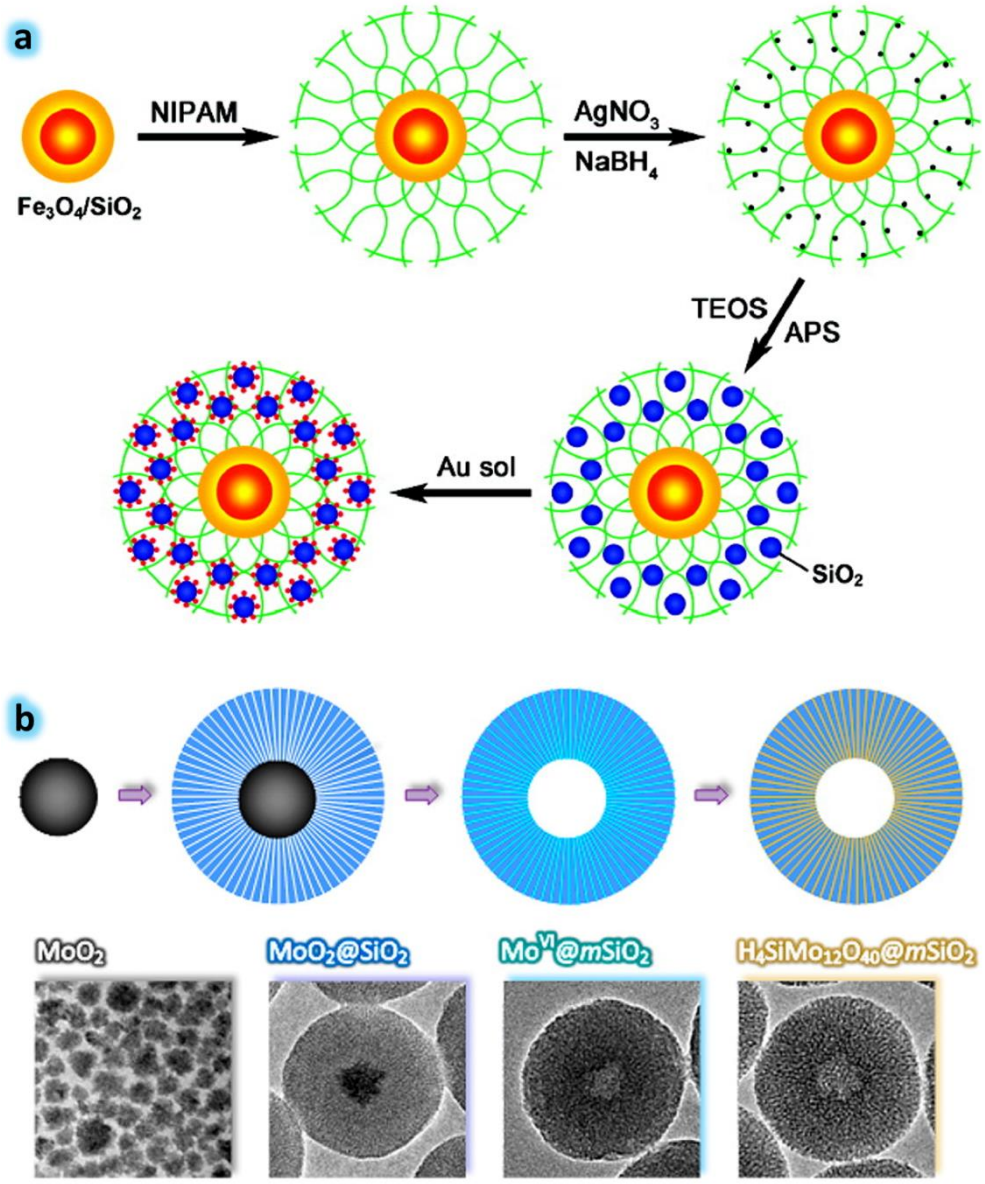

Figure 2.3 (a) A schematic illustration for the synthetic procedure starting from $Fe_3O_4@SiO_2$ NPs to INCs consisting of $(Fe_3O_4@SiO_2)$/p-NIPAM/SiO_2-Au assemblies. p-NIPAM is the polymer network of poly(N-isopropylacrylamide). Reprinted from Ref.[39] with permission from the American Chemical Society. (b) A schematic illustration for a stepwise synthesis of silicomolybdic acid ($H_4SiMo_{12}O_{40}$) supported on the inner wall of mesopores of silica hollow spheres, in which TEM images are corresponding to the starting MoO_2, intermediates and final INCs. Reprinted from Ref.[40] with permission from the American Chemical Society.

2.2.2. Mesoporous silica as encapsulating shells

In addition to playing the role of support materials, mesoporous silica is also an excellent encapsulation material due to their nontoxic nature, high biocompatibility, optical transparency, enhanced suspension stability, adjustable pore sizes, high specific surface area, facile fabrication and easy functionalization.[41-44] Traditional catalysts usually suffer the migration and sintering of active NPs into larger particles during the catalytic reactions, causing the loss of catalytic activities or total deactivation. Encapsulation of active components (*viz.*, various NPs) by silica coating is an elegant way to avoid migration and related aggregation of NPs.[45] Importantly, to achieve the accessibility of encapsulated active centers for reactive substrates, the silica coating layer should own highly open or even ordered mesopores as channels for guest molecules to travel with the least resistance. In general, the use of surfactants (such as PVP, CTAB, and tetradecyltrimethyl-ammonum bromide (TTAB), *etc*) not only prevents NPs from aggregation but also enhances the generation of mesopores within the silica shell. For instance, Pt@*m*SiO_2 catalytic system with Pt cores (size: 14 nm) enwrapped by a mesoporous silica shell (thickness: 17 nm) showed excellent thermal stability, which could be used for high-temperature reactions up to 750°C.[46] In this case, the mesopores (2–3 nm) in silica shell originated from the space of TTAB provided direct access to the Pt cores, making the Pt@*m*SiO_2 as active as a bare Pt metal catalyst for ethylene hydrogenation and CO oxidation reactions. In another study, similarly, Ni@*m*SiO_2 system with Ni NPs of *ca* 6 nm encapsulated by

mSiO_2 shells at a thickness of 15–46 nm exhibited excellent activity and durability for partial oxidation of methane to syngas (H_2/CO).[47]

The core–shell structured metal-NPs@*m*SiO_2 catalysts are just a simple class of INCs, where single metal NP was encapsulated and protected by the mesoporous silica shell. Recently, more advanced INCs with multiple metal cores encapsulated within mesoporous silica shell have also been exploited.[43] Generally speaking, including more active cores inside silica shell brings higher activity to the INCs. For example, it was reported that the (multi-Au)@*m*SiO_2 exhibited much higher catalytic activity in the reduction of 4-aminophenol than (single Au core)@*m*SiO_2, even though the total loading amount of gold in the catalysts was identical.[48] It was reported that the mesopores of the silica shell were created under a thermal treatment in hot water without adding any other additives, facilitating the reactant diffusion to the multiple Au nanodots. Chen *et al* have presented a general application of hot water (90°C) to selectively etch nonporous silica to form mesopores or cavities, because the outer layer of the silica shell is chemically more robust than the inner one, which is especially applicable for silica shells derived from Stöber protocol.[49]

When mesoporous silica is used as encapsulating materials for INCs, we would expect the shell of the silica coating layer as thin as possible, in order to avert excessive mass-transfer resistance and make the encapsulated NPs more

accessible. Thereby, usage of hollow mesoporous silica (HMS) with additional interior cavities for INCs is even more desirable.[50-54] The structural merits of HMS include high surface areas, short traveling distance, and low density; note that the presence of central cavity largely lightens the overall weight of INCs which benefits their dispersion in solution phase. More importantly, interstitial hollow spaces can act as a reservoir for encapsulating more active guest species and thus enhance loading capacity. In this regard, the void space within mesoporous silica spheres can function as a nanoreactor for catalytic reaction. Compared to non-hollowed silica encapsulation, the HMS will render the thin thickness of silica shells in nanoscale, which is highly favorable for mass transfer of reactants and products into and out of the central voids in liquid-phase reactions. Therefore, various preparative methods have been exploited for HMS, particularly, direct transformation methods from sol–gel derived Stöber silica to HMS are springing up in literature (named as self-templating synthesis[55]). The interior of HMS can also be decorated by various catalytically active NPs, forming known as yolk−shell or nanorattle-type HMS. The yolk−shell structured HMS have attracted tremendous research interest in recent years, since they provide a homogeneous environment around each catalytic core, showing both high activity and recyclability in gas- and solution-phase reactions.[56] Because the NPs cores are freely movable within the hollow shell of HMS, the yolk−shell INCs have minimum support effects, and they can still be viewed as freestanding NPs and used as model catalysts

to explore the mechanisms of NP catalysis if the effects of support need to be excluded[57]).

There are two general methods which allow one to enwrap active NPs into the central spaces of HMS.[43] In the first one (named as *preinstalled method*), desired NPs (or metal precursors) are mixed with precursor solutions (*i.e.*, starting chemicals for HMS). Both formation of HMS and encapsulation of NPs can be done in one-pot processes. For example, Ni@HMS nanotubes were synthesized in a water-in-oil (w/o) microemulsion approach, in which $Ni(NO_3)_2$ solution (*i.e.*, metal precursor), tetraethyl orthosilicate (TEOS), N_2H_4, and surfactants were mixed at 50°C for 2 h.[58] The Ni@HMS product had the cylindrical nanotube cavities with diameters of 12−13 nm and lengths up to 2 μm which were developed due to the formation of gases within the surfactant micelles. In the second method (known as *on-site synthetic method*), central hollow spaces in HMS are created firstly (such empty "containers" can be prepared *via* Ostwald ripening technique, or soft or hard templates, *etc*.[51, 59]), and later the NPs are *on-site* synthesized in the central spaces. It is expected that the interior surface of HMS is more reactive than the exterior surface because of higher surface curvature or roughness. Thus, the nucleation of nanomaterials would be selectively taken place inside the cavity, rather than on the outside of HMS.[43]

As presented in Figure 2.4a, Lee *et al* developed a postsynthetic functionalization method to introduce a high density of small noble metal NPs (< 2 nm), such as Pd, Pt, Rh, and Ir and their alloys, to the interior surface of HMS shell.[60] Interestingly, the metal NPs were synthesized based on galvanic replacement reactions on the Mn_3O_4 surface (which was pre-resident inside the cavity of silica), without adding auxiliary reductants. Furthermore, the residual Mn_3O_4 also served as support to prevent the detachment and subsequent aggregation of the generated NPs. Besides the Mn_3O_4, MnO cores could also be used for similar galvanic replacement reactions, leading to product INCs with configurations of NPs@HMS.[61, 62]

As a unique class of INCs, sandwich-structured INCs (with a general formula of A@B@C) have been extensively employed in heterogeneous catalysis, in which A is the common support used to immobilize B, B is the embedded active catalyst (*e.g.*, NPs), and C is the mesoporous silica layer. Depending on the dimension of A and C, the sandwich-structured INCs can be classified as one dimension (1D), 2D, and 3D. An illustrative example of 3D sandwich-structured INCs is given in Figure 2.4b,c.[42] This 4-phase INC (Fe_3O_4@SiO_2-Au@*m*SiO_2 microspheres) possesses a core of nonporous silica-protected magnetite particles, a transient layer of active Au NPs (that is sandwiched cores), and an outer shell of ordered *m*SiO_2 with perpendicularly aligned pore channels. The introduction of Fe_3O_4 as component "A" also brings an additional feature of recyclability. Very recently, Zhang *et al* reported a

system of 2D sandwich-structured INCs (graphene@NPs@*m*SiO_2), in which graphene-supported ultrafine metal NPs (such as Pt, Pd, and Ru) were encapsulated by a thin mesoporous SiO_2 shell.[63] Importantly, the 2D INCs showed high catalytic activity and high stability for gas phase CO oxidation by air and liquid phase 4-nitrophenol reduction by hydrogen. Similar 2D INCs with graphene/silica-based supports were also reported by Dabiri *et al*, in which catalytic gold NPs were deposited on the exterior surface of the composite.[64]

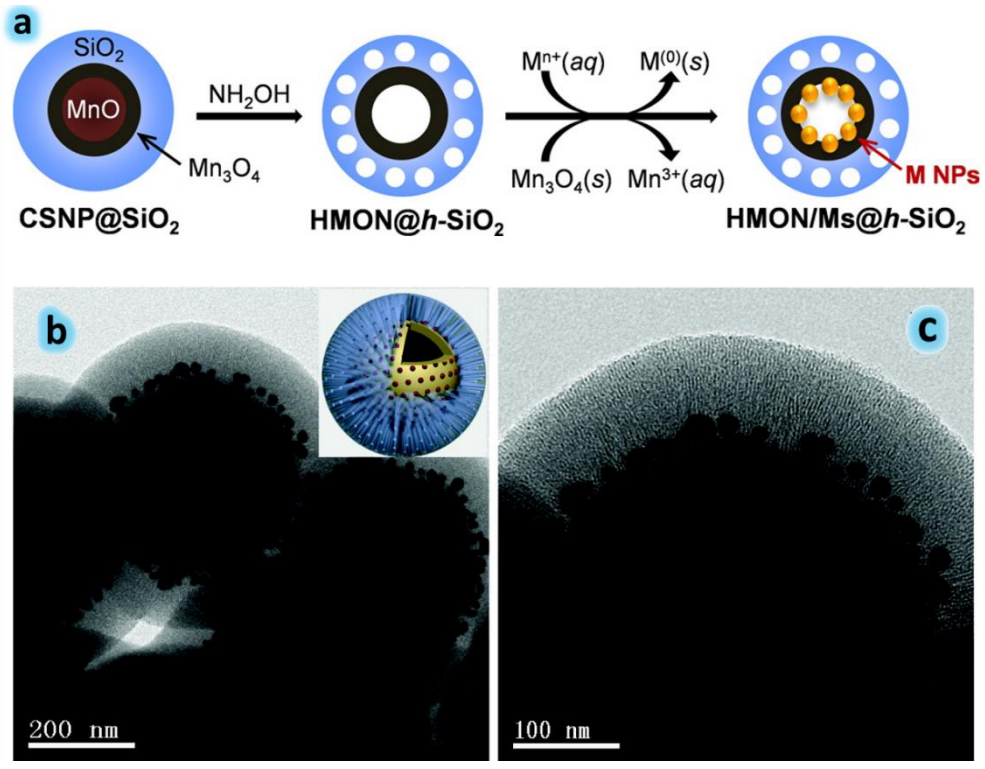

Figure 2.4 (a) Schematic illustration for the immobilization of NPs on the interior surface of a hollow silica nanoparticle. CSNP = core–shell nanoparticle, and HMON = hollow Mn_3O_4 layer. Reprinted from Ref.[60] with permission from the American Chemical Society. (b,c) TEM images of the 3D sandwich-structured Fe_3O_4@SiO_2–Au@*m*SiO_2 microspheres (depicted in the color inset of (b)); the thickness of *m*SiO_2 shell = 90 nm. Reprinted from Ref.[42] with permission from the American Chemical Society.

Integration of nanomaterials into larger assemblages (*e.g.*, centimeter-size) will enhance their utilization efficiency.[65] In principal, the above resulted INCs can also be viewed as primary building blocks for further integration into larger superstructures (or *supracatalysts*[36]). However, controllable ensembles of INCs are very challenging. At the present time, it usually requires multiple step integration for the synthesis of more complex nanocatalysts, similar to the synthesis of hierarchically-ordered nanostructures *via* two discontinuous processes.[66]

2.2.3. Mesoporous metal silicates as metal sources and supports

Silicates are the compounds containing silicon oxoanions and cationic metal ions, and they comprise the most widespread of minerals. In the field of nanomaterials research, nanostructured metal silicates, including main-group-metal and transition-metal silicates, are attracting a lot of interest because of their great potential in catalytic applications. As discussed above, unlike the "inert" silica, metal silicates can be viewed as chemically functionalized silica, that is, they also possess catalytically active sites. For example, aluminum is frequently introduced to create acidic sites in porous silica, and the resultant NPs/aluminosilicate could be utilized as bifunctional INCs.[67] In recent years, various approaches have been reported for making metal silicates with controlled size and shape. Among them, a facile and promising method is employing SiO_2 materials as a hard template as well as a silicon source to

synthesize hollow and mesoporous silicate materials (similar to the above discussed HMS). The final shape and size of the metal silicates are essentially dependent upon the SiO_2 templates. For instance, silica nanotubes can be transformed into various metal silicates with tubular structure, including Mg silicate, Cu silicate, Ni silicate, Co silicate and Mn silicate.[68] 1D silica nanofibers can be used to synthesize hierarchical copper silicate nanofibers which have been proved to be an ideal support for noble metal catalysts.[69] Moreover, spherical Stöber silica can be used to construct metal silicates hollow spheres, including Al silicate, Mg silicate, Cu silicate, Zn silicate, Mn silicate, Fe silicate, Co silicate, and Ni silicate, *etc*..[70-74] Usually, the transformation process from SiO_2 to metal silicates is carried out in a one-pot synthesis under hydrothermal conditions, where urea, or ammonia, or acetates are often added to create an alkaline environment. The synthesis mechanism of metal silicates is generally based on four steps: (i) dissolution of the surface SiO_2 to form silicate anions, (ii) reaction between metal cations and silicate anions, (iii) deposition of metal silicate layer on the surface of SiO_2, and (iv) repetition of dissolution-diffusion-deposition cycles which leads to the formation of hollow void in the center of the nanostructures. Along this line, many transition metal silicates can be fabricated based on easily obtained Stöber silica. The above processes are also applicable for rare-earth silicates such as yttrium silicate, ytterbium silicate, erbium silicate, and thulium silicate.[75]

Hierarchically structured materials *via* self-assembly of nanoscale building blocks into higher dimensional structures, can avoid aggregation and maintain high surface areas at high temperature and high pressures. So far, increasing efforts have been devoted to synthesize hierarchically structured silicates, which are ideal catalyst supports for immobilizing noble metals NPs. In terms of geometrical shapes, the reported metal silicates can be synthesized into a variety of shapes, such as nanotubes, nanobubbles, nanoplates, nanobelts, nanowires, nanoflowers, and so on.[72, 76-78] Some typical hierarchically structured silicates are illustrated in Figure 2.5, with geometries of "tubes in a sphere", "bubbles in a bubble", "sheets in a sphere", and "tubes in a tube". Recently, Xing *et al* designed hierarchical copper silicates with novel "tubes with a tube" structures (Structure 4 in Figure 2.5) for immobilization of 2.2 nm Pt NPs, where the 1D hollow nanotubes (diameters ~300 nm) were constructed from a large number of 1D ultrasmall nanotubes (diameters ~7.4 nm).[69] To prepare such INCs, firstly, the as-prepared hierarchical copper silicates with abundant hydroxyl groups were functionalized with Sn^{2+} ions through inorganic grafting. After Pt precursors ($PtCl_6^{2-}$) were added, the anchored Sn^{2+} ions can *in-situ* reduce Pt^{4+} on the copper silicates. In addition, the INCs were highly active and stable materials for gas phase CO oxidation reaction. In another study, 8.3 nm Ag NPs were assembled on the surface of hierarchical flower-like Ni silicates ("sheets in a sphere", Structure 3 in Figure 2.5) through an *in-situ* reduction of Ag^{+} by Sn^{2+}.[78] The as-prepared INCs

exhibited good activities in catalyzing the reduction of 4-nitrophenol and also good reusability for recycling. The Sn^{2+} ion functionalization or reduction method can also be applied to the synthesis of hollow nanocomposites of Au-NPs/yttrium-silicate.[75] In addition, Wang *et al* immobilized highly active Pd and PdO NPs on Ni,Mg-silicates nanotubes (general formula: $(Ni_{1-x},Mg_x)_3Si_2O_5(OH)_4$); the catalysts were tested in 10 successive cycles of Suzuki−Miyaura cross-coupling reaction with yields of ~99% at an extremely low metal leaching of ~0.02 ppm.[79]

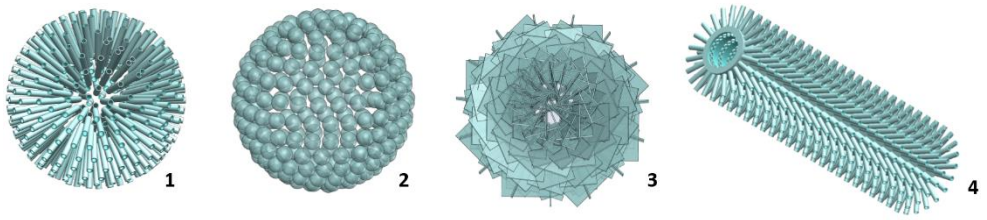

Figure 2.5 Typical hierarchically structured metal silicates: (1) "tubes in a sphere", (2) "bubbles in a bubble", (3) "sheets in a sphere", and (4) "tubes in a tube", where hollow cavities are in the center of each assembled structure.

As mentioned above, one of the characteristics of INCs is that multiple active NPs can be arranged into a single integrated unit. Although the one-pot synthesis is convenient, in which active components can be directly mixed with the precursor solution of silicates during the synthesis, structural control for more elaborative INCs is often difficult to achieve.[80] Therefore, a multistep strategy is normally more practical for the preparation of INCs using metal silicates as supports. For example, as illustrated in Figure 2.6a, a series of complex Ru/ZnO/Zn-doped SiO_2 INCs can be prepared by controlled

deposition and sequential assembly of zinc oxide phase and ruthenium NPs onto the external surfaces of zinc silicates (or Zn-doped SiO_2, depending on the ratio of Zn to Si) in solution phase.[81] Importantly, the multicomponent INCs have shown superior activity, sufficient robustness, and easy recovery in hydrogenation of toluene to methyl-cyclohexane, in which both Ru and ZnO phases contribute to the hydrogenation. It is obvious now that the active sites with multiple catalytic components on metal silicates would lead to synergetic effects for catalysis. For example, Au−Ag alloy NPs deposited on mesoporous aluminosilicate showed a much higher catalytic activity for low-temperature CO oxidation than their monometallic counterparts Au/aluminosilicate and Ag/aluminosilicate.[80]

Considering the high metal content within silicate materials, transition metals like copper, zinc, nickel, or iron can be internally generated from thermochemical reductions of their corresponding silicates by using hydrogen or methane as reducing agents.[82] For instance, recently, Zeng *et al* reported the fabrication of copper nanocatalyst by using "tubes in a sphere" copper silicates (Structure 1 in Figure 2.5) as precursors.[71] In terms of the crystal structure, copper silicates are layered clays, in which metal ions can travel relatively freely through the interlamellar space, allowing for a certain degree of ion exchange. Therefore, INCs based on mesoporous silicates, can be easily doped with other different metals by complexation-assisted ion exchange methods.[71] As shown in Figure 2.6b, each silicate lamellae is composed of an octahedral

metal hydroxide layer sharing oxygen atoms with another tetrahedral $[Si_2O_5]^{2-}$ layer. By treating these copper silicates with various divalent 3*d* transition metal salts (such as $Mn(CH_3COO)_2$, $FeSO_4$, $Co(NO_3)_2$, $Ni(NO_3)_2$ or $Zn(NO_3)_2$) at 60–80°C in alkaline conditions for 2–6 h, up to 80% of Cu in the silicate lamellae can be replaced with the respective dopant metals, while retaining the original tubular structure. Furthermore, under reducing conditions (H_2/N_2 (10%/90%), 200°C for 2 h), copper silicate nanotubes could be transformed into Cu NPs (size at ~3 nm) based INCs, and particularly, the INCs with Zn or Ni doping showed a significant improvement in catalytic activity and methanol selectivity for gas phase CO_2 hydrogenation. Other investigations have also been conducted to prepare Mn-doped zinc silicate and cadmium silicate with 1D micro/nanowire bundle shapes.[83]

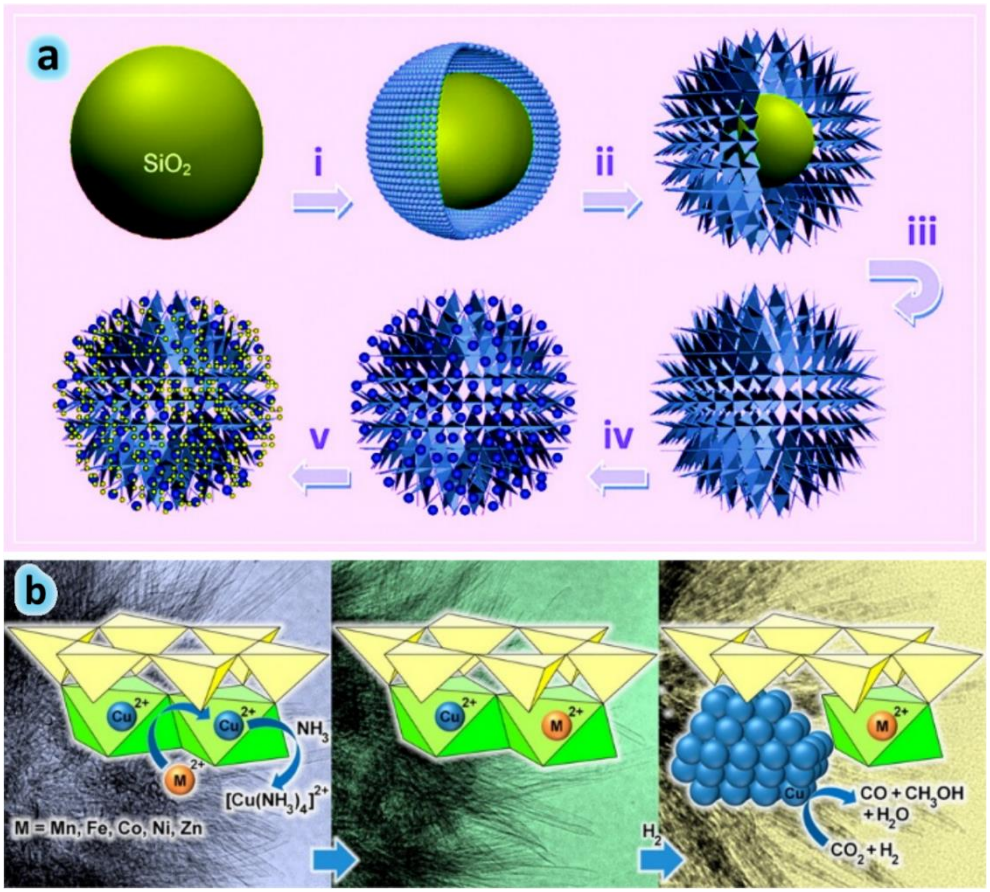

Figure 2.6 (a) A process illustration for the synthesis of INCs: (i) surface modification of SiO_2 and formation of yolk–shell structured SiO_2@(Zn-doped SiO_2), (ii) reduction of yolk size and formation of "sheet-like" shell, (iii) formation of plate-interlaced zinc silicate hollow sphere (consumption of silica totally), (iv) deposition of ZnO NPs (blue dots) on zinc silicate support, and (v) addition of secondary phase (Ru NPs, small yellow dots) on zinc silicate support. Reprinted from Ref.[81] with permission from the American Chemical Society. (b) A process illustration for the synthesis of a series of single-walled copper silicate nanotubes containing other 3*d* transition metal elements (M = Mn, Fe, Co, Ni, and Zn), and the formation of copper based INCs by hydrogen reduction, which were later used in CO_2 hydrogenation. Reprinted from Ref.[71] with permission from the American Chemical Society.

2.2.4. Mesoporous metal silicates as encapsulating shells

Similar to the above mentioned NPs@silica, sophisticated core–shell or yolk–shell or rattle–type INCs consisting of NPs encapsulated by mesoporous metal silicates are another new class of active, stable nanocatalysts. Mesoporous

silica often suffer from poor thermal or hydrothermal stability because of its amorphous state. Nevertheless, mesoporous metal silicates are commonly crystalline. For example, transition metal and lanthanide silicates hollow nanoshells are very stable even treating at temperature >800°C,[72, 84] which is more suitable for high-temperature applications. Li *et al* demonstrated high thermal and hydrothermal stability of Cu silicate and Mg silicate nanotubes, which could maintain their crystalline state, tubular morphology, and porosity even after a calcination at 600°C or 800°C for 12 h in flowing water vapor, or treating in boiling water for 240 h.[85] Therefore, INCs based on metal silicates as encapsulating shells should be promising for high-temperature catalysis.

Apart from the bubble-type INCs, NPs@silica spheres can also be used as solid precursors for transformative syntheses of hollow mesoporous aluminium-silicate encapsulated Au NPs, bimetallic Au/Pd NPs, Fe_3O_4 NPs, and α-Fe_2O_3 NPs.[73] Briefly, the NPs@silica precursors were treated with a hot alkaline solution at 80°C for 8 h in the presence of sodium aluminate ($NaAlO_2$) and surfactant CTAB. Similarly, bifunctional Fe_3O_4@Mg-silicate sub-microspheres with superparamagnetic property can be prepared by treating Fe_3O_4@SiO_2 with $Mg(NO_3)_2$ and NaOH at 140°C for 10 h.[86] Lately, Ren *et al* prepared the yolk–shell structured Au@Mg-silicate nanospheres from the core–shell Au@SiO_2 *via* a hydrothermal method at 140°C for 12 h.[87] The mesoporous Mg silicate shells with pore sizes of 2–4 nm were assembled through a large number of $MgSiO_3$ nanosheets ("sheets in a sphere", Structure

3 in Figure 2.5). The resultant Au@Mg-silicate was superior to naked Au NPs owing to the high catalytic stability for the reduction of 4-nitrophenol. This template strategy can be extended to fabricate other INCs, such as Fe_3O_4@Y-silicate,[75] Fe_3O_4@Cu-silicate,[88] spindle α-Fe_2O_3@Mg-silicate,[89] and γ-Fe_2O_3@Mg-silicate nanotubes.[90]

Similar to the above mentioned "*on-site* synthetic method" for functionalization of HMS, noble metal NPs can be introduced to the hollow cavity of mesoporous silicates by a sequential deposition–reduction method. For instance, Gong *et al* have reported a core–sheath INC (Cu@Cu-silicate nanotubes), which were prepared via a two-step process: (i) metal ions were induced into the hollow cavities of copper silicate on the basis of the capillary forces under a N_2 atmosphere (thus metal deposition on the outer surface was eliminated), and (ii) the metal ions in the hollow cavities were *on-site* reduced in pure hydrogen at 350°C for 2 h.[91] The copper based INCs are superior to the conventional copper-based catalysts due to the scaffold role of copper silicate and the existence of balanced and stable Cu^0 and Cu^+ active species, which showed high efficiency (ethanol yield at 91%) and steady performance of catalysts (>300 h at 280°C) for carbon–oxygen hydrogenolysis of dimethyl oxalate.

2.3. Microporous MOFs for INCs

MOFs with permanent porosity have emerged as new alternatives to conventional materials in many fields such as adsorption, separation, sensing, drug delivery, and especially serving as support materials for INCs design.[92-98] There are basically three strategies for the integration of active NPs and MOFs: (i) metal or metal oxide NPs are attached preferentially at the exterior surfaces of the MOFs structure; (ii) the growth of NPs is confined within the nanopores of MOFs; and (iii) the NPs are encapsulated by MOF shells to form core−shell or yolk−shell nanostructures, in which the microporous MOF shells can provide excellent molecular size/shape selectivity. In the first case, microporous MOFs work similar to the mesoporous silica and silicates, providing large surface areas for dispersion and stabilization of NPs. Reflecting this fact, various NPs have been successfully incorporated into different MOF structures, including Au, Ag, Pd, Cu, or their combinations and so forth.[93, 94, 99] Although NPs on the external surface of MOF particles are highly accessible, interactions between the immobilized metal NPs and the MOFs are very important in order to prevent the agglomeration of the NPs. In the second case, precursors of NPs are firstly introduced into MOF matrices, forming mixed compounds such as precursor@MOFs. The intermediates are then *in-situ* converted into NPs@MOFs by liquid reduction, hydrogenolysis, or photoassisted thermolysis treatments. For example, biphasic NPs (Cu and ZnO) can be immobilized in MOF-5 cavities by the gas-phase infiltration technique with volatile organometallic precursors ([CpCuL] (Cp = 5-

cyclopentadienyl ligand, and L = PMe_3 or CN^tBu) and $ZnEt_2$ for Cu and Zn, respectively).[100] Also, Ni NPs (size < 2 nm) can be embedded in the pores of MesMOF-1, and the combination of Ni NPs and MOF could serve as robust catalysts for hydrogenolysis of nitrobenzene and hydrogenation of styrene.[101] Usually, the average size of the embedded NPs is highly dependent on pore dimensions of the MOFs, because the pore cavities can act as a scaffold to constrain the growth of NPs.[102] In the last case, the migration and aggregation of the small NP cores can be dramatically limited due to space confinement of MOF shells, and the NP@MOF structure retains the size or shape selectivity inherited from the micropores of MOF shells.[103] In addition to the above three strategies for introducing foreign NPs on MOFs, NPs can also be generated from the metal nodes in MOFs by reductive calcination treatments, which produces nanocomposites such as NPs@carbon (similar to the "metal sources" role of silicate materials). However, fine-control over the size and shape of the derived metal or metal oxide NPs from this thermolysis method is rather difficult.[104]

In fact, integration of microporous MOFs and metal NPs into a single nanostructure would create synergetic effects, and thus multifunctional INCs enable tandem reactions. For instance, Pd@IRMOF-3 core−shell nanostructures were highly efficient in a cascade reaction, where IRMOF-3 was used as alkaline catalysts for Knoevengel condensation, and Pd cores could catalyze the selective hydrogenation of the products from Knoevengel

condensation reaction.[52] For preparation of more advanced INCs, NPs with two or more components were prepared and incorporated with MOFs. For instance, Au–Pd alloy NPs loaded on MOFs (MIL-101 and ethylenediamine grafted MIL-101) have a much higher tolerance with respect to CO poisoning in the reaction of dehydrogenation of formic acid than the monometallic Au and Pd counterparts.[105] Xu *et al* also demonstrated that core−shell structured Au@Ag NPs immobilized on zeolitic imidazolate framework (ZIF-8) exhibited a strong bimetallic synergistic effect in the reduction of 4-nitrophenol in water with much higher catalytic activities than their monometallic counterparts.[106]

Unlike the amorphous silica, usually, MOFs are highly crystallized and are easier to be fabricated in well-defined shapes. Similar to the synthesis of inorganic NPs, surfactants can also be used to modulate the oriented growth of MOFs. For example, two different types of ZIF-8 nanocrystals were first prepared: rhombic-dodecahedral ZIF-8 crystals were bounded with 12 {110} facets, while the cubic ZIF-8 crystals were surrounded exclusively by 6 {100} facets.[93] Then, single-layered Au or Ag NPs were added onto exterior surfaces and/or into interior bulk matrices of these two ZIF-8 crystals, as displayed in Figure 2.7. A key factor in the deposition of NPs on the MOF surfaces is the choice of appropriate chemicals to generate interactions between the incorporated NPs and the MOF phase. In this case, such coordination bonding is actually attained from 3-mercaptopropionic acid (MPA, refer to molecular

structure in Figure 2.7), which contains a thiol group on one end (connecting with NPs) and a carboxyl group on the other (linking to the partially coordinated Zn^{2+} ions on the exterior surface of ZIF-8 crystals). Additional epitaxial growth of ZIF-8 was also carried out, which turned the surface metal NPs embedded into ZIF-8 bulk phase and gave rise to sandwich-structured INCs (ZIF-8@Au@ZIF-8). Moreover, the as-designed Au/ZIF-8 INCs showed high catalytic activity for liquid phase 4-nitrophenol reduction reaction. Referring to the methods for loading NPs on mesoporous silica, both sequential adsorption–reduction method and sol-immobilization method can be used for loading NPs on the designated microporous MOFs. In fact, it has been found that the deposited Au NPs on ZIF-8 exterior crystal planes have a very small size of 1–2 nm through the sequential adsorption–reduction approach, compared to those obtained from the sol-immobilization approach (2–3 nm).[93]

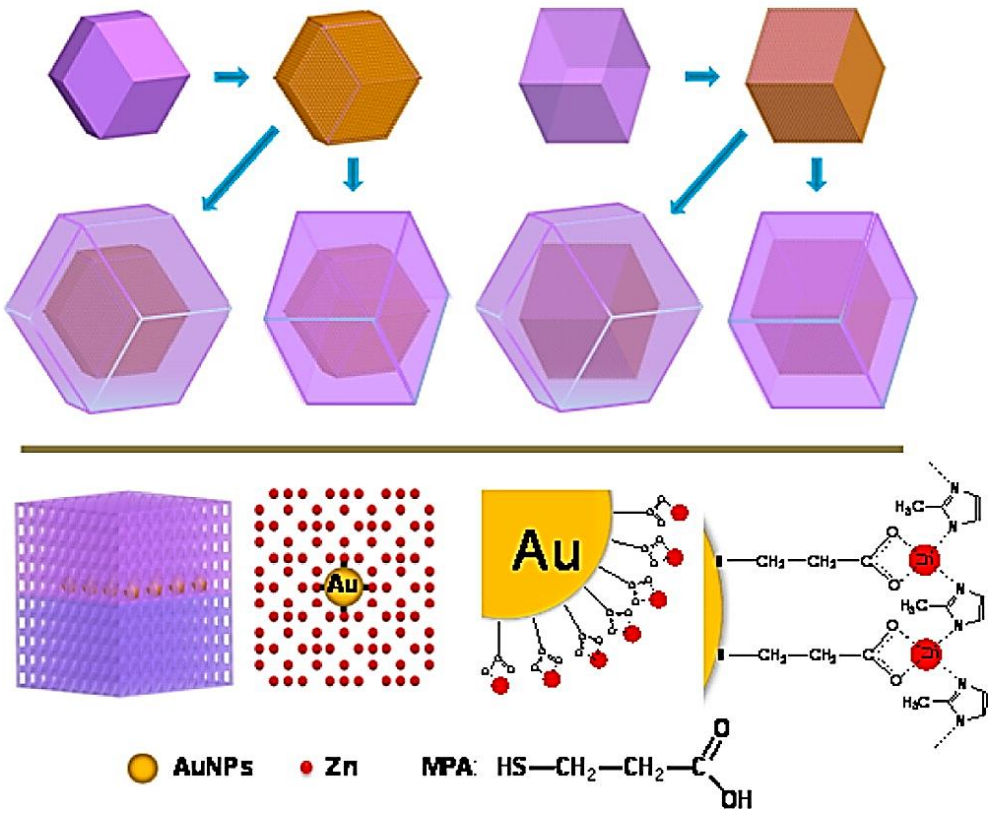

Figure 2.7 Schematic illustrations for the deposition of Au NPs on the exterior surfaces of two different types of ZIF-8 crystals (rhombic dodecahedrons and cubes with exposed {110} and {100} facets, respectively) to form the ZIF-8@Au INCs, and the further epitaxial growth of outer ZIF-8 shells to produce sandwich-structured INCs: ZIF-8@Au@ZIF-8 with four different shapes. Reprinted from Ref.[93] with permission from the American Chemical Society.

Recently, Huo *et al* introduced a general strategy to encapsulate a broad range of metal NPs of various sizes, shapes and compositions inside of ZIF-8 crystals through a PVP-assisted process, as illustrated in Figure 2.8.[98] They demonstrated that PVP not only acts as a general surfactant to stabilize NPs in the reaction solution, but also provides the NPs with an enhanced affinity to ZIF-8 through weak coordination interactions between pyrrolidone rings (C=O) and zinc atoms in ZIF nodes, or also through hydrophobic interactions between apolar groups in PVP and the imidazole linkers in ZIF-8.

Interestingly, the spatial distributions of NPs in MOFs could be controlled by adjusting NPs addition sequence, that is, addition at the beginning (T_0) or after a certain time (T) during the MOFs synthesis, referring the two different configurations (i) and (ii) in Figure 2.8. The as-prepared NPs@ZIF-8 INCs exhibited active catalytic properties that derived from the NPs as well as molecular sieving effects that originated from the MOF phase. It was found that the accessibility of embedded NPs for catalysis was highly depended on the molecular size of reaction substrates because of the restriction of pore apertures (3.4 Å) of ZIF-8 shell. For example, the Pt@ZIF-8 for the hydrogenation of n-hexene was demonstrated by 7.3% conversion efficiency, but the INCs showed no propensity to catalyze hydrogenation of sterically more demanding cyclooctene (conversion rate = 0%). The molecular size-screening property of ZIF-8 shell was also investigated by Tsung *et al*; they revealed that the specific activity of yolk−shell structured Pd@ZIF-8 for hydrogenations of different substrates following the order: ethylene (3.2×10^{-3} $mol\cdot g_{Pd}^{-1}\cdot s^{-1}$) > cyclohexene ($3.2\times10^{-5}$ $mol\cdot g_{Pd}^{-1}\cdot s^{-1}$) > cyclooctene (0), consistent with the sizes of the substrates: ethylene (2.5 Å) < cyclohexene (4.2 Å) < cyclooctene (5.5 Å).[97] Additionally, various catalytic reactions employing INCs based on MOF materials to achieve size-selective or shape-selective catalysis have been reported, such as olefin hydrogenation, aqueous reduction of 4-nitrophenol, and CO oxidation.[107, 108] Three feasible ways to adjust the molecular diffusion of reactant to the encapsulated NPs through

MOFs are: (i) controlling the coating thickness of MOFs, (ii) building hollow cavities inside MOFs, and (iii) controlling the channel size in MOFs which can be possibly achieved by changing the length of organic linkers.[109-112]

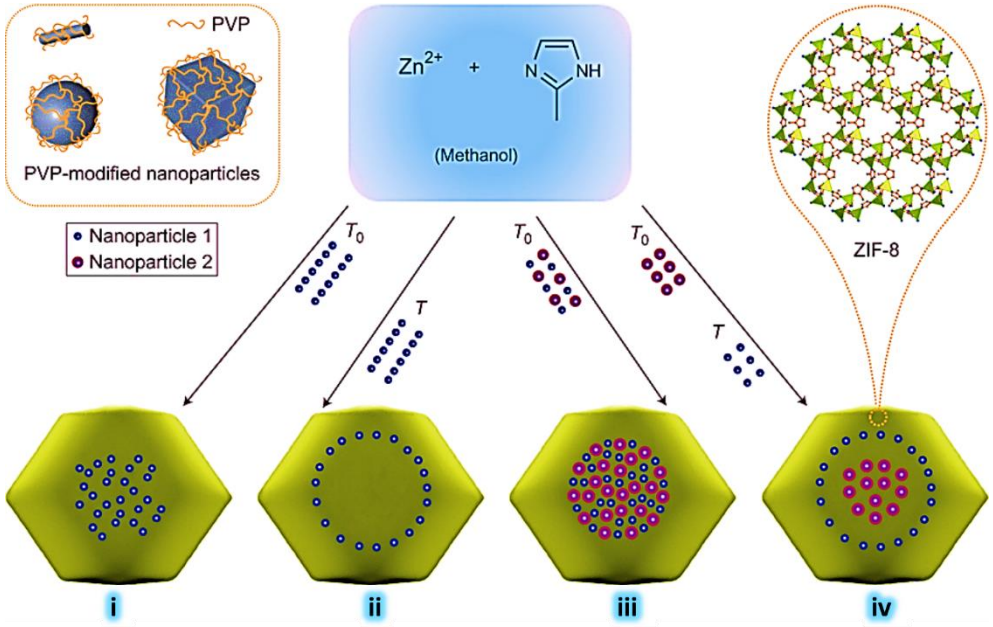

Figure 2.8 Schematic illustrations for the controlled encapsulation of NPs in ZIF-8 crystals. To control the 3D spatial distributions of NPs in MOF, desired NPs were added at the beginning (T_0; see cases i, iii and iv) or after a certain time (T; see cases ii and iv) during the MOF synthesis, therefore achieving NPs in the central region or off the central region of the MOF crystals. Reprinted from Ref.[98] with permission from Nature Publishing Group.

Nanocomposites made from the mesoporous silica and microporous MOFs have been prepared by serval groups.[94, 108, 113] In this type of combinations, the INCs profit the advantages of both materials. Exemplified by Zhou *et al*, three different MOFs have been incorporated into the pore channels of SBA-15.[114] Importantly, the thermal stabilities of MOFs were enhanced upon their confinement in silica pores; the decomposition temperature of the MOF (*e.g.*, MOP 3, a copper based MOF) increased from 318°C to 350°C. Functionalized

self-assembled monolayer (SAM) method for the depositing MOF-5 of thin polycrystalline films on silica surfaces was reported by Fischer *et al.*[115] Likewise, uniform ZIF-8 layer was grown on top of CNT@*m*SiO_2 with the surface modification by poly(sodium 4-styrene-sulfonate) (PSS).[116] Considering that MOFs are soft matters with weak mechanical strength as compared to inorganic materials, to enforce MOF materials for practical applications, one feasible way is transforming them into harder composites *via* coating mesoporous silica on MOFs. Recently, Zeng *et al* reported a general synthetic approach to coat microporous MOFs and their derivatives (*e.g.*, the above mentioned NPs/MOFs composites) with an enforcing shell of *m*SiO_2 (see Figure 2.9).[94] As expected, the hardness for pure ZIF-8, ZIF-8@*m*SiO_2, and ZIF-8@*m*SiO_2@ZIF-8 increased from 560 to 1150 to 1620 MPa, as measured by nanoindentation technique. Moreover, the resultant sandwiched INCs of ZIF-8@Au@*m*SiO_2 and ZIF-8@Cu@*m*SiO_2 were examined respectively for their catalytic activity using reduction of 4-nitrophenol in water. This model reaction confirmed that the enforcing *m*SiO_2 shells are indeed permeable for the reactant and product chemicals. Besides the structures of MOF@NPs@*m*SiO_2, the configuration orders of MOFs and silica phases can be reversed, forming the sandwiched *m*SiO_2@NPs@MOF. For example, Zhang *et al* prepared *m*SiO_2@Pd@ZIF-8 for the selective hydrogenation of alkenes; such INCs could attain a 100% conversion using 1-

hexene as reaction substrate, but only 13.8% when cyclohexene was the substrate.[108]

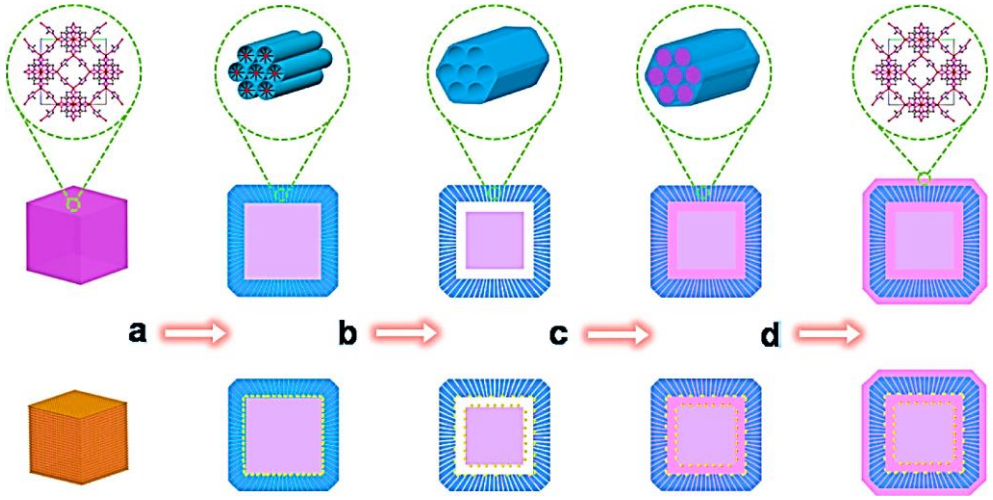

Figure 2.9 Schematic illustrations for coating mesoporous SiO_2 ($m$$SiO_2$) on ZIF-8 (purple cube) and ZIF-8@NPs composites (golden cube): (a) deposition of gel-like SiO_2 shell on the ZIF-8 or ZIF-8@Au cores (the channels of SiO_2 shell are filled with surfactant molecules), (b) thermal conversion of gel-like SiO_2 to $m$$SiO_2$ with partial infusion of ZIF-8 into the $m$$SiO_2$ shell, noting that the ZIF-8 cores are reduced, (c) regrowth of ZIF-8 to fill up the interior space of ZIF-8@$m$$SiO_2$ or ZIF-8@Au@$m$$SiO_2$, and (d) overgrowth of a new ZIF-8 shell on the surface of $m$$SiO_2$ shell to produce multilayer-structured ZIF-8@$m$$SiO_2$@ZIF-8 or ZIF-8@Au@$m$$SiO_2$@ZIF-8. Reprinted from Ref.[94] with permission from the American Chemical Society.

2.4. References

1. M. Du, D. Sun, H. Yang, J. Huang, X. Jing, T. Odoom-Wubah, H. Wang, L. Jia and Q. Li, *J. Phys. Chem. C*, 2014, **118**, 19150-19157.

2. M. Haruta, *Catal. Today*, 1997, **36**, 153-166.

3. F. Baletto and R. Ferrando, *Rev. Mod. Phys.*, 2005, **77**, 371-423.

4. Y. Xia, X. Xia and H.-C. Peng, *J. Am. Chem. Soc.*, 2015, **137**, 7947-7966.

5. F. Kim, S. Connor, H. Song, T. Kuykendall and P. Yang, *Angew. Chem. Int. Ed.*, 2004, **43**, 3673-3677.

6. W. Niu, W. Zhang, S. Firdoz and X. Lu, *J. Am. Chem. Soc.*, 2014, **136**, 3010-3012.

7. H. Xu, W. Wang and W. Zhu, *The Journal of Physical Chemistry B*, 2006, **110**, 13829-13834.

8. W. Niu, Y. Gao, W. Zhang, N. Yan and X. Lu, *Angew. Chem. Int. Ed.*, 2015, DOI: 10.1002/anie.201503148, 8271–8274.

9. M. Kim, Y. Kim, J. W. Hong, S. Ahn, W. Y. Kim and S. W. Han, *Chem. Commun.*, 2014, **50**, 9454-9457.

10. M. Shao, T. Yu, J. H. Odell, M. Jin and Y. Xia, *Chem. Commun.*, 2011, **47**, 6566-6568.

11. L. Zhang, J. Zhang, Q. Kuang, S. Xie, Z. Jiang, Z. Xie and L. Zheng, *J. Am. Chem. Soc.*, 2011, **133**, 17114-17117.

12. D.-F. Zhang, H. Zhang, L. Guo, K. Zheng, X.-D. Han and Z. Zhang, *J. Mater. Chem.*, 2009, **19**, 5220-5225.

13. H. M. Chen, R. S. Liu, H. L. Li and H. C. Zeng, *Angew. Chem. Int. Ed.*, 2006, **45**, 2713-2717.

14. K. X. Yao, X. M. Yin, T. H. Wang and H. C. Zeng, *J. Am. Chem. Soc.*, 2010, **132**, 6131-6144.

15. Y. Zhou and H. C. Zeng, *J. Am. Chem. Soc.*, 2014, **136**, 13805-13817.

16. S. Xiong, B. Xi, K. Zhang, Y. Chen, J. Jiang, J. Hu and H. C. Zeng, *Sci. Rep.*, 2013, **3**, 2177.

17. M. L. Pang, J. Y. Hu and H. C. Zeng, *J. Am. Chem. Soc.*, 2010, **132**, 10771-10785.

18. K. X. Yao, X. Liu, L. Zhao, H. C. Zeng and Y. Han, *Nanoscale*, 2011, **3**, 4195-4200.

19. M. Pang, Q. Wang and H. C. Zeng, *Chem. - Eur. J.*, 2012, **18**, 14605-14609.

20. T. T. Chng, L. Polavarapu, Q. H. Xu, W. Ji and H. C. Zeng, *Langmuir.*, 2011, **27**, 5633-5643.

21. K. X. Yao and H. C. Zeng, *J. Phys. Chem. C*, 2009, **113**, 1373-1385.

22. J. Li and H. C. Zeng, *Angew. Chem. Int. Ed.*, 2005, **44**, 4342-4345.

23. S. M. Zhang and H. C. Zeng, *Chem. Mater.*, 2010, **22**, 1282-1284.

24. H. G. Yang and H. C. Zeng, *J. Am. Chem. Soc.*, 2005, **127**, 270-278.

25. M. Liu and H. C. Zeng, *Langmuir.*, 2014, **30**, 9838-9849.

26. H. G. Yang and H. C. Zeng, *J. Phys. Chem. B*, 2004, **108**, 819-823.

27. M. L. Pang and H. C. Zeng, *Langmuir.*, 2010, **26**, 5963-5970.

28. C. T. Kresge, M. E. Leonowicz, W. J. Roth, J. C. Vartuli and J. S. Beck, *Nature*, 1992, **359**, 710-712.

29. V. Polshettiwar, D. Cha, X. Zhang and J. M. Basset, *Angew. Chem. Int. Ed.*, 2010, **49**, 9652-9656.

30. D. Zhao, J. Feng, Q. Huo, N. Melosh, G. H. Fredrickson, B. F. Chmelka and G. D. Stucky, *Science*, 1998, **279**, 548-552.

31. D. Zhao, Q. Huo, J. Feng, B. F. Chmelka and G. D. Stucky, *J. Am. Chem. Soc.*, 1998, **120**, 6024-6036.

32. J. M. Lopez Nieto, E. Acosta Burga and G. Kremenic, *Ind. Eng. Chem. Res.*, 1990, **29**, 337-342.

33. T. S. R. P. Rao and P. G. Menon, *J. Catal.*, 1978, **51**, 64-71.

34. G. Prieto, J. Zečević, H. Friedrich, K. P. de Jong and P. E. de Jongh, *Nat. Mater.*, 2013, **12**, 34-39.

35. F. Jiao and H. Frei, *Angew. Chem. Int. Ed.*, 2009, **48**, 1841-1844.

36. H. C. Zeng, *Acc. Chem. Res.*, 2013, **46**, 226-235.

37. J. Dou and H. C. Zeng, *ACS Catal.*, 2014, **4**, 566-576.

38. X. Du and J. He, *Langmuir.*, 2011, **27**, 2972-2979.

39. J. Ge, T. Huynh, Y. Hu and Y. Yin, *Nano Lett.*, 2008, **8**, 931-934.

40. J. Dou and H. C. Zeng, *J. Am. Chem. Soc.*, 2012, **134**, 16235-16246.

41. F. Hoffmann, M. Cornelius, J. Morell and M. Fröba, *Angew. Chem. Int. Ed.*, 2006, **45**, 3216-3251.

42. Y. Deng, Y. Cai, Z. Sun, J. Liu, C. Liu, J. Wei, W. Li, C. Liu, Y. Wang and D. Zhao, *J. Am. Chem. Soc.*, 2010, **132**, 8466-8473.

43. D. P. Wang and H. C. Zeng, *Chem. Mater.*, 2011, **23**, 4886-4899.

44. S. Liu and M.-Y. Han, *Chem. - Asian J.*, 2010, **5**, 36-45.

45. G. Li and Z. Tang, *Nanoscale*, 2014, **6**, 3995-4011.

46. S. H. Joo, J. Y. Park, C.-K. Tsung, Y. Yamada, P. Yang and G. A. Somorjai, *Nat. Mater.*, 2009, **8**, 126-131.

47. L. Li, S. He, Y. Song, J. Zhao, W. Ji and C.-T. Au, *J. Catal.*, 2012, **288**, 54-64.

48. J. Pak and H. Yoo, *Microporous Mesoporous Mater.*, 2014, **185**, 107-112.

49. Y. J. Wong, L. Zhu, W. S. Teo, Y. W. Tan, Y. Yang, C. Wang and H. Chen, *J. Am. Chem. Soc.*, 2011, **133**, 11422-11425.

50. H. Blas, M. Save, P. Pasetto, C. Boissière, C. Sanchez and B. Charleux, *Langmuir.*, 2008, **24**, 13132-13137.

51. C. C. Yec and H. C. Zeng, *J. Mater. Chem. A*, 2014, **2**, 4843-4851.

52. M. Zhao, K. Deng, L. He, Y. Liu, G. Li, H. Zhao and Z. Tang, *J. Am. Chem. Soc.*, 2014, **136**, 1738-1741.

53. Q. Zhang, T. R. Zhang, J. P. Ge and Y. D. Yin, *Nano Lett.*, 2008, **8**, 2867-2871.

54. J. Liu, S. Z. Qiao, J. S. Chen, X. W. Lou, X. Xing and G. Q. Lu, *Chem. Commun.*, 2011, **47**, 12578-12591.

55. X. Fang, X. Zhao, W. Fang, C. Chen and N. Zheng, *Nanoscale*, 2013, **5**, 2205-2218.

56. J. Park and H. Song, *Nano Research*, 2011, **4**, 33-49.

57. S. Wang, M. Zhang and W. Zhang, *ACS Catal.*, 2011, **1**, 207-211.

58. K. A. Dahlberg and J. W. Schwank, *Chem. Mater.*, 2012, **24**, 2635-2644.

59. H. C. Zeng, *J. Mater. Chem.*, 2006, **16**, 649-662.

60. S. M. Kim, M. Jeon, K. W. Kim, J. Park and I. S. Lee, *J. Am. Chem. Soc.*, 2013, **135**, 15714-15717.

61. J. G. Kim, S. M. Kim and I. S. Lee, *Small*, 2015, **11**, 1930-1938.

62. D.-G. Lee, S. M. Kim, H. Jeong, J. Kim and I. S. Lee, *ACS Nano*, 2014, **8**, 4510-4521.

63. L. Shang, T. Bian, B. Zhang, D. Zhang, L.-Z. Wu, C.-H. Tung, Y. Yin and T. Zhang, *Angew. Chem.*, 2014, **126**, 254-258.

64. S. K. Movahed, M. Shariatipour and M. Dabiri, *RSC Advances*, 2015, **5**, 33423-33431.

65. Z. Ren, V. Botu, S. Wang, Y. Meng, W. Song, Y. Guo, R. Ramprasad, S. L. Suib and P.-X. Gao, *Angew. Chem. Int. Ed.*, 2014, **53**, 7223-7227.

66. Q. Liu, Z. Sun, Y. Dou, J. H. Kim and S. X. Dou, *J. Mater. Chem. A*, 2015, **3**, 11688-11699.

67. Y. Sheng and H. C. Zeng, *ACS Appl. Mater. Interfaces*, 2015, **7**, 13578-13589.

68. J. Qu, W. Li, C.-Y. Cao, X.-J. Yin, L. Zhao, J. Bai, Z. Qin and W.-G. Song, *J. Mater. Chem.*, 2012, **22**, 17222-17226.

69. R. Jin, Y. Yang, Y. Xing, L. Chen, S. Song and R. Jin, *ACS Nano*, 2014, **8**, 3664-3670.

70. J. Zheng, B.-H. Wu, Z.-Y. Jiang, Q. Kuang, X.-L. Fang, Z.-X. Xie, R.-B. Huang and L.-S. Zheng, *Chem. - Asian J.*, 2010, **5**, 1439-1444.

71. Y. Sheng and H. C. Zeng, *Chem. Mater.*, 2015, **27**, 658-667.

72. C. C. Yec and H. C. Zeng, *ACS Nano*, 2014, **8**, 6407-6416.

73. X. Fang, Z. Liu, M.-F. Hsieh, M. Chen, P. Liu, C. Chen and N. Zheng, *Acs Nano*, 2012, **6**, 4434-4444.

74. Y. Wang, C. Tang, Q. Deng, C. Liang, D. H. L. Ng, F.-l. Kwong, H. Wang, W. Cai, L. Zhang and G. Wang, *Langmuir.*, 2010, **26**, 14830-14834.

75. R. Jin, Y. Yang, Y. Zou, X. Liu and Y. Xing, *Chem. - Eur. J.*, 2014, **20**, 2344-2351.

76. X. Wang, J. Zhuang, Q. Peng and Y. Li, *J. Solid State Chem.*, 2005, **178**, 2332-2338.

77. C. Manjunatha, B. M. Nagabhushana, H. Nagabhushana and R. P. S. Chakradhar, *J. Mater. Chem.*, 2012, **22**, 22392-22397.

78. R. Jin, Y. Xing, X. Yu, S. Sun, D. Yu, F. Wang, W. Wu and S. Song, *Chem. - Asian J.*, 2012, **7**, 2955-2961.

79. W. Zhu, Y. Yang, S. Hu, G. Xiang, B. Xu, J. Zhuang and X. Wang, *Inorg. Chem.*, 2012, **51**, 6020-6031.

80. J.-H. Liu, A.-Q. Wang, Y.-S. Chi, H.-P. Lin and C.-Y. Mou, *The Journal of Physical Chemistry B*, 2005, **109**, 40-43.

81. K. X. Yao and H. C. Zeng, *Chem. Mater.*, 2012, **24**, 140-148.

82. U. Sazama and A. Reller, *Journal of thermal analysis*, 1996, **47**, 357-364.

83. J. Wang, J. Ge, H. Zhang and Y. Li, *Small*, 2006, **2**, 257-260.

84. X.-H. Zhang, X. Yi, J. Zhang, Z. Xie, J. Kang and L. Zheng, *Inorg. Chem.*, 2010, **49**, 10244-10246.

85. X. Wang, J. Zhuang, J. Chen, K. Zhou and Y. Li, *Angew. Chem.*, 2004, **116**, 2051-2054.

86. Q. Ou, L. Zhou, S. Zhao, H. Geng, J. Hao, Y. Xu, H. Chen and X. Chen, *Chem. Eng. J.*, 2012, **180**, 121-127.

87. K. Dong, Z. Liu and J. Ren, *CrystEngComm*, 2013, **15**, 6329-6334.

88. H. Chen, X. Lu, C. Deng and X. Yan, *J. Phys. Chem. C*, 2009, **113**, 21068-21073.

89. J. Zheng, C. Cheng, R.-W. Yan, W.-J. Fang, C. Chen, H.-X. Huai and C.-C. Wang, *J. Alloy. Compd.*, 2014, **596**, 5-9.

90. C.-Y. Cao, F. Wei, J. Qu and W.-G. Song, *Chem. - Eur. J.*, 2013, **19**, 1558-1562.

91. H. Yue, Y. Zhao, S. Zhao, B. Wang, X. Ma and J. Gong, *Nat. Commun.*, 2013, **4**.

92. P. Hu, J. V. Morabito and C.-K. Tsung, *ACS Catal.*, 2014, **4**, 4409-4419.

93. Z. Li and H. C. Zeng, *Chem. Mater.*, 2013, **25**, 1761-1768.

94. Z. Li and H. C. Zeng, *J. Am. Chem. Soc.*, 2014, **136**, 5631-5639.

95. D. Esken, S. Turner, O. I. Lebedev, G. Van Tendeloo and R. A. Fischer, *Chem. Mater.*, 2010, **22**, 6393-6401.

96. T. Ishida, M. Nagaoka, T. Akita and M. Haruta, *Chem. - Eur. J.*, 2008, **14**, 8456-8460.

97. C.-H. Kuo, Y. Tang, L.-Y. Chou, B. T. Sneed, C. N. Brodsky, Z. Zhao and C.-K. Tsung, *J. Am. Chem. Soc.*, 2012, **134**, 14345-14348.

98. G. Lu, S. Li, Z. Guo, O. K. Farha, B. G. Hauser, X. Qi, Y. Wang, X. Wang, S. Han, X. Liu, J. S. DuChene, H. Zhang, Q. Zhang, X. Chen, J. Ma, S. C. J. Loo, W. D. Wei, Y. Yang, J. T. Hupp and F. Huo, *Nat. Chem.*, 2012, **4**, 310-316.

99. S. Gao, N. Zhao, M. Shu and S. Che, *Appl. Catal. A*, 2010, **388**, 196-201.

100. M. Müller, S. Hermes, K. Kähler, M. W. E. van den Berg, M. Muhler and R. A. Fischer, *Chem. Mater.*, 2008, **20**, 4576-4587.

101. Y. K. Park, S. B. Choi, H. J. Nam, D.-Y. Jung, H. C. Ahn, K. Choi, H. Furukawa and J. Kim, *Chem. Commun.*, 2010, **46**, 3086-3088.

102. M. Meilikhov, K. Yusenko, D. Esken, S. Turner, G. Van Tendeloo and R. A. Fischer, *Eur. J. Inorg. Chem.*, 2010, **2010**, 3701-3714.

103. Y. Liu and Z. Tang, *Adv. Mater.*, 2013, **25**, 5819-5825.

104. C. Wei, X. Li, F. Xu, H. Tan, Z. Li, L. Sun and Y. Song, *Anal. Methods*, 2014, **6**, 1550-1557.

105. X. Gu, Z.-H. Lu, H.-L. Jiang, T. Akita and Q. Xu, *J. Am. Chem. Soc.*, 2011, **133**, 11822-11825.

106. H.-L. Jiang, T. Akita, T. Ishida, M. Haruta and Q. Xu, *J. Am. Chem. Soc.*, 2011, **133**, 1304-1306.

107. W. Zhang, G. Lu, C. Cui, Y. Liu, S. Li, W. Yan, C. Xing, Y. R. Chi, Y. Yang and F. Huo, *Adv. Mater.*, 2014, **26**, 4056-4060.

108. T. Zhang, B. Li, X. Zhang, J. Qiu, W. Han and K. L. Yeung, *Microporous Mesoporous Mater.*, 2014, **197**, 324-330.

109. J. Liu, B. Lukose, O. Shekhah, H. K. Arslan, P. Weidler, H. Gliemann, S. Brase, S. Grosjean, A. Godt, X. Feng, K. Mullen, I.-B. Magdau, T. Heine and C. Woll, *Sci. Rep.*, 2012, **2**, 921.

110. Z. Zhang, Y. Chen, S. He, J. Zhang, X. Xu, Y. Yang, F. Nosheen, F. Saleem, W. He and X. Wang, *Angew. Chem. Int. Ed.*, 2014, **53**, 12517-12521.

111. Z. Zhang, Y. Chen, X. Xu, J. Zhang, G. Xiang, W. He and X. Wang, *Angew. Chem. Int. Ed.*, 2014, **53**, 429-433.

112. X. Xu, Z. Zhang and X. Wang, *Adv. Mater.*, 2015, **27**, 5365-5371.

113. T. Zhang, L. Lin, X. Zhang, H. Liu, X. Yan, J. Qiu and K. L. Yeung, *Mater. Lett.*, 2015, **148**, 17-21.

114. L.-B. Sun, J.-R. Li, W. Lu, Z.-Y. Gu, Z. Luo and H.-C. Zhou, *J. Am. Chem. Soc.*, 2012, **134**, 15923-15928.

115. S. Hermes, D. Zacher, A. Baunemann, C. Wöll and R. A. Fischer, *Chem. Mater.*, 2007, **19**, 2168-2173.

116. G. Zhan and H. C. Zeng, *Chem. Mater.*, 2015, **27**, 726-734.

Chapter 3 A General Strategy for Preparation of Carbon-Nanotube-Supported Nanocatalysts with Hollow Cavities and Mesoporous Shells

3.1. Introduction

Architectural design of integrative catalysts with compositional and structural complexities has attracted considerable attention in both fundamental science and industrial research over the past decades, owing to its importance to the development of heterogeneous catalysts.[1-3] As a special class of novel catalysts, hollow-structured mesoporous catalysts (HMCs) with a central cavity, a permeable shell and catalytically active cores (*e.g.*, metal or metal oxide nanoparticles (NPs)) integrate the advantages of both hollow and porous systems.[4-7] In this type of catalysts, reactants or products can diffuse between inner cavity and bulk solution *via* the permeable porous shell by design. Meanwhile, catalytic reactions can take place inside the cavity where nanostructured catalysts are confined. In this sense, a HMC becomes virtually a reactor or factory in nanoscale. So far, much effort has been devoted to fabricating HMCs for industrially interested reactions.[8-17] The engineering of HMCs is mainly achieved with synthetic approaches from integrating individual components into a multifunctional edifice in a step-by-step manner. Regarding the creation of hollow interior, several synthetic strategies have been developed, including well-known hard- or soft-templating, oriented

attachment, Kirkendall diffusion, Ostwald ripening effect, *etc*.[18] Up till now, all the existing HMCs are realized using hollow spherical hosts together with some core units, especially SiO_2, periodic mesoporous organosilica, carbon or polymer hollow spherical moulds. In most cases, the overall morphology of HMCs (*i.e.*, yolk-shell) is spherical or zero-dimensional (0D). It should be pointed out that in such 0D HMCs, core nanoparticles are mostly unsupported or freestanding inside their interior space. As a result, catalyst–support interaction is normally unanticipated in 0D HMCs. Rather surprisingly, no attempt so far has been made to prepare the HMCs into one-dimensional (1D) configuration. In a recent report, copper NPs were assembled within the 1D pore channels of the support, appearing to be a 1D configuration.[19] However, the access of reactants to the copper NPs was only realized through the two open ends of 1D channels and no porosity perpendicular to the 1D channels is present, which is different from the above proposed 1D HMCs. Conceptually, such 1D HMCs could also be viewed as linearly integrated 0D HMCs and they would still possess nanoscale features in the radial direction while extending along the axial direction macroscopically, which is of paramount importance to practical handling and separation for this class of catalysts. We noted that carbon nanotubes (CNTs) are generally recognized as one of the best and most easily available 1D nanostructures.[20] Therefore, to advance the above research, we try to use CNTs as a backbone for the preparation of 1D HMCs. Although composites of CNTs and metal nanoparticles have shown excellent catalytic

performance in a wide range of chemical reactions, such as hydrogenation, oxidation-reduction, and direct methanol fuel cells, *etc.*,[21-24] a general strategy for preparation of complex CNT-based HMCs is still lacking.

In principle, we would expect the CNT-based HMCs still keep the essence of traditional ‘‘catalyst-plus-support” configuration for their practical applications.[1] Here we summarize three basic features for them: (a) the CNTs provide large specific surface areas to support catalytic components; (b) a tubular cavity space between CNT-supported catalysts and porous shell allows high-throughput chemical processes, including sequential reactions at different catalytically active phases. Besides this, the cavity space also permits better chemical mixing and mass transport, and the overall system can be viewed as a 1D nanoreactor for confined catalysis, which may be superior to some non-hollow catalysts (with a closely packed cable-like configuration where NPs are trapped between the CNT and shell)[21, 22]; and (c) the porous shell serves as a cell membrane to isolate the catalytic systems from undesired reactive environments, because it can impose size-restriction to the unwanted chemical species. In heterogeneous catalysis, a major challenge in making supported catalysts is to avoid agglomeration and leaching of active components, especially under harsh reaction conditions and long term usage (*e.g.*, industrial applications).[25-27] Although, the growth of NPs could be inhibited by controlling the spatial distribution of the NPs and maximizing the interparticle spacings,[19] the long traveling path for the molecules within 1D channels

remains as a problem. If the pore size of the shell is smaller than that of encapsulated particles, moreover, agglomeration or loss of catalyst can also be hindered.[28] Taking together, it is believed that the dual protection of catalyst cores by the CNTs (chemical support) and the porous shell (physical barrier) would also lead to higher stability for the 1D HMCs. Compared to the support free 0D HMCs, furthermore, the above proposed 1D HMCs could take on more catalytic NPs and allow more flexible compositional manipulation, because catalyst–support interaction becomes more appreciable with chemically modified or functionalized CNTs that serve as catalyst carrier in targeted HMCs.

In this work, therefore, we propose a general strategy for preparation of CNT-based HMCs: core materials (*i.e.*, catalysts) will be wrapped by permeable shells along with a cavity space between them, wherein the catalyst nanoparticles can be precisely placed on CNTs and be protected by the porous shells. Besides their pristine properties, the CNTs also endow inherent tubular geometry, and it would be very interesting to see whether 1D HMCs can be fabricated or not using CNTs as a support or template. As depicted in Figure 3.1, this synthetic investigation for the 1D HMCs can be divided into three parts: (i) preparing catalytic core materials (1 to 3); (ii) generating cavity space and engineering shell structure and functionality (4 to 6); and (iii) forming targeted 1D HMCs (7 to 9). Furthermore, in this study, the prepared catalysts

were also used in benzyl alcohol oxidation to demonstrate their workability and performance advantage.

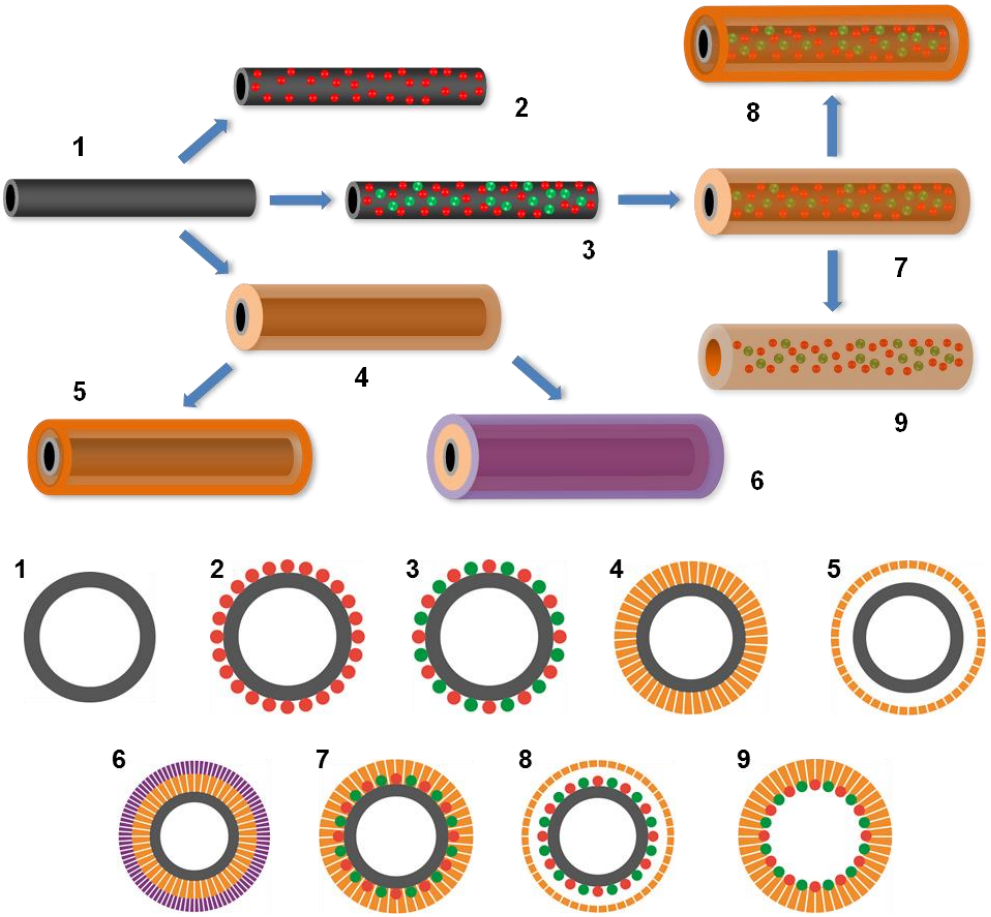

Figure 3.1 Synthetic strategy of one-dimensional hollow-structured mesoporous catalysts (1D HMCs) with their starting CNTs and various intermediates and analogues: (1) CNTs, (2) CNT@STNPs, (3) CNT@DTNPs, (4) CNT@*m*SiO_2, (5) hollow-structured CNT@*m*SiO_2 (a structural analogue with a hollow interior required by 1D HMCs), (6) CNT@*m*SiO_2@ZIF-8 or CNT@*m*SiO_2@Nb_2O_5, (7) cable-like CNT@NPs@*m*SiO_2, (8) hollow-structured CNT@NPs@*m*SiO_2 (*i.e.*, 1D HMC product), and (9) NPs@*m*SiO_2 nanotubes after removal of CNTs from (7). STNPs = single-type nanoparticles, DTNPs = double-type nanoparticles, and *m*SiO_2 = mesoporous SiO_2. The overall configuration of catalysts is designated as A@B@C, where A is located in the innermost part (*i.e.*, mostly CNTs in this study), C is in the outmost part, and B is positioned between A and C. More complete descriptions can be found along the text.

3.2. Experimental Section

3.2.1. Materials

The following chemicals were used as received without further purification: tetraethylorthosilicate (TEOS, Aldrich, 98%), gold (III) chloride trihydrate (Aldrich, 99.9%), palladium (II) chloride (Aldrich, 99.9%), zinc acetate dihydrate (Aldrich, 98%), zinc nitrate hexahydrate (Aldrich, 98%), cobalt (II) acetate tetrahydrate (Aldrich, 97%), titanium (IV) n-propoxide (Aldrich, 98%), niobium (V) ethoxide (Strem Chemicals, 99.9%), 2-methylimidazole (2-MeIM, Aldrich, 99%), 1-dodecanethiol (DDT, Aldrich, 98%), dodecylamine (DDA, Aldrich, 98%), oleic acid (OA, Aldrich, 90%), cetyltrimethylammonium bromide (CTAB, Fluka, 96%), tetra-n-octylammonium bromide (TOAB, Alfa Aesar, 98%), tert-butylamine (Aldrich, 98%), sodium borohydride ($NaBH_4$, Aldrich, 99.99%), ammonia solution (Merck, 25%), Tween-85 (Tw85, Sigma), poly(diallyldimethyl-ammonium chloride) solution (PDDA, Aldrich, 20%, MW 400000-500000 Da), poly(sodium 4-styrene-sulfonate) (PSS, Aldrich, MW 70 000 Da), (3-aminopropyl)trimethoxysilane (APTMS, Acros, 95%), potassium hydroxide (Merck, 85%), sodium hydroxide (Merck, 99%), benzaldehyde (Aldrich, 99%), benzyl alcohol (Aldrich, 99%), hydrogen peroxide (Merck, 30%), ethyl acetate (Merck, 99.5%), toluene (Fisher, 99.99%), methanol (Fisher, 99.99%), acetone (Fisher, 99.9%), ethylene glycol (EG, Merck, 99.5%), and ethanol (Fisher, 99.99%). Commercially available CNTs were supplied from CNano Technology Limited Company, China. Deionized water was used for all experiments.

3.2.2. Core materials for HMCs

In a typical synthesis of CNT@STNPs, CNTs (15 mg) and CTAB (0.20 g) were dispersed into toluene solvent (20.0 mL) under sonication for 2 h. Then, a specific NPs suspension (also in toluene) was added dropwise into the mixture, and continuously sonicated for 2 h. After that, the mixture was stirred for another 17 h at room temperature without sonication. The product was washed thoroughly with ethanol twice and dried in an electric oven at 60°C overnight. To prepare CNT@DTNPs, two different types of NPs were successively added into the CNTs suspension under the same ultrasonic treatment.

3.2.3. Structural intermediates for HMCs

CNT@*m*SiO_2 was prepared through a surfactant-modified sol-gel process.[29] Briefly, CNTs (100 mg) and CTAB (1.0 g) were dispersed into a mixture of deionized water (30.0 mL) and ethanol (80.0 mL) under sonication for 2 h. Then, ammonia (2.0 mL) was added to the above suspension under vigorous stirring for 5 min. Afterward, TEOS (2.0 mL of TEOS in 40.0 mL of ethanol) was added dropwise and the mixture was further stirred for another 12 h. Finally, the product was recovered *via* centrifugation, followed by washing with ethanol twice, drying at 60°C overnight. The obtained CNT@*m*SiO_2 was calcined in air at 500°C for 5 h to remove the residual surfactants. Following the similar procedures, *m*SiO_2 coating layers of variable thickness can be

achieved by adjusting the TEOS concentration in the starting solution. CNT@NPs@*m*SiO_2 samples were also prepared in a similar way, except that the CNTs were substituted by the CNT@STNPs or CNT@DTNPs. Additionally, the CNTs core of CNT@NPs@*m*SiO_2 could be completely removed *via* air oxidation at high temperature to produce NPs@*m*SiO_2.

3.2.4. Formation of hollow interior for HMCs

For surface treatment, 0.5 g of the above prepared CNT@*m*SiO_2 or CNT@NPs@*m*SiO_2 was dispersed in PDDA aqueous solution (200 mL, 2 wt%) under sonication for 1 h. Afterward, 0.10 g of the surface-modified CNT@*m*SiO_2 or CNT@NPs@*m*SiO_2 was re-dispersed in a dilute NaOH solution (20 mL, 2 mM), followed by hydrothermal treatment at 160°C for 24 h. After reaction, the hollow products were collected *via* centrifugation, followed by washing with ethanol twice, drying at 60°C overnight and calcination at 350°C for 5 h.

3.2.5. Shell functionalization for HMCs

For surface treatment, CNT@*m*SiO_2 (17 mg) was dispersed in deionized water (20 mL) under sonication for 1 h, and then APTMS (70 μL) was added. The mixture was stirred vigorously at room temperature for 18 h. Subsequently, the solid was washed with ethanol twice and re-dispersed in PSS aqueous solution (30 mL, 0.3 wt%) under sonication for 0.5 h to allow PSS adsorption. Afterward, the surface modified CNT@*m*SiO_2 was centrifuged to remove

excess PSS and re-dispersed in a $Zn(NO_3)_2$ aqueous solution (25 mL, 6.7 mM) with stirring for 10 min. Then 2-MeIM aqueous solution (10 mL, 0.12 M) was added dropwise into the above system with stirring at room temperature for another 6 h. Finally, the products were collected by centrifuging, washing with methanol twice, and drying at 60°C overnight. For the synthesis of CNT@*m*SiO_2@Nb_2O_5, CNT@*m*SiO_2 (10 mg) was firstly dispersed into EG (20 mL) under sonication for 1 h. Then, niobium ethoxide (0.10 mL) was added to the mixture under vigorous stirring for another 0.5 h. The mixture was then transferred to a Teflon-lined stainless steel autoclave and hydrothermal treated at 120°C for 3 h. After that, the mixture was poured into acetone (120 mL) and stirred vigorously for 3 h. The gray precipitate was harvested through centrifuging, washing with deionized water twice, and then drying at 60°C overnight.

3.2.6. Oxidation reactions of benzyl alcohol

The oxidation of benzyl-alcohol was carried out in a magnetically stirred glass reactor (capacity: 50 mL) by dispersing the catalysts in 10 mL of aqueous medium composed of benzyl-alcohol (9.6 mmol) and H_2O_2 (26.5 mmol). The reaction was conducted at 80ºC for 3 h. After the reaction, the samples were centrifuged to separate the catalyst from the reaction mixture. The products were analyzed by GC and GC–MS. External calibration method was used for quantitative analysis of the amounts of reactants consumed (conversion) and

products generated (selectivity). The amount of catalyst used in the reaction depends on the metal loading, *e.g.*, 10 mg of CNT@Au-Pd catalyst was used as the total metal loading was 27.2 wt% (see more cases later).

3.2.7. Characterization techniques

Six major characterization techniques were employed in this work. Morphologies of samples were characterized by field-emission scanning electron microscopy (FESEM, JSM-5600LV), transmission electron microscopy (TEM, JEM-2010) and high-resolution TEM (HRTEM, JEM-2100F). The crystallographic information was analyzed by X-ray diffraction (XRD, Bruker D8 Advance) equipped with a Cu K_α radiation source. The elemental mapping was done by energy-dispersive X-ray spectroscopy (EDX, Oxford Instruments, Model 7426). Thermogravimetric analysis (TGA) studies for some as-prepared samples were carried out on a thermobalance (TGA-2050, TA Instruments) under flowing air or nitrogen atmosphere at a heating rate of $10^oC \cdot min^{-1}$. Specific surface areas, pore volume, and pore size of some representative samples were also determined using N_2 physisorption isotherms at 77 K (Quantachrome NOVA-3000 system). Metal loading in the catalyst samples was determined by inductively coupled plasma optical emission spectrometry (ICP-OES, Optima 7300DV, Perkin Elmer, USA). The surface composition of the samples were analyzed by X-ray photoelectron spectroscopy (XPS, AXIS-HSi, Kratos Analytical).

3.3. Results and Discussion

3.3.1. Synthesis of core materials for HMCs

Firstly, we prepared the core materials for HMCs with a single type of nanoparticles (STNPs) anchoring onto surfaces of CNTs. To obtain the CNT@STNPs (Figure 3.1, structure (2)), as received CNTs were first treated with CTAB surfactant under ultrasonic conditions, which could facilitate dispersion of CNTs in aqueous or organic media.[30] The assembling forces involved in this molecularly mediated protocol are: (i) van der Waals interaction between the hydrophobic surfactant and the hydrophobic part of CNTs, and (ii) hydrogen-bonding interaction between the functional groups of both the organic mediators and the CNTs (*e.g.*, –COOH).[31] Herein, the studied nanoparticles include DDT-capped Au NPs, DDA-capped Pd NPs, DDA-capped Au-Pd (alloy) NPs, Tw85-capped Co_3O_4 NPs, Tw85-capped ZnO NPs and OA-capped TiO_2 NPs. We have obtained six CNT@STNPs core materials, as reported in Figure 3.2, CNT@Au, CNT@Pd, CNT@ Au-Pd, CNT@Co_3O_4, CNT@ ZnO and CNT@TiO_2. The small dark dots (*i.e.*, the supported nanoparticles) in these images were well distributed on the CNTs, noting that the CNT surfaces become rougher after particle loading. Understandably, the uniform dispersion of these active NPs on CNTs will be instrumental to their catalytic performance. Combinatorial integration of two different types of catalytic NPs on CNTs can diversify the functionality of the catalysts

applicable for tandem reactions. Using a similar strategy, we have also prepared three CNT@DTNPs core materials (Figure 3.1, structure (3)), namely, CNT@Au/TiO_2, CNT@Pd/TiO_2 and CNT@Au-Pd/TiO_2. For example, the CNT@Au/TiO_2 core material can be obtained by the successive additions of the Au NPs and TiO_2 NPs to the CNTs suspension with the aid of ultrasonic treatment. As revealed in Figure 3.3, uniform and well dispersed double-type NPs were deposited on the surfaces of CNTs. Along the similar line, the attachment of a third or even a fourth component on CNTs is still possible, if one wishes.

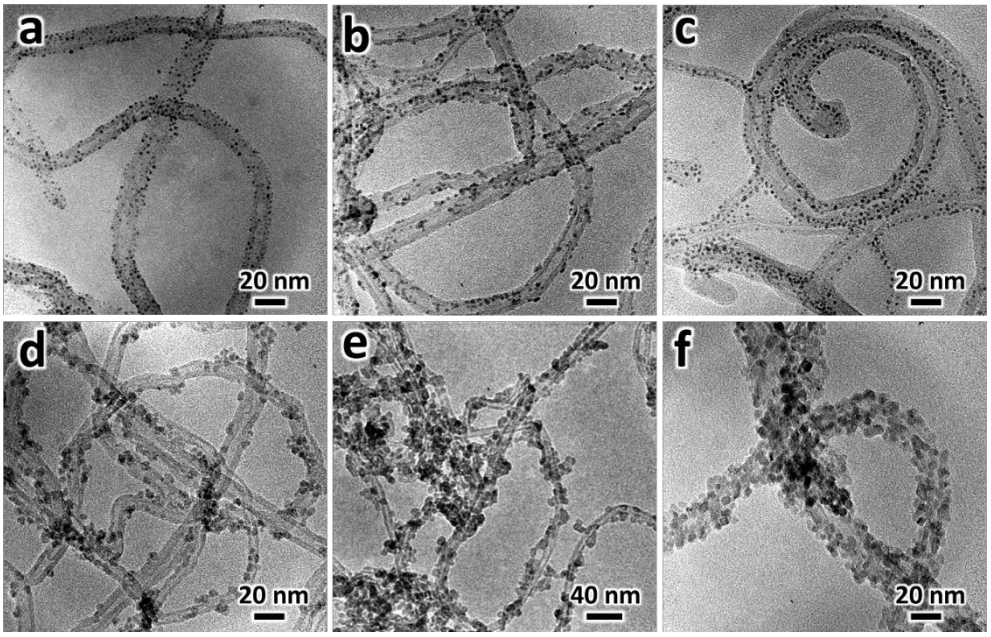

Figure 3.2 TEM images of representative CNT-supported core materials (CNT@STNPs refer to Figure 3.1, structures (2)) for HMCs: (a) CNT@Au, (b) CNT@Pd, (c) CNT@Au-Pd, (d) CNT@Co_3O_4, (e) CNT@ZnO, (f) CNT@TiO_2.

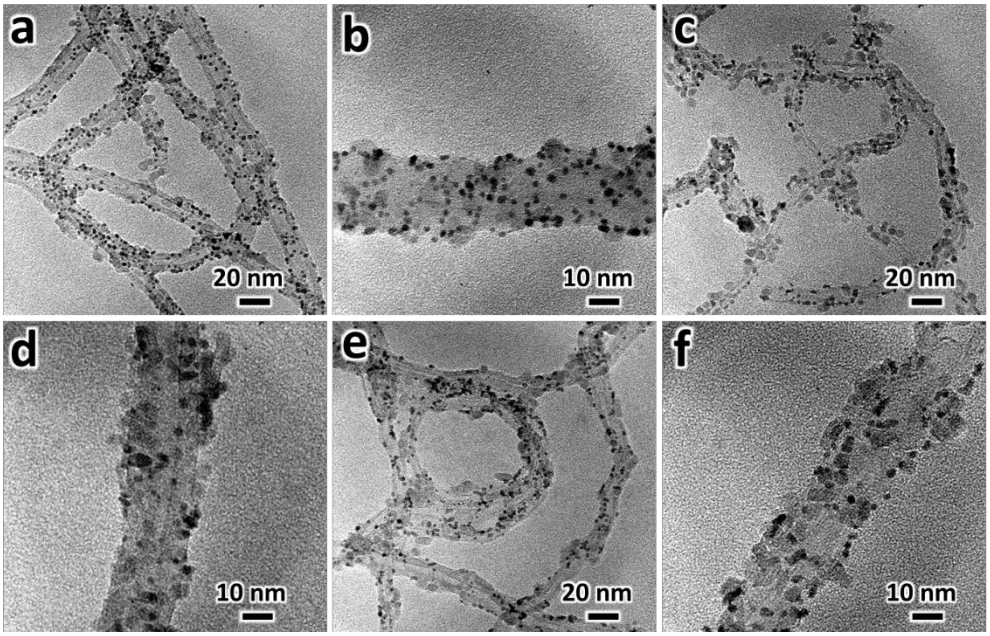

Figure 3.3 TEM images of representative CNT-supported core materials (CNT@DTNPs refer to Figure 3.1, structures (3)) for HMCs: (a,b) CNT@Au/TiO_2, (c,d) CNT@Pd/TiO_2, and (e,f) CNT@Au-Pd/TiO_2.

3.3.2. Cavity generation and shell functionalization for HMCs

It is believed that the SiO_2 coating not only favors the dispersion of CNTs in the aqueous media but also provides them with a silica-like surface, which allows further modification via silylation of the silanol group.[32] In this work, mesoporous SiO_2 coated CNTs core-shell structure (CNT@*m*SiO_2) was prepared through a surfactant-template sol-gel process with TEOS as a silica source and CTAB as a structure-directing agent. Figure 3.4a-c presents the morphology of as-obtained CNT@*m*SiO_2 samples. As can be seen, a uniform *m*SiO_2 shell of *ca* 15 nm in thickness was formed on the outer surface of CNTs, affirming a complete coverage. The analysis of N_2 physisorption isotherms shows that the CNT@*m*SiO_2 has a large specific surface area of 751

$m^2 \cdot g^{-1}$ (Brunauer-Emmett-Teller (BET) method), with mesopores in the silica sheath of *ca* 2 nm and a specific pore volume of 0.55 $mL \cdot g^{-1}$.

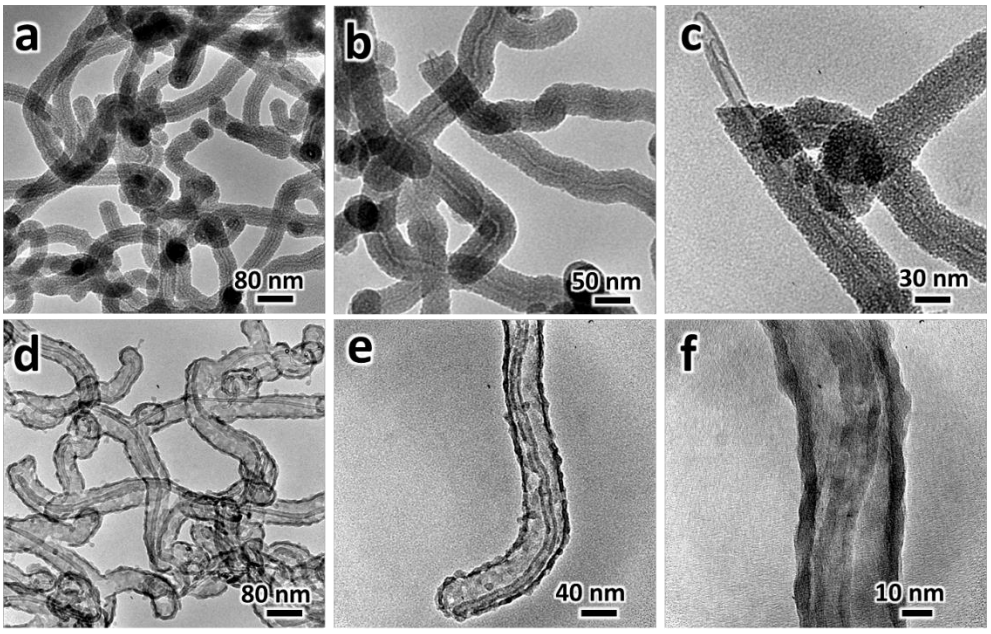

Figure 3.4 TEM images of (a-c) pristine CNT@*m*SiO_2, (d-f) hollow-structured CNT@*m*SiO_2 (i.e., a structural analogue to 1D HMCs). Refer to Figure 3.1 (structures (4) and (5)).

A cavity space inside the CNT@*m*SiO_2 can be further generated by the selective etching the SiO_2 coating *via* hydrothermal treatments with PDDA serving as a surface protecting agent and NaOH as an etchant. As shown in Figure 3.4d-f, the CNTs are now detached from silica phase and a large central interior is created for the CNT@*m*SiO_2. Note that the thickness of SiO_2 shell is reduced to around 6 nm. It is believed that the dissolution of silica and co-assembly of silicate species (*e.g.*, oligomers) on PDDA layer are responsible for the etching and reconstruction of silica shell.[33] It was also confirmed that the silica shell cannot be successfully formed without the PDDA template. In

relation to this shell reconstruction, process parameters such as NaOH concentration, reaction temperature and time had been investigated. It was found that the pristine SiO_2 coating gradually dissolved and regrew into interlaced flakes that structured the shells; a longer reaction led to complete dissolution of interior silica and regrowth of a new but thinner outer shell. Basicity of reaction environment is also important. At a low base concentration (*e.g.*, 1 mM), for example, the silica coating layer was only partially dissolved. However, at a higher base concentration (*e.g.*, 4 mM), the core-sheath (or yolk-shell) structure could not be preserved due to the exhaustive dissolution of silica and thus failure of reformation of silica tube. The BET specific surface area of this hollow-structured CNT@*m*SiO_2 is still as high as 237 $m^2 \cdot g^{-1}$, despite the significant loss of silica phase. Although other strategies have been developed to functionalize CNTs with silica, few report has been carried out on CNTs/SiO_2 hybrid structure with central voids.[34] Nevertheless, the interior cavity of the CNT@*m*SiO_2 system will benefit its catalysis applications, when the CNT core is further functionalized into 1D HMCs.

It has been well-known that the surfaces of silica are covered with abundant hydroxyl group.[32] Thus, it is possible to further functionalize the CNT@*m*SiO_2 with additional thin layer(s) on the outmost surfaces of *m*SiO_2. To exploit this possibility, a ZIF-8 shell was grown on top of the *m*SiO_2 shell, which turned the mesoporous CNT@*m*SiO_2 into microporous CNT@*m*SiO_2@ZIF-8

because the new phase ZIF-8 added in is microporous. In this synthesis, the precursor CNT@*m*SiO_2 was first decorated with a layer of negatively charged polyelectrolyte (PSS).[35] The negative surface charges could ensure a rapid capture of Zn^{2+} *via* electrostatic interaction. The surface enrichment of Zn^{2+} ions would then favor the formation of ZIF-8 phase. As can be seen in Figure 3.5a-c, central CNTs were covered with two distinctly different coatings, *viz*. inner shell of *m*SiO_2 (*ca* 18 nm) and outer shell of ZIF-8 (*ca* 25 nm, with a lighter image contrast). Elemental mapping images (Figure 3.6a) further confirm the composition of the outer shell on the CNT@*m*SiO_2 is indeed ZIF-8 phase (see Zn and N signals). On the contrary, in the absence of surface PSS, only isolated ZIF-8 granules and CNT@*m*SiO_2 mixtures were obtained in the product, similar to the previous works.[36, 37] This novel hierarchical pore structure combines both merits of microporous ZIF-8 (high gas uptake) and mesoporous silica (high diffusion rate), which could have potential application in gas separation,[38] or membrane reactor. Furthermore, we also added Nb_2O_5 coating on the surface of CNT@*m*SiO_2 *via* an antisolvent precipitation approach based on the non-solvating ability of acetone to the glycolated niobium oxide.[39] As can be seen from Figure 3.5d-f, the double shelled feature is evident, with CNTs as the core, mesoporous SiO_2 as the inner shell and Nb_2O_5 as the outer shell (*ca* 9 nm, with a darker image contrast). Again, results from elemental mappings (Figure 3.6b) confirm the presence of Nb_2O_5. Consistent with this observation, our XRD study (Figure 3.7) also

demonstrates the success of the depositions of ZIF-8 and Nb_2O_5 phases on the CNT@*m*SiO_2. This finding suggests that the CNT@*m*SiO_2 could be more versatile for functionalization compared with bare CNTs. In the similar ways, it is expected that other functionalized shells can also be added on.

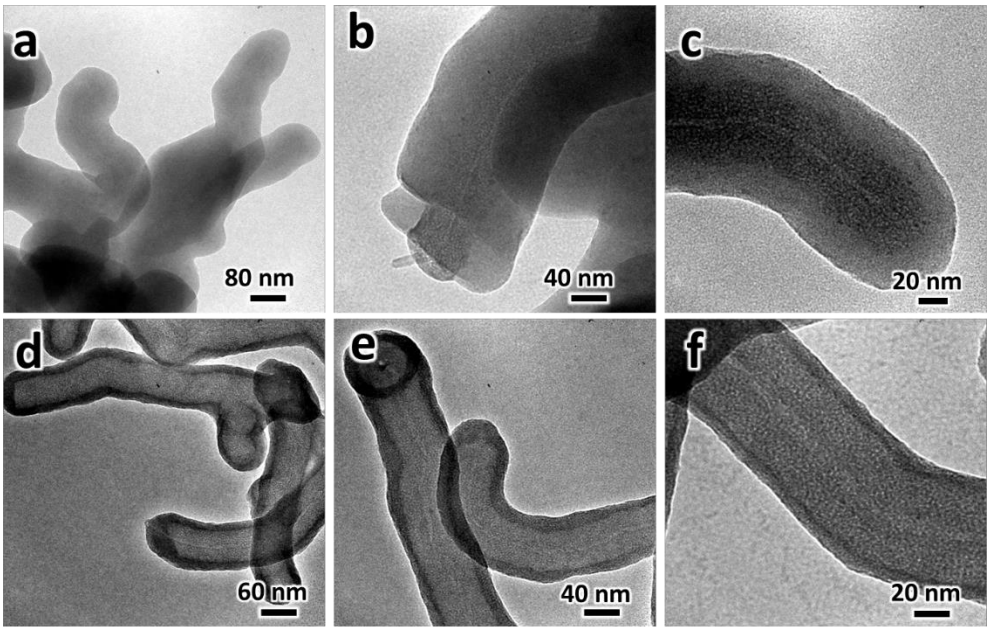

Figure 3.5 TEM images of (a-c) CNT@*m*SiO_2@ZIF-8, (d-f) CNT@*m*SiO_2@Nb_2O_5. Refer to Figure 3.1 (structures (6)).

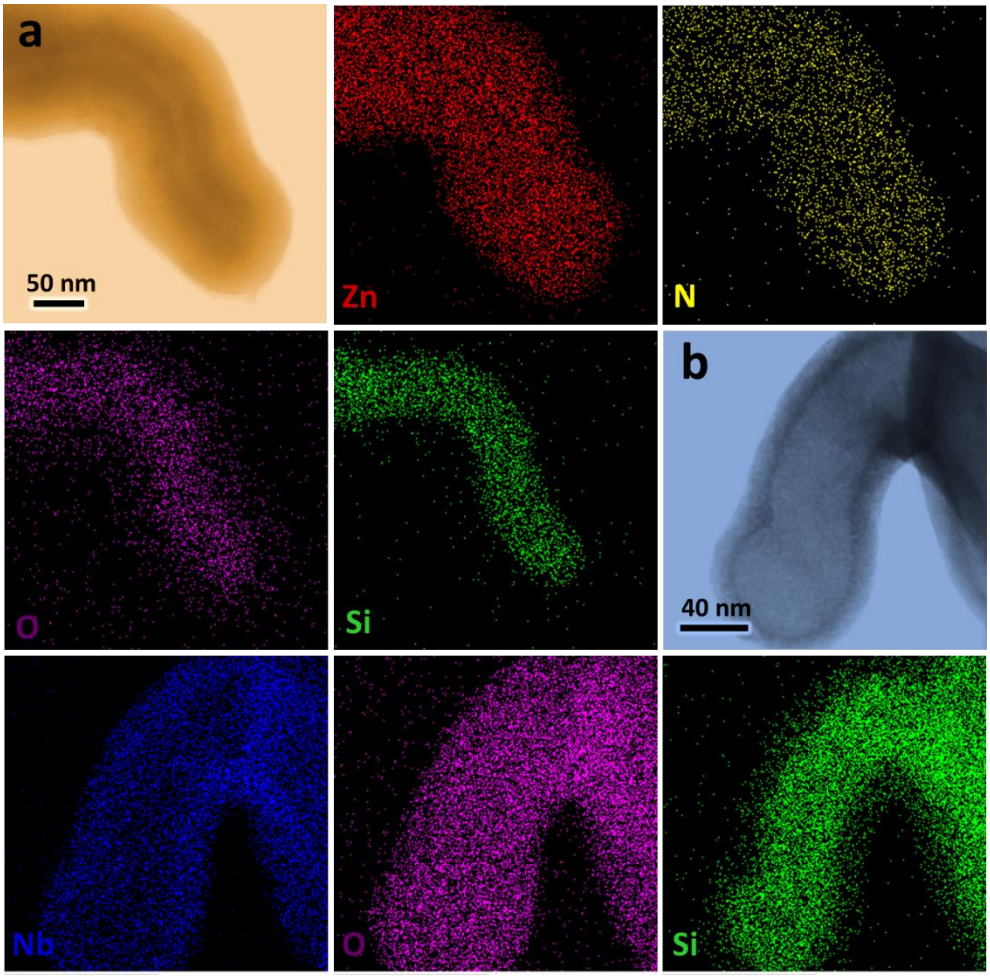

Figure 3.6 EDX elemental mappings of two representative samples with an additional outer shell: (a) CNT@*m*SiO_2@ZIF-8 (note that Zn and N signals are from ZIF-8 outer shell while O and Si signals from silica inner shell) and (b) CNT@*m*SiO_2@Nb_2O_5 (Note that herein Nb_2O_5 is also an outer shell). The two composite products have the same structural configuration (refer to Figure 3.1, structure (6) for graphic illustration).

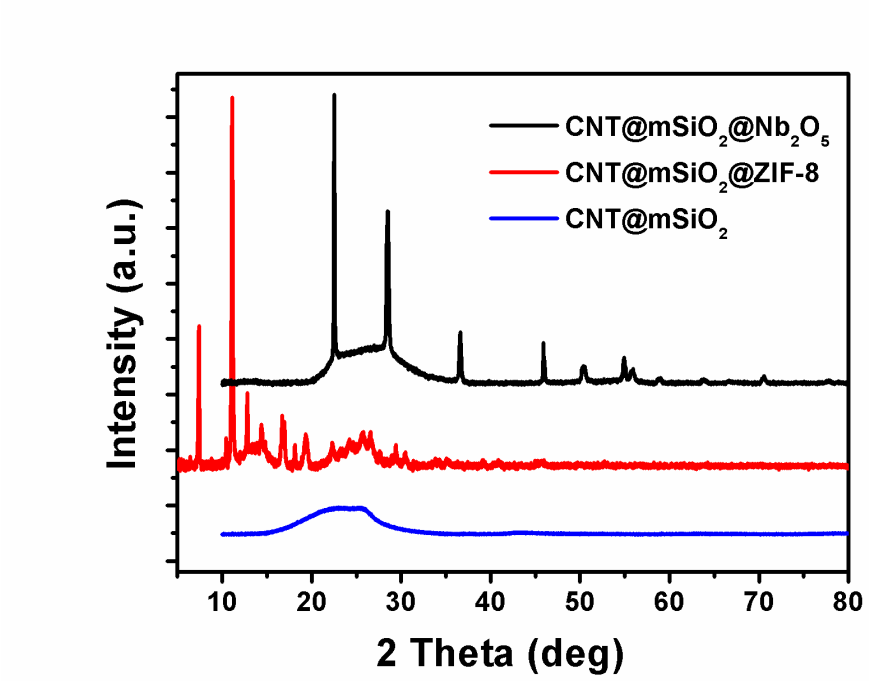

Figure 3.7 XRD patterns of the as-prepared CNT@*m*SiO_2, CNT@*m*SiO_2@ZIF-8 and CNT@*m*SiO_2@Nb_2O_5 samples. CNTs (JCPDS card no. 58-1638) and Nb_2O_5 (JCPDS card no. 71-0336).

3.3.3. Formation routes of 1D HMCs

The above structural analogue (*i.e.*, CNT@*m*SiO_2) can be easily turned into 1D HMCs. For example, by replacing the bare CNTs with the catalytic core materials of Figure 3.2 and Figure 3.3 (*i.e.*, structures (2) and (3), Figure 3.1), 1D HMCs can be readily obtained. The above CTAB-assembly sol-gel process can also add a uniform SiO_2 shell onto these catalytic core materials, resulting in a concentric cable-like assemblage. To implement this idea, we have synthesized five such solid intermediates for HMCs: CNT@Au-Pd@*m*SiO_2, CNT@TiO_2@*m*SiO_2, CNT@Au/TiO_2@*m*SiO_2, CNT@Pd/TiO_2@*m*SiO_2, and CNT@Au-Pd/TiO_2@*m*SiO_2 in Figure 3.8a-c. Indeed, all the NPs were moored between the silica shell and CNT. The thickness of *m*SiO_2 shell was tunable

simply *via* varying the concentration of TEOS in the starting solution when the amount of the CNT@NPs was fixed in synthesis. For instance, the thickness of *m*SiO_2 shell was tuned in the range from 4.6 to 36.2 nm by adjusting the TEOS concentration from 1.63 to 23.7 mM. The *m*SiO_2 shell of such CNT@NPs@*m*SiO_2 is permeable with an average pore size of 2 nm. Thus, the residing NPs (on CNTs) are still accessible by solvents and reactants, acting as catalysts with size-selection from the *m*SiO_2 shell.

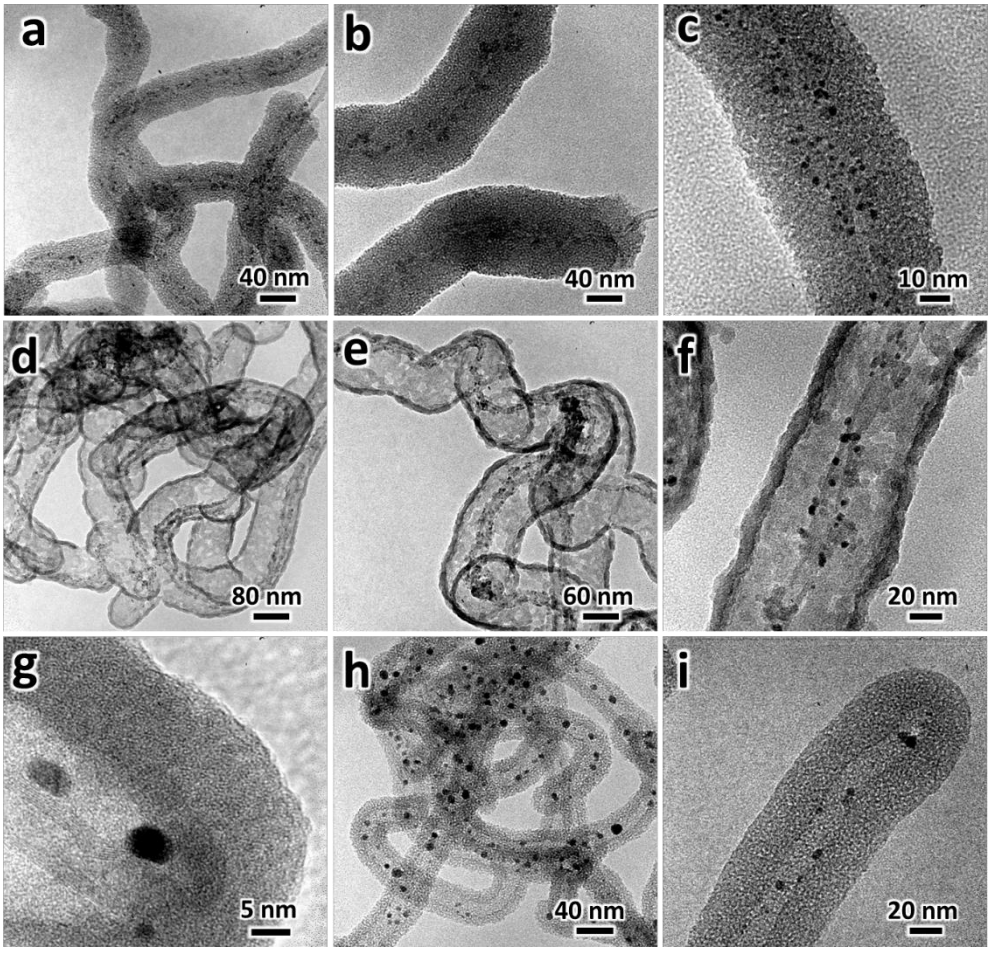

Figure 3.8 Representative TEM images of (a) CNT@Au-Pd@*m*SiO_2, (b) CNT@TiO_2@*m*SiO_2, (c) CNT@Au/TiO_2@*m*SiO_2, (d-g) hollow-structured CNT@Au-Pd@*m*SiO_2 (*i.e.*, a 1D HMC) and (h-i) Au-Pd@*m*SiO_2 nanotubes produced by calcination at 500°C. Refer to product structures (7), (8) and (9) of Figure 3.1.

In the cable-like CNT@NPs@*m*SiO_2, the NPs are sandwiched between the CNT and *m*SiO_2. Such immobilization can prevent the NPs from migration and/or detachment under turbulent reaction environments, since inter-collision of particulate catalysts may cause loss of active components from their supports.[26] Thus, catalytic nanoparticles are better protected by the silica phase, which is beneficial to their longevity. Strictly speaking, however, the simple cable-like configuration may not be the most effective for practical reactions due to (i) shortage of interior space between the porous silica shell and the catalyst NPs, (ii) long diffusion path for reactants in pore channels, and (iii) nonoptimized usage of catalysts, noting that some of NPs are covered underneath of the *m*SiO_2. Therefore, it is highly desirable to create an interior cavity in the cable-like CNT@NPs@*m*SiO_2 in order to increase the accessibility to all the NPs. As described earlier in Figure 3.4d-f, the etching and dissolution-regrowth process is a viable means to create a central cavity. Employing this method, the 1D HMC of CNT@NPs@*m*SiO_2 (where NPs = Au-Pd) with a continuous 1D central space has been obtained (Figure 3.8d-g). Interestingly, during the hollowing process, the NPs could still be preserved on the CNTs surface without changing their particle size and location. To further confirm that metal NPs were fully covered by the mesoporous SiO_2 shell, a compositional analysis with XPS was performed. It showed that the atomic ratio of silicon to metals (Au, Pd) was higher than 200:1, since the metals are indeed capped within the shell, noting that XPS is a surface

sensitive analytical technique. It can be envisioned that the permeable silica shell in this 1D HMC offers a two-way traffic for selected molecules travelling between inner reaction cavity and outer bulk solution, and the central cavity serves as a reactor to hold the reactants and products while the NPs supported by CNTs work as nanocatalysts. The performance of this 1D HMCs will be evaluated shortly with a testing reaction: selective oxidation of benzyl alcohol.

In addition to restructuring the preformed *m*SiO_2 phase, hollow-structured catalysts can also be prepared by removing CNTs. For example, nanoparticle-loaded mesoporous silica nanotubes, namely NPs@*m*SiO_2 (Figure 3.1, structure (9)) can be further obtained from the CNT@NPs@*m*SiO_2 by burning off the CNT support. Usually, combustion temperature of pristine CNTs in air can be as high as 600–700°C.[40] Nevertheless, the presence of Au-Pd alloy NPs would facilitate the same oxidation reaction at a much lower temperature (*ca* 400°C).[41, 42] In this way, a large variety of inorganic phases could be incorporated onto the inner wall of silica shell, producing a series of tubular catalysts, as exampled in Figure 3.8h-i for the Au-Pd@*m*SiO_2. In this process, the CNTs served as a mould to shape the *m*SiO_2 shell for the final products. After the heat-treatment, all of the samples exhibited a type IV N_2 isotherm and a characteristic hysteresis loop for mesoporous materials (see Figure 3.9 and Figure 3.10). In general, the surface area and pore volume increased continuously when increasing heating temperature. And the mean pore sizes in these NPs@*m*SiO_2 products are all around 2 nm, which is smaller than the size

of the NPs entrapping on the inner tubular walls. In this regard, the resultant *m*SiO_2 shell should be able to effectively protect the NPs from losing.

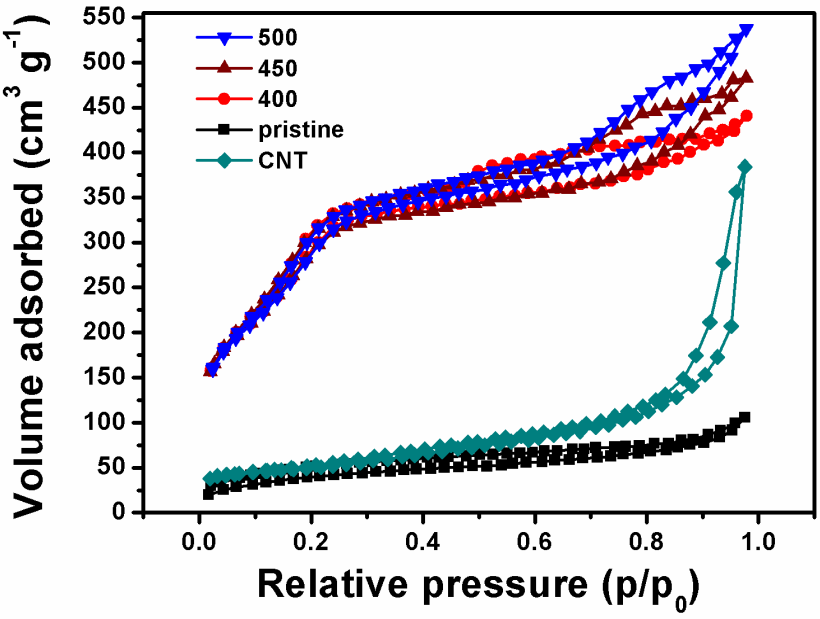

Figure 3.9 N_2 adsorption/desorption isotherms of cable-like CNT@Au-Pd@*m*SiO_2 samples calcined at different temperature (*e.g.*, 400°C, 450°C, and 500°C). Note: the curves marked with 'pristine' represent the sample without calcination treatment.

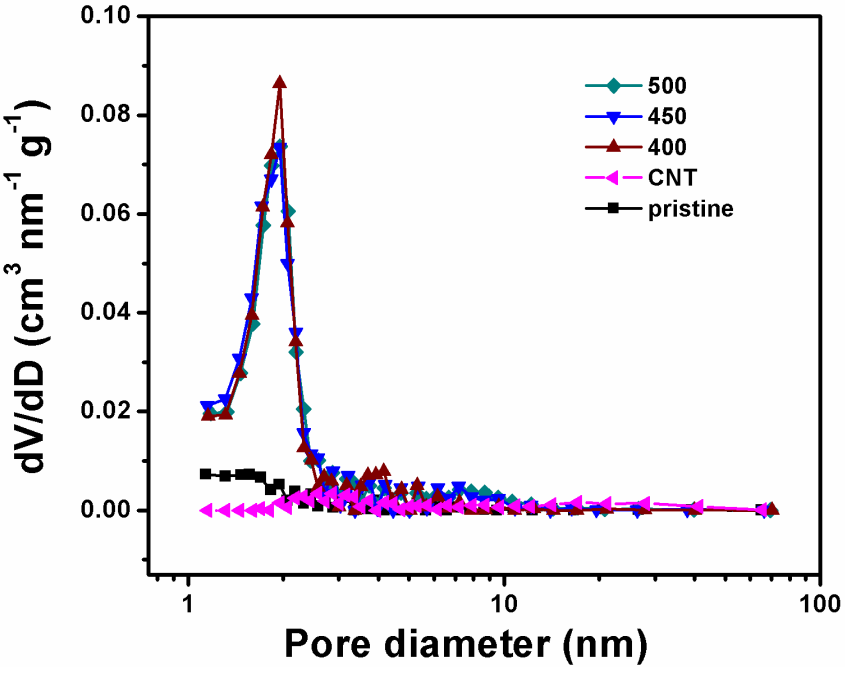

Figure 3.10 Pore size distributions of cable-like CNT@Au-Pd@*m*SiO_2 samples calcined at different temperature (e.g. 400ºC, 450ºC, and 500ºC). Note: the curves marked with 'pristine' represent the sample without calcination treatment.

3.3.4. Application of HMCs

After the above additions of metal, metal oxide, *m*SiO_2 and MOF onto the CNTs, a number of 1D HMCs can be obtained. In order to demonstrate the effectiveness and advantage of this type of catalysts, we carried out the selective oxidation of benzyl alcohol to benzaldehyde as a testing reaction. Three catalysts prepared in this work were evaluated, that is, CNT@Au-Pd, cable-like CNT@Au-Pd@*m*SiO_2, and hollow-structured CNT@Au-Pd@*m*SiO_2 (*i.e.*, 1D HMC). The metal loadings of these catalysts were 27.2 wt%, 4.94 wt%, and 14.2 wt%, respectively, as determined by inductively coupled plasma (ICP) analysis. Therefore, the amounts of the three catalysts used in the reaction were 10, 55 and 20 mg, respectively, in order to keep the same metal loading. First of all, for comparison, blank experiments were carried out under the same conditions without catalyst or using pristine CNTs as a catalyst. The conversions of benzyl alcohol were negligible (< 4% at 3 h) for the latter two cases. The reactions and the catalytic performance of the as-designed catalysts with respective to conversion and selectivity are reported in Figure 3.11. Apart from the main product benzaldehyde, benzoic acid and benzyl benzoate were also found as by-products (Figure 3.11a). As a conventional non-capsulated catalyst, the CNT@Au-Pd sample exhibits the

highest conversion of benzyl alcohol at 99.3% but a relatively low selectivity of benzaldehyde at 53.8% at 3 h (Figure 3.11b). As the reaction time increased, the conversion of benzyl alcohol whereas the benzaldehyde selectivity decreased continuously due to subsequent reaction of benzaldehyde to benzoic acid.[43] The time dependence of catalytic oxidation of benzyl alcohol was also performed on the two kinds of CNT@Au-Pd@*m*SiO_2 catalysts (*i.e.*, the cable-like and the hollow-structured). It is understandable that with the silica coating the catalytic activity of the Au-Pd NPs must be affected. Indeed, only 60.0% of benzyl alcohol conversion was achieved at 3 h using the cable-like CNT@Au-Pd@*m*SiO_2 sample (Figure 3.11c). The observed decrease in conversion is due to (i) mass-transfer limitation through pore channels and (ii) some active NPs buried underneath the silica phase, which are not accessible to the reactants. However, this catalyst gave the highest selectivity toward benzaldehyde of 91.1% at 3 h. Quite encouragingly, the CNT@Au-Pd@*m*SiO_2 catalyst (*viz.* complex 1D HMC) displays remarkable selectivity of 82.1% and conversion of 90.7% at 3 h (Figure 3.11d), as it likely strikes a balance between the selectivity and conversion owing to presence of both silica mesopores and interior space which provides more catalytic nanoparticles accessible to the reactant. Under similar conversion levels, both kinds of *m*SiO_2 protected catalysts exhibit higher selectivity then the bare CNT@Au-Pd catalyst, as shown in Figure 3.11e. For example, under a similar benzyl alcohol conversion of about 50%, the selectivities toward benzaldehyde

were 78%, 96% and 92%, for CNT@Au-Pd, cable-like CNT@Au-Pd@*m*SiO_2, and hollow-structured CNT@Au-Pd@*m*SiO_2, respectively. The enhanced selectivity towards benzaldehyde suggests that the *m*SiO_2 shell may serve as a porous membrane, since the permeation process normally exerts strong size dependence.[44] The diffusivity of the penetrants has this trend: benzaldehyde > benzyl alcohol > benzoic acid > benzyl benzoate, because the molecular size has a reverse sequence: benzyl benzoate (12.22 Å) > benzoic acid (7.61 Å) > benzyl-alcohol (7.05 Å) > benzaldehyde (6.64 Å). Obviously, the diffusion rate of these molecules from the catalytic surface to bulk solution would be significantly affected by the mesoporous silica shells. It should be noted that benzaldehyde is not only the product for benzyl alcohol oxidation, but also the reactant for producing byproducts, such as benzoic acid. Due to the smallest size, the diffusion rate of benzaldehyde is faster than other products and reactant (*i.e.*, benzyl alcohol), indicating a large part of benzaldehyde would diffuse outside the silica shell. Therefore, the possibility of benzaldehyde to be further oxidized becomes lower, because it requires the benzaldehyde in solution to pass through the silica channels to contact with the NPs. Nevertheless, this was not the case for the bare CNT@Au-Pd catalyst because there was no blocking shell. Under this condition, the as-formed benzaldehyde will contact with the NPs again after the formation, so it can be easily to be oxidized to benzoic acid.

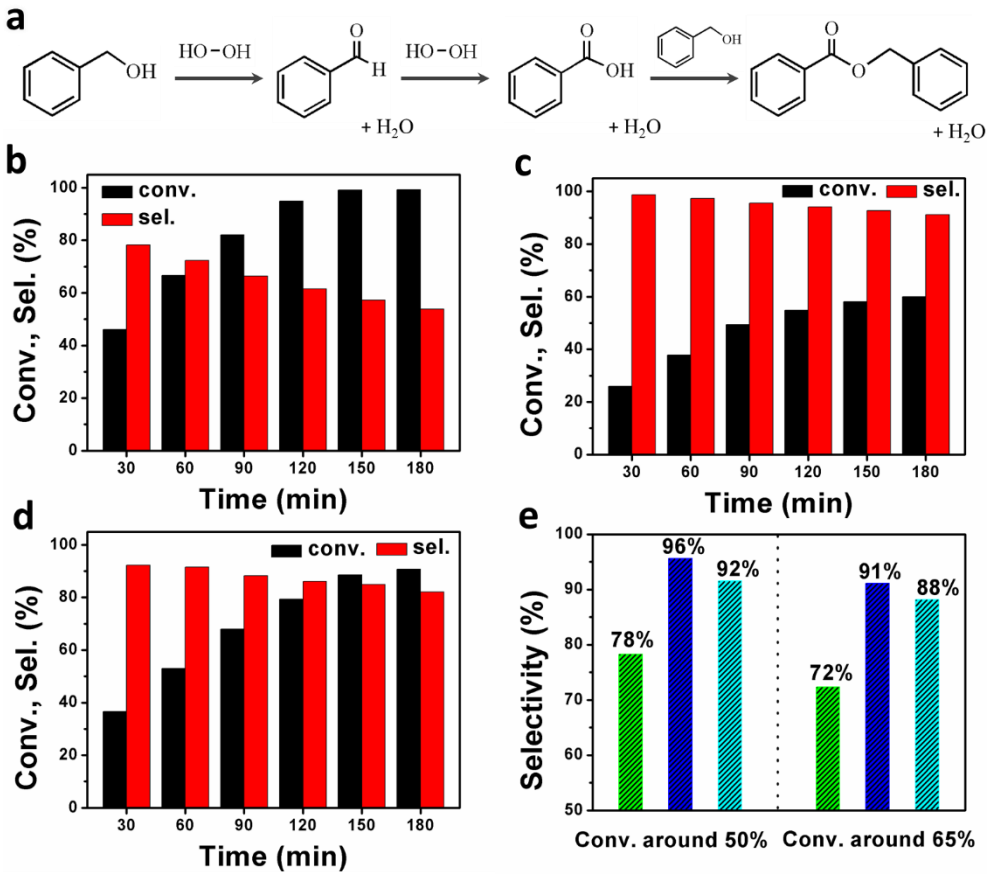

Figure 3.11 (a) Reactions involved in benzyl alcohol oxidation process. (b-d) Catalytic performance versus reaction time presented with conversion of benzyl alcohol and selectivity toward benzaldehyde of (b) core catalyst CNT@Au-Pd, (c) cable-like CNT@Au-Pd@*m*SiO_2, and (d) hollow-structured CNT@Au-Pd@*m*SiO_2 (i.e., 1D HMC). (e) Comparison of selectivities toward benzaldehyde by using three different catalysts at similar conversion levels (green bar: CNT@Au-Pd; dark blue bar: cable-like CNT@Au-Pd@*m*SiO_2; and light blue bar: hollow-structured CNT@Au-Pd@*m*SiO_2). Conv. = conversion, Sel. = selectivity.

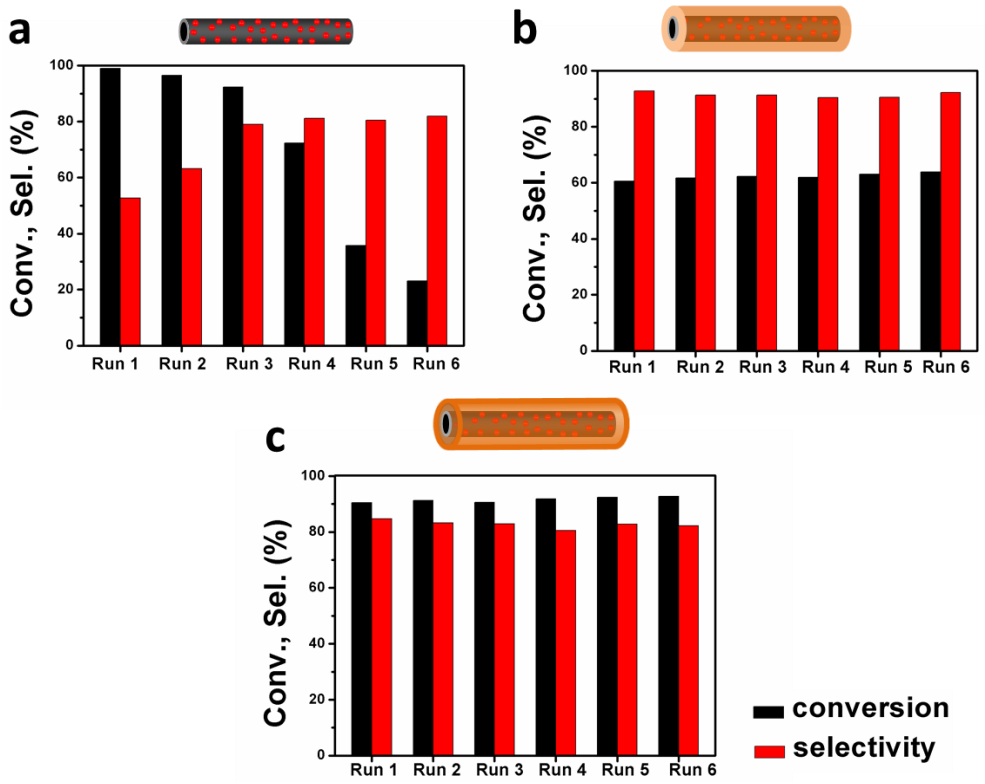

Figure 3.12 Catalyst stability presented with conversion of benzyl alcohol and selectivity toward benzaldehyde of (a) core catalyst CNT@Au-Pd, (b) cable-like CNT@Au-Pd@*m*SiO_2 and (c) hollow-structured CNT@Au-Pd@*m*SiO_2 (*i.e.*, 1D HMC). The corresponding models represent the three different kinds of catalyst structures (also refer to Figure 3.1).

We also investigated the reusability of the three catalysts over a process of 6 repeated experiments (Figure 3.12). The catalysts after each reaction run were recovered through centrifugation followed by extensive washing and sonication treatments, then dried and reused in a subsequent experiment under the same reaction conditions. In Figure 3.12a, the catalytic activity of the reused core catalyst CNT@Au-Pd (*i.e.*, without silica shell) decreases dramatically with the 6 consecutive runs. The distinct loss of catalytic activity was caused by both metal particles aggregation and detachment. We found that the leaching of the Au-Pd metal into the liquid phase was significant

under the operating condition. The metal content of Au-Pd in the reaction solution at 3 h was determined as 6.87 ppm by ICP. Moreover, the metal loading in the spent CNT@Au-Pd after first run was decreased to 21.4 wt% from the initial loading of 27.2 wt%. As revealed by the TEM images of the recycled catalysts (Figure 3.13a-c), the particle growth of Au-Pd NPs was also observable, and several congregated particles with diameters up to 40 nm were seen. Therefore, we believed that the growth of Au-Pd NPs was mainly contributed by the metal dissolution–deposition mechanism (*i.e.*, Ostwald ripening), as reported in literatures.[25, 45] And the loss of metal loading was probably due to both the metal leaching and metal detachment from the supports because of the collision among unprotected catalysts in the reaction solution. Compared to the unprotected CNT@Au-Pd, both the cable-like and hollow-structured CNT@Au-Pd@*m*SiO_2 catalysts exhibit much better stability for reuse. As shown in Figure 3.12b,c, the conversion of benzyl alcohol and selectivity of benzaldehyde were kept at almost constants during the 6 consecutive reaction cycles. The high stability of NPs in the hollow-structured CNT@Au-Pd@*m*SiO_2 catalyst can be attributed to dual stabilization with the CNTs as an effective support and the *m*SiO_2 shell as a robust protecting shield. TEM images of the recycled catalysts also indicate that there was no significant change in NP size or morphology during the reactions (Figure 3.13d-i). Therefore, these 1D catalysts show promising potential for future industrial application. In particular, 1D HMCs can be

considered as the optimum catalysts in view of the achieved balance among conversion, product selectivity, and the catalyst longevity. For a further comparison, a referenced catalyst with 5 wt % of Au-Pd loading on SBA-15 was also prepared by wet impregnation method. Using this SBA-15@Au-Pd catalyst, the conversion of benzyl alcohol was 48.1% at 3 h in the first run. However, the catalyst stability was very poor, where the conversion decreased to 5% at the second run (due to the presence of large metal agglomerates). It should be pointed out that mass transport may pose a problem in the SBA-15@Au-Pd, since molecules can only enter or exit from the two open ends of each 1D-channel and the catalyst located in the inner parts of the channel may not be accessible. Therefore, we believed that the thin mesoporous silica shell, supported catalyst cores, and a working interior space are the three critical factors contributing to the good performance and high durability of 1D HMCs.

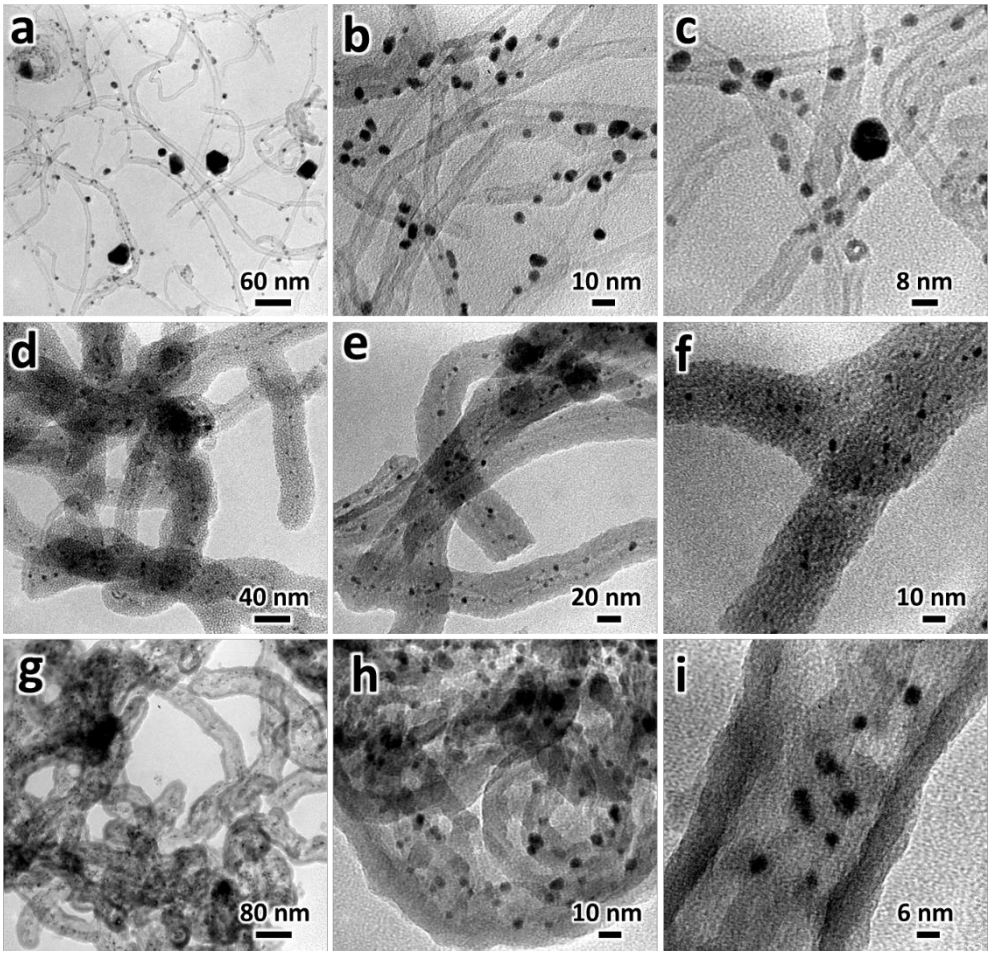

Figure 3.13 TEM images of used catalysts after 6 runs of benzyl alcohol oxidation reaction: (a-c) the CNT@Au-Pd (*i.e.*, core catalyst, without *m*SiO_2 shell), (d-f) cable-like CNT@Au-Pd@*m*SiO_2, and (g-i) hollow-structured CNT@Au-Pd@*m*SiO_2 (*i.e.*, 1D HMC).

3.4. Conclusions

In summary, the proposed CNT@Au-Pd@*m*SiO_2 (1D HMC type) catalyst with an interior space and a mesoporous shell can be prepared from its cable-like precursor. The CNT-based HMCs have shown good performance in the conversion of benzyl-alcohol to benzaldehyde in terms of activity, selectivity and recyclability. The robustness of catalyst can be attributed to dual protection of catalytic nanoparticles by both CNT support and mesoporous

silica shell. Furthermore, pore-size restriction of shell also suppresses by-product formation and thus increases product selectivity while the interior space can boost the conversion activity. Compared to simpler 0D HMCs, the CNT-based 1D HMCs developed here can hold more catalytic nanoparticles and gain additional flexibility in compositional tailoring, owing to the presence of catalyst–support interaction. These technological merits will benefit HMCs for a wider scope of applications in heterogeneous catalysis.

3.5. References

1. H. C. Zeng, *Accounts. Chem. Res.*, 2013, **46**, 226-235.

2. D. R. Rolison, *Science*, 2003, **299**, 1698-1701.

3. Y. Deng, Y. Cai, Z. Sun, J. Liu, C. Liu, J. Wei, W. Li, C. Liu, Y. Wang and D. Zhao, *J. Am. Chem. Soc.*, 2010, **132**, 8466-8473.

4. X. Fang, Z. Liu, M.-F. Hsieh, M. Chen, P. Liu, C. Chen and N. Zheng, *Acs Nano*, 2012, **6**, 4434-4444.

5. Y. Li and J. Shi, *Adv. Mater.*, 2014, **26**, 3176-3205.

6. Z. Chen, Z.-M. Cui, F. Niu, L. Jiang and W.-G. Song, *Chem. Commun.*, 2010, **46**, 6524-6526.

7. D. M. Vriezema, M. Comellas Aragonès, J. A. A. W. Elemans, J. J. L. M. Cornelissen, A. E. Rowan and R. J. M. Nolte, *Chem. Rev.*, 2005, **105**, 1445-1490.

8. S. M. Kim, M. Jeon, K. W. Kim, J. Park and I. S. Lee, *J. Am. Chem. Soc.*, 2013, **135**, 15714-15717.

9. G. Yang, N. Tsubaki, J. Shamoto, Y. Yoneyama and Y. Zhang, *Journal of the American Chemical Society*, 2010, **132**, 8129-8136.

10. G. Yang, C. Xing, W. Hirohama, Y. Jin, C. Zeng, Y. Suehiro, T. Wang, Y. Yoneyama and N. Tsubaki, *Catal. Today*, 2013, **215**, 29-35.

11. Y. H. Ng, S. Ikeda, T. Harada, S. Higashida, T. Sakata, H. Mori and M. Matsumura, *Adv. Mater.*, 2007, **19**, 597-601.

12. J. Guo, W. Yang, Y. Deng, C. Wang and S. Fu, *Small*, 2005, **1**, 737-743.

13. J. Liu, S. Z. Qiao, J. S. Chen, X. W. Lou, X. Xing and G. Q. Lu, *Chem. Commun.*, 2011, **47**, 12578-12591.

14. J. Liu, H. Q. Yang, F. Kleitz, Z. G. Chen, T. Yang, E. Strounina, G. Q. Lu and S. Z. Qiao, *Adv. Funct. Mater.*, 2012, **22**, 591-599.

15. P. M. Arnal, M. Comotti and F. Schüth, *Angew. Chem. Int. Ed.*, 2006, **45**, 8224-8227.

16. R. Güttel, M. Paul, C. Galeano and F. Schüth, *J. Catal.*, 2012, **289**, 100-104.

17. R. Guttel, M. Paul and F. Schüth, *Chem. Commun.*, 2010, **46**, 895-897.

18. H. C. Zeng, *J. Mater. Chem.*, 2011, **21**, 7511-7526.

19. G. Prieto, J. Zečević, H. Friedrich, K. P. de Jong and P. E. de Jongh, *Nat. Mater.*, 2013, **12**, 34-39.

20. S. Iijima, *Nature*, 1991, **354**, 56-58.

21. Z. Sun, H. Zhang, Y. Zhao, C. Huang, R. Tao, Z. Liu and Z. Wu, *Langmuir.*, 2011, **27**, 6244-6251.

22. S. Takenaka, T. Arike, H. Matsune, E. Tanabe and M. Kishida, *J. Catal.*, 2008, **257**, 345-355.

23. W. Li, C. Liang, W. Zhou, J. Qiu, Zhou, G. Sun and Q. Xin, *J. Phys. Chem. B*, 2003, **107**, 6292-6299.

24. P. Serp, M. Corrias and P. Kalck, *Appl. Catal. A*, 2003, **253**, 337-358.

25. X. Yu and S. Ye, *J. Power Sources*, 2007, **172**, 145-154.

26. J. D. Webb, S. MacQuarrie, K. McEleney and C. M. Crudden, *J. Catal.*, 2007, **252**, 97-109.

27. A. Taguchi and F. Schüth, *Microporous Mesoporous Mater.*, 2005, **77**, 1-45.

28. X. Huang, C. Guo, J. Zuo, N. Zheng and G. D. Stucky, *Small*, 2009, **5**, 361-365.

29. M. Zhang, Y. Wu, X. Feng, X. He, L. Chen and Y. Zhang, *J. Mater. Chem.*, 2010, **20**, 5835-5842.

30. L. Vaisman, H. D. Wagner and G. Marom, *Adv. Colloid Interface Sci.*, 2006, **128–130**, 37-46.

31. L. Han, W. Wu, F. L. Kirk, J. Luo, M. M. Maye, N. N. Kariuki, Y. Lin, C. Wang and C.-J. Zhong, *Langmuir.*, 2004, **20**, 6019-6025.

32. P. Van Der Voort and E. F. Vansant, *J. Liq. Chromatogr.*, 1996, **19**, 2723-2752.

33. K. X. Yao and H. C. Zeng, *Chem. Mater.*, 2012, **24**, 140-148.

34. M. Grzelczak, M. A. Correa-Duarte and L. M. Liz-Marzán, *Small*, 2006, **2**, 1174-1177.

35. M. A. Correa-Duarte, A. Kosiorek, W. Kandulski, M. Giersig and L. M. Liz-Marzan, *Chem. Mater.*, 2005, **17**, 3268-3272.

36. L. Dumee, L. He, M. Hill, B. Zhu, M. Duke, J. Schutz, F. She, H. Wang, S. Gray, P. Hodgson and L. Kong, *J. Mater. Chem. A*, 2013, **1**, 9208-9214.

37. S. J. Yang, J. H. Cho, K. S. Nahm and C. R. Park, *Int. J. Hydrogen Energy*, 2010, **35**, 13062-13067.

38. S. R. Venna and M. A. Carreon, *Journal of the American Chemical Society*, 2010, **132**, 76-78.

39. C. C. Li, J. Dou, L. Chen, J. Lin and H. C. Zeng, *ChemCatChem*, 2012, **4**, 1675-1682.

40. Y. Yang, S. Qiu, W. Cui, Q. Zhao, X. Cheng, R. Li, X. Xie and Y.-W. Mai, *J. Mater. Sci.*, 2009, **44**, 4539-4545.

41. H. Ogihara, M. Sadakane, Y. Nodasaka and W. Ueda, *Chem. Mater.*, 2006, **18**, 4981-4983.

42. B. C. Satishkumar, A. Govindaraj, M. Nath and C. N. R. Rao, *J. Mater. Chem.*, 2000, **10**, 2115-2119.

43. G. Zhan, J. Huang, M. Du, D. Sun, I. Abdul-Rauf, W. Lin, Y. Hong and Q. Li, *Chem. Eng. J.*, 2012, **187**, 232-238.

44. R. Wang, C. Cao and T. S. Chung, *J. Membr. Sci.*, 2002, **198**, 259-271.

45. I. W. C. E. Arends and R. A. Sheldon, *Appl. Catal. A*, 2001, **212**, 175-187.

Chapter 4 Bubble-like Manganese Silicate as a Versatile Platform for Design and Synthesis of Nanostructured Catalysts

4.1. Introduction

Hollow-structured mesoporous materials consisting of a cavity or void within a mesoporous shell have been attracting a great deal of attention across various fields.[1-5] Usually, the mesopore channels are generated by using self-assembled surfactant micelles as structural directors, similar to the preparation of MCM-41 type mesopores,[6] and the templating surfactants are removed by thermal treatment or solvent extraction.[7] However, both methods may not be very cost-effective at industrial scale and it is difficult to remove surfactants completely. A concept of "surfactant-free" has thus been realized if the mesopore channels can be created by the stacking of nano-building blocks (*e.g.*, sheets and crystallites).[8-11] Unfortunately, the uniformity of pores arising from the inter-particle space is usually low due to disordered aggregation and polydispersity of the building blocks. Therefore, the control of mesoporous nanostructures without using surfactants is particularly challenging.

In this chapter, we report a facile surfactant-free approach for fabricating sophisticated yolk-shell nanocatalysts with mesopore channels on the shell. Manganese silicate (MS) was used as the shell framework, since manganese has been explored as an essential component in numerous catalytic materials,

especially important in electron-transfer reactions.[12-14] In order to pursue the multifunctional catalysis or synergetic effects between the different active species, various catalytic nanoparticles (NPs) were encapsulated/or immobilized into hollow cavities or surfaces of the mesoporous MS, including Au, Ag, Pt, Ni, Co, Au-Pd alloy, MoO_2, Fe_3O_4, carbon nanotubes (CNTs) and their combinations. We demonstrate their enhanced catalysis for both liquid reaction (*e.g.*, 4-nitrophenol reduction) and gas reaction (*e.g.*, CO_2 hydrogenation). MS also allows doping of rare-earth ions into its silicate framework,[15] therefore, catalytic properties brought in by the dopants could be further tuned.

4.2. Experimental Section

4.2.1. Materials

The following chemicals were used as received without further purification: tetraethylorthosilicate (TEOS, Aldrich, 99%), manganese (II) sulfate monohydrate (Alfa Aesar, 99%), gold (III) chloride trihydrate (Aldrich, 99.9%), palladium (II) chloride (Aldrich, 99.9%), potassium tetrachloroplatinate (II) (Aldrich, 98%), silver (I) nitrate (Merck,99.8%), iron (III) chloride anhydrous (Aldrich, 98%), ammonium heptamolybdate (AHM, Merck, 99%), polyvinylpyrrolidone (PVP, Aldrich, K-30), cetyltrimethylammonium bromide (CTAB, Aldrich, 96%), cetyltrimethylammonium chloride (CTAC, Aldrich, 25%), tetra-*n*-

octylammonium bromide (TOAB, Alfa Aesar, 98%), dodecylamine (DDA, Aldrich, 98%), sodium borohydride (Aldrich, 99.99%), sodium maleate (Fluka, 98%), sodium acetate (Fisher, 99.9%), sodium citrate (Aldrich, 99%), L-ascorbic acid (Aldrich, 99%), triethanoamine (Acros Organics, 99%), ammonia solution (Merck, 32%), ethylene glycol (EG, Merck, 99.5%), toluene (Fisher, 99.99%), isopropanol (Fisher, 99.99%) and ethanol (Fisher, 99.99%). Commercially available CNTs were supplied by CNano Technology Limited Company, China. Deionized water was used for all experiments.

4.2.2. Synthesis of NPs@SiO_2 core-shell

The silica beads were prepared with a modified Stöber process *via* hydrolysis/condensation of TEOS in aqueous solutions containing ethanol (or isopropanol), ammonium (or triethanoamine), surfactants (*e.g.*, CTAB, CTAC and PVP) and core materials (*e.g.*, Au, Ag, Au-Pd, MoO_2, Fe_3O_4, CNT and CNT@Au-Pd). For instance, to prepare the Au@SiO_2, for example, 3 mL of PVP-stabilized Au NPs was dispersed into a mixture of isopropanol (25 mL) and H_2O (5 mL) with ultrasonication for 0.5 h. Then 0.6 mL of ammonium and 1.2 mL of TEOS were added successively into the mixture. The mixture was further stirred for 16 h at room temperature before collecting the solid by centrifuging and washing with ethanol twice.

4.2.3. Synthesis of NPs@MS yolk-shell

In a typical synthesis, 10−50 mg of the above prepared NPs@SiO_2 core-shell was dispersed in 10 mL of H_2O with ultrasonication for 0.5 h. During this period, 50−150 mg of $MnSO_4$ and 50−200 mg of sodium malate were dissolved in another 10 mL of H_2O. Afterwards, the solid suspension was poured into the $MnSO_4$ and sodium malate solution under vigorous stirring for 10 min. The mixture was then transferred to a Teflon-lined autoclave and hydrothermal treated at 180℃ for 12 h. After the reaction, the yolk-shell products were collected *via* centrifugation, followed by washing with ethanol twice and drying at 60℃ overnight.

4.2.4. Synthesis of MS@Pt catalysts

Briefly, SiO_2 beads (60 mg) were dispersed in 10 mL of H_2O with ultrasonication for 0.5 h. During this period, 136.6 mg of $MnSO_4$, 180 mg of sodium malate and 0.6 mL of K_2PtCl_4 (75 mM) were dissolved in another 10 mL of H_2O, into which the suspension of SiO_2 beads was poured under vigorous stirring for 10 min. The mixture was then transferred to a Teflon-lined stainless steel autoclave and hydrothermally treated at 180℃ for 12 h. The brown product was harvested *via* centrifugation, followed by washing with ethanol twice and drying at 60℃ overnight. Rare-earth-metal doped MS@Pt catalysts were also prepared in a similar way, except that 136.6 mg of $MnSO_4$ were mixed together with 0.04 mmol of rare-earth metal salts such as $Y(NO_3)_3$, $La(NO_3)_3$, $Ce(NO_3)_3$, $Nd(NO_3)_3$, and $Sm(NO_3)_3$.

4.2.5. CO_2 hydrogenation evaluation

The CO_2 hydrogenation was carried out in a continuous flow fixed bed reactor made of stainless-steel by using 0.20 g of the catalyst. A feed mixture (H_2/CO_2 = 3) was introduced with the space velocity of 9600 mL $g_{catalyst}^{-1}h^{-1}$. The temperature was measured with a thermocouple located at the centre of the catalyst bed. Concentrations of reactants and products were measured online by a gas chromatographic system.

4.2.6. Catalytic reduction of 4-nitrophenol

The accessibility of the core materials in MS shell during the catalytic reaction was examined through the reduction of 4-nitrophenol with $NaBH_4$ in water. Typically, 2.5 mL of 10 mM 4-nitrophenol was mixed with 0.12 mL of catalyst aqueous suspension (1 mg mL^{-1}). Then 0.5 mL of 100 mM $NaBH_4$ was added into the system with stirring for 10 s. The mixture was immediately transferred into a quartz cell for UV-Vis measurement. UV-Vis absorption spectra were recorded in the range of 200 to 600 nm to monitor the changes of the reaction mixture.

4.2.7. Characterization techniques

Morphologies of samples were characterized by field-emission scanning electron microscopy (FESEM, JSM-5600LV), transmission electron microscopy (TEM, JEM-2010) and high-resolution TEM (HRTEM, JEM-

2100F). The crystallographic information was analyzed by X-ray diffraction (XRD, Bruker D8 Advance) equipped with a Cu K_α radiation source. The elemental mapping was done by energy-dispersive X-ray spectroscopy (EDX, Oxford Instruments, Model 7426). The surface composition and oxidation state of the samples were further analyzed by X-ray photoelectron spectroscopy (XPS, AXIS-HSi, Kratos Analytical). Specific surface areas, pore volume, and pore size of some representative samples were determined using N_2 physisorption isotherms at 77 K (Quantachrome NOVA-3000 system).

4.3. Results and Discussion

4.3.1. Synthesis of Au@MS

We started with introducing Au NPs into the framework of MS, in view of their excellent catalytic activity.[16] Shown in Figure 4.1a, the Au@SiO_2 core-shell structure was first synthesized. This solid precursor has a highly uniform size (*ca* 226 nm) and contains a single Au NP core (*ca* 15 nm) at the centre. Then 80 mg of the solid precursor was mixed with 20 mL of aqueous solution of $MnSO_4$ (6.8 $g{\cdot}L^{-1}$) and sodium maleate (9 $g{\cdot}L^{-1}$). The mixture was stirred vigorously for 10 min before a hydrothermal treatment (180 ^oC for 12 h). Interestingly, the transformations of structure (core-shell $\rightarrow$ yolk-shell) and composition (silica $\rightarrow$ MS) could be achieved in this one-pot hydrothermal process. The as-prepared yolk-shell structure with a movable Au NP core

inside the MS shell (denoted as Au@MS) are shown in Figure 4.1b,c. The TEM images reveal that the thickness of MS shell is *ca* 22 nm, which was composed of numerous smaller hollow bubbles (*ca* 7 nm, Figure 4.2), and the overall size of MS hollow spheres is ca 215 nm. The size of the Au@MS yolk-shell is very uniform (Figure 4.1d). Occasionally, mechanically fractured spheres (< 3%) were also observed under large-area FESEM screening (Figure 4.3), proving the existence of hollow interior. The bubble-like shell was produced due to CO_2 bubbles (*via* maleate anions decomposition under hydrothermal condition), which serve as soft templates for the deposition of manganese silicate (through the ion-exchange of Mn^{2+} with H_4SiO_4).[15] Our XRD result (Figure 4.1e) indicates the presence of both metallic gold and blythite phase ($Mn_3^{+2}Mn_2^{+3}[SiO_4]_3$, JCPDS no. 89-5709) in the Au@MS yolk-sell catalyst, while the Stöber silica is in its amorphous state. The crystal structure of MS is similar to other garnet-group minerals with a general chemical formula of $A_3B_2(XO_4)_3$ (Figure 4.1f).[17, 18] Furthermore, our EDX mapping study also confirms the formation of the Au@MS yolk-shell structure (Figure 4.1g).

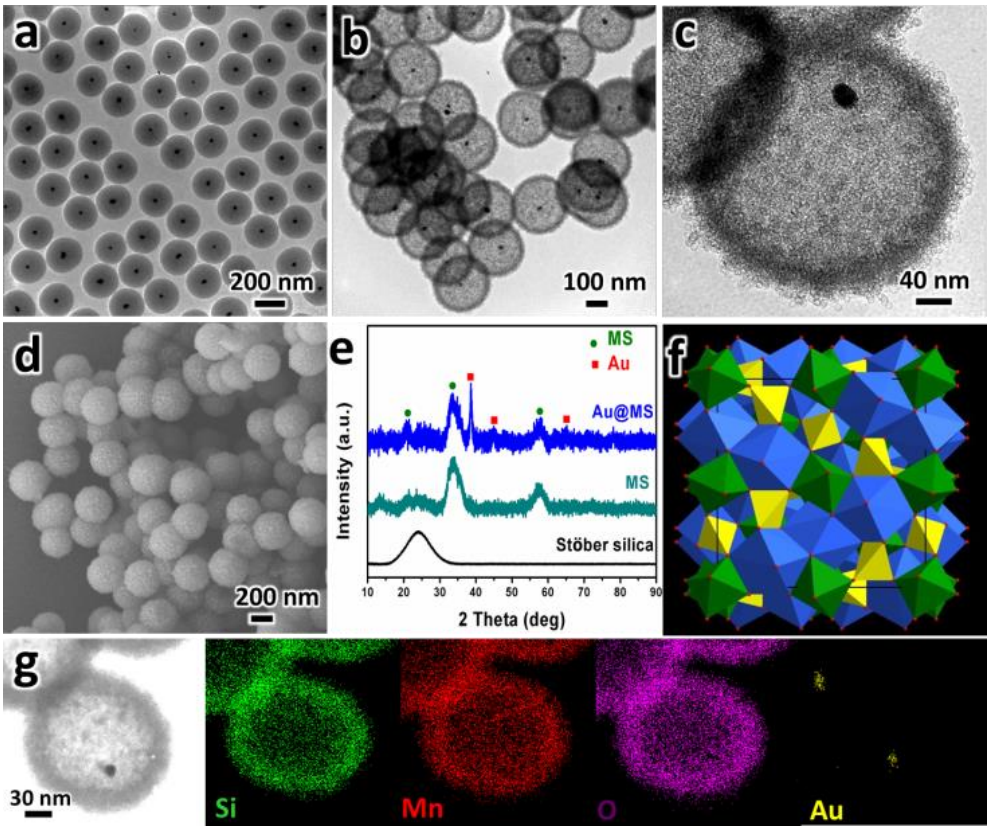

Figure 4.1 TEM images of (a) Au@SiO_2 core-shell, (b-c) Au@MS yolk-shell, (d) FESEM image of Au@MS yolk-shell, (e) XRD patterns of the "bubble catalysts", (f) the ideal crystallographic structure of MS: yellow, green, and blue colours represent 4-coordinated Si^{4+} (tetrahedrons), 6-coordinated Mn^{3+} (octahedrons) and 8-coordinated Mn^{2+} (irregular polyhedron), respectively, and (g) elemental mappings of the Au@MS yolk-shell.

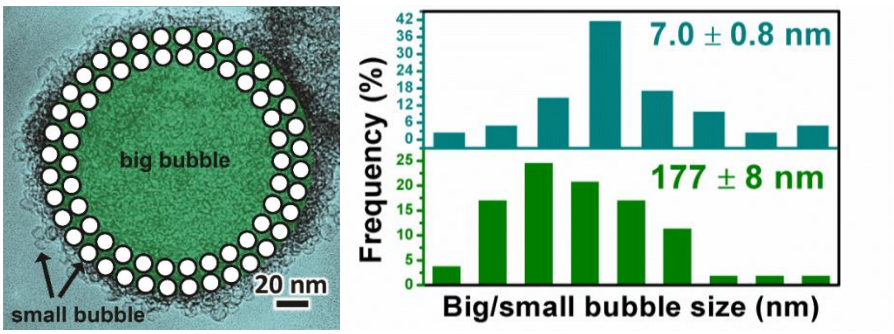

Figure 4.2 A typical TEM image of MS together with the size distribution histograms of the big (bottom) and small (top) bubbles.

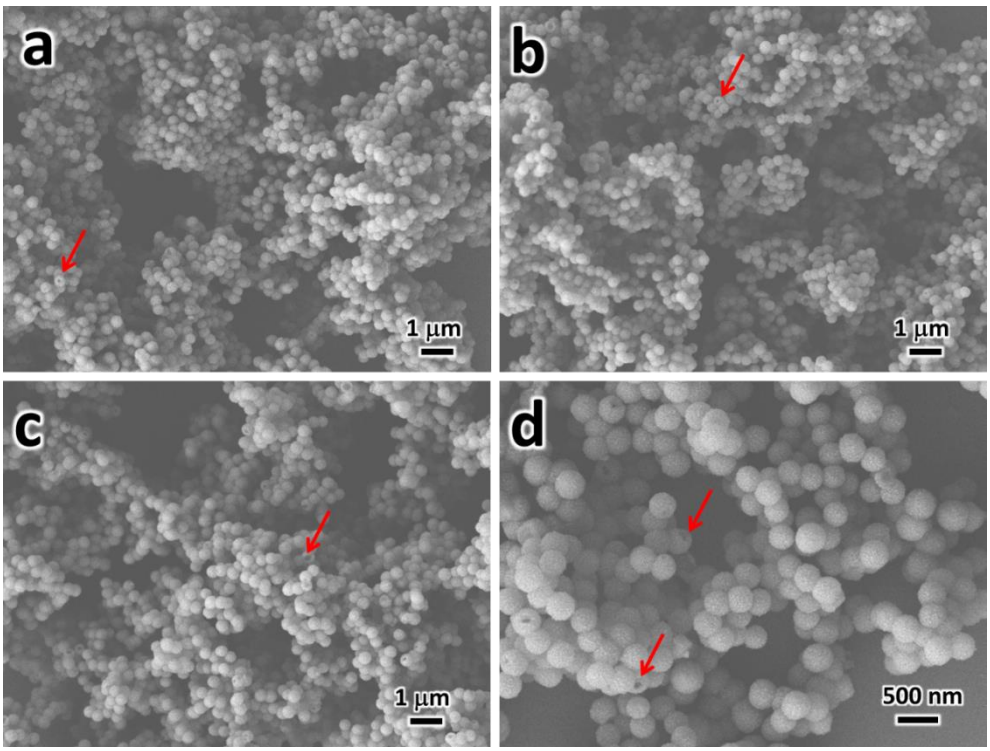

Figure 4.3 FESEM images of the Au@MS yolk-shell structure. Red arrows indicate few mechanically fractured particles (< 3%), proving their hollow interiors.

As expected, N_2 physisorption measurements (Figure 4.4a) reveal the highly porous nature of Au@MS spheres. The "bubble catalysts" followed Langmuir type IV isotherm with a hysteresis loop at high P/P_0 (which is characteristic of mesopores). The Brunauer-Emmett-Teller (BET) surface areas are 341 $m^2 \cdot g^{-1}$ for the pristine MS and 217 $m^2 \cdot g^{-1}$ for the Au@MS, both of which are much higher than that of 15 $m^2 \cdot g^{-1}$ for nonporous Stöber silica beads. Intriguingly, the Au@MS gives pore volume of 0.20 $cm^3 \cdot g^{-1}$ and mesopores of 3.3 nm (Figure 4.4b), similar to those obtained by CTAB micelles as a soft-template.[19] Using the reduction of 4-nitrophenol as a testing example,[20] we confirmed that the mesoporous MS shell indeed allows a convenient access for the reactant (*viz.*, 4-nitrophenol with a molecular size of 0.66 nm × 0.43 nm [21]) to travel

into the central cavity where the Au NP catalyst is located. As shown in Figure 4.4c, the intensity of the characteristic absorption peak at 400 nm (assigned to 4-nitrophenol) quickly decreased upon the addition of catalysts. The reduction reaction was completely finished in 12 min, along with the colour change from bright yellow to colourless. This reaction can be considered as a pseudo-first-order reaction, and the rate constant was determined to be 0.18 min^{-1}, much higher than that using pristine MS as a catalyst (0.03 min^{-1}).

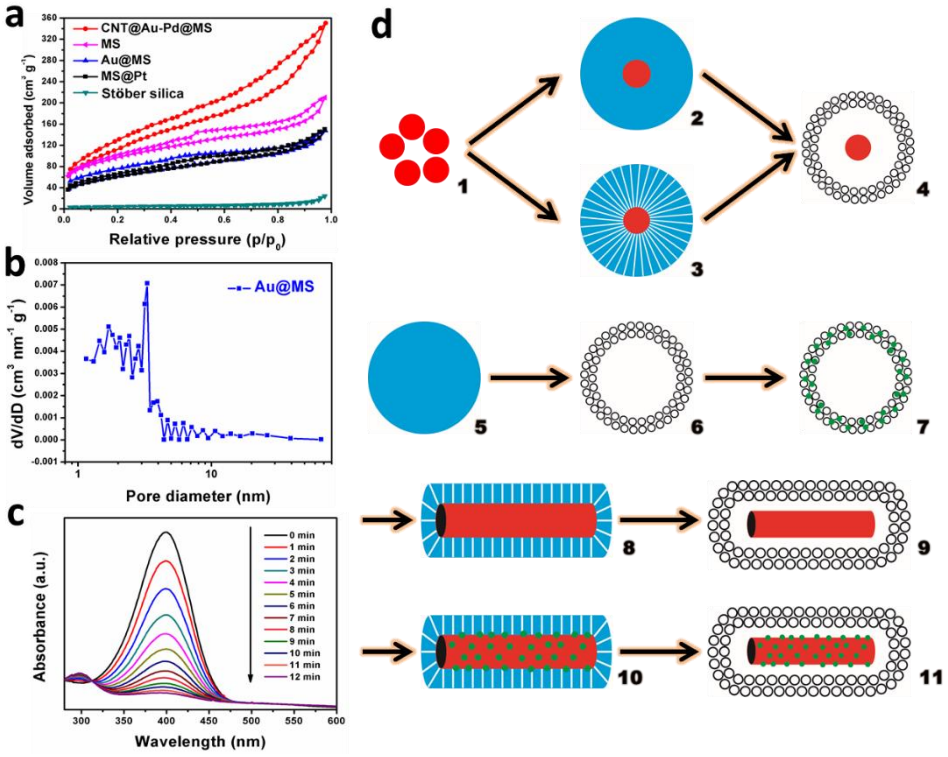

Figure 4.4 (a) N_2 adsorption/desorption isotherms of the "bubble catalysts", (b) pore size distribution of the Au@MS yolk-shell spheres, (c) time-dependent UV-vis spectra of the reaction mixture of reduction of 4-nitrophenol by $NaBH_4$ using Au@MS yolk-shell as a catalyst, and (d) preparation procedures of "bubble catalysts": (1) pristine catalytic NPs, (2) NPs@SiO_2 core-shell, (3) NPs@*m*SiO_2 core-shell, (4) NPs@MS yolk-shell, (5) silica bead, (6) hollow MS sphere, (7) MS@NPs, (8) CNT@*m*SiO_2 core-shell, (9) CNT@MS yolk-shell, (10) CNT@NPs@*m*SiO_2 core-shell, and (11) CNT@NPs@MS yolk-shell.

4.3.2. Synthesis of other NPs@MS

This thesis also demonstrated a broad scope of applications of this approach by introducing other catalytic metal species to diversify the functions of the MS based nanocatalysts. As illustrated in Figure 4.4d, we have developed various synthetic strategies to produce eleven more representative "bubble catalysts"; they are spherical Ag@MS, Au-Pd@MS, MoO_2@MS, Fe_3O_4@MS, MS@Pt, MS@Au, MS@Ni, and MS@Co, and tubular CNT@MS, CNT@Au-Pd@MS and Au-Pd@MS. Generally speaking, the controlled fabrication can be divided into three steps, (i) synthesis of the discrete NPs with a desirable size and shape, (ii) deposition of silica shell on the as-synthesized NP cores to generate core-shell structures (NPs@SiO_2 or NPs@*m*SiO_2, where SiO_2 = nonporous SiO_2 and *m*SiO_2 = mesoporous SiO_2), and (iii) conversion of NPs@SiO_2 or NPs@*m*SiO_2 core-shell to NPs@MS yolk-shell (*i.e.*, nanocatalysts). Likewise, using the Fe_3O_4@SiO_2 of Figure 4.5a as a precursor, yolk-shell structure of Fe_3O_4@MS was also successfully obtained (Figure 4.5b). The Fe_3O_4@MS exhibits strong magnetic property, as it can be collected easily with an external magnetic bar. Other yolk-shell structures with different compositions and shapes can be readily produced by replacing the core materials, such as Ag NPs, MoO_2 NPs, and flower-shaped Au-Pd alloy NPs. The synthetic conditions were also optimized in order to deposit uniform silica coating on the cores (Figure 4.5c,e,g). As evidenced in the yolk-shell structures of Ag@MS (Figure 4.5d), Au-Pd@MS (Figure 4.5f) and

MoO_2@MS (Figure 4.5h), the silica layer could be converted completely to MS shells, while the preinstalled cores were kept intact. Moreover, the XRD patterns of Figure 4.5i also elucidate the presence of the nano-particles within the MS shells. These design made yolk-shell structures, which could also be viewed as nanoreactors, endow the trapped core materials with excellent anti-aggregation properties. In addition to the applications in solution phase, high thermal stability of MS shells is very suitable for reactions at high temperatures. Such MS-supported catalysts are expected to be workable at harsh conditions,[22, 23] which will be explored later.

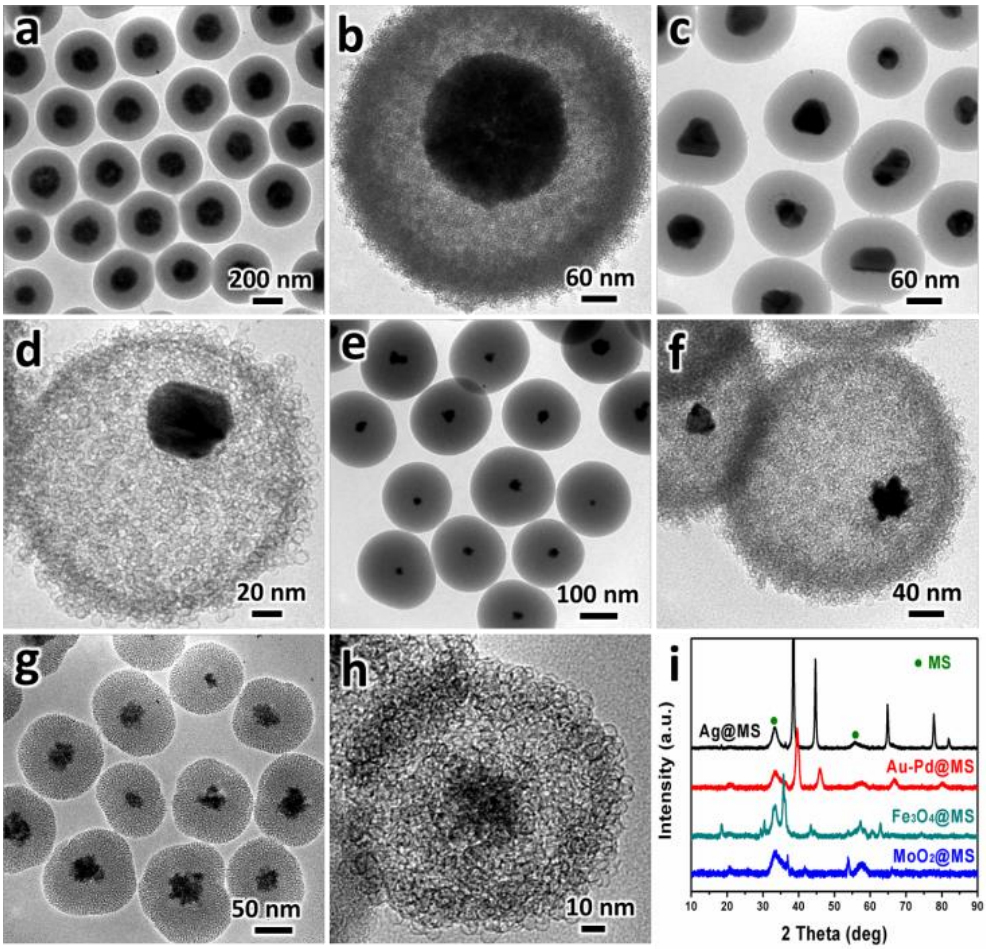

Figure 4.5 TEM images of (a) Fe_3O_4@SiO_2 core-shell, (b) Fe_3O_4@MS yolk-shell, (c) Ag@SiO_2 core-shell, (d) Ag@MS yolk-shell, (e) Au-Pd@SiO_2 core-

shell, (f) Au-Pd@MS yolk-shell, (g) MoO_2@*m*SiO_2 core-shell, (h) MoO_2@MS yolk-shell; and (i) XRD patterns of these studied structures.

CNTs are generally recognized as one of the best and most easily available one-dimensional nanomaterials. In Figure 4.6a, we also extended the spherical MS to one-dimensional structure by using CNT@*m*SiO_2 as a precursor for the same transformative synthesis. Figure 4.6b,c display the typical TEM images of the as-prepared CNT@MS. As expected, the product preserves the shape of the original CNT@*m*SiO_2 and the CNTs were encapsulated within the central cavity. Analogously, we also fabricated CNT@Au-Pd@MS catalysts employing CNT@Au-Pd@*m*SiO_2 as a precursor (Figure 4.6d). TEM images (Figure 4.6e,f) show that the Au-Pd alloy NPs (size: 1.4 to 3.3 nm) are located on the CNTs backbones inside the hollow cavity of the CNT@Au-Pd@MS. The XRD results of Figure 4.6i affirm the presences of Au-Pd alloy, CNTs, and manganese silicate in this product. The CNT@Au-Pd@MS has a surface area of 388 $m^2 \cdot g^{-1}$ and a pore volume of 0.59 $cm^3 \cdot g^{-1}$ (Figure 4.4a). In addition, the CNTs inside this structure could be removed thermally (*e.g.*, at 500^{o}C), and the thus obtained tubular Au-Pd@MS was also characterized by TEM method (Figure 4.6g,h).

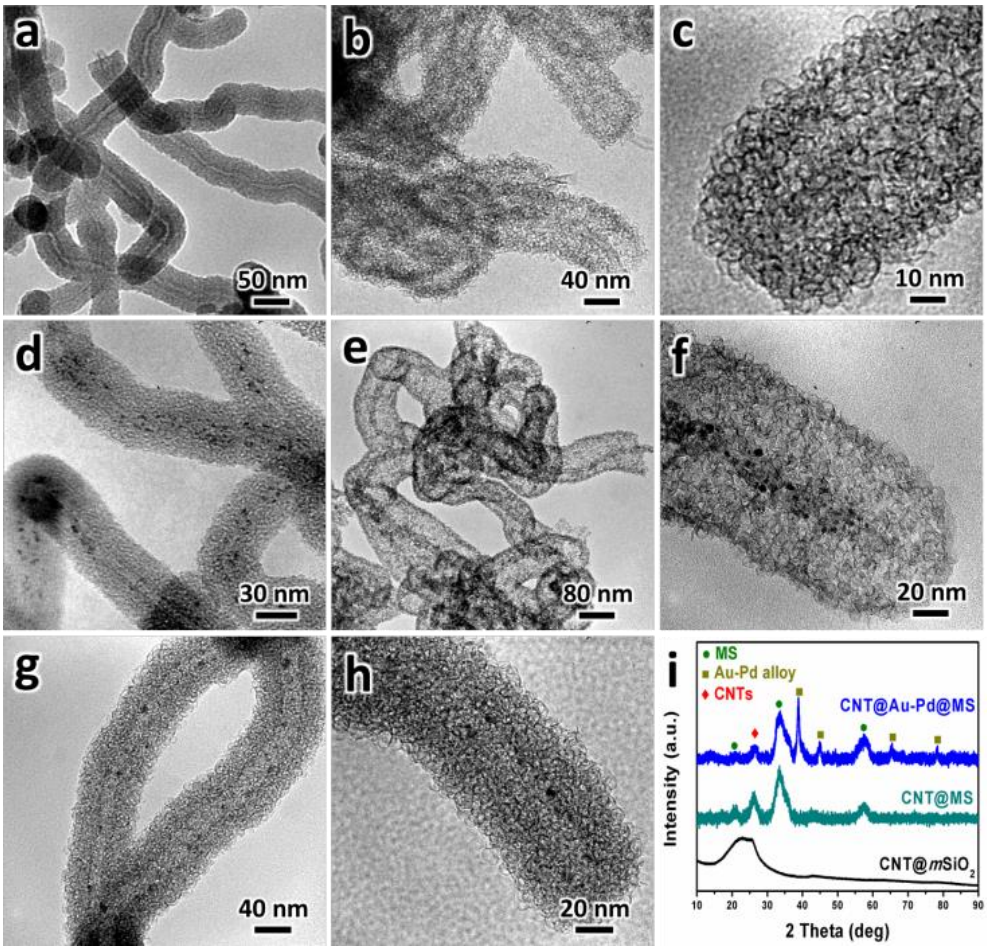

Figure 4.6 TEM images of (a) CNT@*m*SiO_2 core-shell, (b,c) CNT@MS yolk-shell, (d) CNT@Au-Pd@*m*SiO_2 core-shell, (e,f) CNT@Au-Pd@MS yolk-shell, and (g,h) tubular Au-Pd@MS; and (i) XRD patterns of these studied structures.

4.3.3. Synthesis of MS@NPs

The metal NPs not only can be encapsulated inside the MS, but also be dispersed on the external surface of MS (Figure 4.4d(5-7)). The MS@Pt catalyst was prepared under *in-situ* hydrothermal conditions with potassium tetrachloroplatinate. As revealed by TEM (Figure 4.7a,b) and STEM (Figure 4.7c) techniques, Pt NPs with a uniform size of 3.3 nm were highly dispersed on the surfaces of the MS and the bubble feature of MS was well maintained

after metal loading. High-resolution TEM image in Figure 4.7d shows that the lattice fringe of Pt NPs is approximately 2.3 Å, consistent with the d_{111} value of platinum. Furthermore, chemical states of the surface Mn and Pt were investigated by XPS method (Figure 4.7e), revealing that Pt was mainly in Pt^0 (~68%) and surface-oxidized Pt^{II} (~32%). In agreement with the findings from both TEM and XPS analyses, the XRD patterns in Figure 4.7f show that MS@Pt catalyst was composed of platinum (at a size of 3.7 nm; Scherrer method), blythite-type manganese silicate and others (*e.g.*, Mn_2SiO_4 and Mn_3O_4). Again, EDX elemental mappings of Figure 4.7g confirm its structural configuration, and N_2 physisorption study (Figure 4.4a) indicates MS@Pt has a specific surface area of 210 $m^2 \cdot g^{-1}$, a pore volume of 0.23 $cm^3 \cdot g^{-1}$, and an average mesopore size of 3.9 nm. Moreover, other types of NPs can also be immobilized on the external surface of MS, such as Ni, Co and Au NPs (see Figure 4.8 to Figure 4.10).

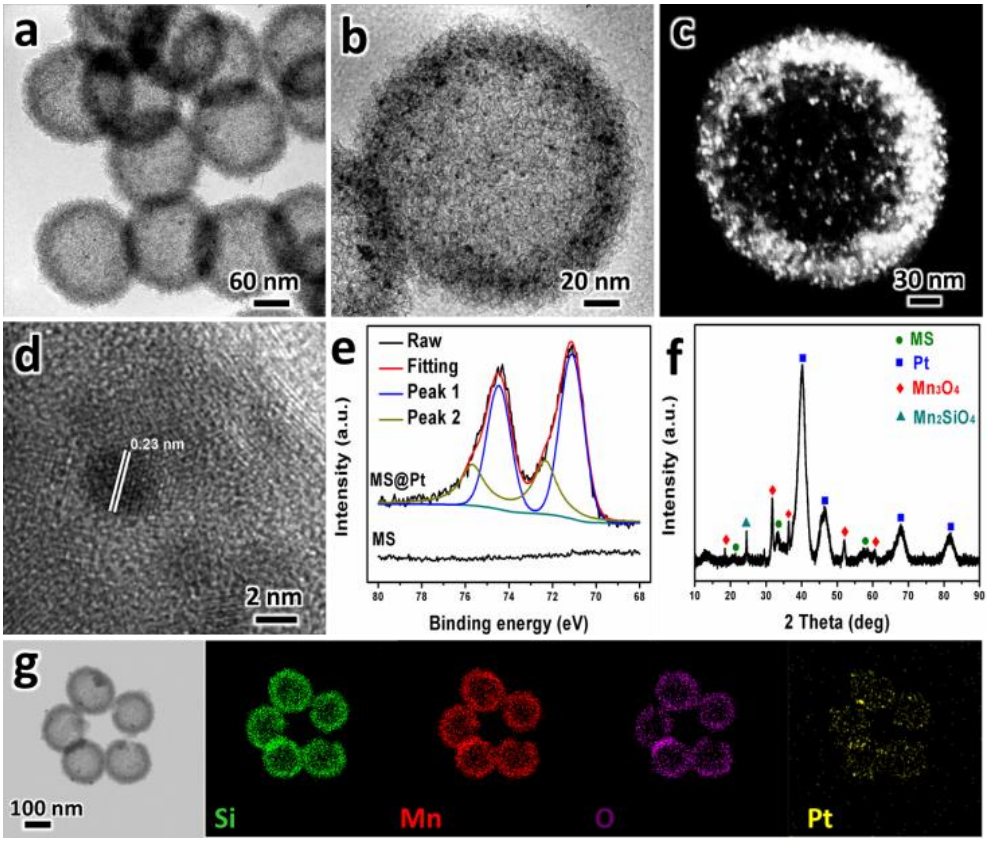

Figure 4.7 (a-d) TEM, STEM and HRTEM images of the MS@Pt catalyst, (e) XPS spectra of Pt 4*f* regions recorded on the MS@Pt catalyst (top) and pristine MS sample (bottom), (f) XRD patterns of the MS@Pt catalyst, and (g) elemental mappings of the MS@Pt catalyst.

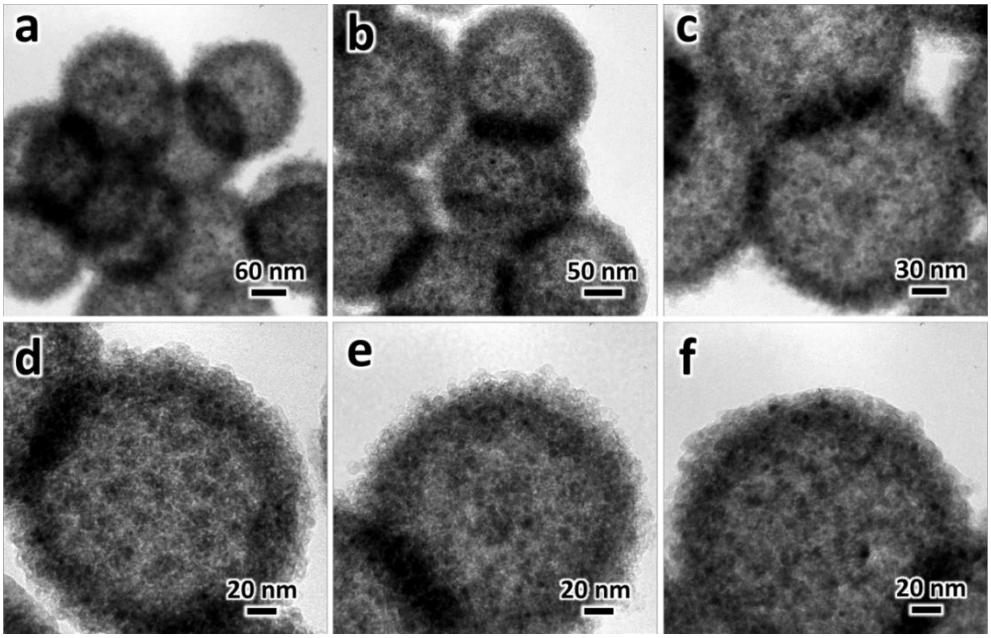

Figure 4.8 Typical TEM images of the MS@Co structure at different magnifications. Preparation method: 5 mg of pure MS was mixed with 3 mL of Buffer solution (pH 4, Merck), then 200 μL of cobalt acetate aqueous solution (50 mM) was added, the final mixture was heated at 60ºC for 1 h.

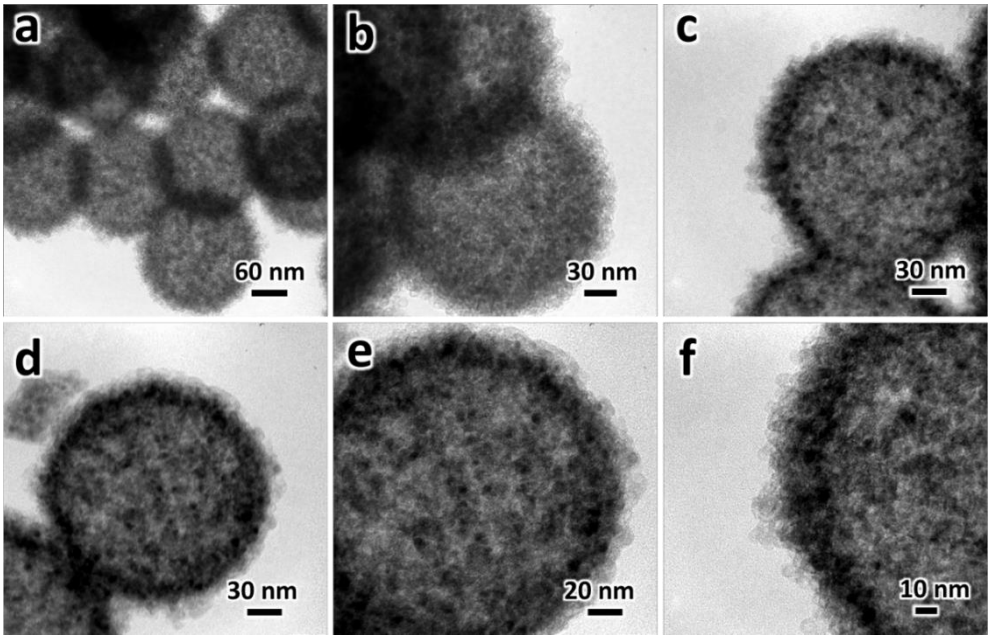

Figure 4.9 Typical TEM images of the MS@Ni structure at different magnifications. Preparation method: 5 mg of pure MS was mixed with 3 mL of Buffer solution (pH 4, Merck), then 200 μL of nickel acetate aqueous solution (50 mM) wad added, the final mixture was heated at 60ºC for 1 h.

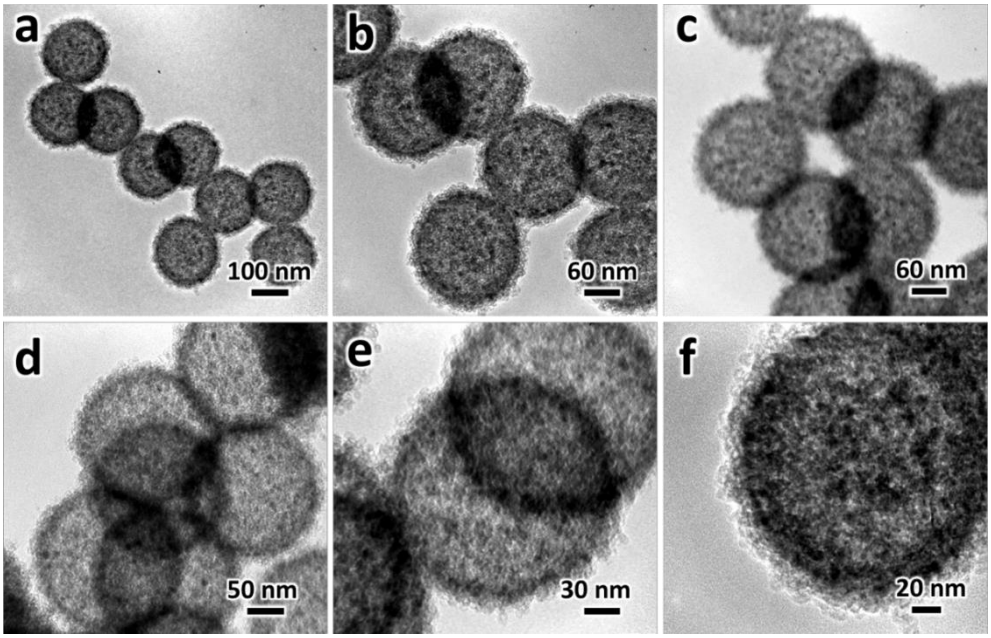

Figure 4.10 Typical TEM images of the MS@Au structure at different magnifications. Preparation method: 5 mg of pure MS was mixed with 4 mL of DI water, then 200 μL of $HAuCl_4$ aqueous solution (24.6 mM) was added, the final mixture was heated at 70°C for 1 h.

4.3.4. Application of MS based catalysts

CO_2 hydrogenation was used as a testing reaction to verify the effectiveness of these hybrid nanocatalysts,[24] namely the MS@Pt, Au@MS and CNT@Au-Pd@MS, at 548 to 673 K and 0.1, 1, 2 and 3 MPa. Firstly, we found that the MS@Pt catalyst was very selective towards the CO formation *via* reverse water gas shift reaction.[25] Some amounts of methanol and methane were found as by-products. Using the MS@Pt, in Figure 4.11a,b, the conversion increased considerably with temperature and pressure due to the endothermic reaction. It should be mentioned that the hydrogenation of CO_2 towards CO was favorable at a high temperature but at a low pressure (Figure 4.11b). Under the same pressure (0.1 MPa), for example, the CO_2 conversion was achieved at 30%

with selectivity to CO at 97% at 673 K, while the selectivity to methanol and methane was 11% and 8% respectively at 548 K. Under the optimal condition, a high turnover frequency (TOF) of 31 h^{-1} was achieved, which is significantly higher than some previous results. In addition, the apparent activation energy (E_a) of the process was determined. As shown in Arrhenius plots of Figure 4.11c, E_a values of the MS@Pt and CNT@Au-Pd@MS were 47 and 32 $kJ \cdot mol^{-1}$ respectively, which are much lower than other literature data.[26] By contrast, very low activity was observed for Au@MS catalyst with only 1.7% CO_2 conversion at 673K and 0.1 MPa, largely due to the big size of Au NPs (*ca* 15 nm; inactive surface sites) and the low metal loading (0.52 wt%). The operating stability of these catalysts is remarkable; Figure 4.11d illustrates the catalyst performance of the MS@Pt over a period of 24 h, showing that there was no significant decrease in both the activity and selectivity. Our TEM investigation on the three types of catalysts after reactions proves that there is no major change in particle size and morphology (see Figure 4.12).

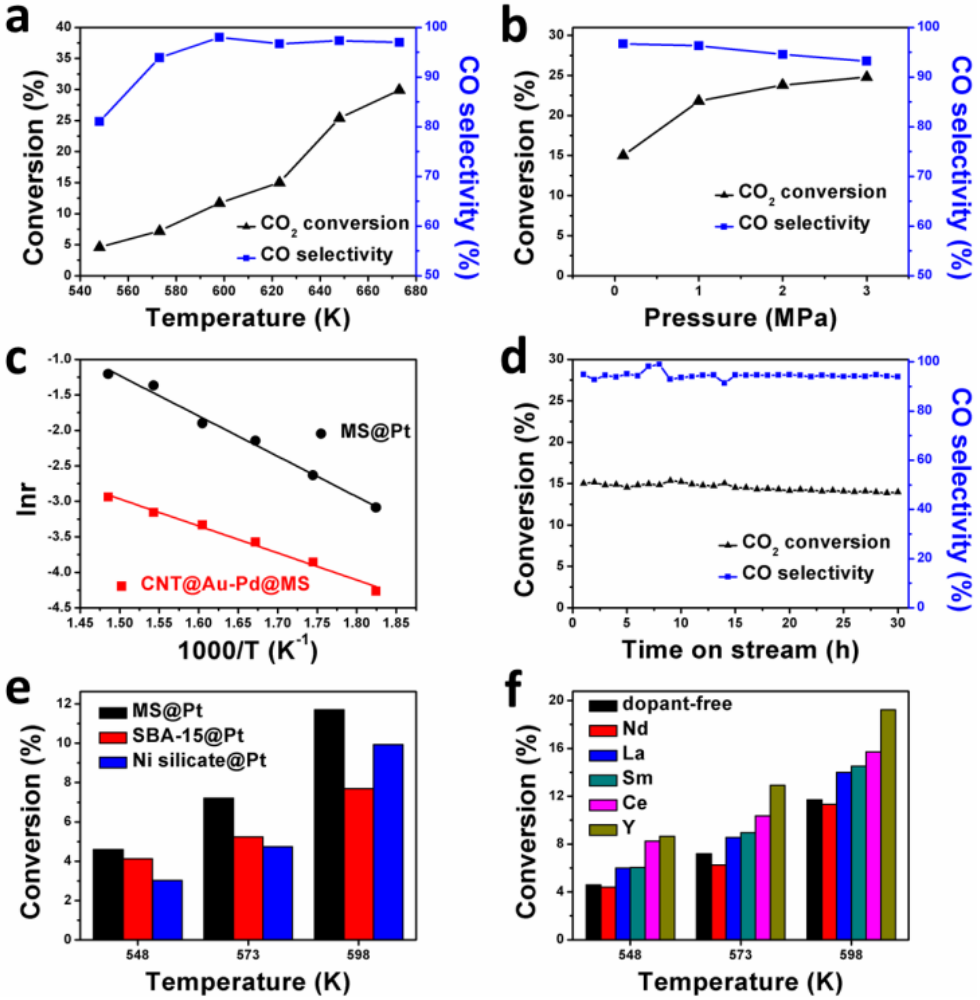

Figure 4.11 (a) Catalytic performance of the MS@Pt as a function of reaction temperature at a feed pressure of 0.1 MPa, (b) catalytic performance of the MS@Pt as a function of pressure at 623 K, (c) Arrhenius plots of ln(r) versus 1/T for CO_2 hydrogenation with different catalysts, (d) catalytic performance of the MS@Pt as a function of time-on-stream at 623 K and 0.1 MPa, (e) comparison of catalytic performance of Pt catalysts over different supports at 0.1 MPa (feed pressure), and (f) comparison of catalytic performance of the MS@Pt catalysts with different rare-earth-metal dopants at 0.1 MPa.

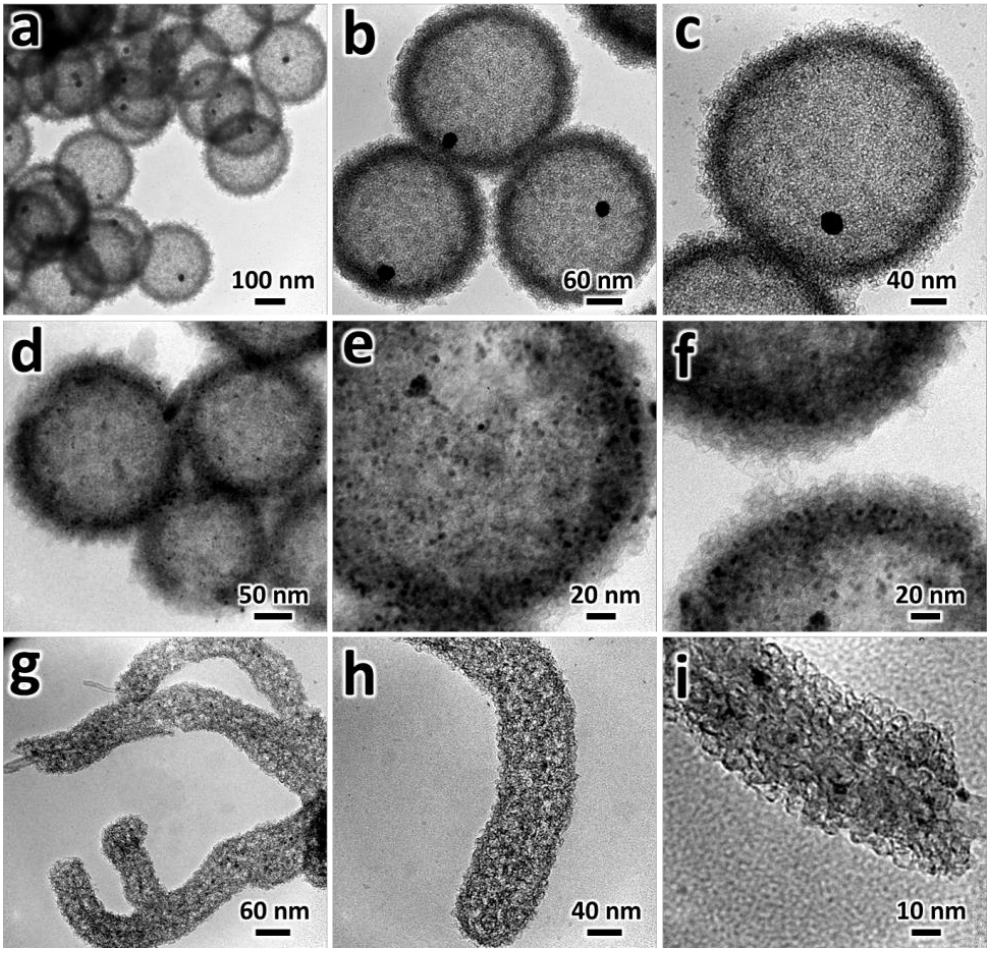

Figure 4.12 TEM images of catalysts after evaluation in the CO_2 hydrogenation: (a-c) Au@MS, (d-f) MS@Pt, and (g-i) CNT@Au-Pd@MS.

In order to demonstrate the synergetic effect between the Pt and MS, we had also studied the catalytic performance of Pt catalysts on other support materials (*e.g.*, SBA-15 and Ni-silicate). Encouragingly, our MS based Pt catalysts exhibited the highest conversion (Figure 4.11e). Concerning the product selectivity, no alcohol products (only CO and methane) were detected over the SBA-15@Pt and Ni-silicate@Pt catalysts. Based on these results, it is believed that the production of methanol is due to the presence of Mn element. Previous studies have shown that Mn can act as both electronic modifier and structural promoter for catalysts, which favors the hydrogenation of CO_2 into

value-added oxygenates or olefin over methane.[27, 28] Furthermore, it has been reported that the catalytic performance for CO_2 hydrogenation can be enhanced *via* adding rare-earth promoters to the catalyst.[29, 30] Herein, the MS shell of MS@Pt catalyst was doped with five different rare-earth elements (*viz.* Y, La, Ce, Nd and Sm) respectively.[15] The effect of the dopant is shown in Figure 4.11f. In general, catalysts with rare-earth doped MS shell could bring about appreciable enhancement in activity. For example, the reaction rate of Y-doped MS@Pt catalyst is about 2 times higher than that of the pristine MS@Pt at 548 K. The apparent activation energy of CO_2 hydrogenation over the doped catalysts decreases in the order of Nd (50 $kJ \cdot mol^{-1}$) > Sm (44 $kJ \cdot mol^{-1}$) > La (43 $kJ \cdot mol^{-1}$) > Ce (38 $kJ \cdot mol^{-1}$) > Y (35 $kJ \cdot mol^{-1}$). The enhanced activities could be ascribed to the change of surface basicity (or amount of oxygen vacancy) of the catalysts, which in turn promotes the adsorption and activation of CO_2.[31, 32]

4.4. Conclusions

In summary, pure or doped nanobubble-like manganese silicate can be used as a versatile platform for the design and synthesis of a range of spherical and tubular catalysts. In addition to the flexibility in structural architecture and compositional tailoring, the attained inter-bubble space can serve as a new form of mesoporosity for protecting and/or supporting catalytically active

phases. Because of their high chemical and thermal stability, the "bubble catalysts" can also work effectively in both solution and gas environments.

4.5. References

1. Y. Li and J. Shi, *Adv. Mater.*, 2014, **26**, 3176-3205.

2. J. Liu, S. Z. Qiao, S. Budi Hartono and G. Q. Lu, *Angew. Chem. Int. Ed.*, 2010, **122**, 5101-5105.

3. Y. Yang, J. Liu, X. Li, X. Liu and Q. Yang, *Chem. Mater.*, 2011, **23**, 3676-3684.

4. H. C. Zeng, *Accounts. Chem. Res.*, 2013, **46**, 226-235.

5. C. C. Yec and H. C. Zeng, *J. Mater. Chem. A*, 2014, **2**, 4843-4851.

6. C. T. Kresge, M. E. Leonowicz, W. J. Roth, J. C. Vartuli and J. S. Beck, *Nature*, 1992, **359**, 710-712.

7. N. Lang and A. Tuel, *Chem. Mater.*, 2004, **16**, 1961-1966.

8. J. Wu, Y.-J. Zhu, S.-W. Cao and F. Chen, *Adv. Mater.*, 2010, **22**, 749-753.

9. S. Fujihara, T. Maeda, H. Ohgi, E. Hosono, H. Imai and S.-H. Kim, *Langmuir.*, 2004, **20**, 6476-6481.

10. J. N. Kondo and K. Domen, *Chem. Mater.*, 2008, **20**, 835-847.

11. Z. Wei Seh, W. Li, J. J. Cha, G. Zheng, Y. Yang, M. T. McDowell, P.-C. Hsu and Y. Cui, *Nat. Commun.*, 2013, **4**, 1331.

12. Y. Meng, W. Song, H. Huang, Z. Ren, S.-Y. Chen and S. L. Suib, *J. Am. Chem. Soc.*, 2014, **136**, 11452-11464.

13. N. N. Tušar, D. Maučec, M. Rangus, I. Arčon, M. Mazaj, M. Cotman, A. Pintar and V. Kaučič, *Adv. Funct. Mater.*, 2012, **22**, 820-826.

14. F. Jiao and H. Frei, *Chem. Commun.*, 2010, **46**, 2920-2922.

15. C. C. Yec and H. C. Zeng, *ACS Nano*, 2014, **8**, 6407-6416.

16. M. Haruta, *Catal. Today*, 1997, **36**, 153-166.

17. T. Arlt, T. Armbruster, R. Miletich, P. Ulmer and T. Peters, *Phys. Chem. Miner.*, 1998, **26**, 100-106.

18. V. Thangadurai, S. Narayanan and D. Pinzaru, *Chem. Soc. Rev.*, 2014, **43**, 4714-4727.

19. D. P. Wang and H. C. Zeng, *Chem. Mater.*, 2011, **23**, 4886-4899.

20. Z. Li and H. C. Zeng, *J. Am. Chem. Soc.*, 2014, **136**, 5631-5639.

21. J. Huang, C. Yan and K. Huang, *J. Colloid Interf. Sci*, 2009, **332**, 60-64.

22. S. H. Joo, J. Y. Park, C.-K. Tsung, Y. Yamada, P. Yang and G. A. Somorjai, *Nat. Mater.*, 2009, **8**, 126-131.

23. P. M. Arnal, M. Comotti and F. Schüth, *Angew. Chem. Int. Ed.*, 2006, **45**, 8224-8227.

24. W. Wang, S. Wang, X. Ma and J. Gong, *Chem. Soc. Rev.*, 2011, **40**, 3703-3727.

25. J. A. Rodriguez, J. Evans, L. Feria, A. B. Vidal, P. Liu, K. Nakamura and F. Illas, *J. Catal.*, 2013, **307**, 162-169.

26. M. C. Román-Martínez, D. Cazorla-Amorós, A. Linares-Solano and C. Salinas-Martínez de Lecea, *Appl. Catal. A*, 1996, **134**, 159-167.

27. R. W. Dorner, D. R. Hardy, F. W. Williams and H. D. Willauer, *Appl. Catal. A*, 2010, **373**, 112-121.

28. L. Xu, Q. Wang, D. Liang, X. Wang, L. Lin, W. Cui and Y. Xu, *Appl. Catal. A*, 1998, **173**, 19-25.

29. N. Perkas, G. Amirian, Z. Zhong, J. Teo, Y. Gofer and A. Gedanken, *Catal. Lett.*, 2009, **130**, 455-462.

30. Y. S. She, Q. Zheng, L. Li, Y. Y. Zhan, C. Q. Chen, Y. H. Zheng and X. Y. Lin, *Int. J. Hydrogen Energy*, 2009, **34**, 8929-8936.

31. P. Gao, F. Li, N. Zhao, F. Xiao, W. Wei, L. Zhong and Y. Sun, *Appl. Catal. A*, 2013, **468**, 442-452.

32. X. Guo, D. Mao, G. Lu, S. Wang and G. Wu, *J. Mol. Catal. A*, 2011, **345**, 60-68.

Chapter 5 Charge-Switchable Integrated Nanocatalysts for Substrate-Selective Degradation in Advanced Oxidation Processes

5.1. Introduction

In the past decade, enormous research work has been devoted to the design and fabrication of nanocatalysts with improved performance and efficiency for catalytic transformations, such as higher activity, selectivity and longevity.[1-3] At present, special research efforts are targeted on the preparation of catalysts with more advanced features.[4-11] In building such smart catalysts, in particular, functional materials whose physical or chemical properties can be changed in response to environmental stimulus have been investigated.[12] For example, it had been found the catalytic activity of Au@(polyphenol-Fe) toward reduction of 4-nitrophenol was depending on the pH of reaction solution, since the coordination state of catechol–Fe^{3+} in the shell varied as the solution pH modified.[4] Recently, it had been reported that pH-sensitive gold nanoparticles for aerobic oxidation of alcohols, which were active and stable at the solution pH of 9, and could be easily separated from the reaction mixture by lowering the solution pH (*e.g.*, pH = 1) which caused the gold nanoparticles to precipitate.[5] Likewise, pH-responsive Pt catalysts were also prepared for catalytic hydrogenation of aldehyde.[6] Besides controlling pH conditions, temperature-dependent catalytic behaviors had also been utilized in

nanocatalyst fabrications.[7-10] For instance, the catalysts prepared with this responsive feature could be completely turned off their activity at temperature above 35°C and the same activity could be resumed after cooling to a temperature below 32°C.[7]

In our research endeavors in this field, we recognized recently that Coulomb attraction or repulsion may serve as another means to add on new smart functions to integrated nanocatalysts.[1, 2] For example, polydopamine (PDA) seems to be a good candidate to pursue this research due to its robust adhesion onto a wide range of inorganic and organic materials, including noble metals, oxides, semiconductors, polymers, and ceramics.[13, 14] The PDA coated functional materials have also exhibited many advantageous features such as enhanced conductivity, biocompatibility, high stability, antioxidation, and strong light absorption; their applications have included catalyst modification, water purification membranes, enzyme immobilization, lithium ion batteries, biosensors, and biomedical application, *etc*.[15-21] Although the structure of PDA is still not elucidated unambiguously at present, it has been generally accepted that this macromolecule is an ampholyte polymer owning a great deal of amino groups and phenolic hydroxyl groups.[22] Consequently, PDA exhibits zwitterionicity: it has a net negative charge at high pH that excludes anions but passes cations, whereas it becomes positively charged at low pH that attracts anions instead of cations.[23, 24] In this regard, we believe that PDA can work as a charge-switchable interface or membrane to design integrated nanocatalysts

which can screen and catalyze substrates according to the molecular charges they bare (*i.e.*, substrate-selective catalysis). It should be mentioned that although it has been used to enhance the hydrophilicity of catalysts or the dispersivity of metal nanoparticles (*e.g.*, as support),[25-28] to the best of our knowledge, the molecular screening ability of PDA based on its pH-dependent charge-switchable behaviors has not yet been elucidated and applied in the field of heterogeneous catalysis.

In this chapter, we will report our recent research on a new type of charge-switchable integrated nanocatalysts. As shown in Figure 5.1, the designed catalysts encompass three basic components: (i) metal nanoparticles serving as catalytically active centers for chemical reactions, (ii) charge-switchable polymer shell (PDA layer) working as dual-function membrane (*i.e.*, screening reactant substrates and protecting catalysts underneath), and (iii) carrier material providing large reaction area/space (*i.e.*, hollow mesoporous support) for immobilizing metal catalysts. Such integrated nanocatalysts are expected to exhibit highly selective catalytic activities toward different charged substrates. Due to the presence of PDA shell, at a given pH environment, molecular substrates with opposite charges are attracted to the charged PDA owing to Coulomb electrical interactions. In contrast, those having the same type of charge as the PDA shell are rejected off due to charge repulsion. Through this way, we should be able to select substrates for chemical reactions, and most importantly the substrate-selectivity is adjustable. In the

following sections, we first investigated the fabrication of this kind of charge-switching integrated nanocatalysts, and conducted selective oxidation reactions with the made catalysts. In particular, we used various organic dyes as reaction substrates in view of their strong colors for easily monitoring the reactions, noting also that the degradation of organic dyes itself is an important issue in the context of water treatment and environmental protection.[29-31] The dyes studied herein include methyl orange (MO), methylene blue (MB), Congo red (CR), rhodamine 6G (R6G), thymol blue (TB), and their representative mixtures (see the photographs in Figure 5.1). The degradation of these dyes was carried out *via* advanced oxidation process (AOP) with hydrogen peroxide as an oxidant.[32, 33] In the AOP, the unsaturated groups (responsible for the dye colors) are cleaved, and dye molecules are broken down chemically into smaller molecules (*e.g.*, some intermediates). Ideally, the organic carbon maybe completely mineralized in the final products.[34] In the designed catalysts, the decomposition of hydrogen peroxide proceeds on the surface of the embedded platinum metal nanoparticles (Pt NPs in orange color, Figure 5.1), which involves the reactions below:[35, 36]

$$Pt + H_2O_2 \rightarrow Pt^+ + OH^- + \cdot OH \quad (1)$$

$$H_2O_2 + \cdot OH \rightarrow H_2O + HO_2\cdot \quad (2)$$

$$HO_2\cdot + OH^- \rightarrow O_2^- + H_2O \quad (3)$$

$$Pt^+ + O_2^- \rightarrow Pt + O_2 \quad (4)$$

Consequently, the radical groups (*e.g.*, ·OH, HO_2·) and superoxide ions (*e.g.*, O_2^-) shown in the above reactions are responsible for the degradation of dye molecules. This process is different from the homogeneous Fenton's peroxidation which is nonselective for different substrates (*i.e.*, dyes) and the hydroxyl radicals are produced by hydrogen peroxide with ferrous ions in an acidic environment.[37, 38] Because the dye molecules can be screened by the PDA layer, those captured by the PDA layer will be degraded preferably (*i.e.*, fast kinetics) on the Pt NPs. In comparison, those repulsed have much lesser chance to access the catalysts, and thus have a significantly lower chance for the degradation. Our following investigation results indeed show that catalyzed reactions for selected substrates (*i.e.*, the degradation of targeted organic dyes) can be achieved through simple control of pH environment. And importantly, such substrate-selective behaviors are adjustable according to pH values of the reaction solution.

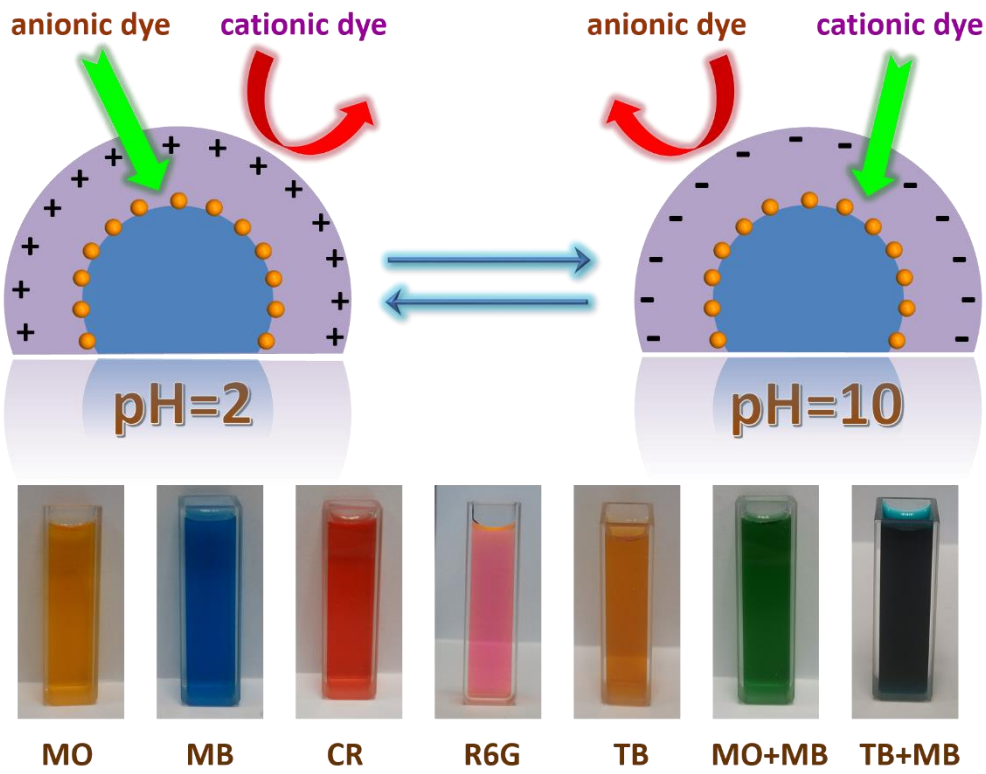

Figure 5.1 Schematic illustration of the selective catalytic degradation of dyes on charge-switchable integrated nanocatalysts (catalytic metal nanoparticles in orange, PDA shell in purple, and hollow mesoporous transition-metal silicates in blue). Color photographs show as-prepared aqueous solutions of various organic dyes studied in this work: methyl orange (MO), methylene blue (MB), Congo red (CR), rhodamine 6G (R6G), and thymol blue (TB). Note: the counter ions in the polydopamine (PDA) layer are ignored for better visual clarity (also refer to Figure 5.2).

5.2. Experimental Section

5.2.1. Materials

The following chemicals were used as received without further purification: tetraethylorthosilicate (TEOS, Aldrich, 99%), manganese (II) sulphate monohydrate (Alfa Aesar, 99%), iron (II) sulphate heptahydrate (Aldrich, 99%), cobalt (II) sulphate heptahydrate (Aldrich, 99%), nickel(II) sulphate hexahydrate (Aldrich, 99%), potassium tetrachloroplatinate (II) (Aldrich,

98%), sodium maleate (Fluka, 98%), sodium acetate (Fisher, 99.9%), ammonia solution (Merck, 32%), hydrogen peroxide (Merck, 30%), Tris(hydroxymethyl) aminomethane (Tris, Sigma, 99.8%), dopamine hydrochloride (Sigma), methylene blue (Merck), methyl orange (Merck), rhodamine 6G (Sigma), Congo red (Sigma), thymol blue (Fluka), buffer solution (Merck) and ethanol (Fisher, 99.99%). Deionized water was used for all experiments.

5.2.2. Synthesis of transition metal silicate

Spherical SiO_2 beads were synthesized according to our previous method.[39] In the synthesis of transition metal silicate (denoted as TMSi hereafter), a suspension (labelled A) was prepared with 50 mg of SiO_2 dispersed in 10 mL of H_2O by ultrasonication for 0.5 h. A solution (labelled B) was also prepared, which contains 136.6 mg of $MnSO_4$ and 180 mg of sodium maleate, or 225 mg of $FeSO_4$ and 500 mg of sodium acetate, or 114 mg of $CoSO_4$ and 180 mg of sodium maleate, or 107 mg of $NiSO_4$ and 180 mg of sodium maleate dissolving in 10 mL of H_2O. Afterward, the suspension A was mixed with the solution B under vigorous stirring for 10 min before hydrothermal treatments at 180°C for 12 h, after which the products were collected *via* centrifugation, followed by washing with ethanol twice and drying at 60°C overnight.

5.2.3. Synthesis of Pt/TMSi

During the preparation of TMSi, additional 0.35 mL of K_2PtCl_4 (129 mM, aqueous solution) was added in solution B. Then, the suspension A was mixed with the solution B under the same hydrothermal treatment mentioned above. The product (Pt/TMSi) was harvested *via* centrifugation, followed by washing thoroughly with ethanol twice and drying at 60°C overnight.

5.2.4. Synthesis of TMSi@PDA and Pt/TMSi@PDA

Typically, 20 mg of TMSi powder was dispersed in 30 mL of Tris-buffer (50 mM, pH 8.5 at 25°C) by ultrasonication for 30 min. Subsequently, a certain amount of dopamine dissolving in 1 mL of Tris-buffer was added to the mixture under stirring. The mixture was subjected to continuous magnetic stirring for 14 h at room temperature. Afterward, the product of TMSi@PDA was collected by centrifugation, washed three times with deionized water, and then dried at 60°C for 12 h. Pt/TMSi@PDA was prepared in a similar way as that of TMSi@PDA, except that the TMSi was replaced by Pt/TMSi (20 mg). Normally, the thickness of the PDA layer on TMSi or Pt/TMSi can be adjusted by varying the amount of added dopamine.

5.2.5. Synthesis of TMSi@NC and Pt/TMSi@NC

The dried sample of TMSi@PDA (or Pt/TMSi@PDA) was calcined in a quartz tube under an Ar flow (30 mL/min) with the following heating routine: 1°C/min to 500°C and at 500°C for 6 h, after which the sample (with black color) was cooled down naturally to room temperature.

5.2.6. Evaluation of catalytic activity toward dye degradation

Firstly, the catalyst (20 mg) was dispersed in 110 mL of various dye solutions (concentration: 50 mg/L). Buffer solution was used to control the pH of the solution. Then, the mixture was immersed in a water bath at 60°C for 15 min under magnetic stirring for full adsorption. Afterward, hydrogen peroxide (5 mL, 30%) was added into the solution and the mixture was stirred for 0.5 h. During this period, liquid samples (1 mL) were withdrawn from the solution and were diluted 5-folds before transferring into a quartz cuvette, and the absorption spectra of the reaction samples were acquired using UV-vis spectroscopy (UV-2450, Shimadzu). Fenton reagent ($FeSO_4$, 3 mmol; H_2O_2, 49 mmol) at pH of 2 was used as a control.

3.2.7. Characterization techniques

Morphologies of samples were characterized by transmission electron microscopy (TEM, JEM-2010). The crystallographic information was analyzed by X-ray diffraction (XRD, Bruker D8 Advance) equipped with a Cu K_α radiation source. The elemental mapping was done by energy-dispersive X-ray (EDX, Oxford Instruments; Model 7426). The surface composition and oxidation state of the samples were further analyzed by X-ray photoelectron spectroscopy (XPS, AXIS-HSi, Kratos Analytical). Specific surface areas, pore volume, and pore size of some representative samples were determined using N_2 physisorption isotherms at 77 K (Quantachrome NOVA-3000

system). Thermogravimetric analysis (TGA) study was carried out on a thermobalance (TGA-2050, TA Instruments) under flowing air atmosphere (flow rate: 50 mL/min) at a heating rate of 10°C/min. Electrokinetic potentials of the PDA coated spheres as aqueous suspensions were measured with ZetaPlus4 Brookhaven zeta-potential analyzer. The Pt loading in catalyst sample was determined by inductively coupled plasma optical emission spectrometry (ICP-OES, Optima 7300DV, Perkin Elmer).

5.3. Results and Discussion

5.3.1. Support materials for integrated nanocatalysts

As mentioned in Figure 5.1, firstly, the charge-switchable integrated nanocatalysts need a suitable support material. Ideally, the support material should provide a high surface area to support active catalytic component(s), avoid the metal sintering, and enable formation of interactions and maximize their synergetic effects.[1] In this regard, silicon-based materials (*e.g.*, silica and silicates) own many advantages as catalyst supports due to their rich porous structures, good mechanical and thermal stability, low toxicity, and low cost.[40-45] Presently, numerous forms of silicon-containing nanomaterials such as particles, wires, ribbons, tubes, platelets, films, polyhedrons and monoliths *etc*. have been exploited and fabricated. Some of them even possess both hollow cavity and mesoporous structures.[41, 44, 45] Therefore, our designed catalysts prefer to utilize metal silicates as supports.

The synthetic routes for integrated nanocatalysts are illustrated in Figure 5.2. Four different kinds of hollow mesoporous transition metal silicates (TMSi, structure (2); TM = Mn, Fe, Co, and Ni) are fabricated by using Stöber silica (structure (1)) as a templating precursor. The TMSi are then used to support catalyst platinum (Pt/TMSi, structure (3)). Both TMSi and Pt/TMSi can then be coated with a uniform PDA shell (TMSi@PDA and Pt/TMSi@PDA; structures (4) & (5)). Moreover, the PDA shell can be thermally converted to nitrogen-doped carbon (NC) *via* carbonization in inert atmosphere. Thus, TMSi@NC (structure (6)) and Pt/TMSi@NC (structure (7)) can be further obtained, respectively.

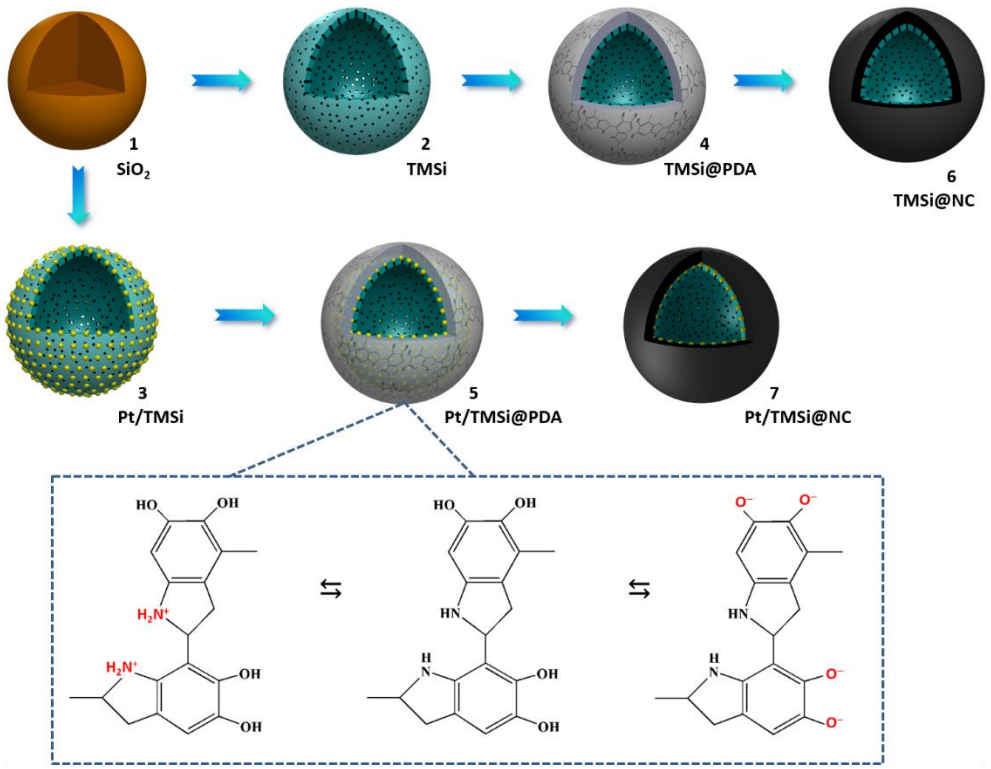

Figure 5.2 Schematic routes for PDA-coated nanocatalysts and their derivatives, where TMSi = transition metal silicates (TM = Mn, Fe, Co, and Ni), PDA = polydopamine, and NC = nitrogen-doped carbon. Catalytic metal nanoparticles (*e.g.,* Pt NPs) are presented as tiny yellow spheres. Three

molecular structures of polydopamine illustrate its charge-switchable property by altering the solution pH (pH = 2, 7, and 10 from left to right).[23]

5.3.2. Synthesis of hollow mesoporous TMSi

In recent years, self-templating strategy has also been developed to fabricate hollow mesoporous silica or silicate effectively.[44, 45] However, the methods are not universally applicable, and they require both surfactants and etching agents in the synthesis. In this work, we intend to develop a general synthetic method for hollow mesoporous transition metal silicates with tailorable composition and hollow morphology. Four types of transition metal silicates (*e.g.*, Mn, Fe, Co or Ni silicates) were prepared from a hydrothermal method using Stöber silica without any additional surfactants. The hydrothermal treatments were carried out at 180°C by mixing a Stöber silica aqueous suspension (2.5 g/L) with an alkali source (*e.g.*, sodium maleate or sodium acetate) in the presence of transition metal sulfates (*e.g.*, $MnSO_4$, $FeSO_4$, $CoSO_4$, and $NiSO_4$). This synthetic approach is based on gradual dissolution of silica followed by regrowth of transition metal silicate species.[44, 46] The following reaction steps might be involved under the hydrothermal conditions: (i) a small portion of the SiO_2 phase on surface is hydrolyzed to form H_4SiO_4, (ii) etching of solid SiO_2 is accelerated in the alkaline solution by sodium maleate or sodium acetate, (iii) transition metal species (*e.g.*, carboxylate) are adsorbed on the surface of SiO_2 sphere, (iv) transition metal silicates are formed through ion exchange of transition metal ions with H_4SiO_4, and (v)

transition metal silicates with specific shapes as primary building units are assembled into an integrated shell as more metal silicates are formed.

TEM images in Figures 5.3 to Figure 5.6 show the typical morphologies of Mn silicate, Fe silicate, Co silicate, and Ni silicate, respectively. As shown, all the transition metal silicates are monodisperse with a spherical hollow structure. The average particle sizes for Mn silicate, Fe silicate, Co silicate, and Ni silicate, are 217, 208, 231 and 212 nm, respectively. Interestingly, the hollow spheres of Mn silicate were actually composed of numerous tiny hollow spheres with diameters only between 7 and 9 nm; however, the hollow spheres of Fe, Co and Ni silicates are built from interlaced thin nanosheets. The different hierarchical structures of transition metal silicates are probably caused by the different interactions between silica oxoanions and transition metal cations. Note that metal silicates can be synthesized into a variety of shapes, such as nanotubes, nanobubbles, nanoplates, nanobelts, nanowires, nanoflowers, and so on.[47, 48] The EDX elemental mapping (Figure 5.7) confirms the successful preparation of these hollow transition metal silicates. Moreover, the incorporation of transition metals in the silicate framework can also be verified visually from the photographs of TMSi powder samples (Figure 5.7), as their colors are distinctively departed from the original white Stöber silica. Different from the amorphous Stöber silica, the inclusion of transition metal ions with silicon oxoanions leads to the crystallized TMSi, as confirmed from the XRD characterization results shown in Figure 5.8a. This is

also different from the transition metal doped silica where heteroatoms have very little influence on the silica structure.[49] The transition metal silicates mainly exhibit four characteristic peaks at 19.8º, 34.5º, 60.2º, and 71.8º, but the intensities of these peaks are relatively weak suggesting a minor crystallinity. The crystallization of TMSi samples is consistent to others prepared under hydrothermal conditions.[47]

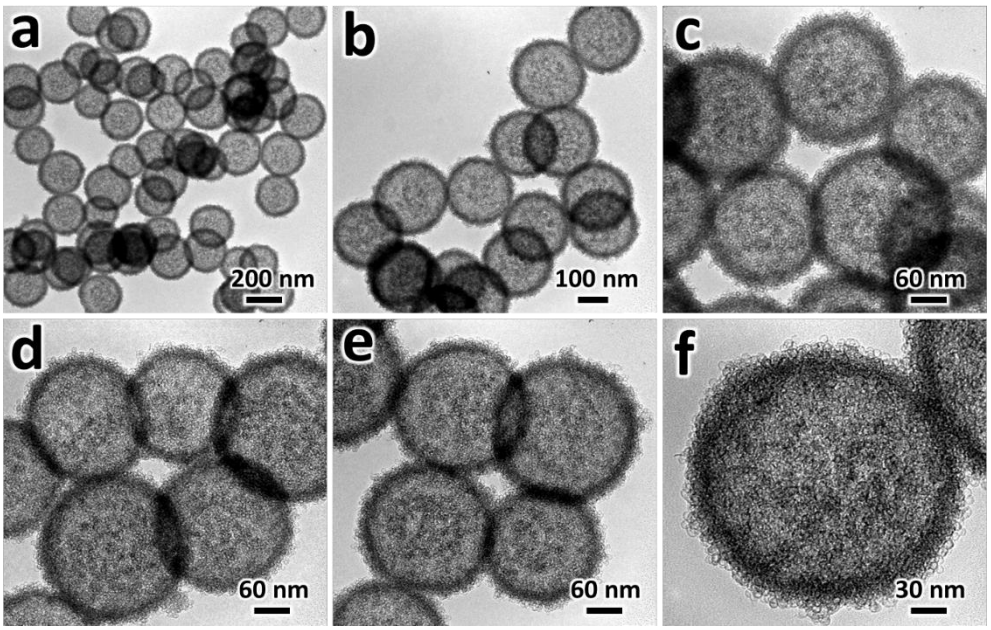

Figure 5.3 TEM images (at different magnifications) of Mn silicate.

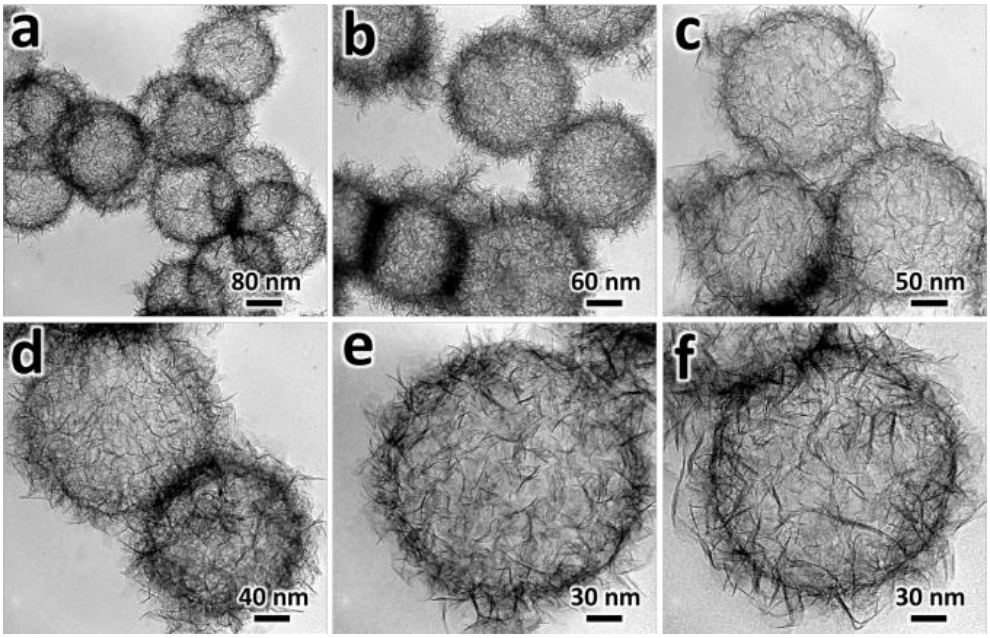

Figure 5.4 TEM images (at different magnifications) of Fe silicate.

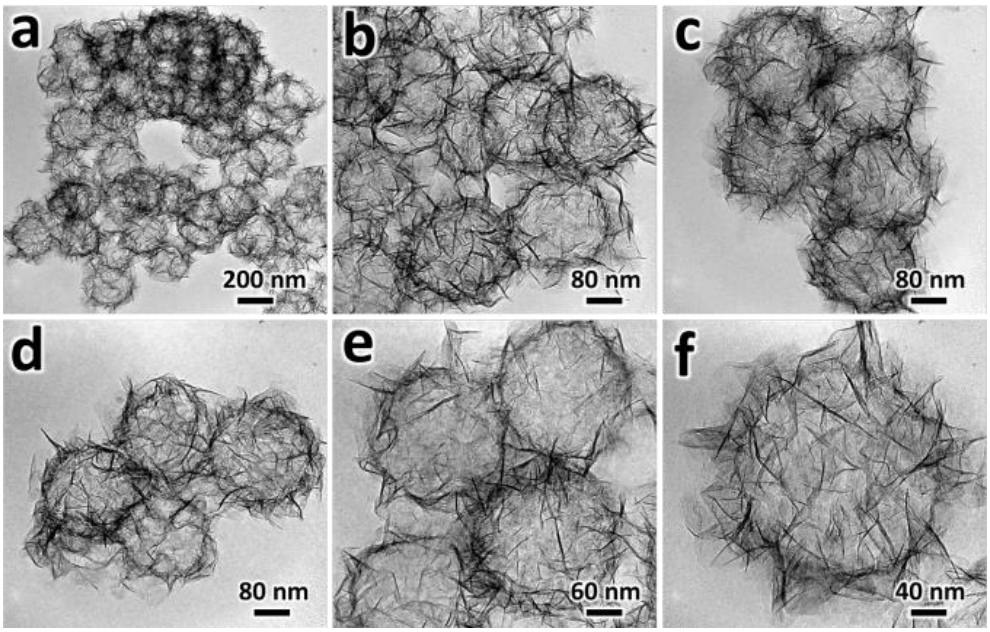

Figure 5.5 TEM images (at different magnifications) of Co silicate.

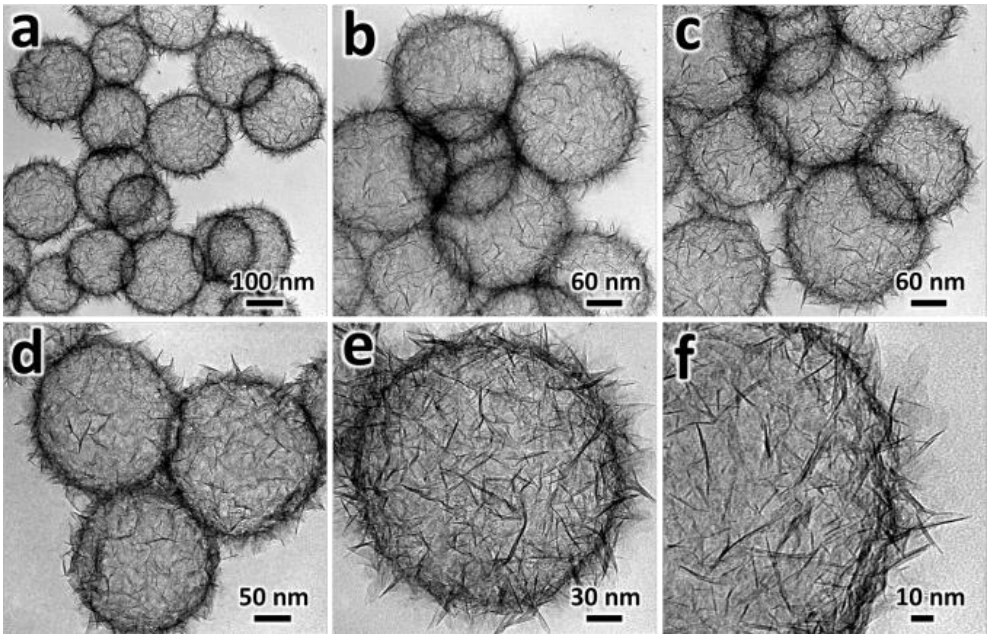

Figure 5.6 TEM images (at different magnifications) of Ni silicate.

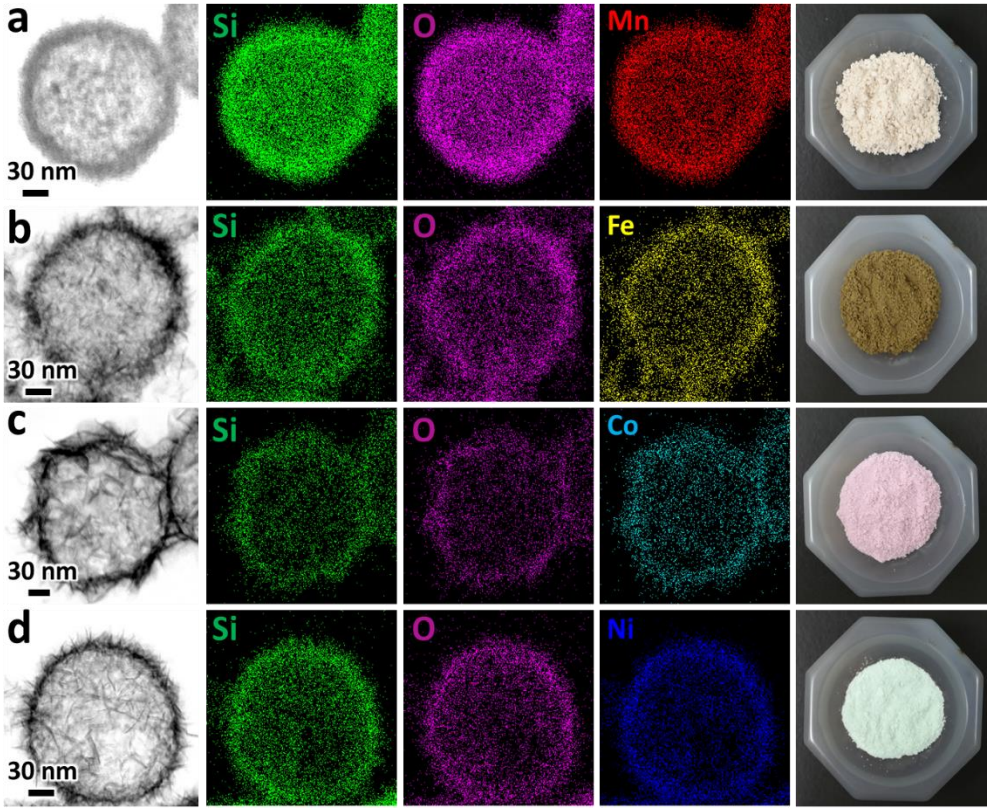

Figure 5.7 EDX elemental maps and color photographs of (a) Mn silicate, (b) Fe silicate, (c) Co silicate, and (d) Ni silicate.

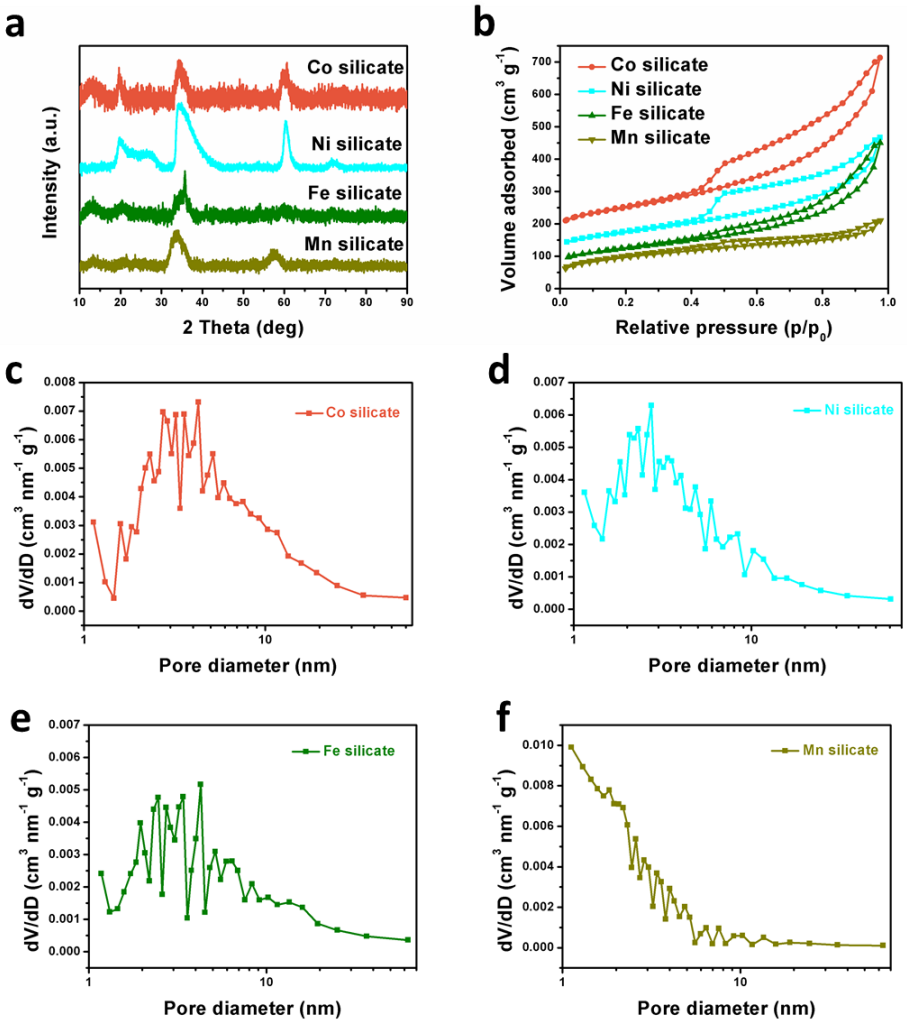

Figure 5.8 (a) XRD patterns of the transition metal silicates, (b) N_2 adsorption-desorption isotherms of the transition metal silicates, and (c-f) the corresponding pore size distribution curves analyzed by the Barrett-Joyner-Halenda (BJH) method (from the adsorption branch of the isotherms).

To investigate their specific surface areas and mesoporosity, N_2 adsorption/desorption isotherms of these silicate samples were measured at 77 K, and the experimental results are presented in Figure 5.8b, along with their corresponding Barrett–Joyner–Halenda (BJH) pore-size distribution in Figure 5.8c-f. As shown, all the samples follow Langmuir type IV isotherms with a distinct hysteresis loop at high P/P_0 (P/P_0 = 0.45–1.0), revealing mesoporous

characteristics. The BET specific surface areas of these samples increase in the order Fe silicate (267 m^2/g) < Ni silicate (338 m^2/g) < Mn silicate (341 m^2/g) < Co silicate (398 m^2/g), which are much higher than that of Stöber silica template (below 20 m^2/g).[39] The total pore volumes increase in the order Mn silicate (0.33 mL/g) < Ni silicate (0.62 mL/g) < Fe silicate (0.64 mL/g) < Co silicate (0.94 mL/g). In addition, we found that the tensile strength effect indeed exists in N_2 isotherms of TMSi samples.[50-52] As shown, the desorption branches of the isotherms show a forced closure at p/p_0 ranged 0.44–0.50 (due to a sudden drop in the volume adsorbed along the desorption branch). Therefore, the desorption branches of the isotherms are not able to determine the accurate pore size. For this reason, we calculated the pore size distribution based on the adsorption branch of the isotherms. The BJH pore-size-distribution curves reveal that all the samples exhibit a wide range of mesopores (from 2 nm to 10 nm), which are resulted from inter-particle-spaces of primary units such as nanosheets or tiny hollow spheres. The high specific surface area, large pore volume, and varying mesopores make these transition metal silicates excellent supports for the anchorage of metal nanoparticles in building integrated nanocatalysts.[53, 54]

5.3.3. PDA shell functionalization for TMSi

The self-polymerization of the dopamine provides a powerful means for coating various substrates with a uniform layer of PDA.[13] Herein,

encapsulation of the above obtained TMSi with PDA was realized by spontaneous polymerization of dopamine in Tris-buffer (pH 8.5) on the surfaces of hollow TMSi cores (0.67 g/L); the product composites are named as TMSi@PDA (structure (4), Figure 5.2). TEM and high-angle annular dark-field scanning TEM (HAADF-STEM) images in Figure 5.9 confirm the successful introduction of a uniform, smooth PDA shell onto the Mn silicate, and the resultant MnSi@PDA shows a well-defined core-shell configuration. The thickness of the PDA shell can be controlled through varying the initial concentration of dopamine in the preparative solution, and it is proportional to the dopamine concentration. Taking Mn silicate as an example, the thickness of PDA shell in the products was 19, 28, 36 and 57 nm, derived from 30 mL of Tris-buffer of 20 mg of Mn silicate in the presence of 10, 20, 40 and 60 mg of dopamine, respectively. Moreover, the EDX elemental maps and line scan profiles in Figure 5.10 further confirm the composition of the shell is PDA and the cores are the hollow structured Mn silicates. In addition to wrapping Mn silicate, this encapsulation method is also applicable for other transition metal silicates. As displayed in Figure 5.11a–f, well-defined core-shell structures were also obtained for FeSi@PDA, CoSi@PDA, and NiSi@PDA. Although TMSi (TM = Fe, Co, and Ni) hollow spheres have rather rough surfaces, *i.e.*, many thin plates are criss-crossly distributed on their surfaces, the formed PDA layer can still bind intimately to them.

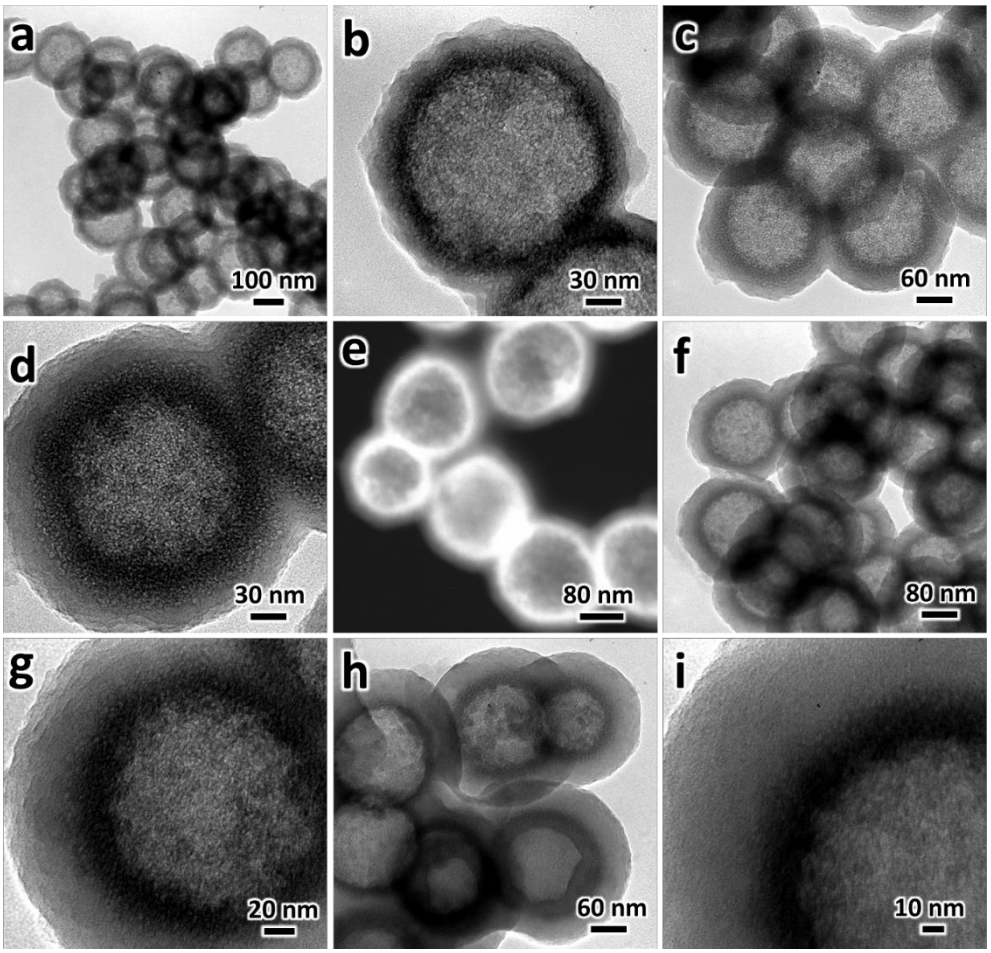

Figure 5.9 Representative TEM and HAADF-STEM images of MnSi@PDA composite, with different PDA thickness of (a,b) 19 nm, (c-e) 28 nm, (f,g) 36 nm, and (h,i) 57 nm.

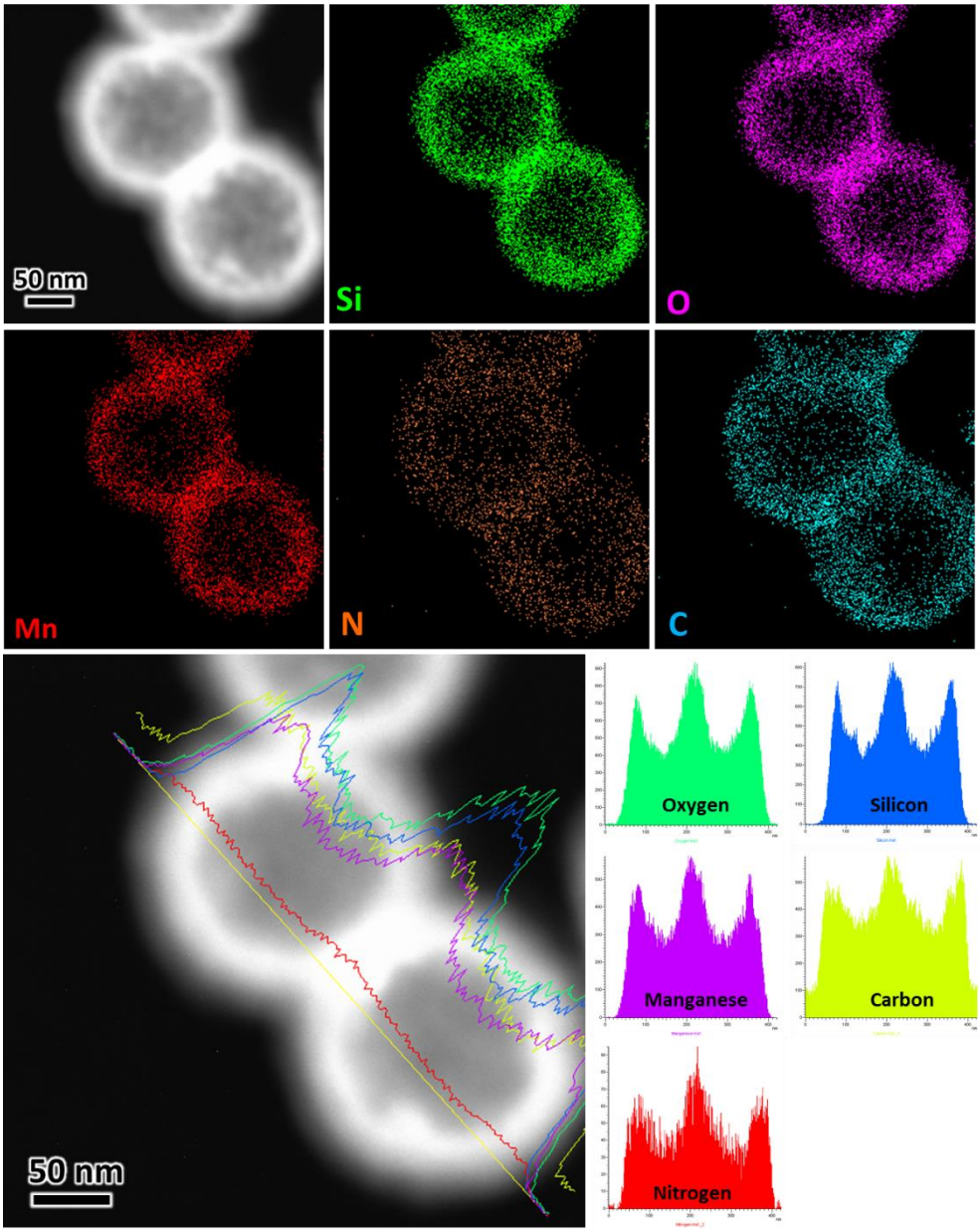

Figure 5.10 HAADF-STEM images and the corresponding EDX elemental maps and line scans of the as-synthesized MnSi@PDA sample.

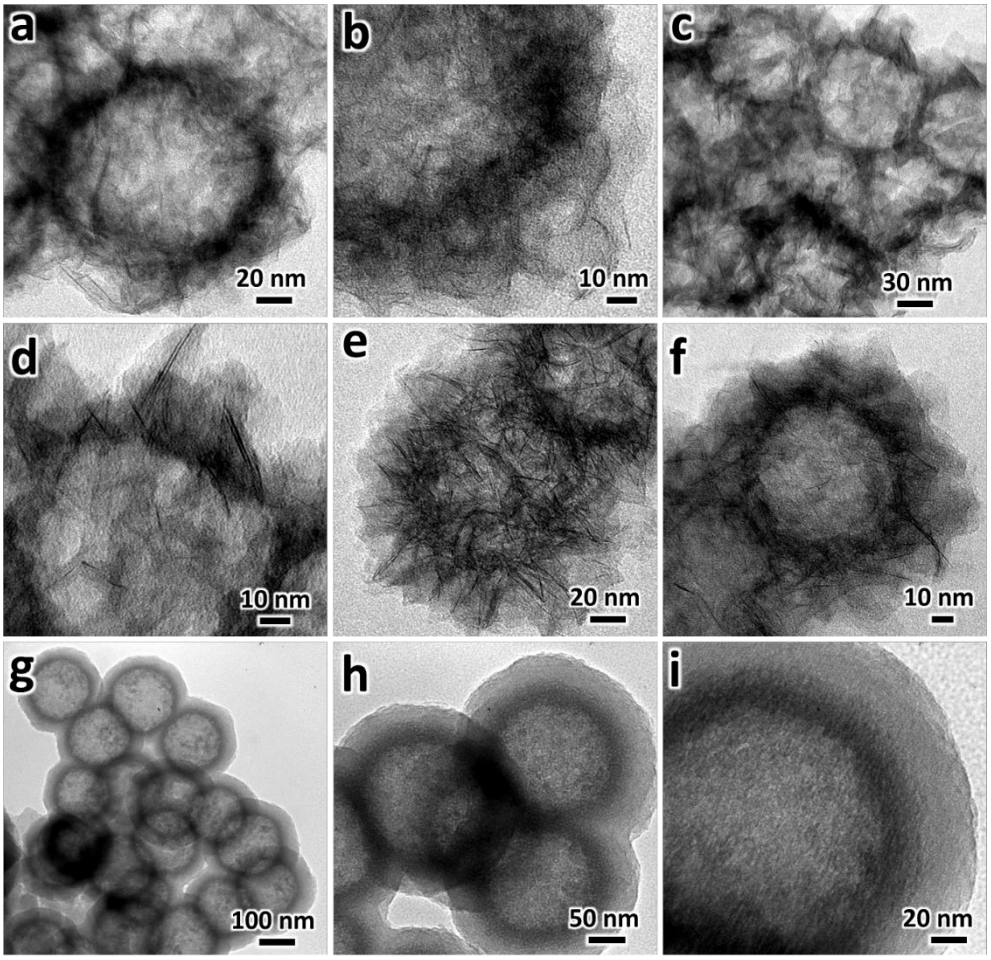

Figure 5.11 Representative TEM images of (a,b) FeSi@PDA, (c,d) CoSi@PDA, (e,f) NiSi@PDA, and (g-i) MnSi@NC (prepared by carbonization of MnSi@PDA sample at 500°C for 6 h).

XPS surface analysis further provides the compositional information on the PDA shell. Representative spectra of the C 1*s*, O 1*s*, and N 1*s* photoelectrons, measured for the MnSi@PDA sample, are displayed in Figure 5.12a-c. The C 1*s* spectrum could be deconvoluted into three components which are assigned to C–C/C–H_x (284.3 eV), C–O/C–N (285.6 eV), and C=O/C=N (287.8 eV).[55] Deconvoluting N 1*s* spectrum gives three nitrogen species R–NH_2 (401.1 eV), R–NH–R (399.8 eV), and =N–R (398.3 eV).[55, 56] The O 1*s* spectrum has two major components, one from O=C (530.7 eV) and the other from O–C (532.4

eV).[17, 55] The atomic ratios of N/C and N/O were determined to be 10.2% and 34.0%, respectively, in good agreement with the values reported on PDA film.[57] On the other hand, no transition metal or Si signal was detected by XPS measurement, confirming that the silicate cores were completely wrapped within the conformal coating of PDA phase.

The PDA content in the TMSi@PDA could be further determined by TGA technique. For example, our TGA study found that *ca.* 36 wt% of PDA is present in the MnSi@PDA sample (Figure 5.12d, where the shell thickness of PDA layer is *ca.* 28 nm). The evolving gases during the measurement were mainly water and CO_2, as determined by thermogravimetry coupled with FTIR (TGA–FTIR) experiments. However, no NO_2 was detected probably due to little amount of N element in PDA.

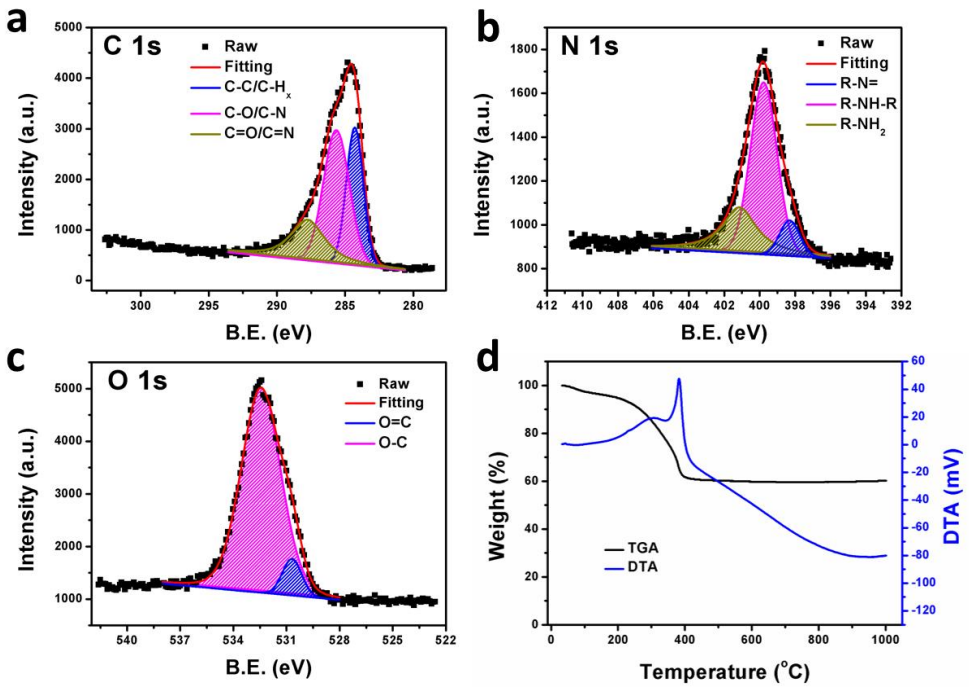

Figure 5.12 (a-c) High resolution XPS spectra of C 1*s*, N 1*s*, and O 1*s* core-levels of MnSi@PDA sample (where B.E. = binding energy). (d) TGA-DTA curves for the MnSi@PDA (DTA = differential thermal analysis).

Meanwhile, PDA can be further used as precursors to obtain nitrogen-doped carbon (NC) by pyrolysis of the TMSi@PDA at 500°C in argon atmosphere; the thus derived composites are named as TMSi@NC (structure (6) in Figure 5.2).[19] As revealed from the TEM images (Figure 5.11g–i), the formed NC shell is also uniform and continuous. The average thicknesses of NC shell in Figure 5.11i is *ca.* 37 nm, which is similar to that of its original PDA shell (36 nm). The resultant powder color was changed from the original brown to black, further indicating the formation of carbon. As reported, the resulting NC coating would increase the electronic conductivity and improve electrochemical performance of the materials.[19, 58] Thus the TMSi@NC may also be workable as a potential anode material in the application of lithium-ion-batteries.

As mentioned above, surface charges of PDA are controllable *via* tuning the pH of a solution. In Figure 5.13, zeta-potentials of the TMSi@PDA aqueous suspensions have been measured at different pHs. In these experiments, a specific pH for the sample aqueous suspension was adjusted by adding HCl (0.20 M) or NaOH (0.20 M) solution. The isoelectric points (IEPs) of the samples were measured, which were slightly lower than that of the original PDA (around pH 4).[59] Different substrates might affect the polymerization of dopamine and thereby alter the packing of the polymer chains and surface

charge. For instance, the IEP increases in the order of MnSi@PDA (2.8) < FeSi@PDA (3.3) < CoSi@PDA (3.7) ≈ NiSi@PDA (3.8). As can be seen in Figure 5.13, the surface charge of TMSi@PDA is indeed varied in response to its pH environment. More specifically, for example, the MnSi@PDA sample is positively charged at pH = 2 and its zeta-potential is +16.2 mV, whereas it becomes negatively charged at pH = 10 with a zeta-potential at –34.1 mV.

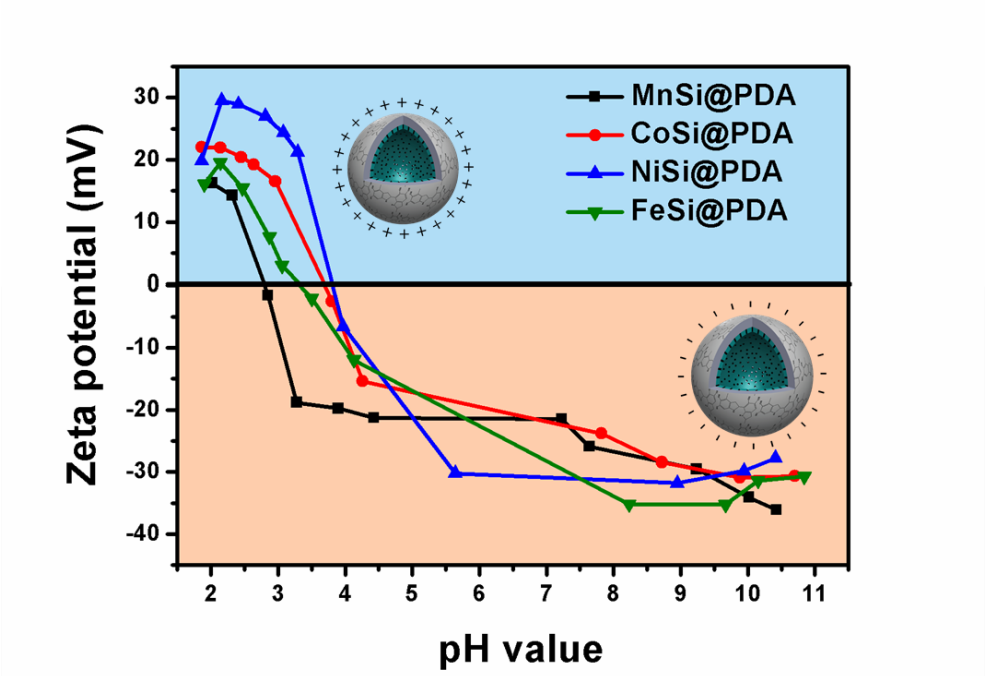

Figure 5.13 Plots of the zeta-potential data of TMSi@PDA (TM = Mn, Co, Ni, and Fe) samples measured as a function of pH value.

5.3.4. Formation routes of Pt/TMSi and Pt/TMSi@PDA

The as-prepared transition metal silicates are ideal support materials for hosting metal nanoparticles for fabricating integrated nanocatalysts. Firstly, TMSi own many advantageous properties, such as the particle uniformity, high specific surface area, hierarchical hollow structures, tunable composition,

and high thermally stability. Secondly, the mesoporosity of shell will enhance the surface area of this type of support, and thus limit the agglomeration of catalytic nanoparticles when they are loaded. In particular, the presence of central cavity leads to a low structural density, which is advantageous for them to suspend in solution for heterogeneous catalysis.[60] Moreover, the hollow TMSi have a shorter diffusion barrier (pathway) than the non-hollow porous SiO_2 spheres, which will facilitate the mass transport of reactants (particularly liquid molecules) during catalysis reactions.[61] Specifically, using Mn silicate as a support, Pt/MnSi can be obtained by the in-situ reduction of K_2PtCl_4 during the hydrothermal treatments (180°C for 12 h). As shown in Figure 5.14a–c, Pt NPs with an average size of *ca.* 4.1±0.9 nm were highly dispersed on the surfaces of hollow Mn silicate. Similarly, Pt NPs could be immobilized on three other types of transition metal silicates. For the same amount of Pt precursor, the Pt loadings were different on each support material, which increase in the order: Pt/FeSi (2.77 wt%) < Pt/MnSi (7.28 wt%) ≈ Pt/NiSi (7.44 wt%) < Pt/CoSi (9.06 wt%), owing to different metal silicates.

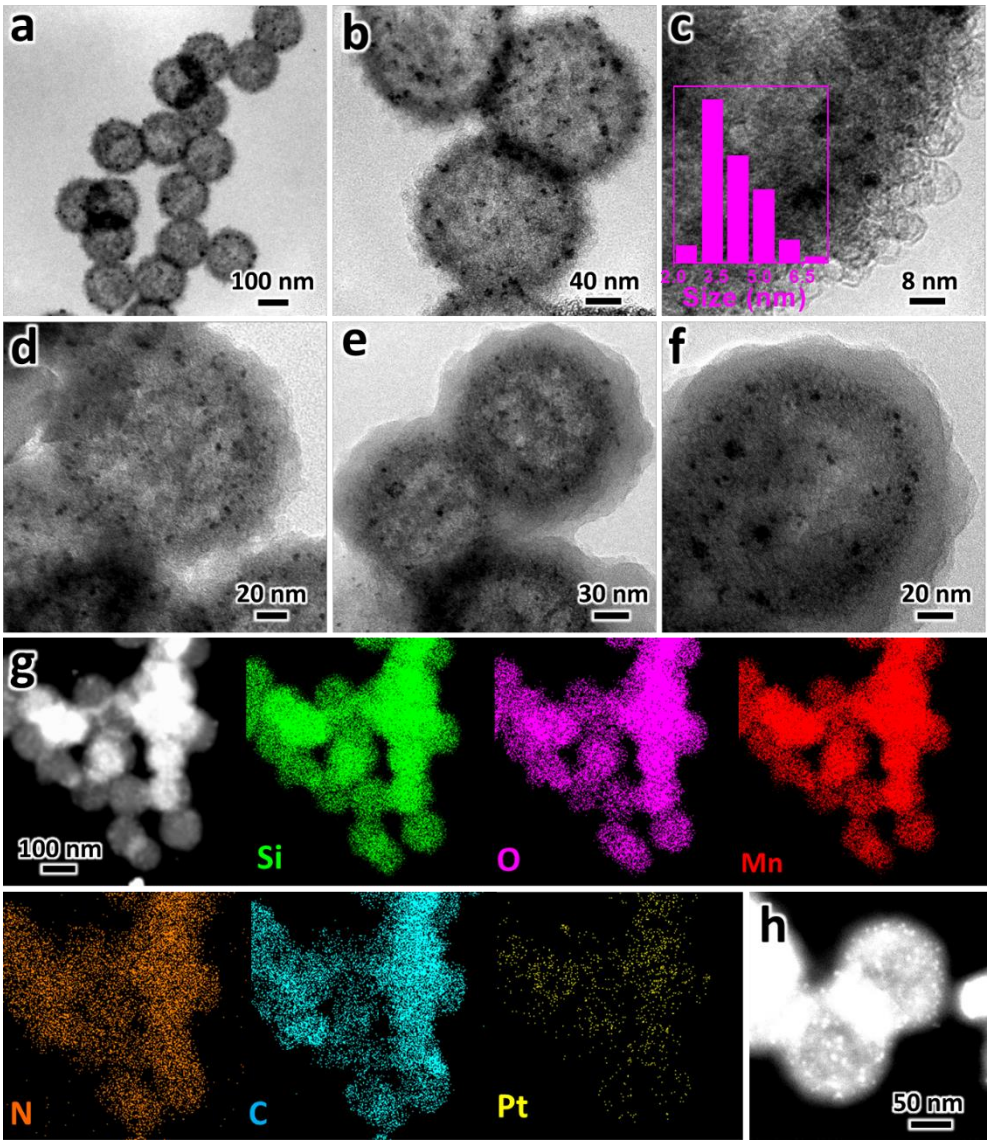

Figure 5.14 Representative TEM images of (a-c) Pt/MnSi, and (d-f) Pt/MnSi@PDA with PDA thickness of (d) 17 nm, (e,f) 27 nm, (g) EDX elemental maps of the Pt/MnSi@PDA catalyst, and (h) HAADF-STEM image of the Pt/MnSi@PDA catalyst. Inset in c: size distribution of the Pt nanoparticles.

By using the similar PDA coating method introduced above, Pt/MnSi@PDA catalysts were obtained (structure (5), Figure 5.2). The corresponding TEM and HAADF-STEM images are displayed in Figure 5.14d-f,h, which strongly indicates the successfully preparation of Pt/MnSi@PDA. Likewise, the thickness of the PDA layer can be controlled by

adjusting the monomer concentration. In this work, Pt/MnSi@PDA catalysts with PDA layer thickness of 17 nm, 27 nm, and 42 nm were obtained when using 5 mg, 10 mg, and 20 mg of dopamine, respectively. The PDA contents in these catalysts were measured as 24.7 wt%, 34.2 wt%, and 47.7 wt%, respectively. Again, EDX elemental maps in Figure 5.14g confirm the expected configuration of Pt in Pt/MnSi@PDA. In addition, no detectable Pt signal was found in XPS spectra, indicating Pt was fully embedded underneath the PDA shell. The variation of zeta-potential with respect to pH for Pt/MnSi@PDA is shown in Figure 5.15. As shown, the IEP of the catalyst is at approximately pH of 3.1, with a zeta-potential of –45.7 mV at pH of 10.6 and a zeta-potential of +6.8 mV at pH of 2.4. Moreover, the Pt/CoSi@PDA, Pt/FeSi@PDA, and Pt/NiSi@PDA can also been prepared using the similar method. To the best of our knowledge, this is the first report on coating PDA onto conventional catalysts (*i.e.*, metal plus support system), which endow the catalytic system with some smart features (*e.g.*, pH responsivity, charge-switchable capability).

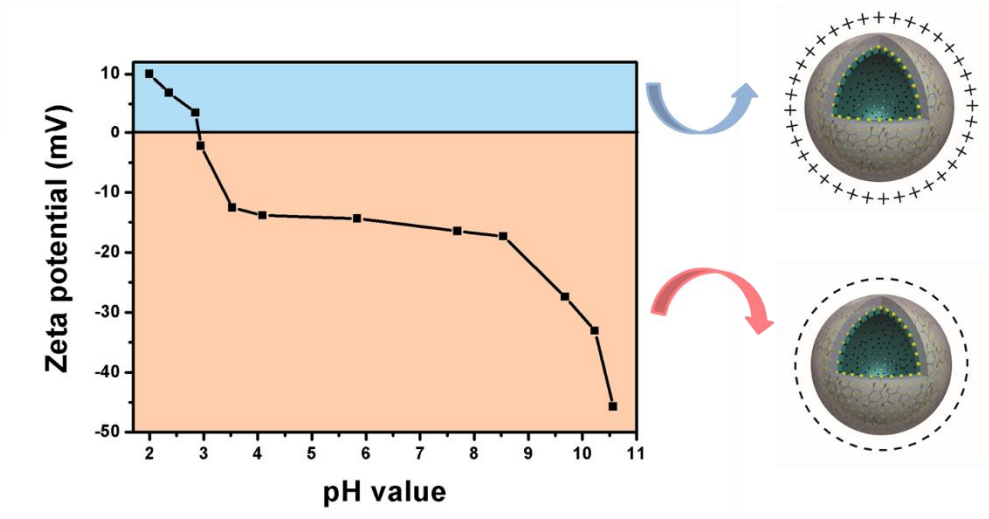

Figure 5.15 Plot of the zeta-potential of Pt/MnSi@PDA samples measured as a function of pH value.

5.3.5. Application of the integrated nanocatalysts

Globally, there are more than 100000 commercially available organic dyes. Although dyes make our world colorful, discharging of these dyes in wastewater poses acute pollution problems.[30, 31] Thus, discoloration treatment of dye effluents has become environmentally important. In order to examine the selective catalytic properties of the exemplary Pt/MnSi@PDA toward the degradation of five organic dyes (MO, MB, CR, R6G, and TB), the advanced oxidation processes (AOP)[32] of these dyes were carried out in this work. Referring to the catalyst in Figure 5.1, the embedded Pt NPs siting between TMSi core and PDA shell serve as active centers to catalyze the decomposition of H_2O_2 to form radicals (*e.g.*, HO· and HO_2·) and superoxide ions (*e.g.*, O_2^-).

In this study, adsorption equilibrium for a period of 15 min was established before adding the oxidant H_2O_2 to eliminate the effect of dye adsorption. Upon the addition of H_2O_2, concentration change of the dyes was monitored by taking the UV-vis spectral absorbance measured at the characteristic peaks. At the solution pH of 10, the characteristic peaks for MO, MB, R6G, CR and TB were at 460, 664 and 525, 495 and 593 nm, respectively. It should be noted that the characteristic UV-vis spectral peaks for the dyes might change at varied pH solutions. As shown in Figure 5.16a-e, interestingly, at pH 10, we found that the Pt/MnSi@PDA catalyst degraded cationic dyes only. For instance, the degradation efficiency (defined as the degradation percentage of dye) of MB was 81.5% just after 3 min of reaction, and the degradation efficiency of R6G was 69.8% at 3 min. On the contrary, under the same solution pH 10, the catalytic activity of the Pt/MnSi@PDA toward anionic dyes was rather poor. As an example, the concentration of MO (50 mg/L) still remained 97% of its initial value after the 30 min of the AOP. Similar results were obtained in two other anionic dyes CR and TB, where negligible amounts of CR and TB were degraded. These results can be rationalized in terms of charge repulsion between anionic dyes and the PDA shell of Pt/MnSi@PDA which was negatively charged at pH of 10 (zeta-potential at *ca.* –30 mV). Due to the electrostatic attraction, however, the cationic dyes (MB and R6G) could easily be captured by the negative PDA shell and be degraded

preferably by the hydroxyl radicals or superoxide ions from the embedded Pt nanoparticles.

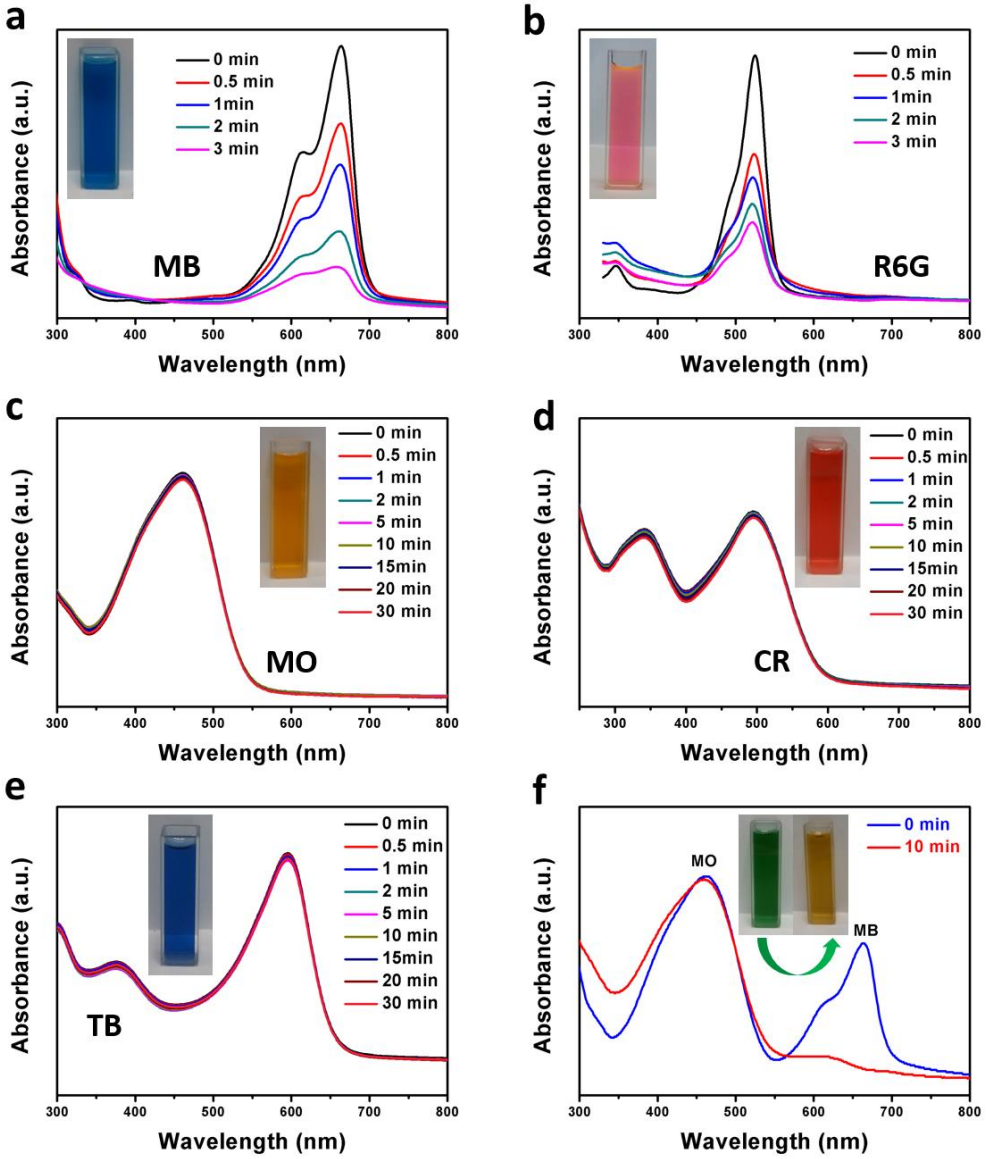

Figure 5.16 UV-vis absorption spectra of various dye molecules as a function of time during the advanced oxidation processes (AOP) at solution pH of 10: (a) MB, 50 mg/L; (b) R6G, 50 mg/L; (c) MO, 50 mg/L; (d) CR, 50 mg/L; (e) TB, 50 mg/L; and (f) mixture of MB (25 mg/L) and MO (25 mg/L).

On the basis of the above results, in principle, our Pt/TMSi@PDA catalysts should also be able to perform catalytic reactions for selected substrate(s) in reactant mixtures. To explore this possibility, selective degradation of a dye

mixture containing MB (25 mg/L) and MO (25 mg/L) was examined. As shown in Figure 5.16f, the overall color of the mixed dyes is green, resulting from their respective pristine blue (*i.e.*, MB) and yellow (*i.e.*, MO). The color removal efficiencies for blue MB and yellow MO are quite different. After 10 min of reaction, the mixture turned to yellow (*i.e.*, color of MO). The UV-vis spectra confirm that the blue MB was degraded mostly, and the remaining dye was MO which was intact. We thus conclude that by tuning PDA into a negatively charged shell at high pH environments (above the IEPs), our integrated nanocatalysts can selectively degrade cationic organic dyes. It should also be pointed out that prior to this work majority organic dyes were oxidized non-selectively using the conventional AOP.[62]

As discussed above, our Pt/MnSi@PDA catalysts exhibit zwitterionicity, that is, surface charges of the catalysts are switchable. Therefore, equally importantly, it is conceivable that these catalysts should also be able to degrade anionic dyes because they possess positive charges under low pH conditions (< IEP). In this regard, we also examined the degradation of dyes at acidic media (*e.g.*, pH 2). The observed performances were summarized in Figure 5.17a-e. As expected, only a certain degree of discoloration was observable for cationic dyes (MB and R6G) at pH 2. The degradation rates were much slower as compared with those of Figure 5.16a,b (pH 10), because the positively charged PDA shell repels these cationic dyes. On the other hand, the degradation efficiencies toward MO, CR and TB were significantly higher

as compared to those shown in Figure 5.16c,d,e (*viz.*, the cases of pH 10). Similarly, degradation performance of dye mixtures was also investigated at the solution pH = 2. As reported in Figure 5.17f, the catalyst was more active in degrading TB than MB in a mixture of the two dyes (each at 25 mg/L). After 10 min, the removal of TB was almost 100%, compared to 46% for MB, since TB molecules exist in the anionic state at pH = 2 (the pK_1 value of TB was reported to be 1.7 in aqueous solution).[63] Thus, the enrichment of TB at the surface of the catalyst *via* the electrostatic attraction between the positively charged PDA shell and the TB anions can definitely improve the degradation kinetics.

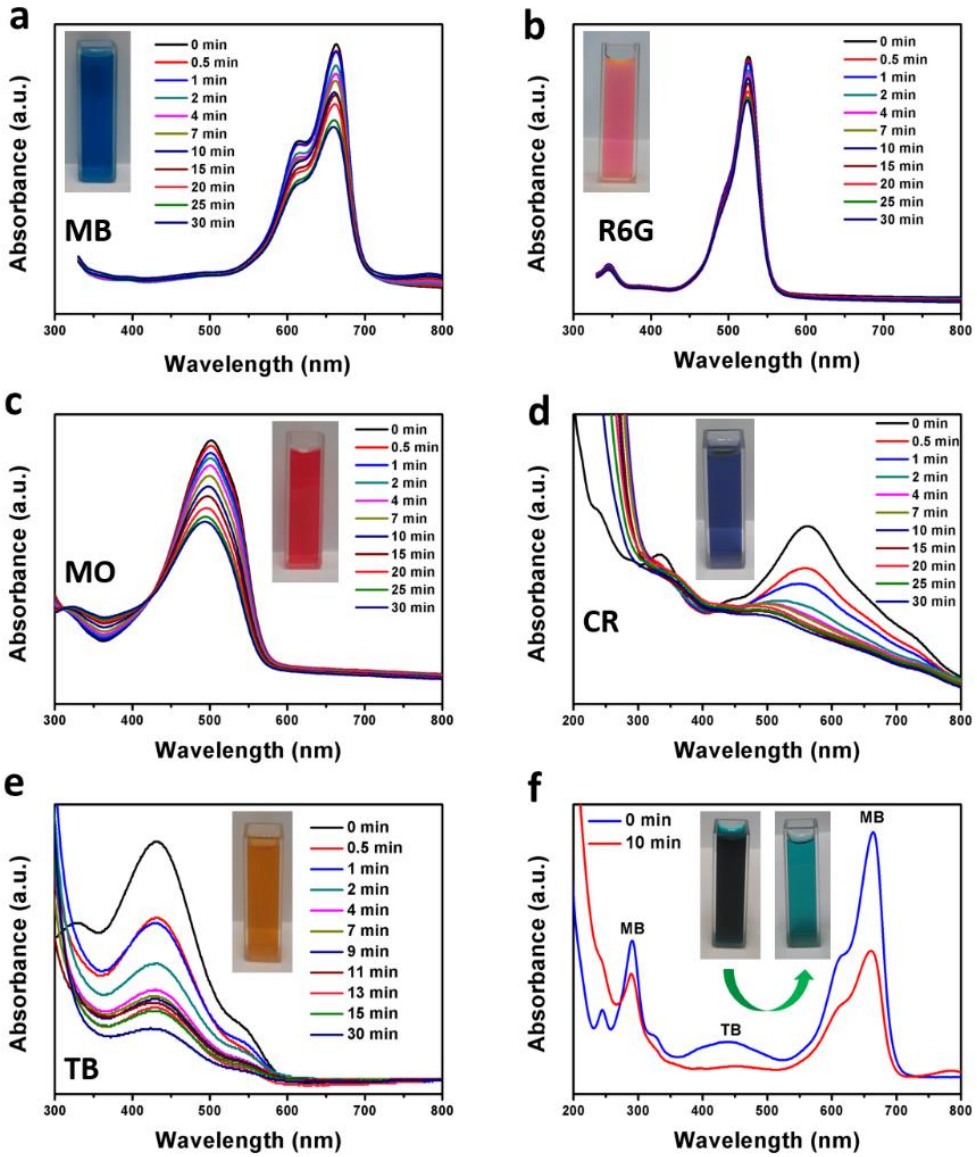

Figure 5.17 UV-vis absorption spectra of various dye molecules as a function of time during the advanced oxidation processes (AOP) at solution pH of 2: (a) MB, 50 mg/L; (b) R6G, 50 mg/L; (c) MO, 50 mg/L; (d) CR, 50 mg/L; (e) TB, 50 mg/L; and (f) mixture of MB (25 mg/L) and TB (25 mg/L). Note that the characteristic peaks for MO, CR and TB at pH 2 were different from those at pH of 10.

In order to better understand how the substrate-selective catalysis performs over the Pt/MnSi@PDA catalyst, several control experiments were carried out using homogeneous Fenton system (based on Fe^{2+}/H_2O_2), and structural intermediates and products, including MnSi (structure 2, Figure 5.2), Pt/MnSi

(structure 3), MnSi@PDA (structure 4), and Pt/MnSi@NC (structure 7). The results regarding their degradation efficiencies toward two representative dyes (MB and MO) at 30 min are summarized in Figure 5.18. Firstly, it is found that homogeneous Fenton system is non-selective, which showed equal degradation efficiency for both cationic and anionic dyes. In contrast, the Pt/MnSi@PDA catalyst substantially enhances the substrate selectivity (93.8% for MB, 0% for MO). The MnSi and Pt/MnSi systems also degrade both MB and MO at the same time, because silicate materials contain hydroxyl groups,[64] and Mn silicate surface bears negative charge at pH 10 (its zeta-potential –17.3 mV, lower than –30 mV of Pt/MnSi@PDA under the same condition). However, without a PDA shell, the Mn silicate surface cannot select cationic MB only, and 37.8% and 49.4% of anionic MO have also been degraded by MnSi and Pt/MnSi, respectively. Furthermore, the surface of Mn silicate was not adjustable to positive charge, even at pH 2 (zeta-potential of –1.0 mV), whereas Pt/MnSi@PDA catalyst has positive charge at pH 2 (zeta-potential of +10 mV). This explains why only limited degradation toward the anionic dye (TB) was observed over Mn silicate at the pH 2, which was much lower than that over Pt/MnSi@PDA catalyst (Figure 5.17e). Although Mn silicate alone shows catalytic activity for dye degradation (probably due to the catalytic decomposition of hydrogen peroxide by Mn compound[65]), the degradation rate was much slower than Pt/MnSi (*e.g.*, 15.3% *vs.* 63.1% degradation efficiency toward MB at the time of 1 min and pH 10). Moreover,

the PDA layer in Pt/MnSi@PDA will not affect the overall degradation rate much. The degradation rate only slightly decreases when increasing the thickness of PDA layer from 17 nm, 27 nm, to 42 nm. By the carbonation treatment of Pt/MnSi@PDA (500^{o}C for 6 h under Ar atmosphere), Pt/MnSi@NC was obtained. Although the size of Pt nanoparticles was only slightly increased (4.7 nm), the Pt/MnSi@NC catalyst did not have the excellent substrate selectivity observed in its precursor Pt/MnSi@PDA. All these findings confirm that the PDA layer is critical for screening the charged dyes and it can absolutely prevent the anionic dyes from degradation at pH 10. We found that MO can also be slowly degraded in a control experiment in the absence of any catalyst. Therefore, we believe that a fast decomposition of H_2O_2 and generation of strong oxidants (*e.g.*, radical groups and superoxide ions) benefit the fast degradation of dyes trapped by the PDA layer. The repelled MO does not degrade at all (degradation efficiency of 0%) due to the total consumption of H_2O_2 within a short time by Pt/MnSi@PDA. By contrary, Mn silicate is significantly less reactive than Pt nanoparticles toward H_2O_2 decomposition, and it cannot degrade the trapped dyes timely and majority of dyes (cationic and anionic) are still in the bulk solution (limited by the adsorption equilibriums). Thereby, under this condition, 37.8% and 33% of anionic MO can be degraded when using MnSi and MnSi@PDA as the catalysts, respectively (Figure 5.18d,f). Therefore, it can be concluded that both PDA shell and Pt nanoparticles present in Pt/MnSi@PDA system

contribute to the successful selective-degradation of cationic and anionic dyes. Similar selective dye degradation results can also be found over Pt/CoSi@PDA, Pt/FeSi@PDA, and Pt/NiSi@PDA catalysts. Therefore, the concept of this type of catalysts may be applied to the selection of cationic and anionic substrates in heterogeneous catalysis.

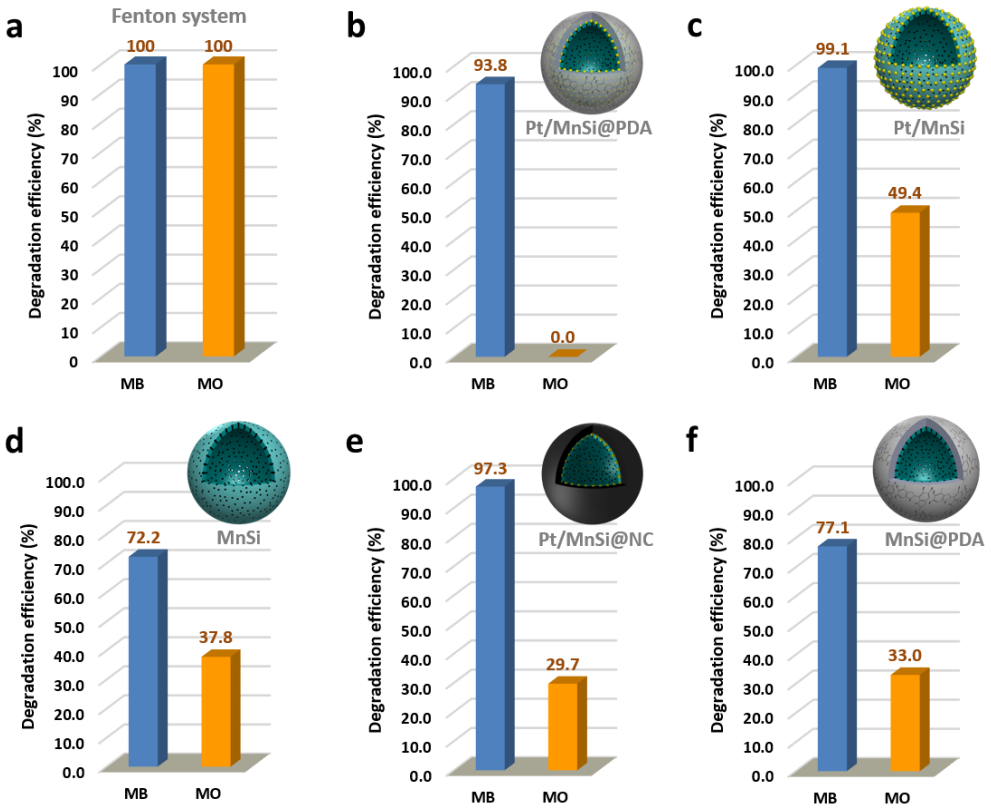

Figure 5.18 Comparative degradation of MB (25 mg/L) and MO (25 mg/L) at pH 10 catalyzed by (a) Fenton system ($FeSO_4$), (b) Pt/MnSi@PDA, (c) Pt/MnSi, (d) MnSi, (e) Pt/MnSi@NC, and (f) MnSi@PDA. Insets in (b-f) show the structural models of the catalysts.

5.4. Conclusions

In summary, we have demonstrated a rationale, design, fabrication and application of a series of "smart" integrated nanocatalysts with charge-

switchable property, which show negative surface charge at pH 10 (zeta-potential at *ca.* –30 mV), and positive charge at pH 2 (zeta-potential at *ca.* +10 mV). In order to prepare carrier materials for the integrated nanocatalysts, we also developed a general self-templating method (based on Stöber silica) to prepare hollow mesoporous transition metal silicates (*e.g.*, Fe, Co, Ni, Mn). The integrated nanocatalysts encompass three basic components: uniform Pt nanoparticles (size of 4.1±0.9 nm) were supported on the hollow mesoporous transition metal silicates and conformably encapsulated by a polydopamine (PDA) layer with controllable thickness ranging from 17 to 42 nm. Most importantly, encapsulation *via* PDA film provides the exemplary nanocatalyst Pt/MnSi@PDA both pH responsive property and substrate-selective activity toward degradation of water-soluble organic dyes, including cationic dyes (*e.g.*, rhodamine 6G, methylene blue), and anionic dyes (*e.g.*, Congo red, methyl orange, and thymol blue). In addition, selective degradation activity toward dye mixtures could also be controlled by adjusting the solution pH. For instance, at pH 10, the cationic dyes were preferably degraded, whereas the anionic dyes were almost intact; at pH 2, such a substrate-selective catalysis trend was reversed. We envision that PDA shell in Pt/TMSi@PDA catalysts would also be able to offer pH-switchable permselectivity for selecting other cationic and anionic substrates in heterogeneous catalysis.

5.5. References

1. H. C. Zeng, *Acc. Chem. Res.*, 2013, **46**, 226-235.

2. M. B. Gawande, R. Zboril, V. Malgras and Y. Yamauchi, *J. Mater. Chem. A*, 2015, **3**, 8241-8245.

3. G. Zhan and H. C. Zeng, *Coordin. Chem. Rev.*, DOI: http://dx.doi.org/10.1016/j.ccr.2016.03.003.

4. T. Zeng, X. Zhang, Y. Guo, H. Niu and Y. Cai, *J. Mater. Chem. A*, 2014, **2**, 14807-14811.

5. Y. Yuan, N. Yan and P. J. Dyson, *Inorg. Chem.*, 2011, **50**, 11069-11074.

6. W. Zhou, J. Wang, C. Wang, Y. Du, J. Xu and P. Yang, *Mater. Chem. Phys.*, 2010, **122**, 10-14.

7. J. Qi, W. Lv, G. Zhang, Y. Li, G. Zhang, F. Zhang and X. Fan, *Nanoscale*, 2013, **5**, 6275-6279.

8. Y. Lu, Y. Mei, M. Drechsler and M. Ballauff, *Angew. Chem. Int. Ed.*, 2006, **45**, 813-816.

9. J. Chen, P. Xiao, J. Gu, Y. Huang, J. Zhang, W. Wang and T. Chen, *RSC Adv.*, 2014, **4**, 44480-44485.

10. N. Yan, J. Zhang, Y. Yuan, G.-T. Chen, P. J. Dyson, Z.-C. Li and Y. Kou, *Chem. Commun.*, 2010, **46**, 1631-1633.

11. Y. Liu, Y. Wang, Y. Wang, J. Lu, V. Piñón and M. Weck, *J. Am. Chem. Soc.*, 2011, **133**, 14260-14263.

12. Z. Chen, Z.-M. Cui, C.-Y. Cao, W.-D. He, L. Jiang and W.-G. Song, *Langmuir.*, 2012, **28**, 13452-13458.

13. H. Lee, S. M. Dellatore, W. M. Miller and P. B. Messersmith, *Science*, 2007, **318**, 426-430.

14. Y. Liu, K. Ai and L. Lu, *Chem. Rev.*, 2014, **114**, 5057-5115.

15. M. Deng, H. Zhao, S. Zhang, C. Tian, D. Zhang, P. Du, C. Liu, H. Cao and H. Li, *J. Mol. Catal. B*, 2015, **112**, 15-24.

16. J.-J. Feng, P.-P. Zhang, A.-J. Wang, Q.-C. Liao, J.-L. Xi and J.-R. Chen, *New J. Chem.*, 2012, **36**, 148-154.

17. M. Zhang, X. He, L. Chen and Y. Zhang, *J. Mater. Chem.*, 2010, **20**, 10696-10704.

18. B. D. McCloskey, H. B. Park, H. Ju, B. W. Rowe, D. J. Miller, B. J. Chun, K. Kin and B. D. Freeman, *Polymer*, 2010, **51**, 3472-3485.

19. C. Lei, F. Han, D. Li, W.-C. Li, Q. Sun, X.-Q. Zhang and A.-H. Lu, *Nanoscale*, 2013, **5**, 1168-1175.

20. C. Xiao, X. Chu, Y. Yang, X. Li, X. Zhang and J. Chen, *Biosens. Bioelectron.*, 2011, **26**, 2934-2939.

21. Q. Liu, N. Wang, J. Caro and A. Huang, *J. Am. Chem. Soc.*, 2013, **135**, 17679-17682.

22. D. R. Dreyer, D. J. Miller, B. D. Freeman, D. R. Paul and C. W. Bielawski, *Chem. Sci.*, 2013, **4**, 3796-3802.

23. B. Yu, J. Liu, S. Liu and F. Zhou, *Chem. Commun.*, 2010, **46**, 5900-5902.

24. Q. Liu, B. Yu, W. Ye and F. Zhou, *Macromol. Biosci.*, 2011, **11**, 1227-1234.

25. X.-C. Liu, G.-C. Wang, R.-P. Liang, L. Shi and J.-D. Qiu, *J. Mater. Chem. A*, 2013, **1**, 3945-3953.

26. F. Ren, C. Zhai, M. Zhu, C. Wang, H. Wang, D. Bin, J. Guo, P. Yang and Y. Du, *Electrochim. Acta*, 2015, **153**, 175-183.

27. S. Xiong, B. Xi, K. Zhang, Y. Chen, J. Jiang, J. Hu and H. C. Zeng, *Sci. Rep.*, 2013, **3**, 2177.

28. A. Ma, Y. Xie, J. Xu, H. Zeng and H. Xu, *Chem. Commun.*, 2015, **51**, 1469-1471.

29. N. Shi, X. Li, T. Fan, H. Zhou, J. Ding, D. Zhang and H. Zhu, *Energy Environ. Sci.*, 2011, **4**, 172-180.

30. J. Fan, Y. Guo, J. Wang and M. Fan, *J. Hazard. Mater.*, 2009, **166**, 904-910.

31. T. Sriskandakumar, N. Opembe, C.-H. Chen, A. Morey, C. King'ondu and S. L. Suib, *J. Phys. Chem. A*, 2009, **113**, 1523-1530.

32. R. Andreozzi, V. Caprio, A. Insola and R. Marotta, *Catal. Today*, 1999, **53**, 51-59.

33. W. H. Glaze, J.-W. Kang and D. H. Chapin, *Ozone: Sci. Eng.*, 1987, **9**, 335-352.

34. I. K. Konstantinou and T. A. Albanis, *Appl. Catal. B*, 2004, **49**, 1-14.

35. Y. Ono, T. Matsumura, N. Kitajima and S. Fukuzumi, *J. Phys. Chem.*, 1977, **81**, 1307-1311.

36. J.-Z. Guo, H. Cui, W. Zhou and W. Wang, *J. Photochem. Photobiol. A*, 2008, **193**, 89-96.

37. E. Neyens and J. Baeyens, *J. Hazard. Mater.*, 2003, **98**, 33-50.

38. J. J. Pignatello, E. Oliveros and A. MacKay, *Crit. Rev. Env. Sci. Tec*, 2006, **36**, 1-84.

39. G. Zhan, C. C. Yec and H. C. Zeng, *Chem. - Eur. J.*, 2015, **21**, 1882-1887.

40. J. Dou and H. C. Zeng, *ACS Catal.*, 2014, **4**, 566-576.

41. D. P. Wang and H. C. Zeng, *Chem. Mater.*, 2011, **23**, 4886-4899.

42. N. Huesing, C. Raab, V. Torma, A. Roig and H. Peterlik, *Chem. Mater.*, 2003, **15**, 2690-2692.

43. H. Hoffmann, *Angew. Chem. Int. Ed.*, 2009, **48**, 2457-2459.

44. X. Fang, C. Chen, Z. Liu, P. Liu and N. Zheng, *Nanoscale*, 2011, **3**, 1632-1639.

45. X. Fang, X. Zhao, W. Fang, C. Chen and N. Zheng, *Nanoscale*, 2013, **5**, 2205-2218.

46. C. C. Yec and H. C. Zeng, *ACS Nano*, 2014, **8**, 6407-6416.

47. J. Qu, W. Li, C.-Y. Cao, X.-J. Yin, L. Zhao, J. Bai, Z. Qin and W.-G. Song, *J. Mater. Chem.*, 2012, **22**, 17222-17226.

48. Y. Sheng and H. C. Zeng, *Chem. Mater.*, 2015, **27**, 658-667.

49. M. T. Bore, M. P. Mokhonoana, T. L. Ward, N. J. Coville and A. K. Datye, *Microporous Mesoporous Mater.*, 2006, **95**, 118-125.

50. J. C. Groen, L. A. A. Peffer and J. Pérez-Ramírez, *Microporous Mesoporous Mater.*, 2003, **60**, 1-17.

51. P. I. Ravikovitch and A. V. Neimark, *Langmuir.*, 2002, **18**, 9830-9837.

52. T. M. Eggenhuisen, G. Prieto, H. Talsma, K. P. de Jong and P. E. de Jongh, *J. Phys. Chem. C*, 2012, **116**, 23383-23393.

53. R. Huirache-Acuña, R. Nava, C. Peza-Ledesma, J. Lara-Romero, G. Alonso-Núez, B. Pawelec and E. Rivera-Muñoz, *Materials*, 2013, **6**, 4139-4167.

54. J. Evans, A. B. Zaki, M. Y. El-Sheikh and S. A. El-Safty, *J. Phys. Chem. B*, 2000, **104**, 10271-10281.

55. R. A. Zangmeister, T. A. Morris and M. J. Tarlov, *Langmuir.*, 2013, **29**, 8619-8628.

56. L. Mouhong, H. Haoliang, L. Yingju, L. Canjian, F. Shidong, C. Xiaofen and N. Chunlin, *Nanotechnology*, 2013, **24**, 065501.

57. J. Liebscher, R. Mrówczyński, H. A. Scheidt, C. Filip, N. D. Hădade, R. Turcu, A. Bende and S. Beck, *Langmuir.*, 2013, **29**, 10539-10548.

58. N. Liu, H. Wu, M. T. McDowell, Y. Yao, C. Wang and Y. Cui, *Nano Lett.*, 2012, **12**, 3315-3321.

59. M. Vaselbehagh, H. Karkhanechi, S. Mulyati, R. Takagi and H. Matsuyama, *Desalination.*, 2014, **332**, 126-133.

60. J. Liu, S. Z. Qiao, J. S. Chen, X. W. Lou, X. Xing and G. Q. Lu, *Chem. Commun.*, 2011, **47**, 12578-12591.

61. G. Zhan and H. C. Zeng, *Chem. Mater.*, 2015, **27**, 726-734.

62. D.-F. Zhang, H. Zhang, L. Guo, K. Zheng, X.-D. Han and Z. Zhang, *J. Mater. Chem.*, 2009, **19**, 5220-5225.

63. T. Fujii and K. Toriumi, *J. Chem. Soc., Faraday Trans.*, 1993, **89**, 3437-3441.

64. V. C. Farmer and J. D. Russell, *Spectrochimica Acta*, 1964, **20**, 1149-1173.

65. J. Petlicki, D. Palusova and T. G. M. van de Ven, *Ind. Eng. Chem. Res.*, 2005, **44**, 2002-2010.

Chapter 6 Synthesis and Functionalization of Two-dimensional Metal–Organic Framework Nanosheets

6.1. Introduction

Metal–organic frameworks (MOFs) or supramolecular coordination polymers, are a class of self-assembly functional materials, in which the network of transition metal ions are bridged through organic ligands.[1] Although industrial practices are still in their infancy, the MOFs materials promise exciting potential applications in gas storage, drug delivery, molecular separation, chemical sensing, and catalysis reactions.[2-6] Regarding their catalytic application, for example, there are three basic strategies to put MOFs into use: (i) The inorganic nodes in MOFs can be intrinsic active sites for catalysis, *e.g.*, copper-based MOFs have been demonstrated as an excellent solid Lewis acid catalyst for a few reactions;[4, 7] (ii) extrinsic functional species (*e.g.*, nanoparticles) can be introduced to MOFs structure, either on the external surfaces or inside the bulks or shells of MOFs. Various catalytic nanoparticles have been successfully incorporated into different MOFs matrices, including Au, Ag, Pt, Cu, or their combination etc;[8-10] and (iii) MOFs also serve as solid precursors for metal or metal-oxide catalysts due to their high metal density within the frameworks and easy transformation. Many porous transition metal oxides, such as CuO, Cu_2O, Mn_2O_3, Mn_3O_4, Co_3O_4 and ZnO among others, have been derived through thermolysis under controlled atmospheres.[11-16] For

example, porous CuO hollow architectures with perfect octahedral shape were prepared by annealing HKUST-1 precursor in flowing air.[12] Moreover, zeolitic imidazolate framework-67 (ZIF-67) was used to design and generate Co_3O_4 or structurally more complex $Co_3O_4/NiCo_2O_4$.[13, 14] Although increasing research attention has been paid to the catalytic applications of MOFs, to our knowledge, shapes of the studied MOFs are mostly followed in three-dimensional (3D) isotropic polyhedrons (*i.e.*, high symmetric MOF crystals with sizes greater than 100 nanometers), and the catalytic systems derived from MOFs with anisotropic shapes such as nanofibers or nanosheets with a dimension(s) less than 10 nm, have seldom been explored.

Similar to many inorganic nanomaterials, tailoring of size and shape is essential to customize MOFs for specific applications according to the principle of "structure dictates function".[17] Although a fine control over the size and size-distribution of MOFs has been realized, *e.g.*, in the range of 100 nm to several microns,[18] fashioning MOFs into desired shapes for specific applications remain to be challenging. Nevertheless, several attempts to the architectural control of MOFs shapes have recently appeared in the literature, ranging from one-dimensional (1D), two-dimensional (2D) to 3D nanostructures.[19, 20] For example, nanosheets of MOFs as molecular sieving membranes for gas separation have been made in two recent reports,[21, 22] which achieved much higher separation selectivity than MOFs in other morphologies. It is generally difficult to fabricate 2D MOFs in the forms of

freestanding nanosheets or nanofilms with lateral dimensions in micrometer scale and the thickness in nanometer scale. For example, using *top-down* approaches (*e.g.*, delamination from bulk MOFs), structural deterioration and morphological damage during processes become the main obstacle to generate nanosheets.[23] Although their underlying mechanisms of shape evolution are not fully understood at present, we believe that low-dimensional MOFs can be prepared *via* anisotropic crystal growth under thermodynamically and/or kinetically controlled conditions, similar to shape-controlled syntheses of colloidal metal nanocrystals.[24] It has been that demonstrated that the geometric shape of a MOF is also determined by the relative growth rates of each facet in the crystal, which are inversely proportional to the attachment energy of a defined growth unit on crystal facets, similar to atoms as units in metal nanocrystal growth.[25] In principle, this theorem should be applicable for the growth of low-dimensional MOFs, using growth-blocking agents to inhibit the crystal growth in certain directions.[26]

As one of the most important MOFs, HKUST-1 (*i.e.*, $Cu_3(BTC)_2(H_2O)_3$, where the parent molecule of BTC^{3-} linker is H_3BTC (1,3,5-benzenetricarboxylic acid, see Scheme 6.1)), has been widely studied since it was first reported in 1999.[27] In this MOF, all three carboxyl groups in H_3BTC molecule (through deprotonation) are coordinated with Cu^{2+} ions. But, if a H_3BTC ligand offers only two carboxylate groups to link the Cu ions, it yields the phase of $Cu(HBTC)(H_2O)_3$; likewise, if only one carboxylate anion per

H_3BTC molecule is coordinated to the Cu cations, the phase $Cu(H_2BTC)_2(H_2O)_2$ is produced. Compared with HKUST-1, the latter two MOFs have received much less attention.[16, 28-30] Very recently, however, we recognized that the $Cu(HBTC)(H_2O)_3$ possesses a low symmetric crystal structure (monoclinic; space group $P2_1/c$).[31, 32] Compared to those with higher crystal symmetries, the Cu(HBTC) $(H_2O)_3$ is more likely to undergo anisotropic growth and form low-dimensional MOFs such as 1D nanofibers and 2D nanosheets. We further anticipated that the open accessibility of these 2D nanosheets could be advantageous for immobilizing catalytic nanoparticles (the above mentioned Strategy (ii)) or for self-generating metal nanocatalysts (Strategy (iii)).

To testify their possibilities for catalytic applications, in this chapter, we report our recent research on generation of low-dimensional Cu-based MOFs. The flowchart of this study, starting from solid Cu_2O nanocubes or nanospheres (a copper source) and H_3BTC ligands, is summarized in Scheme 6.1. Besides the HKUST-1 (Structure 1), the $Cu(HBTC)(H_2O)_3$ (denoted as Cu(HBTC)-1 hereafter) with many novel product morphologies such as nanofiber, nanorod, nanocuboid, and nanosheet (Structures 2 to 6) was successfully prepared. We further investigated the preparation of metal or metal-oxide nanocatalysts (*e.g.*, CuO, CuO-Cu_2O composites, or even Cu metals, Structures 7 to 9) by using as-synthesized Cu(HBTC)-1 nanosheets (Structure 5) as a solid precursor (which could also be converted to

thermodynamically more stable HKUST-1, Structure 10). In addition, various noble metal nanoparticles immobilized on external surfaces of Cu(HBTC)-1 nanosheets were also demonstrated by a sequential deposition-reduction method (Structure 11). Lastly, both gas phase CO_2 hydrogenation and liquid phase 4-nitrophenol reduction were carried out to examine the activities of the supported-metal nanocatalysts. This work establishes a new application of MOFs in the field of heterogeneous catalysis when they are prepared into low-dimensional nanostructures by manipulating coordination environments for their metal ions and organic ligands.

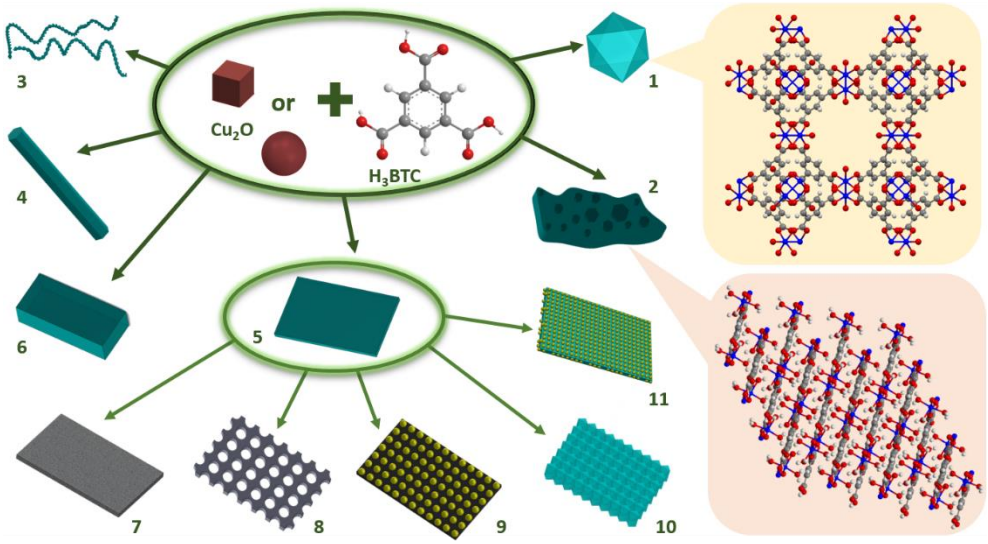

Scheme 6.1 Schematic illustrations of controlled syntheses of MOF-based functional materials, starting with cubic or spherical Cu_2O particles as a metal source and H_3BTC as ligands: (1) octahedral HKUST-1, (2) shape-uncontrolled Cu(HBTC)-1, (3) 1D Cu(HBTC)-1 nanofibers, (4) 1D Cu(HBTC)-1 nanorods, (5) 2D Cu(HBTC)-1 nanosheets, (6) doped 2D Cu(HBTC)-1 nanocuboids, (7) 2D assemblage of CuO nanoparticles, (8) 2D assemblage of CuO-Cu_2O, (9) carbon-supported 2D nanocatalysts of copper, (10) 2D assemblage of HKUST-1, and (11) Cu(HBTC)-1 supported 2D nanocatalysts of noble metals. Ball and sticks models of HKUST-1 (right top) and Cu(HBTC)-1 (right bottom) structures, viewed from the [010] direction. Blue, red, gray, and white spheres represent Cu, O, C and H atoms, respectively.

6.2. Experimental Section

6.2.1. Materials

The following chemicals were used as received without further purification: copper (II) nitrate trihydrate (Merck, 99.5%), copper (II) chloride dihydrate (Aldrich, 99%), zinc nitrate hexahydrate (Aldrich, 98%), cobalt (II) nitrate hexahydrate (Aldrich, 98+%), 1,3,5-benzenetricarboxylic acid (H_3BTC, Aldrich, 95%), gold (III) chloride trihydrate ($HAuCl_4 \cdot 3H_2O$, Aldrich, 99.9%), palladium (II) chloride ($PdCl_2$, Aldrich, 99.9%), potassium tetrachloroplatinate (II) (K_2PtCl_4, Aldrich, 98%), silver nitrate ($AgNO_3$, Merck, 99%), 4-nitrophenol (4-NP, Fluka, 99.5%), sodium borohydride ($NaBH_4$, Aldrich, 99.99%), polyvinylpyrrolidone (PVP, Aldrich, K-30), L-Ascorbic acid (Aldrich, 99%), sodium hydroxide (Merck, 99%), diethylene glycol (DEG, Aldrich, 99%), and ethanol (Fisher, 99.99%). Deionized water was used for all experiments.

6.2.2. General synthesis procedure for HKUST-1

Firstly, spherical and cubic Cu_2O precursors were prepared according to two modified methods. The yellow colored product was then dispersed in ethanol at a concentration of *ca.* 5 mM (copper content: *ca.* 10 mM) before the preparation of MOFs. In the synthesis of HKUST-1, 0.2 g of H_3BTC was dissolved in 60 mL of ethanol. Then, 10 mL of the prepared Cu_2O ethanolic suspension was added, the mixture was continuously stirred at room

temperature (25°C) for 7 h before collecting the solid by centrifugation. The blue product was then rinsed twice by ethanol and vacuum-dried before further investigation.

6.2.3. General synthesis procedure for Cu(HBTC)-1

In the synthesis of nanosheet Cu(HBTC)-1, 0.4 g of PVP was dissolved in 60 mL of water, and then 0.2 g of H_3BTC dissolved in 4 mL of ethanol was added. The white colored mixture was stirred for 5 min before the addition of 10 mL of Cu_2O ethanolic suspension. The mixture generated a transparent solution within 1 min. After stirred for 2 h, the solution became a pale blue turbid suspension, indicating the formation of Cu(HBTC)-1. The mixture was kept stirring for 14 h at room temperature. The solid product was then rinsed twice by ethanol/water and vacuum-dried at room temperature before further investigation. In the preparation of nanofibers, a much larger amount of H_3BTC was used (0.8 g H_3BTC dissolved in 16 mL of ethanol) under any other identical conditions. In the preparation of nanorods, 0.4 g of H_3BTC dissolved in 60 mL of ethanol was used.

6.2.4. General synthesis procedure for MOFs supported metal catalysts

Firstly, 13 mg of the obtained Cu(HBTC)-1 nanosheets were re-dispersed in 10 mL of water with ultrasonication for 10 min. Then, 50 μL of aqueous metal precursor solution (0.01 M, *e.g.*, $HAuCl_4$, $PdCl_2$, $AgNO_3$, or K_2PtCl_4) was mixed with 1.5 mL of the above prepared MOF suspension. The mixture was

stirred for 10 min at room temperature, followed by the addition of 6 μL of $NaBH_4$ aqueous solution (0.13 M). The mixture was stirred for 15 s, followed by centrifuging and washing with water (5 mL) twice. To prepare multimetallic nanoparticles, different metal precursor solutions were simultaneously added into the MOFs suspension under any other identical conditions.

6.2.5. Characterization techniques

Morphologies of samples were characterized by field-emission scanning electron microscopy (FESEM, JSM-6700F), transmission electron microscopy (TEM, JEM-2010), high-angle annular dark-field scanning TEM (HAADF-STEM, JEM-2100F), and atomic force microscopy (AFM, Bruker Dimension Icon). The crystallographic information was analyzed by selected-area electron diffraction (SAED, JEM-2100F) and X-ray diffraction (XRD, Bruker D8 Advance) equipped with a Cu K_α radiation source. The elemental mapping was done by energy-dispersive X-ray (EDX, Oxford Instruments, Model 7426). The surface composition and oxidation state of the samples were further analyzed by X-ray photoelectron spectroscopy (XPS, AXIS-HSi, Kratos Analytical). Specific surface areas, pore volume, and pore size of the samples were determined using N_2 physisorption isotherms at 77 K (Quantachrome NOVA-3000 system). Thermogravimetric analysis (TGA) studies were carried out on a thermobalance (TGA-2050, TA Instruments)

under flowing air atmosphere (flow rate: 50 mL/min) at a heating rate of 10°C/min. The organic groups in the MOFs structures were characterized by Fourier transform infrared spectroscopy (FTIR, Bio-Rad). Electrokinetic potentials of the MOFs aqueous suspensions were measured with ZetaPlus4 Brookhaven zeta potential analyzer.

6.2.6. Evaluation of catalytic properties

The CO_2 hydrogenation was carried out in a continuous flow fixed bed reactor made of stainless-steel loaded with 0.10 g of the above catalysts. A feed mixture (in volume ratio of $H_2/CO_2/N_2$ = 72/24/4) was introduced at the flow rate of 8 stp mL·min^{-1} (equal to a space velocity of 4800 mL·g_{cat}^{-1}·h^{-1}). The reaction temperature was monitored with a thermocouple located at the center of the catalyst bed, and the reaction pressure was controlled at 3 MPa by a backpressure regulator. Concentrations of reactants and products were measured online by a gas chromatographic system (Agilent GC model 7890A). The liquid phase reduction of 4-NP by $NaBH_4$ was chosen as a model reaction to test the workability of the MOFs supported catalysts. Typically, 50 μL of catalyst aqueous suspension (0.4 mg mL^{-1}) was diluted by 3 mL of water. Then 20 μL of 4-NP (20 mM) and 20 μL of $NaBH_4$ (500 mM) were subsequently added into the system. UV-Vis absorption spectra of the mixture (under constant magnetic stirring) were on-line recorded at short time intervals (every 30 s) to monitor the changes of the reaction mixture.

6.3. Results and Discussion

6.3.1. Synthesis of HKUST-1 and Cu(HBTC)-1 by using Cu_2O as a copper source

As shown in Figure 6.1b,c, Cu_2O nanoparticles with cubic or spherical shapes were synthesized according to two previous reports.[33, 34] Firstly, Cu_2O nanocubes were exploited as a template as well as a copper source for the synthesis of octahedral HKUST-1. When an ethanolic Cu_2O suspension was mixed with a H_3BTC ethanolic solution, gradual dissolution of the Cu_2O nanocubes occurred, followed by the formation of octahedral HKUST-1 crystals (Structure 1, Scheme 6.1). In Figure 6.1a, the transformation from Cu_2O to HKUST-1 can be visualized in a color evolution from yellow to blue. Characterized results from TEM (Figure 6.1d) and X-ray diffraction (XRD, Figure 6.2b) confirmed that the final product is indeed octahedral HKUST-1 with average edge lengths of 470 nm. No characteristic reflections for Cu_2O phase were detectable in the XRD pattern, meaning that the Cu_2O precursor was used up for HKUST-1. The porous HKUST-1 products feature Brunauer−Emmett−Teller (BET) and Langmuir specific surface areas of 1016 and 1210 m^2/g, respectively. In this synthetic process, H_3BTC served as both an etching reagent (providing proton) and a coordinative ligand, noting that the pH of solution decreased from 7.2 to 5.5 because of the deprotonation of H_3BTC. The protons generated could gradually etch Cu_2O and the released

Cu^{+} ions would then be oxidized to Cu^{2+} by the dissolved O_2 in the solvent (refer to X-ray photoelectron spectroscopy (XPS) characterization in Figure 6.3c).[35] Later, the Cu^{2+} ions and the deprotonated H_3BTC (*viz.*, BTC^{3-}) would assemble into HKUST-1 spontaneously. On the other hand, the solvent can also alter coordination equilibrium and modify growth behaviors, affecting both crystallographic and morphological aspects of MOFs.[22, 29] Herein, when water and ethanol miscible mixtures were used as a cosolvent, the monoclinic Cu(HBTC)-1 was formed instead of the cubic HKUST-1. In Figure 6.2b, phase pure $Cu(HBTC)(H_2O)_3$ is indeed obtained, as all the diffraction peaks are identical to the simulated XRD pattern of this compound. However, the product looks like as crystal aggregates with indefinite shapes and a broad size distribution, suggesting multiple heterogeneous nucleation occurred (Structure 2 in Scheme 6.1). To regulate the crystal growth of Cu(HBTC)-1, polyvinylpyrrolidone (PVP) was adopted as a modulator. Quite interestingly, oriented crystal growths can be indeed carried out, and several types of low-dimensional nanostructures of Cu(HBTC)-1, such as nanofiber, nanorod and nanosheet (Structures 3, 4 and 5 in Scheme 6.1), can be prepared rather easily with the assistance of this nonionic polymer.

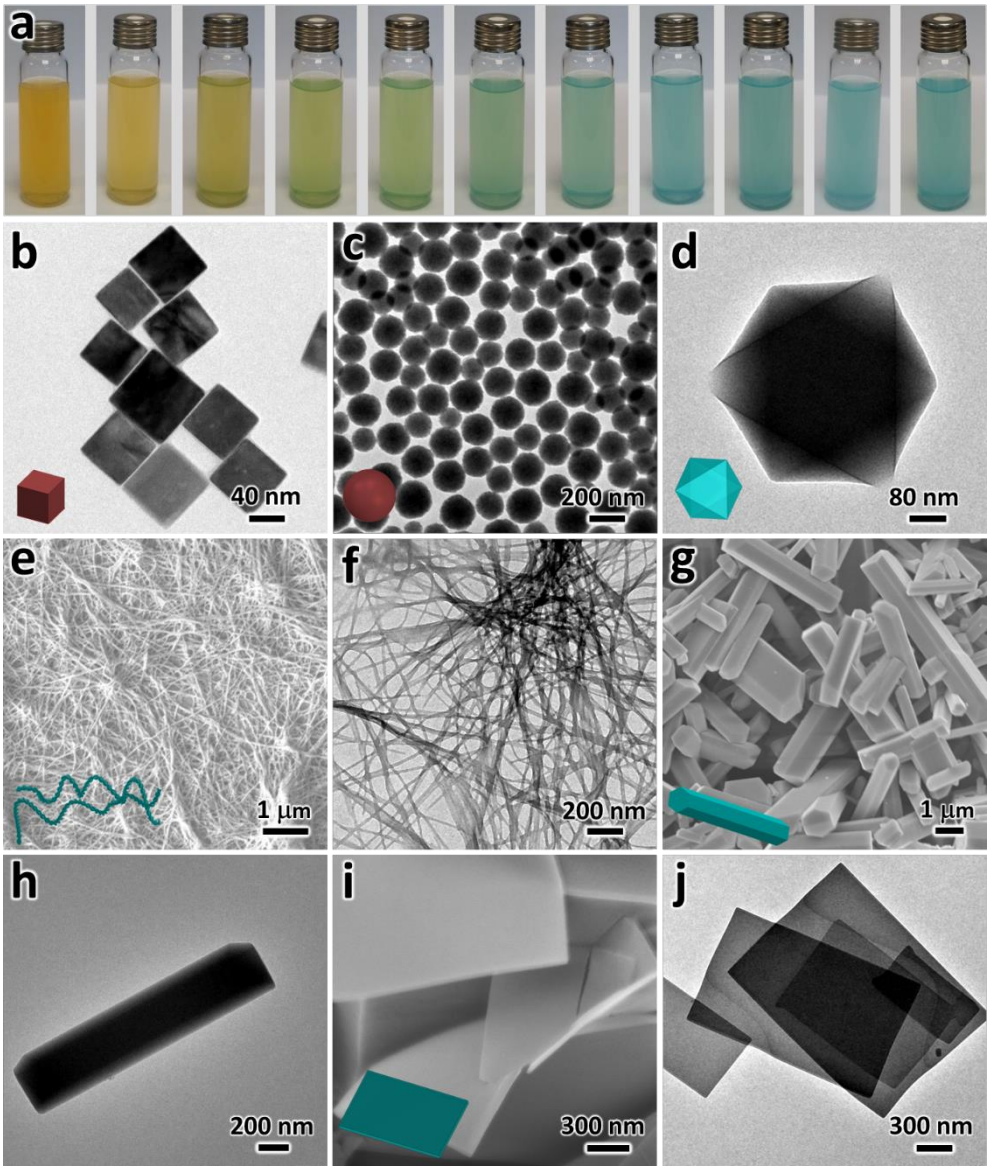

Figure 6.1 Fabrication of low-dimensional MOFs with assistance of solid Cu_2O: (a) color photographs of solutions illustrating the transformation of Cu_2O nanocubes to HKUST-1 at room temperature. Reaction time (left to right): 0 min, 30 min, 50 min, 70 min, 80 min, 90 min, 100 min, 140 min, 3 h, 7 h and 14 h. Sample morphologies (TEM or FESEM images): (b) Cu_2O nanocubes, (c) Cu_2O nanospheres, (d) HKUST-1 octahedrons, (e,f) Cu(HBTC)-1 nanofibers, (g,h) Cu(HBTC)-1 nanorods, and (i,j) Cu(HBTC)-1 nanosheets.

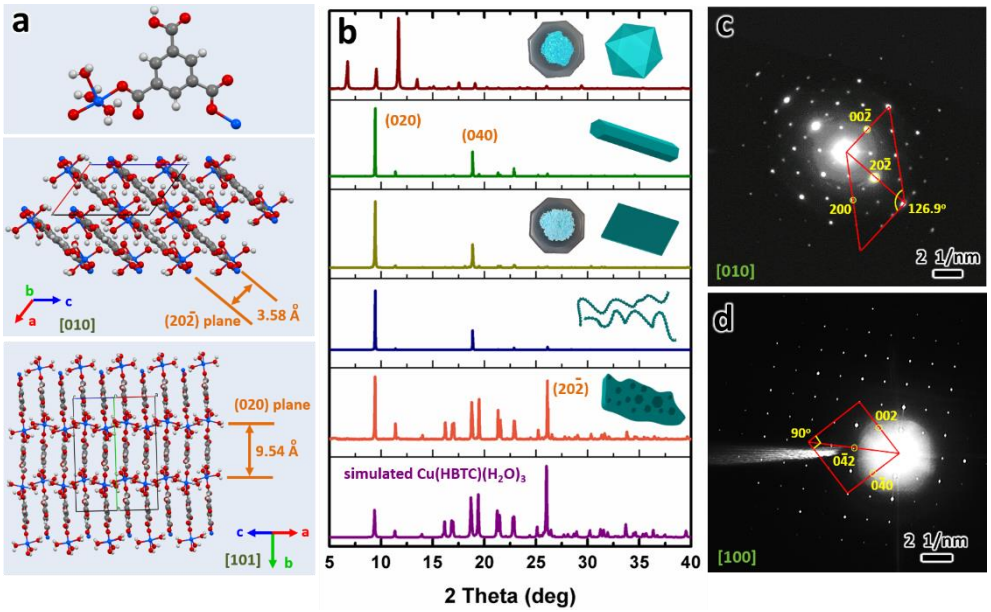

Figure 6.2 (a) Crystal structure of Cu(HBTC)-1: basic building unit, and projections of the crystal structure seen along the [010] and [101] directions, respectively. Small blue, red, gray and white spheres represent Cu, O, C and H atoms, respectively. Lattice fringes of 0.358 and 0.954 nm correspond to the (20-2) and (020) crystallographic planes of Cu(HBTC)-1. (b) XRD patterns and related MOF products (insets; refer to Scheme 6.1). (c,d) SAED patterns of Cu(HBTC)-1 single crystalline samples recorded along the [010] and [100] zone axes.

6.3.2. Shape control of Cu(HBTC)-1 (nanofibers, nanorods, and nanosheets)

Specifically, varying synthesis parameters boosts a morphological control over Cu(HBTC)-1. On the basis of a series of optimization experiments, we found that the ratios of Cu_2O/H_3BTC and water/ethanol are critical to determine the crystallization process and thus the shape, size, and topology of Cu(HBTC)-1 products. Figure 6.1e–j present our FESEM/TEM investigations on the samples prepared by mixing 10 mL of Cu_2O ethanolic suspension with different concentrations of H_3BTC (in ethanol) and PVP (in water) under stirring at room temperature and ambient pressure for 14 h. For example, to

prepare Cu(HBTC)-1 nanofibers, we needed to set mole ratio of Cu_2O to H_3BTC at 1 : 76 and the volume ratio of water to ethanol in their co-solvent at 1:0.43. The length of the nanofibers is typically longer than tens of micrometers, and the average diameter for each fiber is *ca.* 17 nm, which is much smaller than the reported MOFs with fiber shapes where the diameter is 300 nm or even in micrometer size.[16, 28] Alternatively, decreasing the amount of H_3BTC (mole ratio of Cu_2O/H_3BTC at 1:38), together with more ethanol (volumetric ratio of water/ethanol at 1:1.2), Cu(HBTC)-1 could be prepared into rod-like crystals with diameters ranging between 0.5 and 1.5 μm and lengths 1.5 and 7.0 μm. More interestingly, a further decreased amount of H_3BTC (*e.g.*, mole ratio of Cu_2O/H_3BTC as 1:19) gives rise to the growth of thin nanosheets with a rectangular shape at lateral dimensions of 0.7−2 μm. SEM/TEM images of Figures 6.1i,j reveal that the surfaces of Cu(HBTC)-1 nanosheets are very smooth. High-angle annular dark-field scanning TEM (HAADF-STEM) image in Figure 6.3a illustrates soft and highly flexible features of an isolated nanosheet, as evidenced in its slight surface bending. The AFM image in Figure 6.3b shows a few stacked nanosheets with a thickness around 6 nm, but some thicker nanosheets can also be found (in the range 30−55 nm). Generally speaking, the aspect ratio (*i.e.*, lateral dimensions versus thickness) of these nanosheets is very high, usually higher than 20.

Although they are comprised of identical Cu^{2+} ions and H_3BTC ligands, Cu(HBTC)-1 and HKUST-1 possess intrinsically different coordination

topologies. As illustrated in Figure 6.2a, in Cu(HBTC)-1, only two of the three carboxyl groups in H_3BTC act as ligands to Cu atoms, bridging them to give polymeric chains. That is to say, the H_3BTC linkers are partially deprotonated, this is the reason why the pH of Cu(HBTC)-1 suspension in water is around 5.0. The pK_a values of the fairly strong acid (H_3BTC) are 2.12, 3.89 and 4.70;[36] and thus it is not surprising that H_3BTC ligands could maintain one free carboxyl group when it coordinates with copper ions under our synthetic solution pH of *ca.* 3.1. Also, the zeta-potential measurement reveals the slightly negative charged surface of Cu(HBTC)-1 (-6.0 to -7.4 mV). The dry powder of Cu(HBTC)-1 is light blue, while that of the fully coordinated HKUST-1 is in blue (their powder samples are held in a mortar displayed in Figure 6.2b). The Cu^{2+} ion in Cu(HBTC)-1 adopts a distorted square-pyramidal coordination geometry involving two carboxylate O atoms and three water molecules, which is quite different from the di-copper "paddle-wheel" building units in HKUST-1.[31, 32] The crystals of our prepared $Cu(HBTC)(H_2O)_3$ are formed in a monoclinic system with a space group $P2_1/c$; a_o = 6.86 Å, b_o = 18.89 Å, c_o = 10.72 Å, and β = 126.9°.[31] As two of the carboxyl groups act as monodentate oxygen-donor ligands, polymeric zigzag chains are formed, which run along the ***b*** axis of crystal. They are connected into molecular sheets *via* weak intermolecular interactions (*e.g.*, hydrogen bond, π-π stacking, and van der Waals force), and neighboring sheets propagate into a supramolecular assembly (*i.e.*, nanosheets in our present case)

through connecting to each other by the intermolecular interactions too.[37] It is not surprising to see that Cu(HBTC)-1 nanosheets have small BET and Langmuir specific surface areas of only 16 and 22 m^2/g, respectively, which again validates the one dimensional polymeric structure depicted in Figure 6.2a. In addition, we found that the Cu(HBTC)-1 nanosheets were quite stable when they were stored in dry state even for four months.

Importantly, the out-of-plane XRD patterns in Figure 6.2b of the nanorod, nanosheet, and nanofiber samples (*i.e.*, fabricated by adding PVP surfactant) exclusively exhibit the (020) and the (040) diffraction peaks located at 2θ = 9.4° and 18.8° (d_{020} = 9.54 and d_{040} = 4.77 Å), respectively. This indicates that the nanosheets, nanorods, and nanofibers are all actually enclosed by {010} type facets. The appearance of the single crystal {010} facets would be somewhat encouraging, since different facets of nanocrystals possess distinctive electronic structures and catalytic properties.[38] Previous studies have shown that HKUST-1 can be selectively grown as single-crystalline thin films on some modified surfaces, generally by using self-assembled monolayer (SAM) techniques.[39-42] The growth orientation of HKUST-1 is strongly affected by the SAMs it contacted, usually it can be highly oriented along the [111] or [100] directions. In fact, the pronounced diffractions of (020) and (040) in our MOFs samples demonstrate that the crystal growth rate along the [010] axis (*i.e.*, the ***b*** axis) is suppressed, and the growth direction of the monoclinic Cu(HBTC)-1 is perpendicular to the [010], but along the [20-2]

(will be demonstrated in Figure 6.2c,d later) because of the angle between it and the [010] direction is 90°. Apparently, the shapes of Cu(HBTC)-1 products, nanosheet, nanofiber, and nanorod, were highly dependent on the presence of PVP, suggesting that the PVP serves as a capping agent to the {010} planes. According to the extensive literature reports, PVP molecules were frequently used in the shape control of colloidal metal or metal-oxide crystals, *via* preferential adsorption on a specific crystal facet and thus inhibit the growth of the facet.[17, 43] Accordingly, the preferential adsorptions of PVP mainly through its N–C=O groups on Cu(HBTC)-1 crystals should also be associated to the population of Cu^{2+} ions on different crystal planes, which is calculated to be number of metal atom/per unit of surface area.[9] The specific surface densities of Cu^{2+} ions are 1.0, 3.4, and 1.5 nm^{-2} for {100}, {010}, and {001} type facets, respectively. Because of the high surface density of metal ions on {010}, more PVP adsorbed on this set of facets is expected. Therefore, such a hindered growth would lead to their ultimate morphologies largely bounded by these crystal planes. The distance between the adjacent {020} planes is *ca.* 0.95 nm (Figure 6.2a), which implies that a thin nanosheet with thickness of 6 nm only owns six metal-ligand molecular slabs. Thus, we affirmed that the Cu(HBTC)-1 has been indeed prepared into 2D nanostructures with a dimension less than 10 nm.

The single crystal nature of the prepared Cu(HBTC)-1 was also illustrated by selected-area electron diffraction (SAED) analysis in Figure 6.2c,d. The

sharp SAED pattern in Figure 6.2c was measured for the [010] spot zone (*i.e.*, the electron beam injected along the ***b***-axis), displaying the diffraction pattern of the {*h0l*} planes of a nanosheet. The angle between the (200) and (00-2) spots is 126.9°, matching well with the angle β of the monoclinic crystal structure. Therefore, the nanosheets preferentially grow along the ***a-c*** direction and the flat top and bottom surfaces are bounded by the {010} planes. Likewise, when the electron beam was along the ***a***-axis of a nanorod, both {010} and {001} diffraction spots could be imaged (Figure 6.2d).

As shown in Figure 6.3c, for the Cu(HBTC)-1 samples, the characteristic XPS peak of Cu $2p_{3/2}$ is observed at 934.5 eV, together with the presence of the well-known "shake-up satellites" at 939.2 and 943.5 eV, indicating the presence of divalent Cu(II) species.[44] Fitting the C 1*s* spectrum reveals two surface components which can be assigned to hydrocarbon C–C (284.5 eV) and the carboxylate carbon –COO (288.4 eV). Deconvoluting O 1*s* spectrum shows two surface species, one from –C=O/–OH (531.4 eV) and the other from C–O–Cu (532.9 eV).[45] In comparison, XPS peak of Cu $2p_{3/2}$ is observed with a single peak at 931.7 eV in the Cu_2O template. The results confirm that Cu^+ ions are oxidized completely during the reaction. Similar conclusion can be drawn from the fabrication of HKUST-1 from Cu_2O. To determine whether the shape of Cu_2O templates is a key factor for determining the geometric shape of Cu(HBTC)-1, we also conducted a control experiment using spherical shaped Cu_2O for the synthesis of Cu(HBTC)-1. It was found that

perfect nanosheets of Cu(HBTC)-1 were also obtained regardless of starting shape of Cu_2O. Obviously, we believe that all the Cu_2O precursors eventually become Cu^+ ions during the synthesis. Nevertheless, we replaced Cu_2O template with (divalent) CuO nanoparticles in order to understand the function of Cu^+. Under otherwise identical synthetic conditions as those used for the samples of Figure 6.3, however, the nanosheets could no longer be obtained, where the MOF products have an irregular shape totally different from those of Figures 6.1–3 (no preferential growth was found even though the PVP was present). Therefore, the starting Cu^+ solution is essential to promote the growth of oriented Cu(HBTC)-1 crystals instead of HKUST-1. Presumably, a slow oxidation of Cu^+ to Cu^{2+} and thus a gradual release of Cu^{2+} ions in the synthetic process provide an adequate time for PVP to regulate the orientated growth (Figure 6.3). Therefore, the usage of solid-state Cu_2O as a metal ion source actually plays a kinetic role to adjust the coordination behaviors of a targeted MOF. Although metal ions can also be slowly released from the electrode in the electrosynthesis of MOFs (*e.g.*, anodic dissolution), the metal ions are only delivered near the electrode surface instead of the whole solution, and therefore, shape-controlled MOFs *via* electrosynthesis were rarely reported.[46]

We further investigated thermal stabilities of HKUST-1 and Cu(HBTC)-1 using TGA, revealing that the two coordination frameworks are stable up to 300°C. At temperatures higher than 300°C, a sharp weight loss takes place,

due to decomposition of tricarboxylic linker, giving rise to CuO-Cu_2O as final products.[29] Moreover, the TGA profiles further confirm the mole ratios of copper to organic ligands are 1:1 and 3:2 respectively in Cu(HBTC)-1 and HKUST-1, consistent with their chemical formulas. The presence of the copper coordination (*e.g.*, C–O–Cu stretching band) in both MOFs was confirmed by means of FTIR. The characteristic FTIR bands belong to free protonated acid groups (*e.g.*, C=O and C–OH combination bands) are also found in our Cu(HBTC)-1, whereas they are absent in the HKUST-1 sample.[47] Moreover, energy-dispersive X-ray (EDX) elemental maps of Cu(HBTC)-1 sample in Figure 6.3d indicate that Cu, O, and C are distributed evenly across entire nanosheets.

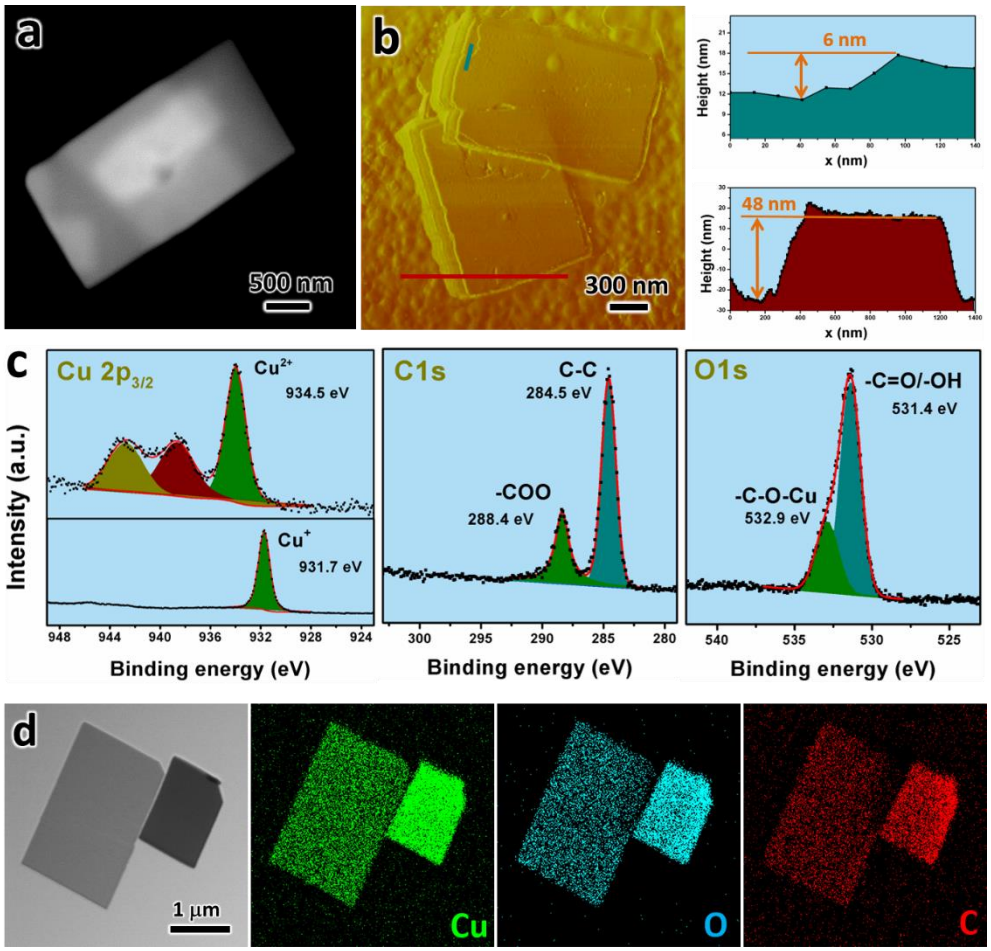

Figure 6.3 Characterization of Cu(HBTC)-1 nanosheets: (a) HAADF-STEM image of a single nanosheet, (b) AFM image (phase mode) of several stacked nanosheets on a silicon wafer substrate, and their height mode profiles with color-coded red and blue, were measured along the corresponding tracks shown in the AFM image. (c) XPS core-level spectra of the nanosheets in Cu $2p_{3/2}$, C 1*s*, and O 1*s* regions respectively, in comparison with the Cu $2p_{3/2}$ spectrum of Cu_2O template (bottom: Cu^+). (d) TEM and EDX elemental map images of two nanosheets.

6.3.3. Doping divalent transition metal ions into Cu(HBTC)-1

Attempts were also made on doping other divalent transition metal ions into the Cu(HBTC)-1.[48] For instance, addition of $Zn(NO_3)_2$ or $Co(NO_3)_2$ (mole ratio of Cu/dopants = 1:2) in the synthetic solution will produce zinc or cobalt-substituted Cu(HBTC)-1. The inclusion of such dopants in Cu(HBTC)-1 was

verified by elemental analyses. As reported in Figure 6.4a,b, some changes in the MOF shapes were found: the plate-like Cu(HBTC)-1 became thicker which means that the aspect ratio of the nanosheets gets reduced. Thus, these products are denoted as nanocuboids (Structure 6 in Scheme 6.1). The metal-substituted Cu(HBTC)-1 are isoreticular to the Cu(HBTC)-1, since they share identical XRD patterns. Similar to other alternative metal substituted MOFs,[48] the dopant content in the obtained zinc or cobalt substituted Cu(HBTC)-1 is much lower than that in its initial feed solution. For example, the Zn/Cu and Co/Cu atomic ratios in the metal-substituted Cu(HBTC)-1 were 1:50, and 1:34, respectively (EDX). This doping method enables us to modify Cu(HBTC)-1 to prepare a wider range of catalyst precursors.

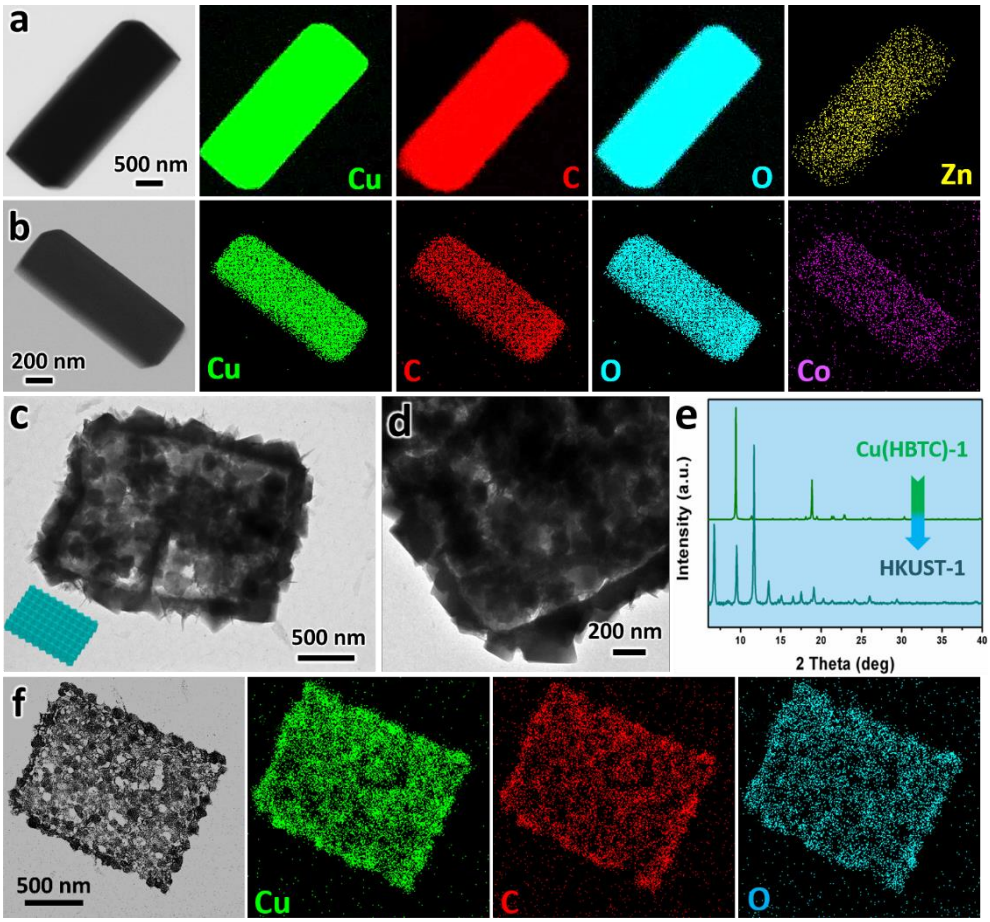

Figure 6.4 Transition metal doped Cu(HBTC)-1 nanocuboids: (a) EDX elemental map images of a Zn-doped Cu(HBTC)-1, and (b) EDX elemental map images of a Co-doped Cu(HBTC)-1. Transformation of Cu(HBTC)-1 nanosheets to 2D assemblage of HKUST-1 (see Scheme 6.1, Structure 10): (c,d) TEM images, (e) XRD patterns, and (f) EDX elemental map images.

6.3.4. Reconstruction of Cu(HBTC)-1 nanosheets into HKUST-1

Although many MOF materials, including HKUST-1, suffer certain degradation by water or humidity,[30] the Cu(HBTC)-1 powders remained stable after re-dispersion in aqueous solution. In addition, we found that the Cu(HBTC)-1 can undergo a slow structural transformation into high-quality HKUST-1 upon soaking them in ethanol at room temperature for a period of 1 to 3 days. It is inferred that the polymeric chains in Cu(HBTC)-1 are stretchable due to the distortable coordination geometry of the metal centers, and the use of external solvent (*i.e.*, ethanol) would disturb the hydrogen bonding within the Cu(HBTC)-1 and help its divalent $HBTC^{2-}$ deprotonate further, which leads to the production of trivalent BTC^{3-} ligands for coordination to nearby Cu^{2+} ions.[30] We also observed that the solvent-induced crystal transformation is irreversible, similar to other reported MOFs showing single-crystal-to-single-crystal transformation.[49, 50] Upon such a structural reconstruction to HKUST-1, however, shape alternation occurred. Interestingly, HKUST-1 can also be prepared into a platelet form after calcining Cu(HBTC)-1 nanosheets at 200°C (Note that Cu(HBTC)-1 decomposes at 300°C) for 10 h, and soaking the calcined sample in ethanol for 3 h. The transformation to phase pure HKUST-1 at room temperature is quite

fast (XRD; Figure 6.4e). Importantly, the reconstructed HKUST-1 (Structure 10 in Scheme 6.1) can retain the morphological integrity as nanoplates (TEM results in Figure 6.4c; and EDX elemental maps in Figure 6.4f). As shown in Figure 6.4d, the edges of each nanoplate are arrayed with multiple octahedral crystals of HKUST-1. In this two-step process, the heat pretreatment likely causes the Cu(HBTC)-1 nanosheets become more rigid (*i.e.*, less structural defects) for reconstruction, which allows more localized nucleation and growth of HKUST-1 in ethanol, resulting in the observed polycrystalline plate-like morphology.

6.3.5. Catalytic functionalization of Cu(HBTC)-1 nanosheets

Among the MOFs we synthesized above, geometric shape of the 2D Cu(HBTC)-1 nanosheets is especially attractive as it is very open and with only a few molecular slabs in thickness. In terms of materials utilization, such a crystal-morphology is highly desirable since it has a very high surface-to-bulk ratio for catalytic applications. In this work, we have treated the Cu(HBTC)-1 nanosheets both as a catalyst precursor for preparing copper-containing nanocatalysts (Structures 7, 8 and 9 in Scheme 6.1) and as a catalyst support for loading noble metal nanoparticles (Structure 11 in Scheme 6.1).

6.3.5.1. Conversion of Cu(HBTC)-1 nanosheets into inorganic catalysts

Firstly, the Cu(HBTC)-1 nanosheets can serve as a self-templating solid to generate CuO or CuO-Cu_2O nanocomposites. For instance, after heat-treated at 275°C in static air, the Cu(HBTC)-1 nanosheets were transformed to CuO powder (XRD, Figure 6.5f; and SAED, Figure 6.5b). The formation of copper oxides was also accompanied by the color change from the original light blue to black. From the HAADF-STEM image of Figure 6.5a, we can see that the surface of product became less smooth after the heat-treatment. Remarkably, the CuO assemblage could still maintain the platelet morphology; no obvious shrinkage was observed. A high-resolution TEM (HRTEM) image (Figure 6.5c) clearly shows lattice fringes with an inter-planar distance of 0.23 nm that corresponds to the {111} planes of monoclinic CuO. The average size of CuO crystallites is 8.2±1.8 nm. EDX elemental maps in Figure 6.5d further confirm total removal of carbon elements upon the calcinations in air and the formation of copper oxides. In comparison, porous CuO-Cu_2O composite oxides were also synthesized by annealing Cu(HBTC)-1 nanosheets at 300°C in static air. The plate-like morphology was still kept, with random pin-holes (Figure 6.5e). The XRD results indicate the presence of both CuO and Cu_2O phases in this sample, and the relative contents of Cu_2O and CuO are *ca.* 41 and 59 wt%, respectively (Figure 6.5f). The average size of CuO and Cu_2O crystallites in the composites is 20±4 nm. Therefore, the calcination under static air allows a controlled synthesis of sheet-like biphasic copper oxides.

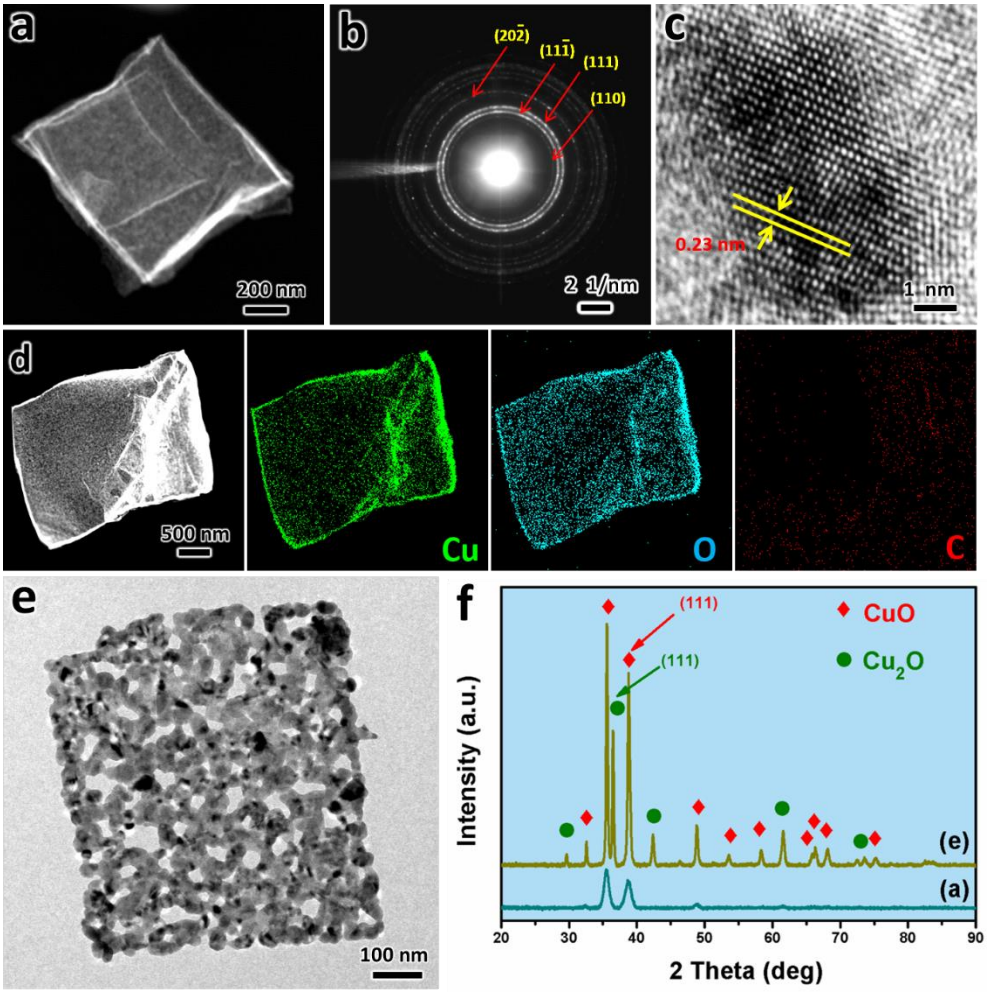

Figure 6.5 Heat-treatments of MOFs in static air: (a) HAADF-STEM image of a CuO nanosheet by heating Cu(HBTC)-1 nanosheet at 275°C in static air for 3 h, (b) SAED pattern recorded from the nanosheet in (a), (c) HRTEM image of a single CuO nanocrystal in (a), (d) EDX elemental map images of a CuO nanosheet, (e) representative TEM image of a porous CuO-Cu_2O platelet obtained by heating Cu(HBTC)-1 nanosheet at 300°C in static air for 3 h, and (f) XRD patterns of the samples shown in (a) and (e).

6.3.5.2. Fabrication of 2D supported copper nanocatalysts from Cu(HBTC)-1 nanosheets

It should be mentioned that the Cu^{2+} ions in Cu(HBTC)-1 nanosheets can also be reduced to copper nanoparticles with size of *ca.* 4 nm during our HRTEM measurements. On the basis of this *in-situ* reduction, we believe that obtaining

supported copper nanocatalysts through more practical reduction routes should also be possible, because of low standard reduction potential of Cu^{2+}/Cu^{0} (0.34 V).[51] In particular, by using Cu(HBTC)-1 nanosheets as the single source precursor, copper ions can be reduced on-site to copper nanoparticles, whereas the remained organic framework can serve as a support (mainly as carbon) to disperse and stabilize the metallic nanoparticles. Indeed, we found that carbon-supported copper catalysts could be prepared from thermal reduction of Cu(HBTC)-1 nanosheets under controlled atmospheres, *e.g.*, pure H_2, or H_2/Ar, or ethanol-vapor/Ar, or simply an Ar stream, where the $HBTC^{2-}$ linkers can also serve as a reducing agent (Figure 6.6).

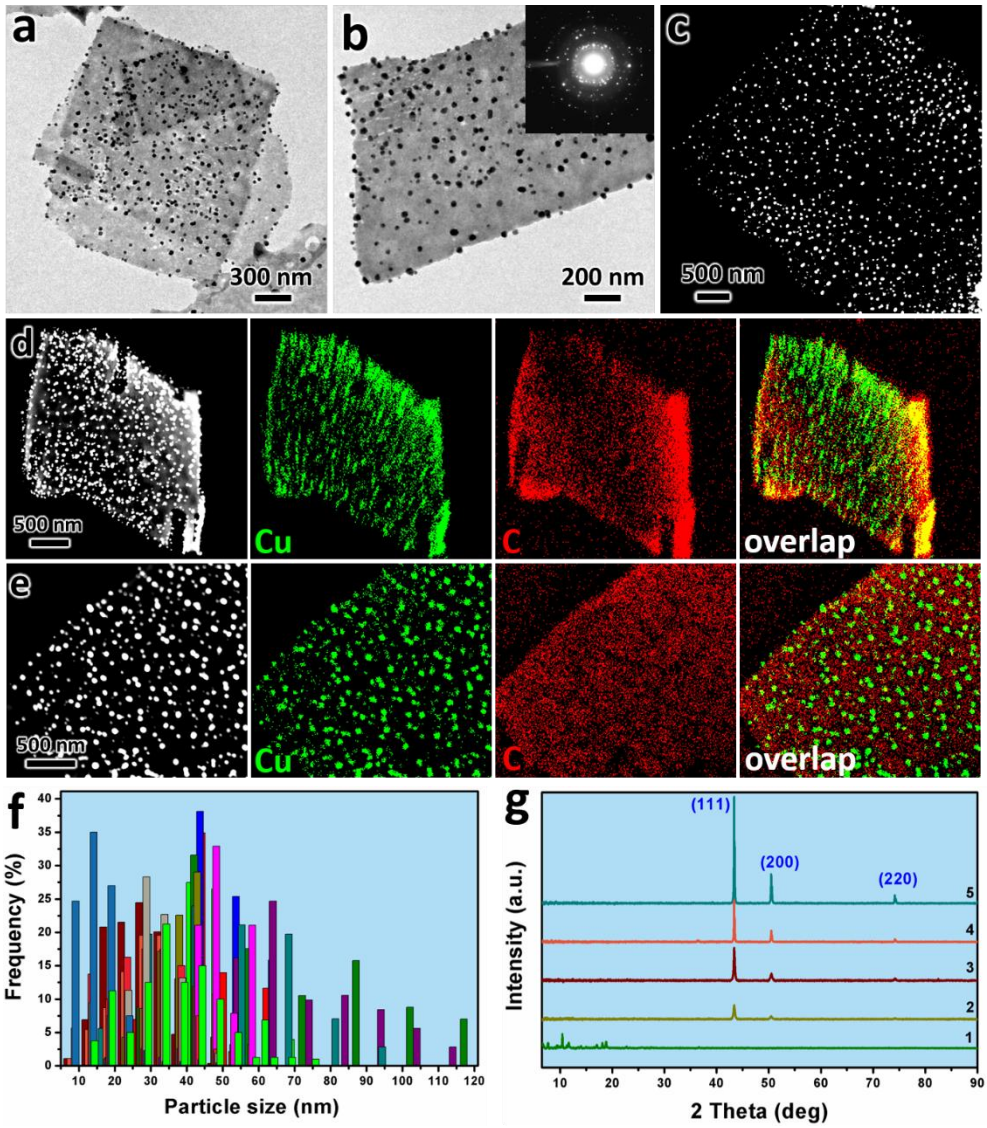

Figure 6.6 Heat treatments of MOFs under reducing or inert atmosphere: (a-c) TEM/HAADF-STEM images of the heated Cu(HBTC)-1 nanosheets under diluted H_2 (Ar/H_2 (45/5)) flowing at 280°C for 70 min (inset of (b) is its SAED patterns), (d,e) EDX elemental map images of two representative Cu(HBTC)-1 nanosheets after the similar heat treatment, (f) size distribution histograms of copper nanoparticles on the derived nanocatalysts (different colors represent different heating conditions), and (g) XRD patterns of the products prepared by heating Cu(HBTC)-1 nanosheets under different processing conditions: (1) Ar/H_2 (45/5) flowing at 250°C for 3 h, (2) Ar/H_2 (45/5) flowing at 275°C for 2 h, (3) ethanol-vapor/Ar (70) flowing at 270°C for 2.5 h, (4) Ar/H_2 (45/5) flowing at 300°C for 2 h, (5) pure Ar (50) flowing at 300°C for 3 h; numbers in parentheses indicate the flowing rates of the gas steam in mL/min.

We also investigated the effect of calcination conditions, including temperature, time, and heating rate on copper nanoparticles. Although the

thermolysis in Ar can produce pure metal nanoparticles, the size of the resultant particles is as large as 310±23 nm, which is unfavorable for catalysis.[52] Nevertheless, the calcination under H_2/Ar or ethanol-vapor/Ar atmosphere would lead to much smaller copper nanoparticles. Importantly, under optimized conditions, overall nanocatalysts could inherit the sheet-like morphology of solid precursor. As revealed in Figure 6.6a-c, each nanosheet contains multiple polycrystalline Cu nanoparticles that are supported, yet well dispersed on the surface. However, on increasing the temperature and time, Cu nanoparticles become severely aggregated. For example, at 300°C for 2 h, the size of copper is 65±26 nm; many holes are found on the substrates. By changing conversion condition, the size of supported Cu can be tuned in the range of 10 to 120 nm. In Figure 6.6f, results from a total of 14 sets of experiments are summarized. Exemplified in the EDX mappings of Figure 6.6d,e, copper nanoparticles are distributed evenly over a 2×2 μm^2 nanosheet and a 3×5 μm^2 nanosheet respectively. The formation of supported copper catalysts was also confirmed by XRD techniques (Figure 6.6g; three marked XRD peaks belong to metallic copper). After this calcination-reduction, it should be noted that the carbon-related materials originated from the $HBTC^{2-}$ ligands disperse and stabilize the copper products. About 46% of the total surface carbon is graphitic (C 1*s* spectrum; its binding energy at 284.6 eV), and remainders are carboxylic and hydroxyl functional groups.[53]

Compared to catalysts with other shapes, inherent advantage of these MOF-derived catalysts is that metal nanoparticles are mostly on the exterior surface of 2D supports. Therefore they are more readily accessible for catalytic species than the conventional copper immobilized catalysts. Since copper is one of the most active components for CO_2 hydrogenation,[54-56] we further evaluated the activity of our catalyst (mean copper size 15±7 nm) toward this reaction. A maximum CO_2 conversion of 10.2% was obtained for the catalysts at 300°C and 3 MPa. Methanol and CO are the two main products *via* exothermic reaction $CO_2 + 3H_2 \rightarrow CH_3OH + H_2O$ ($\Delta H_{298\,K} = -49.5$ kJ· mol^{-1}) and endothermic reaction $CO_2 + H_2 \rightarrow CO + H_2O$ ($\Delta H_{298\,K} = 41.2$ kJ·mol^{-1}). Therefore, an increase in reaction temperature facilitates the CO_2 activation but goes against the synthesis of methanol, based on thermodynamics. Indeed, we found that at a very low conversion of CO_2 (1.1%), the selectivity to methanol was >90% at 230°C and 3 MPa, while the selectivity toward methanol decreased to 25.7% and remarkably higher specific activity of 5.3 mole $CO_2 \cdot kg_{cat}^{-1} \cdot h^{-1}$ (*i.e.*, CO_2 conversion of *ca.* 10%) was achieved at 300°C and 3 MPa. We also observed that the 2D catalyst with large sized copper (*e.g.*, 67±22 nm) showed poor performance for the reaction, as the specific activity of 1.9 mole $CO_2 \cdot kg_{cat}^{-1} \cdot h^{-1}$ was measured at 300°C and 3 MPa. From the catalytic data, we can see a good workability of our 2D-MOF-derived supported copper catalysts.[55] To date, only few MOF materials have been exploited for CO_2 hydrogenation, and the preparative procedures of catalysts

are mostly complicated. The active copper sites were all generated from the foreign ions rather than the intrinsic metal ions within MOF matrices in our present study. For example, Cu@MOF-5 catalyst for methanol synthesis was prepared in a two-step process by first gas-phase infiltration of volatile organocopper precursors ([CpCuL] (L = PMe_3, CN^tBu)) with MOF-5 and followed by hydrogenolysis at 200−220°C.[57] In another report, the conversion of CO_2 to formic acid was performed on Cu-alkoxide-functionalized MOF-5 (Cu-MOF-5), in which the MOF-5 linkers were first modified with hydroxyl groups; then, the protons of the hydroxyl group were exchanged by copper cations via solution methods.[58] In contrast, our supported 2D copper catalysts can be obtained facilely from direct reduction of Cu(HBTC)-1 nanosheets in one single step, and the size of copper is adjustable depending on simple process conditions.

6.3.5.3. Anchoring metal nanoparticles on the external surfaces of Cu(HBTC)-1 nanosheets

Furthermore, we have also developed a surfactant-free approach for fabrication of a series of Cu(HBTC)-1 nanosheets supported noble metal nanocatalysts (Structure 11 in Scheme 6.1). Monometallic, bimetallic, or trimetallic noble-metal nanoparticles with uniform sizes were successfully immobilized on the nanosheets, including Au, Ag, Pt, Pd, $Au_{0.4}Pt_{0.6}$, $Au_{0.4}Pd_{0.6}$, and $Au_{0.3}Pt_{0.3}Pd_{0.4}$. We started with introducing Au nanoparticles on the

exterior surface of Cu(HBTC)-1 nanosheets. As revealed from TEM (Figure 6.7a,c) and HAADF-STEM (Figure 6.7b) images of Au/Cu(HBTC)-1 catalysts, we found that a large number of Au nanoparticles with a mean size of 2.6±0.6 nm were highly dispersed. A HRTEM image in Figure 6.7d shows that the lattice fringe of Au nanoparticle is approximately 0.234 nm consistent with the d_{111} value of gold. XPS investigation (Figure 6.7e) reveals that all the Au nanoparticles exist as metallic Au^0, as the Au $4f_{7/2}$ and Au $4f_{5/2}$ peaks appeared at 83.9 eV and 87.6 eV, respectively. The XRD characteristic peaks of gold were indistinguishable due to low metal loading (3.61 wt%) and ultrafine metal size.[59] Moreover, the presence of gold nanoparticles can also be visually verified by the pink color of product, different from the blue color of pristine MOFs (inset of Figure 6.7f). Both the product morphology and the crystal structure of Cu(HBTC)-1 nanosheets were preserved after introduction of noble metals (XRD, Figure 6.7f; and SAED, inset of Figure 6.7a). Again, results from EDX elemental mapping (Figure 6.7g) confirm the presence of gold nanoparticles on the nanosheets. Because no surfactant was used in synthesis, naked metal nanoparticles should be able to interact with tangling surface carboxylic groups in Cu(HBTC)-1 (particularly the free carboxylic groups in $HBTC^{2-}$ ligands), preventing them from growth. In contrast, additional surfactants, such as PVP or MPA,[9, 10, 60] had been frequently used for the reported NPs/MOFs (NPs = nanoparticles), in order to protect nanoparticles against aggregations.

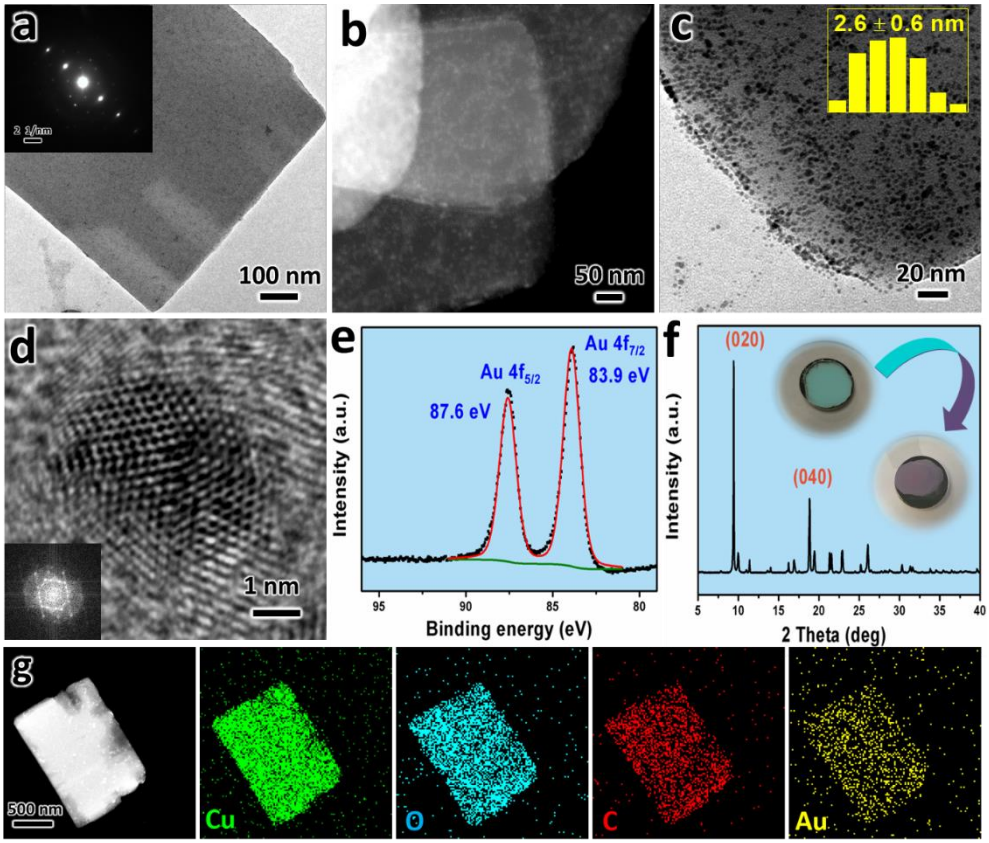

Figure 6.7 Characterization of supported catalyst Au/Cu(HBTC)-1: (a) TEM image (inset: the related SAED pattern), (b) HAADF-STEM image, (c) TEM image (inset: size distribution of Au nanoparticles), (d) HRTEM image (inset: the related FFT-image), (e) XPS spectrum of Au 4*f*, (f) XRD pattern (insets: color photographs of the samples before and after loading Au nanoparticles), and (g) EDX elemental map images.

Along the similar line, attachments of other six noble metals (*i.e.*, Ag, Pt, Pd, $Au_{0.4}Pt_{0.6}$, $Au_{0.4}Pd_{0.6}$ and $Au_{0.3}Pt_{0.3}Pd_{0.4}$) on the Cu(HBTC)-1 nanosheets were also demonstrated. As shown in Figure 6.8a-f, all the nanoparticles are uniformly supported on the thin nanosheets, and the metal nanoparticles have a narrow size range of 1 to 4 nm, except for the Ag nanoparticles (8.7±2.8 nm), revealing that the Cu(HBTC)-1 nanosheets successfully restrict the rapid growth of metals.[61] When used as catalysts, importantly, the obtained NPs/Cu(HBTC)-1 have much shorter diffusion length for substrates than those

immobilized within the interior cavities of MOFs.[62] In particular, EDX results of trimetallic ($Au_{0.3}Pt_{0.3}Pd_{0.4}$)/Cu(HBTC)-1 catalysts (Figure 6.8g) indicate that the all the added metals (Au, Pt, and Pd) are uniformly distributed across the nanosheets. In fact, simultaneous mixing of Au precursors with Pt and/or Pd precursors leads to the formation of bimetallic or trimetallic nanoparticles on the Cu(HBTC)-1 supports, due to the metal halide anions ($AuCl_4^-$, $PtCl_4^{2-}$, and $PdCl_4^{2-}$) are all negatively charged, together with similar reduction potentials.[63] However, the mixing of Au and Ag precursors only lead to the formation of two segregated nanoparticles, which is probably caused by the difference in electrical charges of the two metal precursors.

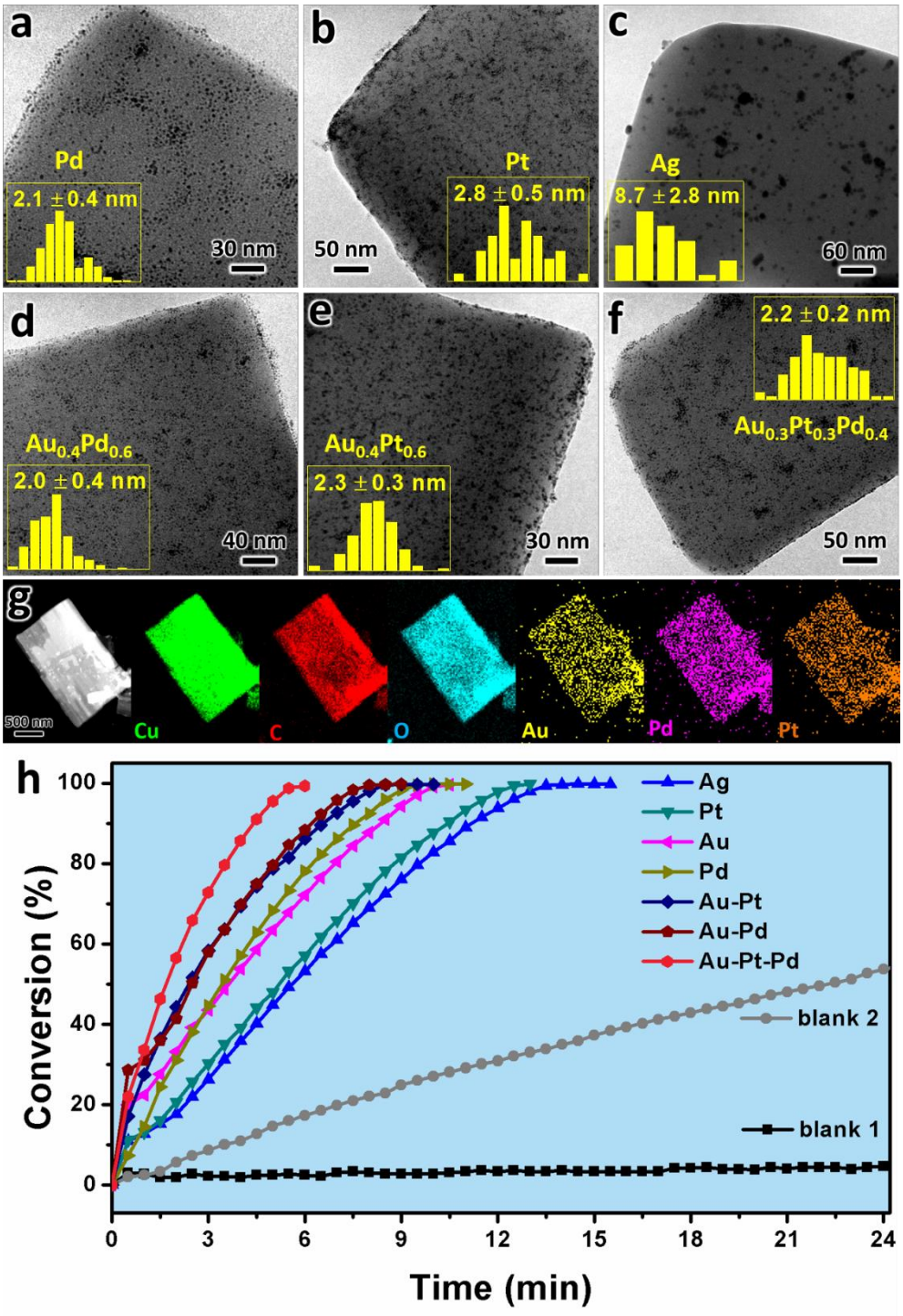

Figure 6.8 Characterization of other NPs/Cu(HBTC)-1 supported catalysts and their catalytic applications: (a) Pd/MOFs, (b) Pt/MOFs, (c) Ag/MOFs, (d) $Au_{0.4}Pd_{0.6}$/MOFs, (e) $Au_{0.4}Pt_{0.6}$/MOFs, (f) $Au_{0.3}Pt_{0.3}Pd_{0.4}$/MOFs, (g) EDX elemental map images of ($Au_{0.3}Pt_{0.3}Pd_{0.4}$)/Cu(HBTC)-1, and (h) Conversion as a function of time in reduction of 4-NP over seven different Cu(HBTC)-1 supported catalysts, where *blank 1* represents the experiment without using any catalyst, and *blank 2* represents the experiment using pristine Cu(HBTC)-1 as catalyst. Insets in (a-f) show the statistics of particle size of the respective noble metals.

Apart from the gas-phase catalysis (CO_2 hydrogenation), we also carried out solution-phase catalysis in this work, considering that Cu(HBTC)-1 nanosheets are quite stable in aqueous solution (as discussed above). In particular, the reduction of 4-nitrophenol (4-NP) to 4-aminophenol (4-AP) by $NaBH_4$ in water was used as a model reaction to investigate the catalytic performance of the above NPs/Cu(HBTC)-1 supported catalysts. The reduction mixture was on-line monitored by UV-Vis absorption spectroscopy (Figure 6.8h). As expected, the reaction did not proceed without a catalyst and proceeded very slow in the presence of pristine Cu(HBTC)-1 nanosheets. However, the reaction rate greatly enhanced as NPs/Cu(HBTC)-1 was used. This reaction can be considered as a pseudo-first-order reaction. Accordingly, the rate constants using different metal catalysts were determined in the following order: Ag (0.174 min^{-1}) < Pt (0.182 min^{-1}) < Au (0.224 min^{-1}) < Pd (0.269 min^{-1}) < $Au_{0.4}Pt_{0.6}$ (0.313 min^{-1}) < $Au_{0.4}Pd_{0.6}$ (0.374 min^{-1}) < $Au_{0.3}Pt_{0.3}Pd_{0.4}$ (0.478 min^{-1}). In general, multimetallic catalysts have much higher catalytic activities than the monometallic catalysts. For instance, the combination of Pd or Pt with Au, could increase the reaction rate by 40% and 67%, respectively. Among them, trimetallic ($Au_{0.3}Pt_{0.3}Pd_{0.4}$)/Cu(HBTC)-1 has the highest catalytic activity with a rate constant of 0.478 min^{-1} (nearly 2.1 times of the data from pure Au catalyst), due to strong synergistic effects among the different metals.[61, 64, 65]

6.4. Conclusions

In summary, we have devised a shape-controlled method for fabrication of a series of low-dimensional copper containing MOF crystals using Cu_2O nanoparticles as a copper source. The utilization of solid-state metal ion source not only prompts the crystallization of MOFs at mild conditions (such as room temperature and ambient pressure), but also leads to highly anisotropic growth of the MOFs *via* kinetically adjusting coordination behaviors. Our investigation also indicates that inclusion of PVP in synthesis is another key factor to obtain single-crystalline Cu(HBTC)-1 with low dimensions (*e.g.*, nanosheets, nanofibers, nanorods, and nanocuboids). The obtained Cu(HBTC)-1 can be viewed as a pre-phase compound of HKUST-1, as it can be irreversibly transformed into high quality HKUST-1 when soaking them in ethanol at room temperature. The copper ions in the Cu(HBTC)-1 can also be replaced by other transition metal ions. For instance, nanocuboids containing other transition metal elements (*e.g.*, Co or Zn) have been prepared. More importantly, the Cu(HBTC)-1 nanosheets can serve as a single-source solid precursor or an ideal support for nanocatalyst fabrication. In this work, on one hand, we have converted them into several copper based nanocatalysts (*e.g.*, CuO, or CuO-Cu_2O, or even Cu). As an example, in a H_2/Ar atmosphere, Cu^{2+} ions of the Cu(HBTC)-1 nanosheets could be reduced to Cu metal with an average particle size of 15±7 nm on openly accessible surfaces. The copper nanoparticles are distributed evenly over sheet-like carbon supports which were derived from the organic linkers of the original framework. On the other

hand, also importantly, our Cu(HBTC)-1 nanosheets can be used as a versatile support for formation and immobilization of various noble metal nanoparticles (*e.g.*, Au, Ag, Pt, Pd, $Au_{0.4}Pt_{0.6}$, $Au_{0.4}Pd_{0.6}$ and $Au_{0.3}Pt_{0.3}Pd_{0.4}$), due to capping roles of the free carboxylic groups in Cu(HBTC)-1. To demonstrate their workability, the MOFs-derived copper-based catalysts have been tested for gas phase CO_2 hydrogenation reaction, which showed a good catalytic performance. And the noble metal deposited MOFs (*viz.*, NPs/Cu(HBTC)-1, Figures 6.7 and 6.8) exhibited excellent catalytic activities for liquid phase reduction of 4-nitrophenol. As reported herein, the transformation of Cu(HBTC)-1 nanosheets into supported metal nanocatalysts would help open up new possibilities to make shape-controlled MOFs with low crystal dimensions for heterogeneous catalysis applications.

6.5. References

1. H.-C. Zhou, J. R. Long and O. M. Yaghi, *Chem. Rev.*, 2012, **112**, 673-674.

2. C. He, K. Lu, D. Liu and W. Lin, *J. Am. Chem. Soc.*, 2014, **136**, 5181-5184.

3. J. Lee, O. K. Farha, J. Roberts, K. A. Scheidt, S. T. Nguyen and J. T. Hupp, *Chem. Soc. Rev.*, 2009, **38**, 1450-1459.

4. E. Pérez-Mayoral and J. Čejka, *ChemCatChem*, 2011, **3**, 157-159.

5. H. B. Wu, B. Y. Xia, L. Yu, X.-Y. Yu and X. W. Lou, *Nat. Commun.*, 2015, **6**, 6512.

6. L. E. Kreno, K. Leong, O. K. Farha, M. Allendorf, R. P. Van Duyne and J. T. Hupp, *Chem. Rev.*, 2012, **112**, 1105-1125.

7. K. Schlichte, T. Kratzke and S. Kaskel, *Microporous Mesoporous Mater.*, 2004, **73**, 81-88.

8. G. Lu, S. Li, Z. Guo, O. K. Farha, B. G. Hauser, X. Qi, Y. Wang, X. Wang, S. Han, X. Liu, J. S. DuChene, H. Zhang, Q. Zhang, X. Chen, J. Ma, S. C. J. Loo, W. D. Wei, Y. Yang, J. T. Hupp and F. Huo, *Nat. Chem.*, 2012, **4**, 310-316.

9. Z. Li and H. C. Zeng, *Chem. Mater.*, 2013, **25**, 1761-1768.

10. Z. Li and H. C. Zeng, *J. Am. Chem. Soc.*, 2014, **136**, 5631-5639.

11. L. Peng, J. Zhang, Z. Xue, B. Han, J. Li and G. Yang, *Chem. Commun.*, 2013, **49**, 11695-11697.

12. R. Wu, X. Qian, F. Yu, H. Liu, K. Zhou, J. Wei and Y. Huang, *J. Mater. Chem. A*, 2013, **1**, 11126-11129.

13. H. Hu, B. Guan, B. Xia and X. W. Lou, *J. Am. Chem. Soc.*, 2015, **137**, 5590-5595.

14. Y. Lü, W. Zhan, Y. He, Y. Wang, X. Kong, Q. Kuang, Z. Xie and L. Zheng, *ACS Appl. Mater. Interfaces*, 2014, **6**, 4186-4195.

15. J. Zhao, M. Li, J. Sun, L. Liu, P. Su, Q. Yang and C. Li, *Chem. - Eur. J.*, 2012, **18**, 3163-3168.

16. S. Zhang, H. Liu, C. Sun, P. Liu, L. Li, Z. Yang, X. Feng, F. Huo and X. Lu, *J. Mater. Chem. A*, 2015, **3**, 5294-5298.

17. A. R. Tao, S. Habas and P. Yang, *Small*, 2008, **4**, 310-325.

18. L. H. Wee, M. R. Lohe, N. Janssens, S. Kaskel and J. A. Martens, *J. Mater. Chem.*, 2012, **22**, 13742-13746.

19. E. A. Flugel, A. Ranft, F. Haase and B. V. Lotsch, *J. Mater. Chem.*, 2012, **22**, 10119-10133.

20. A. M. Spokoyny, D. Kim, A. Sumrein and C. A. Mirkin, *Chem. Soc. Rev.*, 2009, **38**, 1218-1227.

21. Y. Peng, Y. Li, Y. Ban, H. Jin, W. Jiao, X. Liu and W. Yang, *Science*, 2014, **346**, 1356-1359.

22. T. Rodenas, I. Luz, G. Prieto, B. Seoane, H. Miro, A. Corma, F. Kapteijn, F. X. Llabrés i Xamena and J. Gascon, *Nat. Mater.*, 2015, **14**, 48-55.

23. P.-Z. Li, Y. Maeda and Q. Xu, *Chem. Commun.*, 2011, **47**, 8436-8438.

24. Y. Xia, X. Xia and H.-C. Peng, *J. Am. Chem. Soc.*, 2015, **137**, 7947-7966.

25. A. Umemura, S. Diring, S. Furukawa, H. Uehara, T. Tsuruoka and S. Kitagawa, *J. Am. Chem. Soc.*, 2011, **133**, 15506-15513.

26. W. Cho, H. J. Lee and M. Oh, *J. Am. Chem. Soc.*, 2008, **130**, 16943-16946.

27. S. S.-Y. Chui, S. M.-F. Lo, J. P. H. Charmant, A. G. Orpen and I. D. Williams, *Science*, 1999, **283**, 1148-1150.

28. J. Gascon, S. Aguado and F. Kapteijn, *Microporous Mesoporous Mater.*, 2008, **113**, 132-138.

29. Y.-K. Seo, G. Hundal, I. T. Jang, Y. K. Hwang, C.-H. Jun and J.-S. Chang, *Microporous Mesoporous Mater.*, 2009, **119**, 331-337.

30. G. Majano, O. Martin, M. Hammes, S. Smeets, C. Baerlocher and J. Pérez-Ramírez, *Adv. Funct. Mater.*, 2014, **24**, 3855-3865.

31. Y.-H. Ma, P.-Z. Ma, T. Yao and J.-T. Hao, *Acta Crystallogr. E, Structure reports online*, 2013, **69**, m538.

32. R. Pech and J. Pickardt, *Acta Crystallogr. C*, 1988, **44**, 992-994.

33. S. L. Xiong and H. C. Zeng, *Angew. Chem. Int. Ed.*, 2012, **51**, 949-952.

34. C. C. Yec and H. C. Zeng, *Chem. Mater.*, 2012, **24**, 1917-1929.

35. Y. Liu, W. Zhang, S. Li, C. Cui, J. Wu, H. Chen and F. Huo, *Chem. Mater.*, 2014, **26**, 1119-1125.

36. F. H. Herbstein and M. Kapon, *Acta Crystallogr. B*, 1979, **35**, 1614-1619.

37. W. L. Leong and J. J. Vittal, *Chem. Rev.*, 2011, **111**, 688-764.

38. J. Jiang, K. Zhao, X. Xiao and L. Zhang, *J. Am. Chem. Soc.*, 2012, **134**, 4473-4476.

39. C. Carbonell, I. Imaz and D. Maspoch, *J. Am. Chem. Soc.*, 2011, **133**, 2144-2147.

40. E. Biemmi, C. Scherb and T. Bein, *J. Am. Chem. Soc.*, 2007, **129**, 8054-8055.

41. D. Zacher, A. Baunemann, S. Hermes and R. A. Fischer, *J. Mater. Chem.*, 2007, **17**, 2785-2792.

42. S. Li, G. Lu, X. Huang, H. Li, Y. Sun, H. Zhang, X. Chen and F. Huo, *Chem. Commun.*, 2012, **48**, 11901-11903.

43. Y. Yang, S. Matsubara, L. Xiong, T. Hayakawa and M. Nogami, *J. Phys. Chem. C*, 2007, **111**, 9095-9104.

44. H. Chen, L. Wang, J. Yang and R. T. Yang, *J. Phys. Chem. C*, 2013, **117**, 7565-7576.

45. O. Kozachuk, K. Yusenko, H. Noei, Y. Wang, S. Walleck, T. Glaser and R. A. Fischer, *Chem. Commun.*, 2011, **47**, 8509-8511.

46. H. Al-Kutubi, J. Gascon, E. J. R. Sudhölter and L. Rassaei, *ChemElectroChem*, 2015, **2**, 462-474.

47. J. B. DeCoste, G. W. Peterson, B. J. Schindler, K. L. Killops, M. A. Browe and J. J. Mahle, *J. Mater. Chem. A*, 2013, **1**, 11922-11932.

48. R. Li, X. Ren, X. Feng, X. Li, C. Hu and B. Wang, *Chem. Commun.*, 2014, **50**, 6894-6897.

49. T. Qin, J. Gong, J. Ma, X. Wang, Y. Wang, Y. Xu, X. Shen and D. Zhu, *Chem. Commun.*, 2014, **50**, 15886-15889.

50. M. Schlesinger, S. Schulze, M. Hietschold and M. Mehring, *Microporous Mesoporous Mater.*, 2010, **132**, 121-127.

51. L. Zhang, J. Zhang, Q. Kuang, S. Xie, Z. Jiang, Z. Xie and L. Zheng, *J. Am. Chem. Soc.*, 2011, **133**, 17114-17117.

52. C. Wei, X. Li, F. Xu, H. Tan, Z. Li, L. Sun and Y. Song, *Anal. Methods*, 2014, **6**, 1550-1557.

53. I. A. Khan, A. Badshah, M. A. Nadeem, N. Haider and M. A. Nadeem, *Int. J. Hydrogen Energy*, 2014, **39**, 19609-19620.

54. W. Wang, S. Wang, X. Ma and J. Gong, *Chem. Soc. Rev.*, 2011, **40**, 3703-3727.

55. Y. Sheng and H. C. Zeng, *Chem. Mater.*, 2015, **27**, 658-667.

56. F. Arena, K. Barbera, G. Italiano, G. Bonura, L. Spadaro and F. Frusteri, *J. Catal.*, 2007, **249**, 185-194.

57. M. Müller, S. Hermes, K. Kähler, M. W. E. van den Berg, M. Muhler and R. A. Fischer, *Chem. Mater.*, 2008, **20**, 4576-4587.

58. T. Maihom, S. Wannakao, B. Boekfa and J. Limtrakul, *J. Phys. Chem. C*, 2013, **117**, 17650-17658.

59. S. Gao, N. Zhao, M. Shu and S. Che, *Appl. Catal. A*, 2010, **388**, 196-201.

60. H. Liu, Y. Liu, Y. Li, Z. Tang and H. Jiang, *J. Phys. Chem. C*, 2010, **114**, 13362-13369.

61. H.-L. Jiang, T. Akita, T. Ishida, M. Haruta and Q. Xu, *J. Am. Chem. Soc.*, 2011, **133**, 1304-1306.

62. A. Aijaz, A. Karkamkar, Y. J. Choi, N. Tsumori, E. Rönnebro, T. Autrey, H. Shioyama and Q. Xu, *J. Am. Chem. Soc.*, 2012, **134**, 13926-13929.

63. Y. Zhou and H. C. Zeng, *J. Am. Chem. Soc.*, 2014, **136**, 13805-13817.

64. Y.-Z. Chen, Y.-X. Zhou, H. Wang, J. Lu, T. Uchida, Q. Xu, S.-H. Yu and H.-L. Jiang, *ACS Catal.*, 2015, **5**, 2062-2069.

65. X. Gu, Z.-H. Lu, H.-L. Jiang, T. Akita and Q. Xu, *J. Am. Chem. Soc.*, 2011, **133**, 11822-11825.

66. J. Li, C.-y. Liu and Y. Liu, *J. Mater. Chem.*, 2012, **22**, 8426-8430.

67. M. H. Rashid, R. R. Bhattacharjee, A. Kotal and T. K. Mandal, *Langmuir.*, 2006, **22**, 7141-7143.

68. K. Kuroda, T. Ishida and M. Haruta, *J. Mol. Catal. A*, 2009, **298**, 7-11.

69. X. Huang, C. Guo, J. Zuo, N. Zheng and G. D. Stucky, *Small*, 2009, **5**, 361-365.

Chapter 7 Conclusions and Recommendations

7.1. Conclusions

In summary, this dissertation has presented some examples on integrated nanocatalysts (INCs), including the concepts, properties, characterizations, and applications. Rational design and synthesis of INCs on multiple scales is the ultimate goal for catalyst researchers. It is undeniable that the development of mesoporous silica/silicate and microporous MOF based INCs will have significant impacts on both academia and industry. The major findings are summarized as follows:

(1) We have developed a facile synthetic strategy for the preparation of carbon nanotubes (CNTs) based hollow-structured mesoporous catalysts (HMCs), and have investigated a series of structural intermediates or analogues associated to this new class of INCs. Six types of catalytic nanoparticles (namely, Au, Pd, Au-Pd alloy, Co_3O_4, ZnO, and TiO_2) have been anchored individually or combinatorially onto the surfaces of CNTs with good dispersion. Mesoporous silica, or microporous ZIF-8 and Nb_2O_5 can also be integrated as single or double coating shells on CNTs, wherein the nanoparticles are moored between the CNT and shells giving rise to a cable-like configuration.

(2) We have reported a general and facile self-template strategy for the assembly of metal NPs (Au, Ag, Pt), metal alloy NPs (Au-Pd), metal oxide NPs (Fe_3O_4, MoO_2), CNTs, or the hybrid materials (CNT@Au-Pd) with the porous *bubbles within a bubble manganese silicate* to form hierarchical nanocatalysts. We believe that these synthetic approaches have a generality for the design and architecture of hollow mesoporous catalysts. Most importantly, the functionalized manganese silicate based INCs and rare earth-doped derivatives exhibit significantly enhanced activity and stability for CO_2 hydrogenation.

(3) We have demonstrated a successful design, fabrication and application of INCs with sandwich-structures, where uniform Pt nanoparticles were supported on the hollow mesoporous transition metal silicates layer and also encapsulated with polydopamine layer with controllable thickness. The as-prepared MnSi@Pt@PDA catalysts are charge switchable, which show negative surface charge at pH of 10, and positive charge at pH of 2. This charge sensitivity of the nanocatalysts was created by the conformably coated PDA layer. Most importantly, the smart MnSi@Pt@PDA catalysts show selective catalytic degradation of organic dyes depending on pH: they own enhanced degradation efficiency towards cationic dyes at pH of 10, whereas, the anionic dyes were preferably degraded at pH of 2.

(4) We have devised a shape-controlled method for fabrication of a series of low-dimensional copper containing MOF crystals using Cu_2O nanoparticles as a copper source. The utilization of solid-state metal ion source not only prompts the crystallization of MOFs at mild conditions (such as room temperature and ambient pressure), but also leads to highly anisotropic growth of the MOFs *via* kinetically adjusting coordination behaviors. Regarding the catalytic applications, on one hand, we have converted the copper containing MOFs into several copper based nanocatalysts (*e.g.*, CuO, or CuO-Cu_2O, or even Cu). On the other hand, also importantly, Cu(HBTC)-1 nanosheets can be used as a versatile support for formation and immobilization of various noble metal nanoparticles (*e.g.*, Au, Ag, Pt, Pd, $Au_{0.4}Pt_{0.6}$, $Au_{0.4}Pd_{0.6}$ and $Au_{0.3}Pt_{0.3}$ $Pd_{0.4}$), due to the capping roles of the free carboxylic groups in Cu(HBTC)-1. We believe that the transformation of Cu(HBTC)-1 nanosheets into supported metal nanocatalysts would help open up new possibilities to make shape-controlled MOFs with low crystal dimensions for heterogeneous catalysis applications.

7.2. Recommendations

Even though substantial progresses have been made in the past few years, it is still a great challenge for fabrication of high quality integrated nanocatalysts (INCs) with simultaneous controls over their dimensions, morphologies, compositions, and porosities. Toward this move, several considerations must

be addressed for future research activities of this field. We believe that the issues below are significant in terms of promoting INCs into practical applications for industrial markets.

(i) Although some prevailing methods for fabricating INCs have gained great success at a laboratory scale, they are not currently feasible for scale-up. Thus, more research attention should be paid for the production of INCs at a large scale with reasonable cost.

(ii) The integration of different NPs on porous support would produce multiple interfaces, which is important for creating synergistic effects from multiple components, but the global control over the spatial distribution and arrangement of building blocks on INCs is still difficult.

(iii) The multifunctionality of INCs can be realized by integration of more than two active sites such as bimetallic or multimetallic catalysts, but few catalytic applications involving such multistep transformations have been demonstrated. Therefore, more tandem catalysis reactions are needed for proving the role of each component in INCs.

(iv) To enhance the interactions between active components and the porous support, it is conceivable to bridge them chemically. Different from the surfactants for synthesis of single-phase NPs, bridging molecules introduced in anchoring NPs on porous support require multiple chelating abilities to

connect them. However, their bonding descriptions have been largely ignored and a general guideline for choosing appropriate linkers is still lacking.

(v) Further organization of INCs into hierarchically ordered superstructures (*i.e.*, supracatalysts that are ensembles of individual INCs with overall dimensions comparable to industrial catalysts) is important for the applications of chemical processing and the recovery separation after use, especially for their use in fixed bed reactors. With catalytic components in nanoscale, in principle, such supracatalysts should also be able to offer the same superior activities as their initial building blocks. The verification of this postulation is clearly needed in future research when we target at the paradigmatic shift to "make-on-demand" for the INCs.

Publications

Journal papers:

1. **Zhan, G.**; Zeng, H. C., Synthesis and Functionalization of Oriented Metal-Organic-Framework Nanosheets: Toward a Series of 2D Catalysts. Advanced Functional Materials 2016, 26 (19), 3268. (IF: 11.8)

2. **Zhan, G.**; Zeng, H. C., Integrated Nanocatalysts with Mesoporous Silica/Silicate and Microporous MOF Materials. Coordination Chemistry Reviews 2016, 320-321, 181. (IF: 12.994)

3. **Zhan, G.**; Zeng, H. C., General Strategy for Preparation of Carbon-Nanotube-Supported Nanocatalysts with Hollow Cavities and Mesoporous Shells. Chemistry of Materials 2015, 27 (3), 726. (IF: 9.407)

4. **Zhan, G.**; Zeng, H. C., Charge-Switchable Integrated Nanocatalysts for Substrate-Selective Degradation in Advanced Oxidation Processes. Chemistry of Materials 2016, 28 (13), 4572. (IF: 9.407)

5. **Zhan, G.**; Yec, C. C.; Zeng, H. C., Mesoporous Bubble-like Manganese Silicate as a Versatile Platform for Design and Synthesis of Nanostructured Catalysts. Chemistry-A European Journal 2015, 21 (5), 1882. (IF: 5.731)

6. **Zhan, G.**; Zeng, H. C., An Alternative Synthetic Approach for Macro-Meso-Microporous Metal-Organic Frameworks via a "Domain Growth" Mechanism. Chemical Communications 2016, 52, 8432. (IF: 6.567)

Conference presentations:

1. **Zhan, G.**; Zeng, H. C., Architectural Design of Hollow Mesoporous Composite Nanotubes as Robust Catalysts for Benzyl Alcohol Oxidation. In 2014 AIChE Annual Meeting, Atlanta, USA, 16-21 November, 2014 (Oral presentation)
2. **Zhan, G.**; Zeng, H. C., One-Dimensional Capsule Catalysts: Design, Synthesis, Integration, and Application of Carbon-Nanotube-Supported Nanocatalysts with Porous Membrane-like Shells. In 6th Materials Research Society of Singapore (MRS-S) Conference on Advanced Materials, Singapore, 22-24 July, 2014. (Poster presentation)